LA-6024

c.3

UC-20
Reporting Date: July 1975
Issued: January 1976

Conceptual Design Study of a Scyllac Fusion Test Reactor

Compiler

Keith I. Thomassen

Contributors

James L. Anderson
Sumner Barr
Robert Bartholomew
David Blevins
William Bradley
Emmett Brazier
Richard Browning
James Dickinson
Donald Dudziak
Siegfried Gerstl
Roy Haarman
Kenneth Hanks
Lash Hansborough
Donald Houck
Franz Jahoda
Roland Jalbert
Donald Keigher
Edwin Kemp
Charles R. King
David Kirby
Robert Krakowski
John Lillberg
Rulon Linford
Thomas McDonald
Clair Nielson
William Nunnally
Thomas Oliphant
H. Don Orr
William Purtymun
John Rand
John Rogers
Donald Sandstrom
Richard Siemon
Walter Stone
Clarke Swannack
Keith Thomassen
Robert W. Turner
Dwayne Vier
Herbert Vogel
John L. Warren
David Weldon
K. E. Williamson, Jr.

los alamos
scientific laboratory
of the University of California
LOS ALAMOS, NEW MEXICO 87545

An Affirmative Action/Equal Opportunity Employer

UNITED STATES
ENERGY RESEARCH AND DEVELOPMENT ADMINISTRATION
CONTRACT W-7405-ENG. 36

Work supported by the Division of Controlled Thermonuclear Research,
U.S. Energy Research and Development Administration.

Printed in the United States of America. Available from
National Technical Information Service
U.S. Department of Commerce
5285 Port Royal Road
Springfield, VA 22151
Price: Printed Copy $8.75 Microfiche $2.25

SCYLLAC FUSION TEST REACTOR

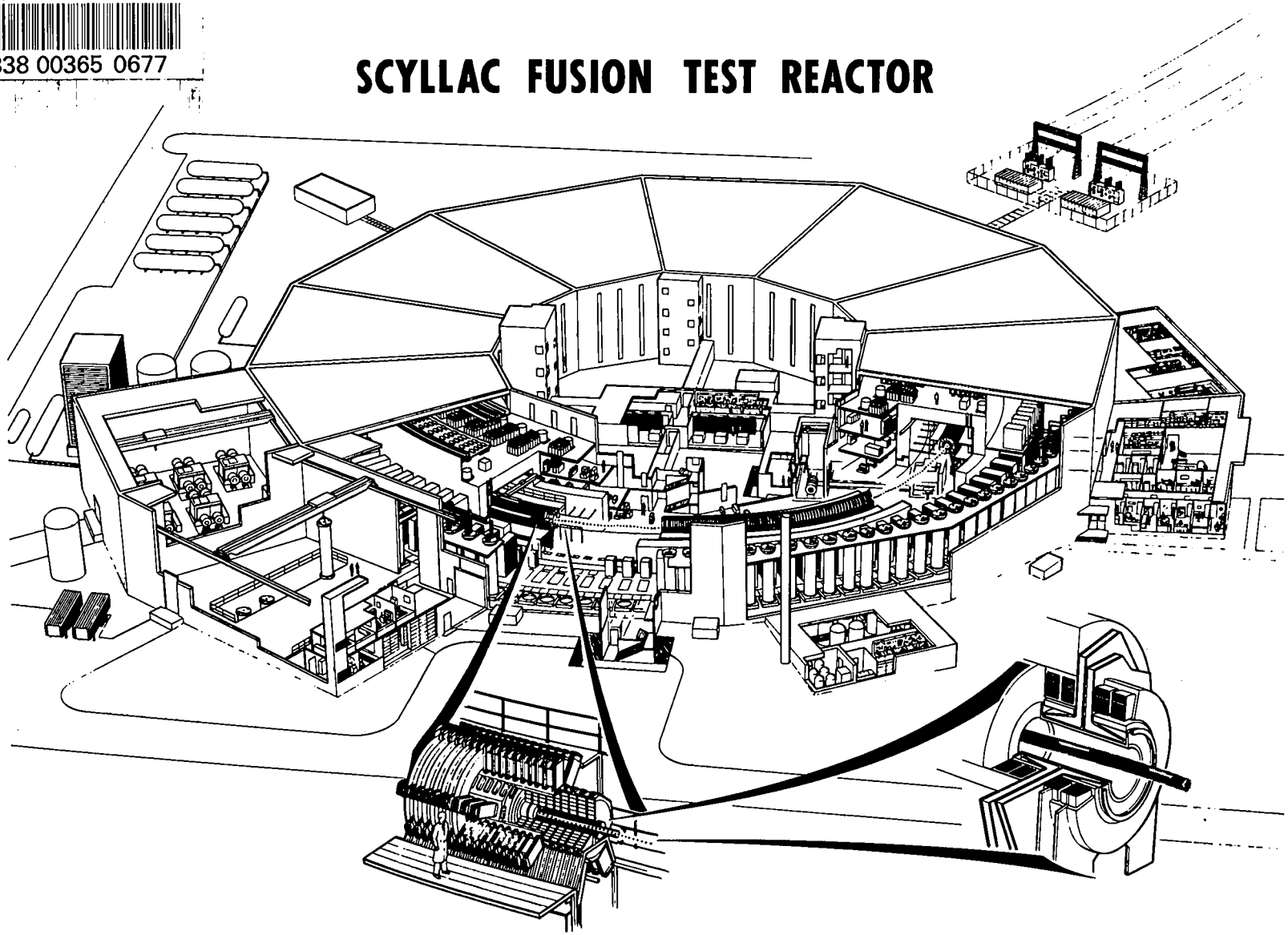

CONTENTS

CONCEPTUAL DESIGN STUDY OF A SCYLLAC FUSION TEST REACTOR

Compiled by

Keith I. Thomassen

I. INTRODUCTION

The report describes a conceptual design study of a fusion test reactor based on the Scyllac toroidal theta-pinch approach to fusion. It is not the first attempt to describe the physics and technology required for demonstrating scientific feasibility of the approach, but it is the most complete design in the sense that the physics necessary to achieve the device goals is extrapolated from experimentally tested MHD theories of toroidal systems, and it uses technological systems whose engineering performance has been carefully calculated to ensure that they meet the machine requirements.

Developmental effort is required in some of the systems, and the extrapolations from presently understood MHD theory and experiment are such that an intermediate device of large major radius is clearly indicated before construction of the Scyllac Fusion Test Reactor (SFTR). The major reason for this early conceptual design is, in fact, to bring into focus the issues in both the theory and technology of the device. In this way, developmental guidance will be available for decisions on technological programs, and the course to be pursued by the experimental physics program will be more sharply defined.

An earlier study[1] proposed a number of the central ideas, such as the separated shock and superconducting energy storage. Here we build on these ideas, give them substance using current knowledge of plasma physics, and propose a complete engineering design.

The machine is designed to achieve one central objective, to demonstrate "breakeven" or feasibility of the concept. The objective can be and has been defined many ways. The first study[1] used the Lawson criterion[2] to define feasibility. As the SFTR is a pulsed high-β machine, one could also define breakeven during some arbitrary time interval during the burn and require the average power output from neutrons to balance the average plasma power loss by radiation and other energy transport mechanisms. For example, the peak neutron power output is ~110 MW, while the bremsstrahlung is ~7 MW. Internal plasma losses are ~20 MW (for classical diffusion losses), hence we more than break even at peak compression. The most restrictive definition, which we adopt here, is that the total energy output in neutrons during the pulse (2 MJ) equals the stored energy in the plasma (at its maximum). In so doing we exceed the Lawson criterion.

To meet the design objective, subject to restrictions on equilibrium, stability, and high voltage technology, a large aspect ratio (major to minor radius) machine is needed. After some trial designs, a 40-m major radius, 10-cm minor radius device was chosen. The minor radius is chosen so as to have a reasonable volume of plasma between the 2- to 3-cm-thick sheaths which form on implosion. The major radius was also chosen somewhat arbitrarily after a preliminary assessment to determine an approximate minimum value.

On completion of this design it was heartening to note that only a few untested ideas or technologies stand between the present program and SFTR. These include wall stabilization of the m = 1 mode, fabrication of the end-fed Marshall coil for implosion heating, and the large superconducting Magnetic Energy Transfer and Storage (METS) system. The last of these can be replaced by very conventional systems, such as capacitors, or by simplified inductive energy storage (room temperature, with motor-generator or line charging). Of course, plasma transport on the millisecond time scale, if it is much faster than classical theory dictates, may also be a problem. However, these studies are to be part of the experimental program for SFTR.

REFERENCES (Chap. I)

1. F. L. Ribe, "Parameter Study of a Long, Separated Shock Θ-Pinch with Superconducting Inductive-Energy Storage," Los Alamos Scientific Laboratory Report LA-4828-MS (December 1971).

2. J. D. Lawson, "Some Criteria for a Power Producing Thermonuclear Reactor," Proc. Phys. Soc. (London) **B70**, 6 (1957).

II. SCIENTIFIC MOTIVATION

2.1 BACKGROUND

Theta-pinch research, since its inception in the mid-1950's, has been centered at Los Alamos. The earliest device, Scylla, was a 10-cm linear device driven by a 30-kJ capacitor bank. The linear work culminated with Scylla-IV, a 1-m linear machine in which ~4-keV ions at $\beta \sim 0.8$ - 1.0 were produced.

End losses dominated the linear pinches, so the closed Scylla, known as Scyllac, was first proposed in 1966. To provide an equilibrium in toroidal geometry the M&S bumpy torus was first proposed, but stability analyses led to the choice of the more favorable stellarator configuration with $\ell = 0,1$ fields providing equilibrium.

The first experiments, in April 1971, were with a 5-m arc of the 2.4-m-radius machine. These experiments demonstrated the existence of the toroidal equilibrium, but plasma was lost to the ends and by gross motion to the wall. The wall motion was either by loss of equilibrium as β changed (with plasma end-cooling), or by an m = 1 mode as predicted theoretically. There was insufficient evidence to distinguish between the two.

The next experiments, in 1973, on an 8-m sector of a 4-m-radius torus, verified the MHD scaling of the plasma equilibrium with major radius. Again, wall motion was observed but its cause could not be unambiguously identified. Conversion to the full Scyllac torus and operation of the device began in April 1974.

To control the unstable m = 1 gross motion of the plasma, the first scheme envisioned was to oscillate the magnetic field for dynamic stabilization. The required amplifier power was quite large, so the idea was soon rejected. Since 1970, a program to develop feedback control amplifiers for Scyllac has been in progress. These amplifiers drive auxiliary $\ell = 0$ coils in the $\ell = 0,1$ system, or $\ell = 2$ coils in an $\ell = 0,1,2$ system.

The main results of experiments on the full torus without feedback were to confirm the existence of the m = 1 mode and verify theoretically predicted MHD growth rates of the toroidal mode numbers n (around the torus). The growth rates decrease with increasing n, with n = 6 being the last unstable mode.

One further result was that the maximum growth time equaled the delay time of the feedback amplifiers, which is the limiting condition for a successful feedback experiment. At this limit, stability can be achieved only if the initial position and velocity of the plasma are zero when the amplifiers are switched on. To accommodate a realistic range of initial conditions, the growth rate times delay time should be ~1/3 rather than unity. Consequently, the $\ell = 0,1$ wavelength, β, and toroidal field were changed to lower the growth rate by a factor of 3. A sector of the derated machine has been operated, confirming the expected lower growth rate, and feedback amplifiers are being installed.

2.2 PRESENT PROGRAM

The toroidal theta-pinch program presently has several components. The major experiment of course is Scyllac, and feedback experiments on the derated sector will soon be under way. Another major direction centers on implosion and staging experiments, designed to create hot, wall-stabilized plasmas. Wall stabilization requires a large ratio of plasma-to-wall radii (a/b). In Scyllac, implosion and compression are inseparable, and the plasmas are too far from the wall for stability.

Implosion heating with a very fast rising magnetic field leaves the plasma radius relatively large, but to bring the field up in a time which is short compared to the time for the plasma boundary to move to its minimum radial position requires very high voltage circuits. The technology of producing the required magnetic field waveforms is being pursued in the Staged Theta Pinch (STP) experiment.

Experiments aimed at understanding the physics of the implosion process are being pursued both in STP and in the Implosion-Heating Experiment (IHX). In the latter, one produces, as nearly as possible, a step function magnetic field waveform in order to compare the dynamics of the process with predictions from plasma simulation codes and other plasma models.

The Scyllac program is expected to culminate in a Large Staged Scyllac (LSS) experiment. In LSS, the major radius will be large (~30 m) to reduce the MHD growth rates and to allow for wall stabilization of the imploded, staged plasma. The ratio a/b which provides for wall stabilization can be smaller for larger major radii, hence more adiabatic compression heating is permitted.

2.3 NEED FOR SFTR

The present Scyllac program is expected to terminate with LSS in which gross MHD stability (to $m \geq 1$ mode) is to be demonstrated. The Scyllac program as such will have tested the salient features of the toroidal high-β stellarator configuration. It remains to show long-term stability and confinement, to reach ignition temperatures, and meet Lawson or breakeven conditions.

The achievement of the Lawson criterion has long been recognized as a milestone toward pure fusion systems. Its achievement is a significant feat, not only for the physics it represents, but for the technology it implies. In the Tokamak program this step lies beyond the Tokamak Fusion Test Reactor (TFTR), but short of planned Engineering Power Reactors (EPR's).

To meet the Lawson criterion one must burn a D-T fuel, a step of major significance for CTR. The intended use of tritium in an experiment has major consequences in the design of the machine, particularly in handling and containment of the tritium. Interestingly, the amounts to be handled are not large, and the techniques for doing so are rather straightforward extensions of present practice at Los Alamos.

A more significant impact of D-T burning is the neutron production and associated activation of structures in the machine. The shielding, remote handling, and safety aspects of the device require very special care and add to the cost and complexity of the machine. Thus, D-T burning is an important step for the program, to be faced for the first time in SFTR, and links the present physics program with the Reference Theta Pinch Reactor (RTPR) and intermediate experimental reactors.

In the theta-pinch program, the experiment is needed to investigate long-term confinement, beyond the 100- to 300-μs time scale of LSS, to the tens of milliseconds, where localized MHD modes or enhanced transport may be important. Also, several new technological systems associated with the longer time scales of the experiment must be tested on the scale of SFTR. The implosion-heating circuitry, including the Marshall coil and ferrite isolation, involves departures from present systems and requires a system test. The METS superconducting system will receive its first large-scale test in SFTR.

The merging of physics and technology in SFTR to achieve breakeven is the primary purpose for the device. The results of the work there form the basis for further steps toward power-producing fusion reactors based on the Scyllac principle.

III. DESIGN CRITERIA

There is one primary objective of the design—the achievement of breakeven. However, a number of secondary criteria which have influenced the design are described in this section, as is the primary goal.

We first define Q, the ratio of thermonuclear output energy to the maximum internal plasma energy W_{pm},

$$Q(t) = \frac{\int_0^t P_n(x)\,dx}{W_{pm}}$$

where P_n is the power output from neutrons, taken at 20 MeV per neutron to account for released binding energy in the structure around the plasma. As the burn proceeds, Q increases, and the objective of breakeven is defined as reaching Q = 1, which occurs near the end of the pulse.

Another criterion is to minimize the machine cost, and this is done intuitively by limiting the major radius. However, a larger aspect ratio gives a greater stability margin, hence a delicate balance must be struck. The major radius is also dependent on the technique chosen for MHD stability, with wall stabilization permitting the least compression, hence requiring a larger radius to maintain the required aspect ratio. If feedback control of the m = 1 mode were feasible, and we believe it may be, a smaller machine could be constructed to reach Q = 1. However, this appears to be the less conservative of the two approaches to stability.

The implosion-heating system involves a number of tradeoffs, centering on the high voltage requirements to achieve significant initial temperatures. One cannot rely almost entirely on slow compression heating since the plasma would be overcompressed for stability. Also, low initial temperatures permit the field to diffuse into the plasma. Finally, too much adiabatic compression implies a large field-to-plasma volume, hence a large magnetic energy to plasma energy ratio. Such a scheme does not extrapolate well to a reactor, which must minimize the amount of pulsed magnetic energy.

The efficiency of energy transfer by implosion is significantly higher than the efficiency of transfer of adiabatic compression energy. Thus, it would appear that one should do as much implosion heating as possible, limited only by high voltage constraints. In fact, one should minimize the implosion-heating energy consistent with maintaining a large plasma radius for stability, and consistent with avoiding too large a compression supply. In so doing, one arrives at a system with voltages near the technological limit.

One technique for getting higher azimuthal electric field strengths in the implosion coil is to use partial turn coils. In this way a given voltage produces more field, hence more implosion heating. The limit to this method is the internal and source inductance of the structure, which should not exceed the load inductance. A partial turn coil to produce a toroidal field, which could be fed from one end, was devised by John Marshall at Los Alamos, hence is called a Marshall coil.

Since the implosion coils are fed by radial feed plates at the ends, the structures resemble nested top hats, with current entering the brim, flowing along the outer hat, back on the inner hat, and out the other brim. The current in the Marshall coil is forced to follow helices on the hats by slotting them in a helical manner, thus producing only toroidal fields inside the structure. The fabricability of this structure, which serves as a first-wall vacuum (and tritium) barrier is one of the more difficult technical developments required in SFTR. There also are limitations on the voltages it can withstand, hence the amount of implosion heating is limited.

The compressional energy source for SFTR can be one of a variety of systems, and we present here a discussion of these choices. The choices are the conventional capacitor bank and many forms of inductive energy-storage systems. At first glance, the 500-MJ requirement would appear to weigh heavily in favor of inductive systems, since the multiplicity of switches and timing circuits in the capacitor bank gives that scheme a reliability problem. However, the inductive energy system must also be modularized because of limitations set by current interrupting switches. The limitations come from the fact that the current to be interrupted, multiplied by the voltage on the switch after interruption, is approximately equal to the energy to be transferred, divided by the transfer time. Since the voltage-current product is a function of the switch characteristics, and the transfer time is fixed, a maximum energy is set by the switch rating. For SFTR, by using two parallel and two series switches, the composite rating of 25 kA times 60 kV limits the energy to 381 kJ, therefore requiring 1280 modules.

Although the multiplicity of components in the inductive system diminishes its inherent advantage of high-energy density storage, we believe the system still has an edge over pure capacitor systems. Further, the energy requirements of future systems almost surely dictate inductive systems, so early development for SFTR should be fruitful.

Various forms of inductive storage and transfer systems were considered. These include superconducting storage, with either superconducting switches or vacuum interrupters, and room temperature or nitrogen-cooled copper or aluminum storage coils, charged from the line, from motor-generator sets, or from a homopolar machine. The option of resonant transfer through a capacitor bank or straight transfer from the storage coil was also considered. The former allows nearly 100% efficiency of transfer, while the latter necessarily dissipates 50% in the switch and leaves 25% in the store. Thus, it requires four times the initial storage. Resonant transfer requires a capacitor bank with half the storage capacity of the inductive store, but cost comparison favors the resonant system. Since there are no start switches and trigger systems for the bank, the reliability is not in question.

The system we chose uses superconducting energy storage, vacuum interrupters, and the resonant transfer scheme. This system makes the least demand on charging supplies and has the most favorable impact on future technology for theta-pinch devices. It is neither the least expensive nor the most straightforward system to develop. Should we run into technical difficulties in superconducting development, we have designed a conventional room temperature inductive storage system with line charging. That design is described in Appendix I.

The tritium handling system is designed to minimize the amount of tritium that could be released in an accident, and is simplified by sending the spent tritium off-site for reclamation. Only 1 week's supply (300 mg for 20 discharges) will be in the vacuum system at any one time, being stored on uranium beds for injection or after-recovery. An on-site vault will store 2 g in gaseous form.

The vacuum wall of the Marshall coil is the primary containment system, and a surrounding cell with concrete walls is the secondary system. There are ventilation hoods over the areas where transfer into the vacuum system occurs, and these hoods are vented to a waste treatment facility. Leakage into the main experimental cell will be handled by replacing all the air in the cell using a large blower (in 1.5 h) and processing the old air in the waste treatment facility. Even after leakage of the entire 15 mg DT in one discharge, one can have routine access to the cell after 1.5 h.

To shield personnel from the 14-MeV neutrons from SFTR requires ~2 m of shielding material. This is accomplished by a 1/2-m primary shield around the toroidal structure between the compression coils and the implosion-heating capacitors. Surrounding this vessel is a cell with 1-1/2-m-thick concrete walls, allowing experimenters unlimited access just outside the cell.

The primary shield allows access to the cell shortly after a discharge, and also protects organic material in the implosion capacitors from radiation damage. Without such a shield, all maintenance inside the cell would have to be done by remote control. As is, only the modules inside the primary shield need be removed by remote handling equipment and transferred to hot cells for repair or transfer.

In designing subsystems for SFTR, many design choices must be made. The major criteria, those with significant impact on the shape and size of the structure or which determine its major characteristics, have been presented here.

IV. THEORETICAL CONCEPTS

4.1 OBJECTIVES

4.1.1 General Description

The basic objectives of SFTR are outlined in Chaps. II and III. Chapter IV presents the theoretical basis of one approach to achieving the two specific goals: (1) Q = 1 and (2) plasma stability. In Sec. 4.1 the plasma geometry and the requirements for the mathematical model are defined, and the general engineering plan to achieve the goals is presented.

4.1.2 Plasma and System Geometry

The parameters of the basic toroidal system are defined in Fig. 4-1. The mathematical model assumes that the plasma has a sharp boundary at an average radius a(t). The system, including the plasma, has a toroidal variation to provide plasma equilibrium.[1-4] This variation, shown in Fig. 4-2, has a wavelength λ and consists of three perturbations: the $\ell = 0$ (sausage-like) parameterized by δ_0, the $\ell = 1$ (helical) parameterized by δ_1, and the $\ell = 2$ (elliptical) parameterized by δ_2. Using the coordinates defined in Fig. 4-2, the plasma surface can be described (for small δ's) by

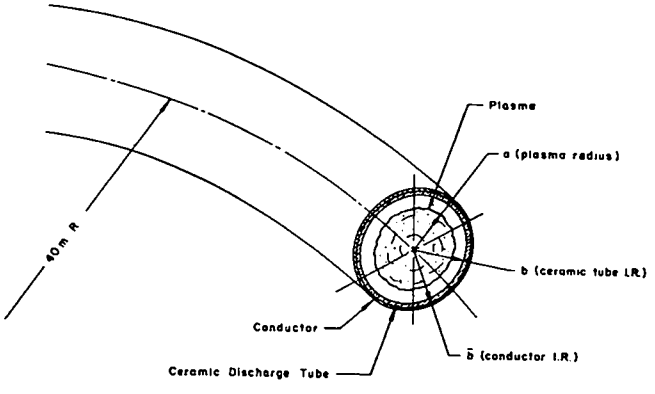

Fig. 4-1.
Geometry of the implosion coil conductor, the vacuum wall, and the plasma.

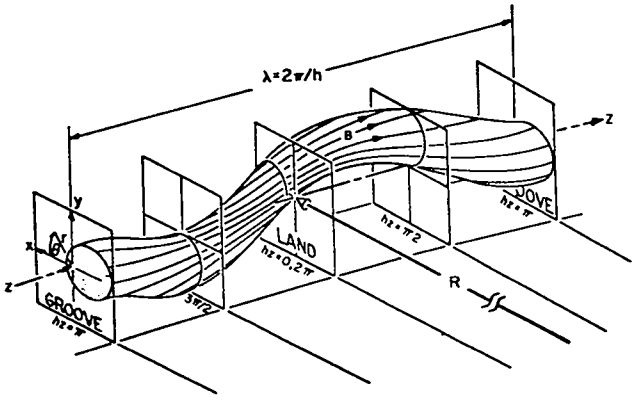

Fig. 4-2.
Plasma surface geometry showing the $\ell = 0$, 1, and 2 perturbations.

$$r = a[1 + \delta_2 \cos(2\theta - hz) + \delta_1 \cos(\theta - hz) - \delta_0 \cos hz]. \quad (1)$$

The addition of the $\ell = 2$ perturbation[5] to the usual Scyllac configuration[6] eases the technological requirements of the SFTR.

4.1.3 System Requirements

The mathematical model is used to determine the possibility of achieving Q = 1 with projected technology while maintaining plasma stability. In this section, Q is mathematically defined and the stability requirements are established.

4.1.3.1 Definition and Significance of Q

For the SFTR system Q is defined as the ratio of the total neutron energy output to the maximum plasma energy. During the burn cycle the plasma density n is assumed to be constant inside the average radius a(t) and the velocity distributions are assumed to be Maxwellian. Thus Q can be defined as

$$Q \equiv \frac{Y \int_0^{\infty} \left(\frac{n}{2}\right)^2 \langle\sigma v\rangle \, dt}{\frac{3}{2} n_c k_B (T_{ec} + T_{ic})} \quad . \tag{2}$$

The average energy yield per neutron Y is assumed to be 20 MeV/n. The subscripts c on the density and temperature in the denominator refer to the peak values which occur at maximum compression.

The goal of Q = 1 is assumed to be the "scientific breakeven" point and it should be noted that for the system described in this report Q = 1 is more stringent than $n\tau = 10^{14}$.

4.1.3.2 Plasma Equilibrium and Stability

The criterion presented here for equilibrium and stability is based on the sharp boundary, MHD model developed for Scyllac,[6] but it has been extended to include an $\ell = 2$ perturbation.[5] The analytic expressions are based on the so-called "old ordering" ($\delta_1 \ll ha \leq 1$, $h \equiv 2\pi/\lambda$)[1,2] which is violated by the SFTR parameters. As is explained in the Scyllac theory review in Ref. 6, the old ordering yields surprisingly accurate results (for $\beta \leq 0.95$ and $\beta\delta_1 < \pi^2/16$) when compared with the numerical results of a more accurate theory.[7] This new theory is based on an appropriate ordering where $ha < 1$ and δ_1 is arbitrary. Recently, the accuracy of the old ordering has been experimentally confirmed at Garching[8] for $\delta_1 = 3$. The usefulness of analytic expressions and the apparent accuracy of the old ordering motivate its use in this report.

Plasma equilibrium requires that the outward grad B force be balanced by the inward force arising from the plasma surface perturbation. For an $\ell = 0$, 1, 2 perturbation the equilibrium condition is

$$f_0\delta_0 + f_2\delta_2 = \frac{1}{h^2 a R \delta_1} \tag{3}$$

where f_0 and f_2 are functions of the plasma β as follows:

$$f_0 \equiv \frac{3 - 2\beta}{2} \tag{4}$$

$$f_2 \equiv \frac{2 - \beta}{2} \quad . \tag{5}$$

The condition for stability against growth of the m = 1 mode is

$$\left(\frac{a}{b}\right)^4 \geq g_0 \left(\frac{\delta_0}{\delta_1}\right)^2 + g_2 \left(\frac{\delta_2}{\delta_1}\right)^2 + g_1 (ha)^2 \tag{6}$$

where the g's are the following functions of β:

$$g_0 \equiv \frac{(3-2\beta)(1-\beta)}{\beta(2-\beta)} \tag{7}$$

$$g_1 \equiv \frac{(4-3\beta)(2-\beta)}{8\beta(1-\beta)} \tag{8}$$

$$g_2 \equiv \frac{(2-\beta)}{2\beta} \quad . \tag{9}$$

This stability criterion contains the stabilizing effect of the wall on the left side of the inequality, and the destabilizing effect due to bad curvature in the $\ell = 0$, 1, and 2 perturbations on the right side. The SFTR design requires that (3) and (6) be satisfied.

The m = 2 mode might also be unstable in the SFTR. The stability requirement for an $\ell = 0$, 1 perturbation is given by

$$\left(\frac{r_L}{a}\right)^2 \geq g_4 h^2 a^2 \delta_1^2 \tag{10}$$

where r_L is the ion Larmor radius and

$$g_4 \equiv \frac{2\beta^2(1-\beta)}{2-\beta} \tag{11}$$

The m = 2 mode has not been experimentally observed in the collisionless regime, so that neither the time asymptotic behavior of the mode nor the accuracy of (10) is known. Because of this lack of information, (10) has not been made a requirement of the SFTR design. However, (10) is never violated for the proposed operating conditions. Proposed experiments on Scylla IV-P (now under construction) will provide the needed information on the m = 2 instability for future iterations of the SFTR design.

The effects of these equilibrium and stability requirements on the design of SFTR are described in Secs. 4.1.4.2 and 4.1.4.3.

4.1.4 Proposed Approach

The proposed method of achieving Q = 1 and satisfying the stability requirements of Sec. 4.1.3 consists of heating the plasma by implosion and adiabatic compression, using the staging concept.[9] Plasma stability is achieved by a combination of wall stabilization and "slow" feedback control. This approach is explained and the reasons for choosing it are presented in the remainder of this section.

4.1.4.1 Staging Concept of Plasma Heating

Standard theta-pinch systems, including Scyllac, use a single capacitor bank to form one magnetic field pulse. The plasma is implosion or "shock" heated at the beginning of this pulse until the average speed of the plasma ions exceeds the magnetic piston speed. At this point the heating process begins the transition from implosion heating to adiabatic compression as the magnetic field continues to increase to its maximum value. When the peak field is reached the capacitor bank is crowbarred, allowing the field to decay exponentially.

The inductance in these standard systems must be sufficiently low to provide the fast-rising fields required by implosion heating. However, this low inductance limits the L/R time of the crowbarred field to the order of 100 μs. In present theta pinches, the plasma confinement time has always been less than the L/R time. In future systems such as SFTR the confinement times must exceed this 100 μs by 2 or 3 orders of magnitude and yet the inductance must be even lower to allow for more implosion heating.

The staging concept was proposed several years ago[9] to meet these disparate requirements of low inductance and long confinement times. Instead of a single bank, two separate systems are used. The low inductance implosion system provides the required fast-rising field (~100 ns) which is crowbarred or "staged" into the slowly rising (~1 ms) compression field. The compression system is sufficiently inductive to provide the long L/R times required by SFTR.

The staging approach is also economically sound. The major portion of the magnetic energy is supplied by the low cost (1-5¢/J) compression system as compared with the expensive (~75¢/J) implosion system. This difference in cost exemplifies the fact that the faster the energy must be transferred, the more technologically difficult and expensive the system. Thus, from an economic and technological view, the amount of implosion heating should be minimized.

4.1.4.1.1 Importance of Implosion Heating

Some implosion heating is required by plasma physics and reactor efficiency constraints. If an adiabatic compression field were applied to the typical 1- to 10-eV preionized plasma, the field would diffuse into the low conductivity plasma, producing virtually no compression. Some method such as electron-cyclotron resonance might be used in place of the implosion heating to increase the electron temperature and hence the conductivity; however, the efficiency requirements of future reactors will not allow the use of pure adiabatic compression to heat the ions.

The inefficiency of pure compression is emphasized by the following example. The adiabatic law requires a volumetric compression of nearly 32 000 to heat a 6-eV plasma to the 6 keV required for burning. If Q = 25 is assumed, as for RTPR,[10] the energy in the compression field would be more than 800 times greater than the thermal energy extracted from the reactor. This would limit the efficiency of the compression system intolerably.

These requirements of reactor efficiency and of high electrical conductivity in the plasma imply that some implosion heating will always be necessary in future theta-pinch reactors unless other techniques are used to heat both ions and electrons. The optimum ratio of implosion and compressional heating must be determined by assessing the plasma physics, technological, and economic goals and constraints of the specific device under consideration. The relevant discussion of SFTR constraints and design is presented in Sec. 4.1.4.3.

4.1.4.1.2 Efficiency of Implosion and Compressional Heating Systems

A few fundamental concepts of plasma heating efficiency presented here are helpful in the design of SFTR and perhaps other theta-pinch systems. To simplify the development, several assumptions are made. A sharp boundary model is assumed and the heating process is defined by an initial state (1) and a final state (2). The surface of the plasma volume in state (1) is chosen as the fixed boundary between the driving circuit and the "load" as shown in Fig. 4-3. The plasma heating efficiency in the load is discussed separately from the circuit transfer efficiency to the load.

The total efficiency of the system e_T is defined by

$$e_T \equiv e_c e_p \tag{12}$$

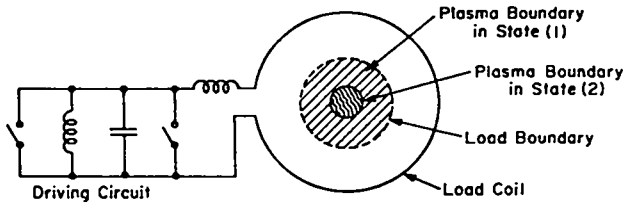

Fig. 4-3.
Schematic diagram of a driving circuit showing the spatial relation of the load coil and the plasma in states (1) and (2). The load boundary separates the "circuit" from the "load" for the purpose of calculating circuit and plasma heating efficiencies. The circuit shown here is similar to a compression circuit described in Sec. 5.4.2, but in this figure it represents a general circuit and no special emphasis is intended.

where e_c is the circuit efficiency and e_p is the plasma heating efficiency within the load boundary as defined by

$$e_c = \frac{\Delta E_L}{E_s} \tag{13}$$

$$e_p = \frac{\Delta E_p}{\Delta E_L} \tag{14}$$

The change in energy in the load ΔE_L includes the sum of the changes in both plasma energy ΔE_p and the field energy ΔE_B inside the load boundary, but does not include the field stored between the load boundary and the load coil. The symbol E_s represents the total stored energy in the circuit in state (1). This distinction between circuit efficiency and plasma heating efficiency allows a more lucid comparison of the implosion and compression systems.

The plasma efficiency can be determined by recognizing that the energy imparted to the plasma by the magnetic field is always given by

$$\Delta E_p = - \int_{V_{p1}}^{V_{p2}} \frac{B^2}{2\mu_0} \, dV_p \tag{15}$$

independent of the detailed state of the plasma. The numerical subscripts refer to the plasma volume V_p in states (1) and (2).

The adiabatic plasma efficiency e_{pa} can be calculated by assuming that the plasma is isotropic over three dimensions and adiabatic so that

$$pV_p^{5/3} = \text{constant} \tag{16}$$

and that pressure balance exists

$$\frac{B^2}{2\mu_0} = nk_B(T_e+T_i) = p \tag{17}$$

Equations (16) and (17) yield the required relation between B and V_p needed in (15). The resulting plasma heating efficiency for adiabatic compression is

$$e_{pa} = \frac{3}{2} \nu \frac{1 - \nu^{2/3}}{1 + \frac{1}{2}\nu^{-\frac{3}{2}}\nu^{5/3}} \tag{18}$$

which is plotted in Fig. 4-4. The value ν is the volumetric compression ratio

$$\nu \equiv \frac{V_{p2}}{V_{p1}} \tag{19}$$

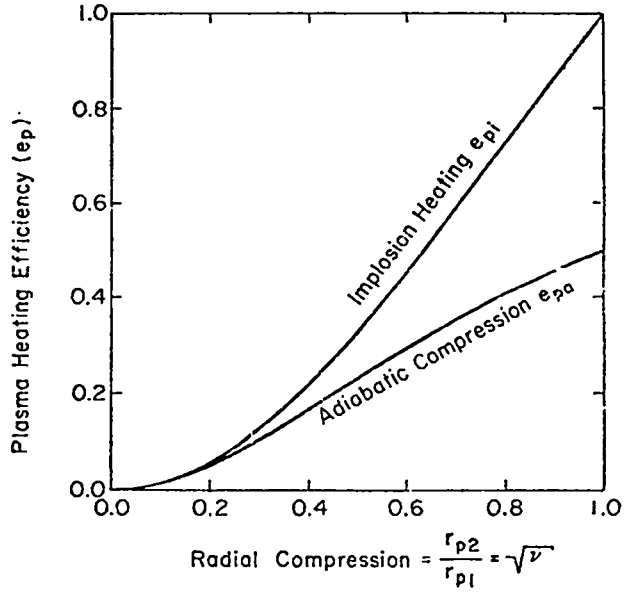

Fig. 4-4.
Comparison of the plasma heating efficiencies for implosion heating and adiabatic compression.

The least restrictive assumptions required to calculate the plasma heating efficiency for an implosion e_{pi} are that the change in plasma energy is large compared with the initial plasma energy.

$$\Delta E_p >> E_{p1} , \tag{20}$$

and that in state (2) the plasma thermalizes, isotropizes into three dimensions, and comes into pressure balance with the field

$$\frac{\Delta E_p}{E_{B_2}} \simeq \frac{E_{p2}}{E_{B_2}} = \frac{\frac{3}{2} V_{p2}}{V_L - V_{p_2}} . \tag{21}$$

The plasma heating efficiency for implosion heating e_{pi} is obtained directly from (21)

$$e_{pi} = \frac{3}{2} \nu \left[\frac{1}{1 + \frac{1}{2} \nu} \right] . \tag{22}$$

This efficiency is compared with e_{pa} in Fig. 4-4.

Several important observations can be made by examining Fig. 4-4 and the assumptions leading to Eqs. (18) and (22). First, nonadiabatic heating is always more "efficient" than adiabatic heating. Note that the asymptotic behavior of (18) and (22) for small ν is a result of the fact that for small ν the adiabatic assumptions are a special case of the implosion assumptions. Also, if a plasma is heated by a process that greatly changes the plasma energy without significantly changing the plasma volume, the process must be nonadiabatic. Finally, in contrast with economic and technological considerations, implosion heating appears most attractive when plasma heating efficiency is considered.

The general statements that can be made about circuit efficiency e_c are much less quantitative than those just made about e_p. One reason for the lack of simplicity in e_c is the virtually limitless variety of circuits that could be used in the implosion and compression systems. However, some qualitative statements can be made with approximate numerical examples for the systems proposed for the SFTR.

Compression circuits like the one in Fig. 4.3 can be built (with rise times on the order of 1 ms) to transfer virtually all of the stored energy E_s into the load coil. In this case, the efficiency e_c depends mainly on the relative volume of the load boundary V_{p1} and the load coil V_L

$$e_{ca} = \frac{1 + \frac{1}{2} \nu - \frac{3}{2} \nu^{5/3}}{\frac{V_L}{V_{p1}} + \frac{1}{2} \nu - \frac{3}{2} \nu^{5/3}} \tag{23}$$

The total efficiency becomes, using (12), (18), and (23),

$$e_{Ta} = \frac{3\nu(1 - \nu^{2/3})}{2 \frac{V_L}{V_{p1}} + \nu - 3\nu^{5/3}} . \tag{24}$$

Using $V_L/V_{p1} = 8.2$ for the SFTR compression system, Eq. (24) is plotted in Fig. 4-5. The value of $\sqrt{\nu}$ for the compression system in SFTR is about 0.5, thus

$$e_{Ta} \simeq 0.03 . \tag{25}$$

In general, implosion circuits are much more dissipative than compression circuits because of the greater speed of energy transfer. In addition to resistive losses, the circuit described in Sec. 4.3 is optimized with the source inductance comparable

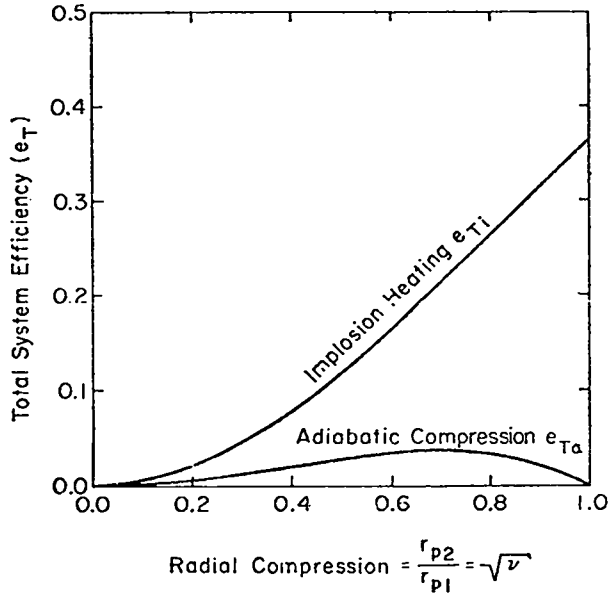

Fig. 4-5.
Comparison of total system efficiency for implosion heating and adiabatic compression in the SFTR system.

with the load coil inductance. These resistive and inductive losses limit the efficiency of energy transfer into the load coil to about 40%. Hence,

$$e_{ci} \simeq 0.4 \frac{1 + \frac{1}{2}\nu}{\frac{V_L}{V_{p1}} + \frac{1}{2}\nu} \quad . \tag{26}$$

The total implosion efficiency becomes, using (12), (22), and (26),

$$e_{Ti} \simeq 0.6 \frac{\nu}{\frac{V_L}{V_{p1}} + \frac{1}{2}\nu} \quad . \tag{27}$$

Using $V_L/V_{p1} = 1.14$ for the SFTR implosion system, Eq. (16) is compared with e_{Ta} in Fig. 4-5. The value of $\sqrt{\nu}$ for the implosion system in SFTR is about 0.7, so

$$e_{Ti} \simeq 0.3 \quad . \tag{28}$$

The comparison in Fig. 4-5 indicates that, in spite of the dissipative nature of the implosion circuit, the implosion system transfers a far larger fraction of its stored energy to the plasma than does the compression system. This fact might mislead one into doing all of the heating with the implosion system. If this mistake were made, the compression system would still have to supply essentially the same amount of energy simply to contain the plasma (no compression, i.e, $\sqrt{\nu} = 1.0$) during the long burn cycle. Hence the same compression system could have supplied a major portion of the plasma energy with essentially the same amount of stored energy. Obviously, the more heating done by the compression system, the more the cost and the technological difficulty of the implosion system are reduced. Looking beyond SFTR, in future reactor systems the compression field energy will be retrieved by the circuit and recycled with a high degree of efficiency in contrast to retrieving only a small portion of the wasted implosion field energy in the form of heat.

All these considerations indicate that as much of the plasma heating as possible should be done by adiabatic compression. The limitation on the fraction of heating done by compression will arise from some plasma physics consideration such as electrical conductivity or plasma stability, or it may be set by an efficiency requirement of the reactor. The remainder of the heating will have to be provided by the implosion system which should be made as efficient as possible by minimizing the complexity of the circuit and by maximizing the value of $\sqrt{\nu} = x_s$ for the implosion. A quantitative analysis of the dominant factors limiting the fraction of heating done by compression in SFTR is presented in Sec. 4.1.4.3.

4.1.4.2 Wall Stabilization and Slow Feedback Control

There are two conceptual techniques for achieving plasma stability. The design of the SFTR presented in this report is based on the concept of wall stabilization in conjunction with slow feedback control. Straight feedback (like that being developed for Scyllac) appears to have merit, but its impact on an SFTR design has not been fully investigated. The properties of both concepts are discussed and briefly compared in the remainder of this section.

4.1.4.2.1 Necessity for Slow Feedback Control in a Wall-Stabilized SFTR

The m = 1 mode cannot be wall-stabilized by the finite (noninfinite) conductivity implosion coil[11] even though the growth rate of the mode might be greatly reduced. The mode can be examined as the conductivity of the wall is theoretically increased from $\sigma = 0$.[12] In general, γ decreases as σ increases. When the inertial effects are no longer important compared with the dissipative effects of the conducting wall, the growth rate is given by the field diffusion rate through the wall. Thus, for a wall of finite conductivity, γ can be reduced but not to zero. Since the confinement time required in SFTR exceeds the field diffusion time, some feedback control is necessary.

The field diffusion time depends on the specific geometry of the system shown schematically in Fig. 4-6. The separation of the implosion and compression systems discussed in Sec. 4.1.4.1 requires the use of two distinct coils. The fractional turn implosion coil (see Sec. 5.2.2.1.1) provides the low inductance load for the implosion system. The multiturn, high-inductance compression coil, described in Sec. 5.2.2.1.2, is required to produce the 250-ms decay time for SFTR. The field diffuses through the metal of the implosion coil with the characteristic time

$$\tau_0 = \frac{\mu_0 \sigma \delta^2}{2} \quad . \tag{29}$$

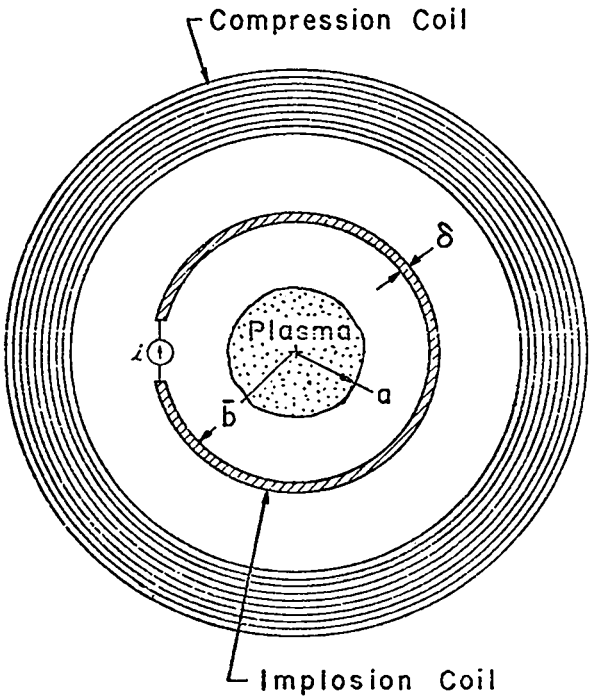

Fig. 4-6.
Schematic representation of the fractional turn implosion coil and multiturn compression coil.

However, the field enclosed by the coil decays at a slower rate given by the L/R time of the coil. For the simple coil shown in Fig. 4-6 with no plasma present,

$$\tau_{L/R} = \frac{\mu_0 \sigma \bar{b} \delta}{2} \quad . \tag{30}$$

Two complexities modify this simple model of field diffusion. The implosion coil is crowbarred by a switch. If the resistance of the switch is sufficiently high compared with that of the coil, the switch will dominate the L/R decay, invalidating Eq. (30). Even if the crowbar were perfect, the presence and motion of the plasma in conjunction with the $\ell = 1$ perturbation generate field perturbations that are responsible for wall stabilization. In the perfect crowbar condition, these field perturbations will decay at a rate given by (30) with $\bar{b}$ replaced with some characteristic length of the perturbation which could range from $\bar{b}$ to δ.

It is advantageous to increase the field decay time as much as possible because as τ increases, γ decreases. In addition, the required rise time of the compression field increases. The thickness of the conductor δ can be increased until the crowbar switch resistance dominates the L/R time. If δ were increased further, the L/R time would not increase appreciably, but the dissipation and distortion of the rising compression field would begin to increase sharply.

To maximize the L/R time and minimize dissipation of the compression field, the following limits are placed on δ

$$\frac{\mu_0 \sigma \delta^2}{2} < \tau_s << \frac{\mu_0 \sigma \bar{b} \delta}{2} \quad , \tag{31}$$

where τ_s is the crowbar-dominated L/R time of the implosion circuit. The subscript s is used to refer to the implosion or "shock" process to be consistent with the literature and to avoid confusion with subscript i for ions. As was mentioned in Sec. 4.1.4.1 the maximum crowbar times achieved on present systems have been on the order of 100 μs. The value projected for SFTR is $\tau_s = 230$ μs. Using this τ_s in (31) yields

$$0.059 << \delta < 2.5 \text{ mm} \quad . \tag{32}$$

The value chosen for SFTR is $\delta = 1.5$ mm.

With τ_s and δ determined, the following limits can be placed on the wall-stabilized growth rate

$$\frac{1}{\tau_s} \lesssim \gamma_{ws} \lesssim \frac{1}{\tau_0} \quad . \tag{33}$$

Simply stated, the growth rate is bounded on the lower side by the field decay rate due to the crowbar gap, and on the upper side by the diffusion rate of the field into the metal of the implosion coil. Evaluating (33) yields

$$4.3 \times 10^3 \lesssim \gamma_{ws} < 1.2 \times 10^4 \text{ s}^{-1} \quad . \tag{34}$$

Since $\gamma_{ws} \tau_r \lesssim 0.4$ is required for stabilization in a practical feedback system[13] with rise time τ_r,

$$\tau_r \lesssim 33 \text{ } \mu\text{s} \tag{35}$$

in the wall-stabilized SFTR.

4.1.4.2.2 Comparison of Straight Feedback with the Wall-Stabilization Feedback Combination

The major advantage of the wall-stabilized approach over straight feedback is the slower rise time required of the feedback system. In the case of straight feedback it is assumed that the plasma is compressed significantly beyond the limit imposed by (17), thus eliminating the effect of wall stabilization. Equation (17) was obtained from the growth

rate of the m = 1 mode for infinitely conducting walls ($\sigma = \infty$).

$$\gamma = hv_\alpha\beta\left[-\left(\frac{a}{b}\right)^4\delta_1^2 + g_0\delta_0^2 + g_2\delta_2^2 + g_1(ha)^2\delta_1^2\right]^{1/2} \quad (36)$$

where v_α, the Alvén speed, is

$$v_\alpha \equiv \frac{B}{(\mu_0 nm)^{1/2}} \quad . \quad (37)$$

The straight feedback system must be capable of responding to a growth rate given by (36) when the wall-stabilizing term (first term in the brackets) is ignored. Using typical SFTR parameters, this growth rate is

$$\gamma_f \simeq 3.5 \times 10^5 \ s^{-1} \quad . \quad (38)$$

Since $\gamma_f \tau_r \lesssim 0.4$, the required rise time is

$$\tau_r \lesssim 1.1 \ \mu s \quad . \quad (39)$$

A comparison of (39) with (35) indicates that the straight feedback system would have to be 30 times faster than the slow feedback system used in the wall-stabilized approach.

This faster rise time makes it more difficult to electrically isolate the straight feedback system from the implosion system. Both types of feedback system would have to use the implosion coil as the feedback drive coil. Feedback coils cannot be placed inside the implosion coil as in Scyllac because of the stringent, low source inductance requirements of the SFTR implosion system. They cannot be placed outside the implosion coil because the field penetration time through the implosion coil would be too slow to satisfy $\gamma\tau_r < 0.4$. Since the feedback system must be attached to the 270-kV implosion system, very effective electrical isolation is required to protect the feedback system. The greater the difference in the rise time between the feedback system and the implosion system (100 ns) the more effective the isolation can be made.

The major disadvantage of the wall-stabilized approach is that it requires a larger ratio of $a/\overline{b}$ and hence more implosion heating than the straight feedback approach. However, the reduction in implosion heating allowed by straight feedback may be small because of a constraint on the minimum DT filling pressure described in Sec. 4.1.4.3. This pressure restriction may produce economic limitations on the reduction of implosion heating that would dominate over the plasma conductivity limitation discussed in Sec. 4.1.4.1.1. Since the present SFTR design utilizes the minimum allowed filling pressure of 4 mtorr, a decrease in implosion heating necessitates high compressional heating. The result is a plasma with similar temperature but higher density, and this higher plasma pressure must be confined by a higher magnetic field from the compression system. A preliminary investigation indicates that limitations on the cost of the compression system may prevent the lowering of the implosion bank voltage by more than 20%. Although small, this reduction could be technologically important.

At this time the wall-stabilized approach appears the most promising, but the straight feedback system is not without merit. The experimental experience with wall stabilization, implosion heating, and feedback stabilization is much too scant to permit a final decision between wall stabilization and straight feedback at this time. The feedback experiments on Scyllac and the results from the STP, IHX, and resonant heating experiments will aid greatly in making that decision.

4.1.4.3 Operating Point Determination

The staging concept and wall-stabilization approach form the basis of this SFTR design. This approach was chosen as a result of the concepts presented in Secs. 4.1.4.1 and 4.1.4.2. In the remainder of this section, relationships derived elsewhere in Chap. IV are used to determine the numerical value or limits on a variety of machine and plasma parameters.

To aid in the following presentation, the temporal behavior of the magnetic field is plotted in Fig. 4-7 on a logarithmic time base. (A more complete discussion of the field behavior and the implosion and compression circuits is found in Secs. 4.2 and 4.3.) The implosion field rises in about 100 ns, oscillates briefly, and settles down to a value B_s at a time t_s. The implosion field decays at an exponential rate τ_s associated with the L/R time of the crowbarred implosion or "shock" circuit. During this decay, the compression field rises to a peak value of B_c in a time t_c. The compression circuit is crowbarred at $t = t_c$, allowing the field to decay at the exponential rate τ_c.

Several reasons for minimizing the amount of implosion heating were presented in Sec. 4.1.4.1.1. Another reason is apparent from a study of Fig. 4-7. As the ratio B_s/B_c is reduced, τ_s/t_c can be reduced,

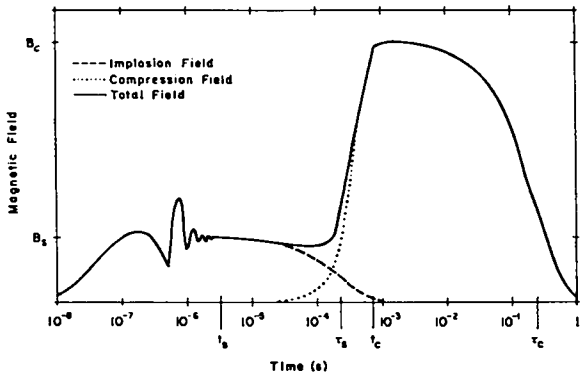

Fig. 4-7.
Temporal behavior of the magnetic field produced by the implosion and compression system.

thus decreasing the requirements of the implosion crowbar system (for a fixed fractional sag in the total field during the staging process).

4.1.4.3.1 Minimization of the Electric Fields and Voltages Required by the Implosion Process

As is discussed in Sec. 4.1.4.1, one of the main reasons for minimizing the amount of implosion heating is that the implosion system is technologically much more difficult than the compression system. A major problem is the high fields and voltages required by the implosion process. A number of the system and plasma parameters are specified by the process of minimizing these fields and voltages.

Plasma physics considerations determine the required value of the electric field E_θ induced around the plasma by the implosion system. In turn, E_θ and the circuit efficiency determine the voltage V_o needed on the implosion bank. Thus E_θ is minimized first, then the circuit is optimized to reduce V_o to the smallest allowed value.

Six important parameters determine the value of E_θ (see Sec. 4.3):

$$x_c = \frac{a(t_c)}{\bar{b}} , \tag{40}$$

$$x_s = \frac{a(t_s)}{\bar{b}} , \tag{41}$$

the maximum average plasma temperature

$$T_c = \frac{T_{ic} + T_{ec}}{2} \quad \text{at } t = t_c , \tag{42}$$

the compression field decay time τ_c, the DT filling pressure p_o, and Q. The value of Q = 1 must be reached in a time $t_Q < \tau_c$ since the neutron production drops sharply as plasma expands and cools. Thus τ_c should be made as large as possible. Results from Sec. 5.4 indicate that the maximum reasonable L/R time is

$$\tau_c = 250 \text{ ms}. \tag{43}$$

To minimize the chance of losing the plasma before Q = 1 is reached, the value of t_Q is set at

$$t_Q = 150 \text{ ms}. \tag{44}$$

From the code described in Sec. 4.2.3, the final value of Q required to satisfy (44) is

$$Q_f \simeq 1.1 . \tag{45}$$

In agreement with Sec. 4.1.4.3.2, x_s should be maximized to optimize the implosion-heating efficiency, and x_c should be minimized to minimize the amount of required implosion heating. Implosion codes indicate (see Sec. 4.3.3) that

$$x_s \simeq 0.7 \tag{46}$$

is obtainable, yielding an implosion efficiency of

$$e_{Ti} \simeq 0.21 \tag{47}$$

from Fig. 4-5. The minimum value of x_c consistent with stability requirements is obtained in Sec. 4.1.4.3.2.

The quantities p_o and T_c are related to x_c through the definition of Q. If no additional constraints are placed on p_o, T_c = 8 keV yields the lowest value of E_θ. The filling pressure p_o is then determined by the value of Q (see Sec. 4.3.3). Unfortunately, the resulting value of p_o is less than the minimum value of 4 mtorr at which standard theta pinches have been operated at LASL. If p_o is too low, an adequate sheath for implosion fails to form. Although this lower limit has not been thoroughly explored, past experience indicates that it is between 1 and 4 mtorr. If the pressure is set at

$$p_o = 4 \text{ mtorr} \tag{48}$$

then T_c can be reduced as far as Eq. (45) will allow. Even though the value of T_c depends on x_c, the strong dependence of the $\langle\sigma v\rangle$ curve (see Sec. 4.2.2) on T_c limits the range of T_c to

$$4.6 \lesssim T_c \lesssim 6 \text{ keV} \tag{49}$$

for $0.23 < x_c < 0.4$.

Using the values of the four parameters Q, x_s, τ_c, and p_o just established in this section, the value of E_θ is approximately given by [see Eq. (199)]

$$E_\theta[\text{kV/cm}] \simeq 65\, x_c^{4/3}/\ell n(5.3/x_c^2 Q)\,. \tag{50}$$

To obtain the minimum value of E_θ, x_c must be minimized within the constraints imposed by (3) and (6).

4.1.4.3.2 Minimization of x_c for a Wall-Stabilized System

As discussed in the previous section, a reduction in E_θ reduces the technological problems associated with the implosion system. From (50) it is apparent that E_θ is reduced by minimizing x_c within the plasma equilibrium and stability constraints given by (3) and (6).

This minimization is easily accomplished by eliminating one of the variables between (3) and (6) and minimizing a with respect to the rest of the variables. Since h has essentially no effect on the cost or complexity of the system, it is the ideal variable to eliminate, giving

$$a^4 - \frac{g_1 \bar{b}^4}{R\delta_1(f_0\delta_0 + f_2\delta_2)}\, a - \frac{\bar{b}^4}{\delta_1^2}(g_0\delta_0^2 + g_2\delta_2^2) = 0\,. \tag{51}$$

From (51) it can be shown that the following inequalities hold, independent of the other variables

$$\frac{\partial a}{\partial R} < 0\,, \tag{52}$$

$$\frac{\partial a}{\partial \bar{b}} > 0\,, \tag{53}$$

$$\frac{\partial a}{\partial \delta_1} < 0. \tag{54}$$

These inequalities indicate that R and δ_1 should be chosen as large as possible and $\bar{b}$ should be chosen as small as possible.

The upper bound on R is set by economics and the operational and reliability problems associated with a large system. A compromise between those limitations and the relatively weak dependence of a on R [see (63)] resulted in the choice of

$$R = 40 \text{ m}. \tag{55}$$

The inequality (53) and the desire to minimize the cost of SFTR imply that $\bar{b}$ should be made as small as possible. However, the plasma sheath thickness must be small compared with b or $\bar{b}$ for an adequate implosion. In present theta-pinch systems the sheath thickness is 2 or 3 cm. The sheath thickness is often assumed to be c/ω_{pi}, although the sheath formation is probably much more complex than is indicated by this simple relation. For a filling pressure of 4 mtorr [see (48)] this relation yields

$$\frac{c}{\omega_{pi}} = 2.1 \text{ cm}, \tag{56}$$

which agrees with the experimental observations. Thus, to insure an adequate implosion, the vacuum wall radius is set at

$$b = 10 \text{ cm}. \tag{57}$$

The radius of the implosion coil conductors is chosen to be

$$\bar{b} = 10.7 \text{ cm} \tag{58}$$

to allow for the 7 mm of insulation required by the fabrication process described in Sec. 5.2.3.1.

The maximum allowed value of δ_1 is really not known. As described in Sec. 4.1.3.2, the analytic model used here theoretically breaks down for $\delta_1 \gtrsim 1$, and yet the model has been experimentally verified[8] for $\delta_1 = 3$. There is a strong motivation to maximize δ_1 because a is more strongly dependent on δ_1 than on either R or $\bar{b}$ [see (63)]. One is also reluctant to set $\delta_1 = 3$ or larger because of the lack of extensive experimental experience at these large values.

Before the final design of SFTR is made, future experiments will provide additional information about the limitations on p_o, E_θ, and δ_1. This information will allow a more rational choice of design values for these parameters than can be made at the present time. In this report, the pressure is set

at $p_o = 4$ mtorr, and δ_1 remains a free parameter within the range

$$1. \lesssim \delta_1 \lesssim 4. \tag{59}$$

This variation in δ_1 will produce a corresponding range of values for x_c, E_θ, V_o, and other related parameters. This range of operating conditions will allow the impact of future experiments on the SFTR design to be more readily assessed.

Now, R, $\bar{b}$, and δ_1 can be considered fixed quantities in Eq. (51). When δ_0 and δ_2 are varied to minimize a,

$$\delta_0 = \frac{f_o}{g_o}\left(\frac{g_1\delta_1 a}{2R}\,\Lambda^2\right)^{1/3}, \tag{60}$$

$$\delta_2 = \frac{f_2}{g_2}\left(\frac{g_1\delta_1 a}{2R}\,\Lambda^2\right)^{1/3} \tag{61}$$

where

$$\Lambda \equiv \frac{g_0 g_2}{f_0^{\,2} g_2 + f_2^{\,2} g_0}\,. \tag{62}$$

Substituting (60) and (61) into (51) yields

$$\frac{a}{\bar{b}} = \frac{(3\Lambda^{1/3})^{3/10}}{\delta_1^{\,2/5}}\left(\frac{g_1\bar{b}}{2R}\right)^{1/5}. \tag{63}$$

The corresponding wave number becomes

$$h = \left(\frac{2\Lambda}{g_1}\right)^{1/6}\left(\frac{1}{a^2 R\delta_1^{\,2}}\right)^{1/3}. \tag{64}$$

Equations (60) through (64) can be numerically evaluated (except for δ_1) for an appropriate value of β. This analytic old-ordering model is normally evaluated with $\beta = 0.8$ for high-β plasmas because results agree well with the more accurate model[7] for $0.8 \lesssim \beta < 1.0$. For $\beta \to 1.0$ the old ordering possesses unphysical singular behavior as is evident in Eq. (19). Using

$$\beta = 0.8\,, \tag{65}$$

$$\delta_0 = 0.13\,\delta_1^{\,1/5}\,, \tag{66}$$

$$\delta_2 = 0.044\,\delta_1^{\,1/5}\,, \tag{67}$$

$$\lambda[\mathrm{m}] = 2.7\,\delta_1^{\,2/5}\,, \tag{68}$$

$$a[\mathrm{cm}] = \frac{4.0}{\delta_1^{\,2/5}}\,, \tag{69}$$

and from (40) and (58)

$$x_c = \frac{0.37}{\delta_1^{\,2/5}}\,. \tag{70}$$

Equation (70) yields the desired minimum value of x_c, dependent only on the choice of δ_1.

From an engineering point of view, the length of individual implosion and compression coils should be an integral fraction of $\lambda/4$. To facilitate the design of these coils and their related circuits, a fixed length

$$\ell = 20 \text{ cm} \tag{71}$$

was chosen. This choice is a compromise between minimizing the multiplicity of coils and minimizing the voltage on the implosion circuit. As a result, λ must be an integral multiple of $4\ell = 80$ cm instead of the continuous function (68).

If x_c is minimized for a fixed value of λ, h cannot be eliminated between (14) and (17), and the following sixth order equation replaces (51)

$$a^6 - g_1 h^2 \bar{b}^4 a^4 - \frac{g_0 f_2^{\,2} + g_2 f_0^{\,2}}{f_0^{\,2}} \cdot \left(\frac{\delta_2}{\delta_1}\right)^2 \bar{b}^4 a^2 + \frac{g_0 f_2}{f_0^{\,2}}\left(\frac{2\delta_2 \bar{b}^4}{h^2 R\delta_1^{\,3}}\right) a - \frac{g_0}{f_0^{\,2}}\left(\frac{\bar{b}}{hR^{1/2}\delta_1}\right)^4 = 0\,. \tag{72}$$

Equations (60) and (61) become

$$\delta_0 = \frac{f_0}{g_0}\,\frac{\Lambda}{h^2 aR\delta_1}\,, \tag{73}$$

$$\delta_2 = \frac{f_2}{g_2}\,\frac{\Lambda}{h^2 aR\delta_1} \tag{74}$$

but no simple solution similar to (63) can be obtained from the combination of (72), (73), and (74)

$$a^6 - g_1 h^2 \bar{b}^4 a^4 - \frac{\Lambda \bar{b}^4}{h^4 R^2 \delta_1} = 0 \quad . \qquad (75)$$

Figure 4-8 compares Eq. (70) with the numerical solution of (75) for $\lambda = 3.2$ m and $\lambda = 4.0$ m. These two values of λ are integral multiples of 4ℓ. This figure indicates that (70) is an acceptable approximation of (75) if

$$\lambda = 3.2 \text{ m} \qquad 1 \lesssim \delta_1 \lesssim 2$$

$$\lambda = 4.0 \text{ m} \qquad 2 \lesssim \delta_1 \lesssim 4 \quad . \qquad (76)$$

Thus, to retain the analytic simplicity of (70), the constraint on λ given by (76) will be assumed. Now that x_c has been minimized, the plasma and field parameters can be calculated.

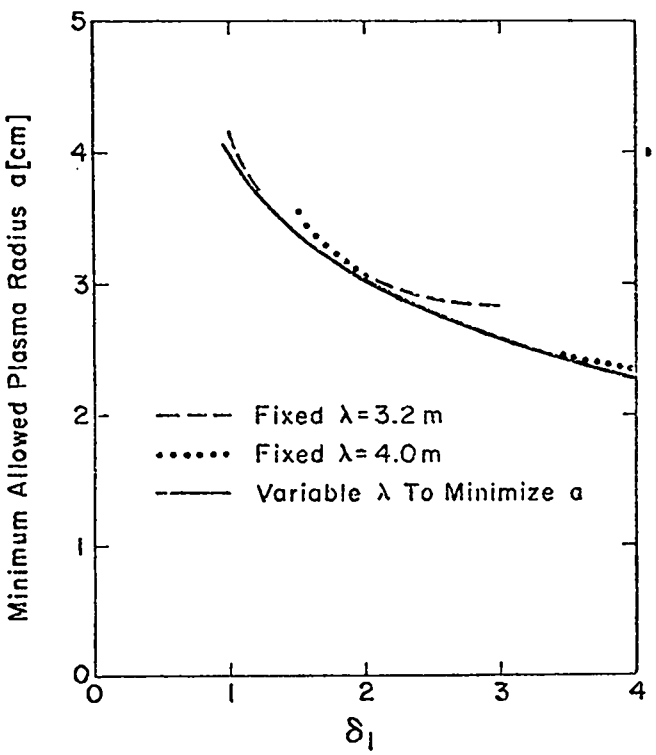

Fig. 4-8.
Comparison of the effect of fixed and variable λ on the minimization of the stable ($m = 1$) plasma radius.

4.1.4.3.3 Determination of the Plasma and Field Parameters

Using the minimum allowed x_c given by (70), the plasma and field parameters can be expressed in terms of δ_1. From (50) the maximum induced electric field E_θ becomes

$$E_\theta [\text{kV/cm}] \simeq \frac{24}{\delta_1^{8/15} \ell n(70\delta_1)} \quad . \qquad (77)$$

The plasma parameters at maximum compression are

$$n_c [\text{cm}^{-3}] \simeq 1.8 \times 10^{15} \delta_1^{4/5} \qquad (78)$$

and

$$T_c [\text{keV}] \simeq \frac{26}{\ell n(70\delta_1)} \quad . \qquad (79)$$

These formulas are derived in Sec. 4.2.2. The values of τ_c, Q, x_s, and p_o are assumed to be those given by (43), (45), (46), and (48). The value of the compression field can be obtained from (78) and (79) by assuming $\beta = 1$:

$$B_c [\text{kG}] \simeq 61 \, \delta_1^{2/5} / [\ell n(70\delta_1)]^{1/2} \quad . \qquad (80)$$

Note that T_c is the average plasma temperature given by

$$T_c = \frac{T_{ec} + T_{ic}}{2} \quad . \qquad (81)$$

The corresponding parameters n_s, T_s, and B_s evaluated at $t = t_s$ can be obtained from the adiabatic law for 3 degrees of freedom

$$\frac{B_s}{B_c} = \left(\frac{x_c}{x_s}\right)^{5/3} = \left(\frac{T_s}{T_c}\right)^{5/4} = \left(\frac{n_s}{n_c}\right)^{5/6} \quad . \qquad (82)$$

Evaluating (82) yields

$$n_s [\text{cm}^{-3}] \simeq 5.8 \times 10^{14} \quad , \qquad (83)$$

$$T_s [\text{keV}] \simeq \frac{12}{\delta_1^{8/15} \ell n(70\delta_1)} \quad , \qquad (84)$$

$$B_S\,[kG] \simeq \frac{2.4}{\delta_1^{4/15}\,[\ell n(70\delta_1)]^{1/2}} \quad ; \qquad (85$$

again, T_s is an average temperature given by

$$T_s = \frac{T_{es} + T_{is}}{2} \quad . \qquad (86)$$

These parameters are plotted as a function of δ_1 in the next section, which is a summary of all the parameter values derived in Sec. 4.1. The parameters, such as capacitance and voltage, associated with implosion and compression circuits are presented in Secs. 4.2 and 4.3.

4.1.4.3.4 Operating Point Summary

Table 4-1 and Figs. 4-9, 4-10, and 4-11 summarize the SFTR parameters discussed in Sec. 4.1. Where applicable, the relevant equation numbers are listed to aid in locating the discussion of a given variable in the text. When the parameter is dependent on δ_1, a figure number is listed instead of the parameter value. The denoted figure contains a graph of the parameter's dependence on δ_1 for $1 < \delta_1 < 4$.

The values of the circuit parameters and voltages are discussed in other sections. The compression circuit is described in Secs. 5.2.2.1.2 and 5.4, while the implosion circuit is discussed in Secs. 4.3, 5.2.2.1.1, and 5.3.

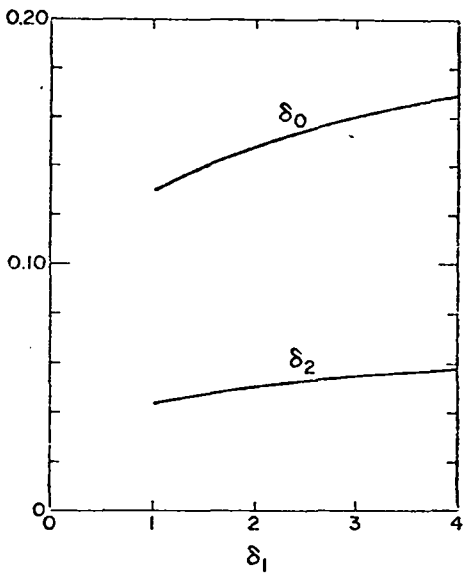

Fig. 4-9
Dependence of δ_0 and δ_2 on δ_1, as given by Eqs. (66) and (67).

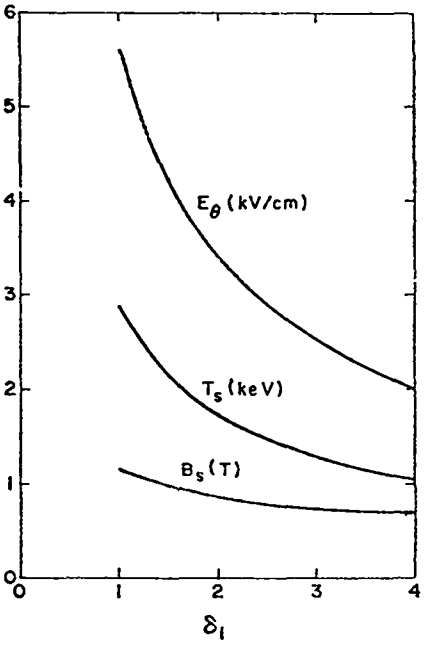

Fig. 4-10.
Dependence of E_θ, T_s, and B_s on δ_1, as given by Eqs. (77), (84), and (85).

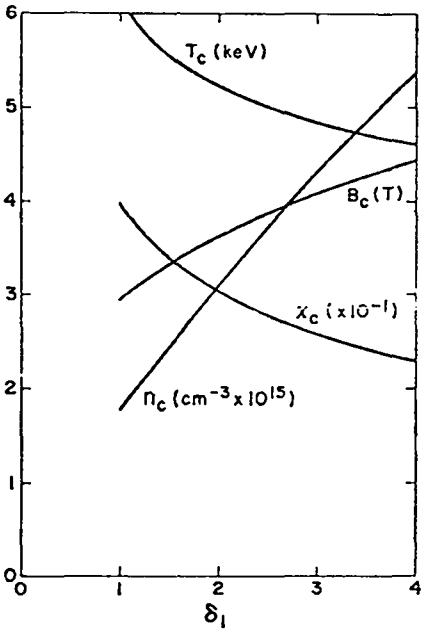

Fig. 4-11.
Dependence of T_c, B_c, x_c, and n_c on δ_1, as given by Eqs. (79), (80), (70), and (78).

TABLE 4-1

OPERATING POINT SUMMARY

Description of the Variable	Symbol	Value or Figure Number	Equation Number Reference
SYSTEM			
Major radius	R	40 m	(55)
Minor radius of the vacuum wall	b	10 cm	(56)
Minor radius of the implosion coil	$\bar{b}$	10.7 cm	(57)
Magnitudes of the $\ell = 0$	δ_0	Fig. 4-9	(60), (66)
$\ell = 1$, and $\ell = 2$ perturbations	δ_2	Fig. 4-9	(61), (67)
	δ_1	independent variable with the range $1 \leq \delta_1 \leq 4$	
Wavelength of the toroidal variations	λ	3.2 m $1<\delta_1<2$ 4.0 m $2<\delta_1<4$	(64), (68)
Length of implosion coil segments	ℓ	20 cm	(71)
FIELDS			
Implosion:			
Magnetic field at $= t_s$	B_s	Fig. 4-10	(85)
Time required for the imploded plasma to isotropize and thermalize	t_s	$\sim 3\,\mu s$	
Decay time of B_s	τ_s	230 μs	(31)
Maximum induced electric field, (It occurs at about t = 100 ns)	E_θ	Fig. 4-10	(50), (77)
Compression:			
Magnetic field at $t = t_c$	B_c	Fig. 4-11	(80)
Time of peak compression	t_c	700 μs	
Decay time of B_c	τ_c	250 ms	(43)
PLASMA			
Filling pressure	p_o	4mtorr	(48)
Plasma β	β	1	
Implosion ($t = t_s$):			
Average temperature	T_s	Fig. 4-10	(84)
Density	n_s	$5.8 \times 10^{14}\,cm^{-3}$	(83)
Normalized radius	x_s	0.7	(46)
Compression ($t = t_c$):			
Average temperature	T_c	Fig. 4-11	(79)
Density	n_c	Fig. 4-11	(78)
Normalized radius	x_c	Fig. 4-11	(70)
BURN			
Maximum allowed time to reach Q = 1	t_Q	150 ms	(44)
Time asymptotic value of Q	Q_f	1.1	Obtained from the numerical model
Time to achieve Q = 1/2	$t_{Q/2}$	35-40 ms	
Time to achieve $n\tau = 10^{14}$	$t_{n\tau}$	47-49 ms	

4.2 COMPRESSION AND BURN

4.2.1 General Description

The plasma is brought to ignition by adiabatic compression, and the magnetic field is then held while thermonuclear burning occurs. Theoretical models are needed to describe the processes of heating, equilibration of species, neutron and α-particle production, and bremsstrahlung as the external magnetic field is changed. An analytic model has been derived which gives approximate answers for several of the above processes. This model is described in the next section.

The best model available to us is a thermonuclear burn code developed by Oliphant.[14] It is a numerical solution of the Fokker-Planck equation and has been used in determining the thermonuclear burnup and other parameters. It uses the external magnetic field waveform for the SFTR circuit. That waveform is a $\sin^2\pi t/2t_c$ variation between the initial implosion field and final compression field, followed by an exponential field decay with a 250-ms time constant. A description of the numerical model and results is given below.

4.2.2 Analytic Model

The approximate model developed in this section relates the goals of Q = 1 and m = 1 plasma stability to the plasma parameters at the beginning of the compression cycle. In order to generate a tractable, analytic model, several effects such as electron-ion equilibration, α-particle heating and bremsstrahlung are omitted. These effects are included in the numerical model described in the next section.

The following assumptions form the basis for the model:

1. The adiabatic law holds for $t > t_s$ with $\gamma = 5/3$. The time t_s, defined in Fig. 4-7, marks the end of the implosion phase and the beginning of the compression phase. The adiabatic law for $\gamma = 5/3$ is given in (82).

2. The magnetic field decays with a simple exponential from its peak value at $t = t_c$.

$$B = B_c e^{-t/\tau_c} \tag{87}$$

where $\tau_c = 250$ ms as in (43).

3. For this model t is set to zero at t_c since neutron production for $t < t_c$ can be ignored in the equation for Q (12).

4. The energy yield per neutron is assumed to be

$$Y = 20 \text{ MeV/neutron} . \tag{88}$$

5. The $\langle\sigma v\rangle$ curve is approximated by

$$\langle\sigma v\rangle = Ge^{-\Theta/T} \tag{89}$$

where

$$G = 10^{-21} \text{ m}^3/\text{s} \tag{90}$$

and

$$\Theta = 20.8 \text{ keV} . \tag{91}$$

Equation (89) is compared with the known D-T reaction rates[15] in Fig. 4-12.

6. A sharp boundary model is assumed, with no radial variations inside the boundary. Since the classical energy loss time is long compared with τ_c, the radial particle and energy transports are ignored.

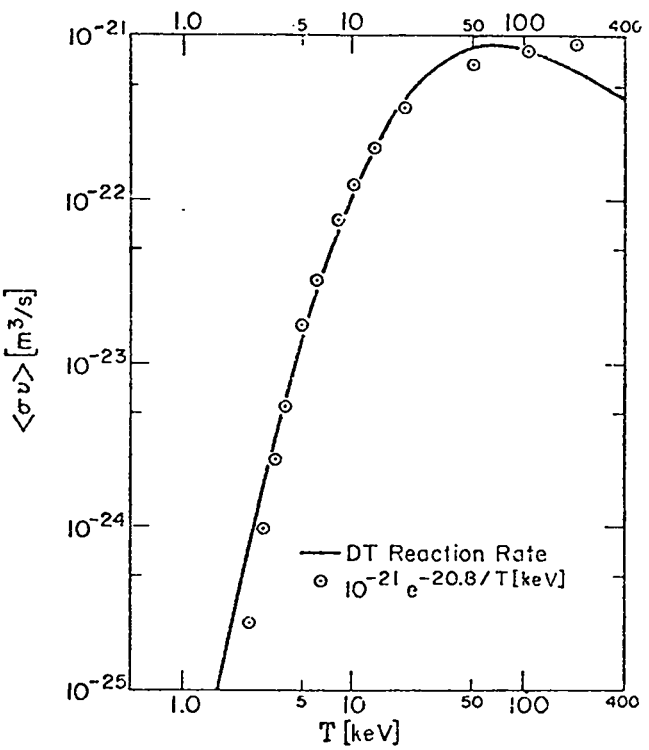

Fig. 4-12.
Comparison of the D-T thermonuclear reaction rate[15] with the approximation given by (78).

7. The electrons and ions are assumed to be equilibrated for $t \geq t_c$ (or from assumption 3, $t > 0$)

$$T = T_e = T_i \quad . \tag{92}$$

8. The effects of bremsstrahlung, α-particle heating, and electron-ion equilibration are ignored except for a single parameter α which is used to correlate the numerical model with this analytic model.

9. To evaluate the integral in (13), it is assumed that

$$T < \Theta \quad . \tag{93}$$

Equation (13) can now be evaluated using (82), (87), (89), and (92)

$$Q = \frac{Yn_c}{12k_B T_c} \quad x \cdot \int_o^\infty \exp\left\{ -\frac{12}{5}\frac{t}{\tau_c} - \frac{\Theta}{T_c} e^{4t/5\tau_c} \right\} dt. \tag{94}$$

When (93) is satisfied, the major contribution to the integral in (94) occurs for $t \ll \tau_c$. This restriction allows the second term in the exponential to be expanded, thus rendering a tractable integral. The result is

$$Q = \frac{\eta n_c}{H} \tag{95}$$

where

$$H \equiv \frac{3 + \frac{\Theta}{T_c}}{\Theta/T_c} e^{(\Theta/T_c)} \tag{96}$$

and

$$\eta \equiv \frac{5}{48}\frac{GY\tau_c}{k_B \Theta} \quad . \tag{97}$$

Equation (95) uniquely determines the relation between the plasma density and temperature at maximum compression for a given value of Q in the SFTR systems. The value of η is a constant for the SFTR determined by (88), (90), (91), and (43)

$$\eta = 2.5 \times 10^{-20} \ m^3/\text{neutron} \ . \tag{98}$$

The variable H depends only on T_c, as is evident in (96). The time asymptotic value of Q is chosen to be

$$Q_f = 1.1 \tag{99}$$

so that Q = 1 will be reached before 150 ms into the compression.

The numerical model described in the next section indicates that the α-particle heating dominates bremsstrahlung losses and ion cooling due to electron-ion equilibration. The result is a slightly larger Q than predicted by (95). A comparison of (95) with the numerical results shows that by using a constant

$$\alpha \simeq 0.72 \tag{100}$$

excellent agreement can be obtained between the numerical model and the empirical relation

$$Q_f = \frac{\eta n_c}{\alpha H} \quad . \tag{101}$$

Equation (101) can be easily solved for n_c in terms of T_c

$$n_c = \frac{\alpha Q_f H(T_c)}{\eta} \tag{102}$$

and by using (98), (99), and (100)

$$n_c[\text{cm}^{-3}] = 3.2 \times 10^{13} H(T_c) \ . \tag{103}$$

In the SFTR design it would be most useful to solve (103) for T_c, since n_c is already determined by p_o and the maximum compression allowed by stability. The form of (96) does not allow a simple solution, but the following approximate solution is compared to (96) in Fig. 4-13

$$T_c \simeq \frac{\Theta}{\ell n(0.537\ H)} \ . \tag{104}$$

Substituting (103) into (104) yields

$$T_c = \frac{\Theta}{\ell n\left[\frac{n_c[\text{cm}^{-3}]}{6.0 \times 10^{13}}\right]} \ . \tag{105}$$

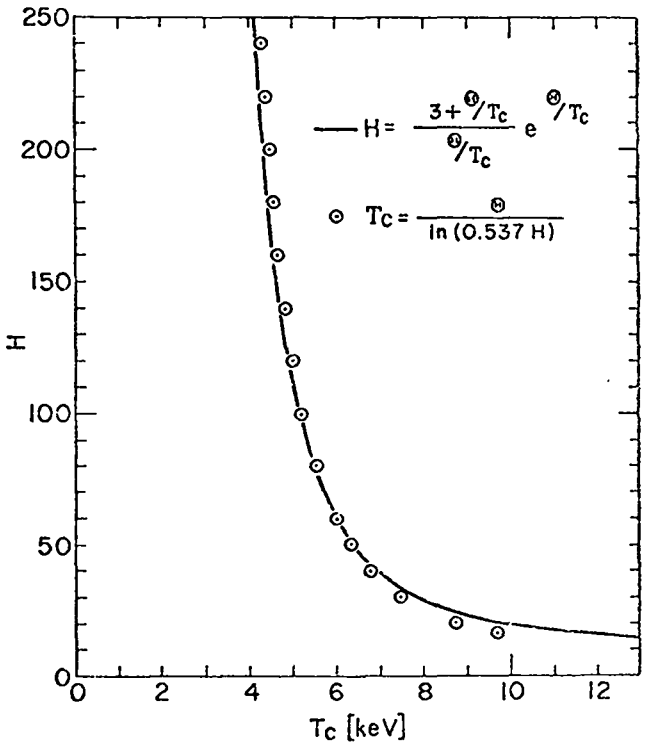

Fig. 4-13.
Comparison of the approximate relation for T_c (104) with the definition of H given by (96).

Conservation of particles requires that

$$n_c = \frac{n_o}{x_c^2} \tag{106}$$

and by using (48) and (70), (106) becomes

$$n_c[cm^{-3}] = 1.8 \times 10^{15}\ \delta_1^{4/5} . \tag{107}$$

Combining (107), (105) and (91) yields

$$T_c[keV] = \frac{26}{\ell n(70\delta_1)} . \tag{108}$$

Equations (107) and (108) appear as (78) and (79) in the previous section. The values of n_c and T_c given by (107) and (108) describe the plasma that can provide the desired Q and stability for the minimum induced field E_θ.

The plasma parameters at $t = t_s$ are related to n_c and T_c through the adiabatic law. Thus the goals of Q = 1 and m = 1 stability have been related to n_s and T_s under the constraint that E_θ should be minimized.

Minimizing E_θ minimizes the technological strain on the implosion system, but it also increases the energy required from the compression systems. Using pressure balance, the peak magnetic energy density required during compression can be expressed in terms of T_c by using (96) and (103)

$$W_B[MJ/m^3] = 0.11 \frac{(3 + \Theta/T_c)}{(\Theta/T_c)^2} e^{\Theta/T_c} . \tag{109}$$

This function is plotted in Fig. 4-14. The minimum required energy density of 0.98 MJ/m^3 is required at T_c = 12.6 keV. To minimize E_θ for $\delta_1 = 4$ (see Fig. 4-11), T_c = 4.6 keV, and the required energy density is nearly four times larger. However, since the required 45 kG is still within reasonable technological limits, E_θ should still be minimized.

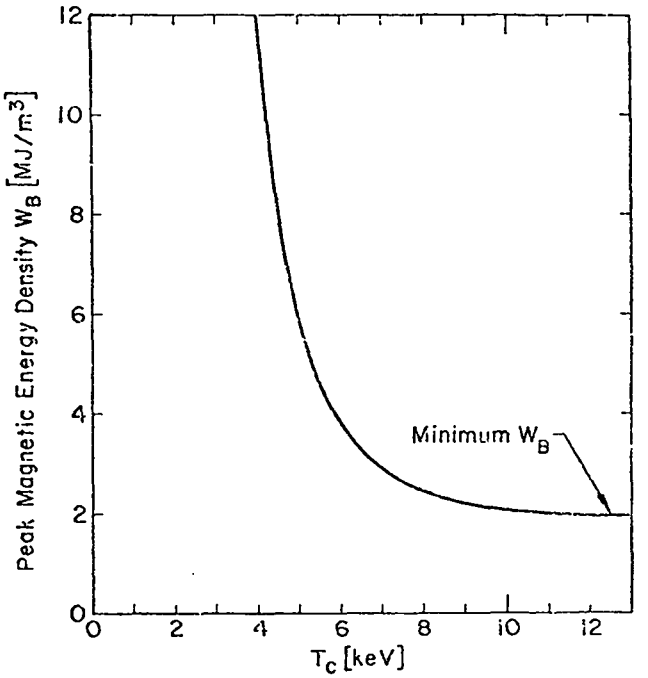

Fig. 4-14.
Magnetic energy density at peak compression W_B as a function of the average temperature T_c.

4.2.3 Numerical Model

The thermonuclear burn model assumes that there is a sharp boundary between a uniform density cylindrical plasma and the magnetic field. The field is excluded from the plasma, so $\beta = 1$ and the plasma and field pressures are equal at all times.

The ion and electron distribution functions are Maxwellian, with different temperatures. The α-particles are born at 3.5 MeV, with a Doppler-broadened half-width determined by the ion temperature, in accordance with the D-T cross section. The α-particle production is assumed uniform, but since the α-particle orbits take some of the α-particles out of the hot core we assume a certain fraction to interact with the plasma only on part of their orbits.

These three distribution functions are determined from the Fokker-Planck equation, and the distributions evolve in time according to the coulomb collision rate and adiabatic changes in the external field. One can therefore monitor electron and ion temperature, α-particle production and heat input to the plasma, neutron and bremsstrahlung emission, direct conversion work by expansion of the plasma against the external field, and plasma density and size.

The analytic model is used to explore possible operating points and to do parameter variation studies. The more promising parameter sets are used in the numerical model to compute the required information.

4.3 IMPLOSION HEATING

4.3.1 General Description

The implosion-heating system must heat the plasma to the conditions specified in Table 4-1 so that the compression and burn cycle can achieve Q = 1 while maintaining m = 1 stability. The theoretical model presented in this section is needed to connect the field and plasma parameters in Table 4-1 to the implosion circuit parameters.

The resonant heating approach involves tuning the implosion bank and crowbar switching time to the natural implosion time of the plasma. For this approach the strong interaction between plasma and circuit requires a mathematical model which can handle the plasma and circuit dynamics simultaneously. Computer codes have been developed that satisfy this requirement,[9,16] but the present sophistication of the plasma modeling does not yield results that are significantly different from simple analytic models. These codes are presently being improved. Although some results of these codes are used in this section, for simplicity an analytic model is used as the basis of the theoretical description.

The simple bounce model (no overtaking) is used in describing the ion sheath interaction. The obvious errors involved in using such a simple model have been discussed by Oliphant,[17] who describes a more accurate, but more complex model. The simple model is used to illustrate the basic plasma circuit interaction, leaving the numerical accuracy to the computer codes. As previously stated, the codes and the simple model do not deviate significantly except where indicated in Sec. 4.3.3.

4.3.2 Resonant Heating Concept

The optimization of the implosion-heating system consists of obtaining the required T_s and x_s (see Fig. 4-10 and Table 4-1) for the smallest possible E_0 and V_0 using the simplest possible circuit (V_0 is the capacitor bank voltage). Freidberg, Morse, and Ribe[9] determined that the programmed field shown in Fig. 4-15 yielded larger x_s and T_s for a given V_0 than a simple implosion field. The first field pulse implodes the plasma, but the field is dropped to zero during the expansion of the plasma so that the plasma does not give its energy back to the field. As the plasma approaches the wall, the field is raised to the minimum value required to prevent the plasma from hitting the wall.

An error was made in Ref. 9 in calculating the relative sizes of the first and second field pulse. Figure 4-15 shows the correct factor of 2 instead of $\sqrt{2}$. As a result of this error the value of x_s is mistakenly given as 0.76 instead of the correct value of

$$x_s = \left(\frac{22}{45}\right)^{1/2} = 0.70 \ . \qquad (110)$$

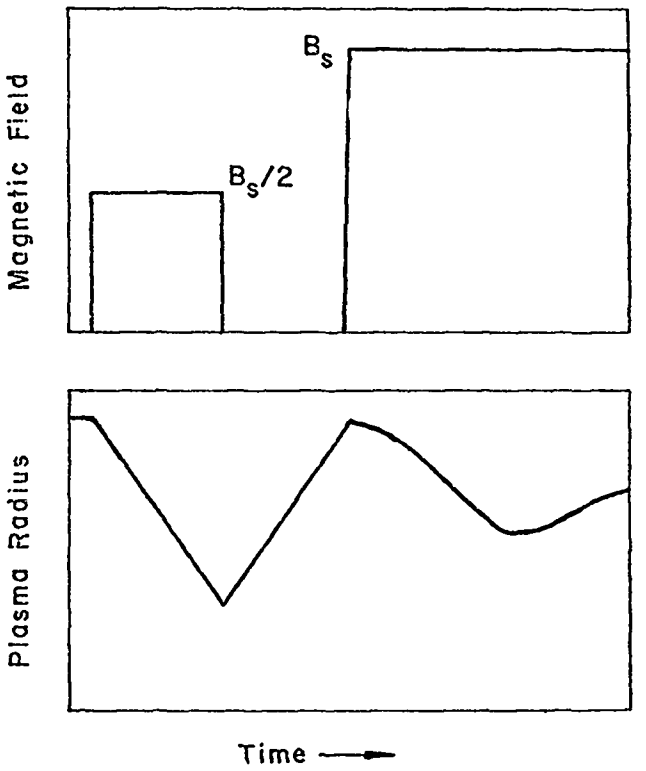

Fig. 4-15.
Programmed implosion field allowing free expansion of the plasma.

Although the field waveform of Fig. 4-15 cannot be generated by a realistic circuit, the basic features can be produced by the simple circuit shown in Fig. 4-16. The temporal behaviors of the magnetic field and plasma radius shown in this figure were obtained from a hybrid simulation code developed by Nielson.[16] The field is not zero during the plasma expansion, but it is less than the initial implosion field. As a result, only a small fraction of the plasma energy is given back to the field during the expansion.

The circuit is topologically the same as the classical theta-pinch circuit used in Scyllac. However, the source and crowbar inductances L_s and L_c are made smaller than the empty load coil inductance L_o. In addition the bank capacitance C is chosen so that the circuit is tuned to the implosion time of the plasma, hence the name resonant heating.

More precisely, the circuit is tuned so that by the time of the maximum implosion t_{cr} the field has peaked and decayed to a specific value B_{cr}. At this time t_{cr} the crowbar switch is closed and the magnetic flux corresponding to B_{cr} is compressed by the expanding plasma. If L_s and L_c are sufficiently small and if B_{cr} is chosen properly, the pulse of field at t_e will be just sufficient to prevent the plasma from hitting the wall. For $t > t_e$ the oscillations in the field and the plasma radius dampen rapidly as the plasma thermalizes and isotropizes. Of course the field exponentially decays on a much longer time scale as is shown in Fig. 4-7.

The second field pulse at t_e (Fig. 4-16) is not twice as large as the initial pulse mainly because of the plasma energy lost during the expansion against a nonzero field.

Any analysis of this resonant heating system must handle the circuit and plasma dynamics simultaneously. The interaction of the circuit and plasma cannot be ignored because of the dominant effect of $L_p(t)$ in the circuit. The analytic model described in the next section includes this plasma-circuit interaction. The model is used to determine

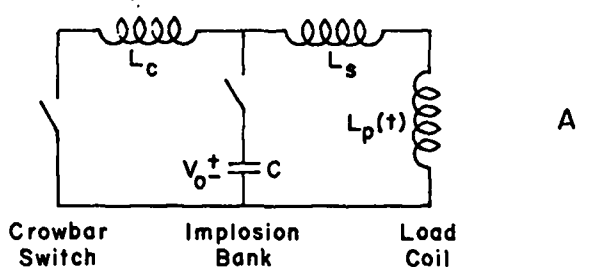

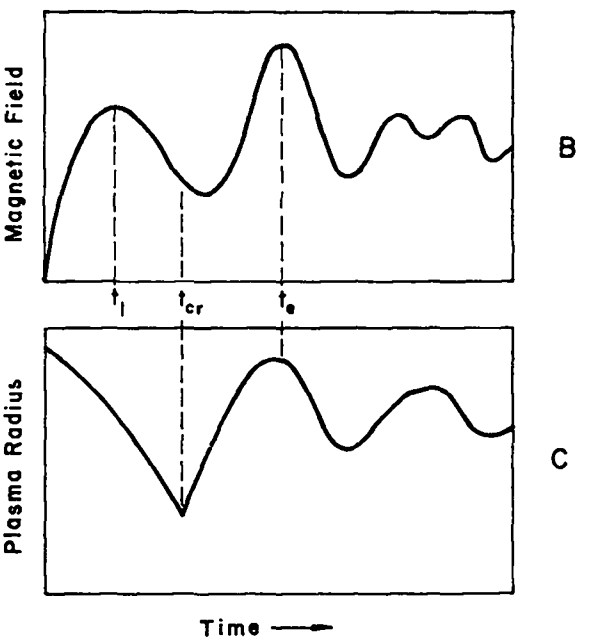

Fig. 4-16.
Resonant heating circuit showing the temporal behavior of the B-field and the plasma radius.

the values of the circuit components and the relation between T_s, x_s, E_θ, and V_o. In addition, the minimum V_o is obtained by optimizing the number of turns on the implosion coil. The relation between the turns and the inductance of the implosion coil is derived in Sec. 5.2.2.1.1.

4.3.3 Modeling of the Implosion

The analytic model for the implosion process described in this section actually consists of three separate models used in sequence. Each of the models describes a separate portion of the time history of the plasma. The segments of time are delineated by t_{cr} and t_e in Fig. 4-16, and are denoted by the following descriptive names:

1. Initial Implosion $0 < t < t_{cr}$
2. Expansion and Reflection $t_{cr} < t < t_e$
3. Isotropization and Thermalization $t_e < t < t_s$.

The isotropization and thermalization are assumed to be complete by $t = t_s$, where t_s is defined by Fig. 4-7. A brief description of the three models is given before any calculations are presented.

4.3.3.1 Description of the Models

1. Initial Implosion

The plasma is described by a sharp boundary, simple bounce model with no overtaking. That is, each ion is assumed to bounce elastically off the magnetic piston only once. Physically, the ions struck by the piston at very early times will be overtaken one or more times by the accelerating piston, but this fact is ignored by the model. This problem of overtaking as well as inelastic collisions between piston and ions (snowplow model) has been treated analytically by Oliphant.[17] Finite sheath thickness and overtaking have been included in simulation codes.[9,16] Although the effects of finite sheath thickness, overtaking, and snowplowing are observable, they do not appear to dominate the gross plasma-circuit interaction. Thus for the sake of simplicity they are omitted from the models presented here. The end of the initial implosion at $t = t_{cr}$ is defined by the time when the first accelerated ions strike the sheath on the opposite side of the plasma after passing through the center of the system.

The circuit used in this portion of the model is one loop of the circuit shown in Fig. 4-16. The loop containing the crowbar switch is not needed since the switch is not closed until $t = t_{cr}$. The plasma effects are introduced to the one loop equation through $L_p(t)$. A single time varying inductor to model the plasma effects can be used only if a sharp boundary plasma model is used.

The equation arising from this simple model has a closed form solution in only a few special cases. Analytic scaling laws obtained from the equation are helpful in understanding the system, but the equation must be solved numerically for some of the final results. The results include the required relations between the induced electric field E_θ, the bank voltage V_o, the peak circuit current i_1, and the peak plasma energy E_{cr} (the subscripts 1 and cr refer to the times t_1 and t_{cr} shown in Fig. 4-16).

2. Expansion and Reflection

The simple bounce concept used in the first model breaks down at $t = t_{cr}$ when fast ions begin striking the piston. At this time the crowbar switch is closed and this also complicates the circuit model. Thus a new model is needed for $t_{cr} < t < t_e$ that takes advantage of the new boundary conditions of the system.

Two basic assumptions are made. First, the crowbar is assumed to be "perfect" thus causing the total magnetic flux ϕ_T and the total energy (magnetic plus plasma) to be constants of the motion. This assumption is justified if the transfer time of the current from the capacitor branch to the crowbar is short compared with the implosion time. The second assumption is that pressure balance exists during the reflection at $t = t_e$. An accurate description of the dynamic plasma pressure at $t = t_e$ would require a knowledge of the phase space distribution of the plasma. Since this information is not obtainable in analytic form, the plasma is assumed to be thermalized with a finite degree of isotropization parameterized by ϵ.

The results of this model are combined with the initial implosion results to determine requirements for tuning the circuit to the plasma implosion time. The actual calculation of the sizes of the circuit parameters is presented in Sec. 4.3.4.

3. Isotropization and Thermalization

The purpose of this model is to determine the x_s and T_s of the plasma as a function of initial plasma and circuit parameters. The conservation of flux and total energy is assumed as in the Expansion and Reflection model. The plasma is assumed to be thermalized, isotropized in three dimensions, and in pressure balance with the field at $t = t_s$. As a pessimistic assumption

$$T_{es} \simeq \tfrac{1}{2} T_{is} \tag{111}$$

which is less than that observed in Scyllac.[14] Equation (111) is in approximate agreement with a

simple model for ohmic heating due to field diffusion for sheath widths comparable with those experimentally observed (on the order of 2 cm).

The results of this model agree reasonably well with simulation codes for the adiabatic invariant $T_s x_s^{4/3}$. However, the value of x_s is typically higher than that generated by the codes because the electron temperature is inserted in the model in an ad hoc manner, increasing the plasma pressure and radius. Since the major electron heating probably occurs during the initial implosion before the crowbar limits the flux, a smaller x_s is expected than this model predicts. For this reason

$$x_s = 0.7 \tag{112}$$

is assumed because it agrees with the simulation codes as well as the simple model[9] previously described in Sec. 4.3.2 [see (110)].

The three models described above are outlined mathematically in the remainder of this section.

4.3.3.2 Initial Implosion

A new normalized radial variable simplifies the algebraic description of the plasma model

$$z \equiv 1 - x \ . \tag{113}$$

Using this variable, the momentum balance equation for $t < t_{cr}$ is

$$\frac{B^2}{2\mu_0} = 2n_0 m(\dot{z}b)^2 \tag{114}$$

where n_o is the filling density and m the average ion mass. Solving for the piston velocity yields

$$b\dot{z} = \frac{v_\alpha}{2} \tag{115}$$

where v_α is the Alvén velocity

$$v_\alpha \equiv \frac{B}{\sqrt{\mu_0 n_0 m}} \ . \tag{116}$$

The relation between the magnetic field B and the current flowing in the circuit i (see Fig. 4-16) is given by the boundary conditions

$$B = \frac{\mu_0 N i}{\ell} \tag{117}$$

where ℓ is the length of the implosion coil and N is the effective number of turns in the coil [see (16) in Sec. 5.2.2.1.1].

The form of the loop equation for the circuit in Fig. 4-16 can be simplified by defining several new variables. Let Q_c be the initial charge on the capacitor C,

$$Q_c \equiv V_o C, \tag{118}$$

while Q_p is an effective "charge" associated with the plasma

$$Q_p \equiv \frac{b\ell}{N}\left(\frac{n_0 m}{\mu_0}\right)^{1/2} \ . \tag{119}$$

The ratio of these charges is defined as

$$q \equiv \frac{Q_p}{Q_c} \ . \tag{120}$$

The inductance associated with the empty vacuum vessel is

$$L_o \equiv \frac{\mu_0 N \pi b^2}{\ell} \tag{121}$$

and the normalized source inductance

$$\Lambda_s \equiv \frac{L_s}{L_o} \tag{122}$$

is evaluated in (26) of Sec. 5.2.2.1.1. Using (113) and (121), the time-dependent load inductance can be expressed as

$$L_p(t) = L_o z(2-z). \tag{123}$$

Finally, the current and time are normalized to

$$I \equiv \frac{i}{i_c} \tag{124}$$

$$T = \frac{t}{t_o} \tag{125}$$

where

$$i_o \equiv V_o \left(q\,\frac{C}{L_o}\right)^{1/2} \tag{126}$$

$$t_o \equiv (q\Lambda_s L_s C)^{1/2} \ . \tag{127}$$

Using these variables, the loop equation can be written in the following form

$$\frac{dI}{dT}\left[1 + \left(\int I dT\right)\left(1 - \tfrac{1}{4}\,\Lambda_s \int I dT\right)\right] + I^2\left(1 - \tfrac{1}{2}\Lambda_s \int I dT\right) = 1 - q\Lambda_s \int I dT \,. \tag{128}$$

In addition, (115) can be integrated yielding

$$z = \tfrac{1}{2}\,\Lambda_s \int I dT. \tag{129}$$

Thus the displacement of the piston from the wall is linearly related to the charge removed from the capacitor.

Some understanding of the solution of (128) can be obtained by examining the equation at early times, i.e.,

$$z << \tfrac{1}{2}\,\Lambda_s < 1. \tag{130}$$

If

$$q \gtrsim 2 \tag{131}$$

then (128) can be approximated by

$$\frac{dI}{dT} + I^2 = 1 \,. \tag{132}$$

The solution of (132) is

$$I = \tanh T \tag{133}$$

which is plotted in Fig. 4-17. Condition (130) breaks down for $T \gtrsim 1/2$ as is evident in Fig. 4-17 where (133) is compared with a numerical solution of (128). The agreement with (133) for $T < 1/2$ is good for a wide range of Λ_s and q.

The effects of q and Λ_s on the solution of (128) can be compared with the solution in Fig. 4-17. As is stated in (118), (119), and (120), q essentially compares plasma mass with the charge on the capacitor bank. If $q \sim 1$ then the current is similar to the plotted example. As q is decreased (bank capacity or voltage increased), the normalized peak current increases and the drop in current following the peak is slower. Thus it approaches (133) for $q \ll 1$. This condition corresponds to classical theta-pinch systems such as Scyllac. The model then is only valid for $T \ll 1$ since ions traverse the plasma in a time short compared with the current rise time. As q is increased beyond 1, the peak normalized current decreases and the current falls to zero more quickly. In fact, for

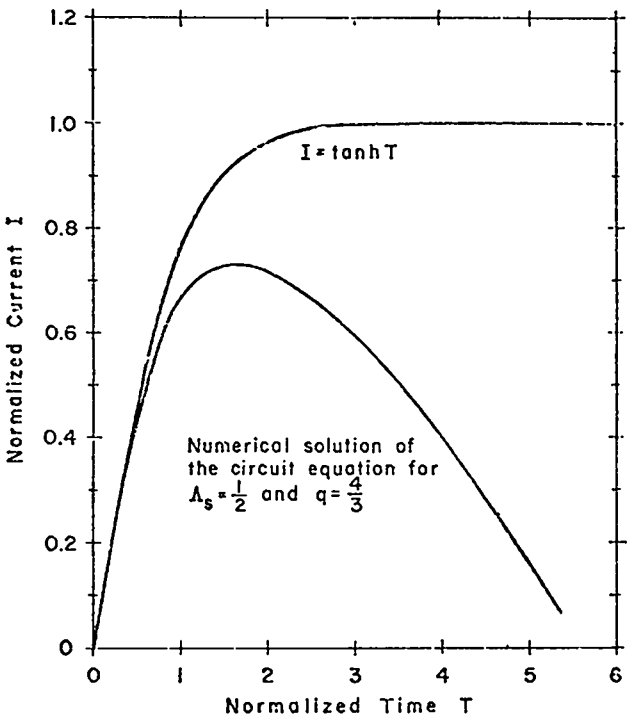

Fig. 4-17.
Comparison of the numerical solution of (128) and the solution of (132) given by (133).

$q \gtrsim 1.5$ the current goes negative before the ions traverse the plasma. Equation (128) can be made valid for $I < 1$ if the I's in the integrands on the left side of (128) are bracketed by absolute magnitude signs [the same with the I in (129)]. This is required to correctly model the field pressure as being independent of the direction of B (or I).

This range of $q > 1.5$ resulting in negative current is an inefficient and hence uninteresting regime. As has been described in the Expansion and Reflection model, a specified amount of flux must be in the system at $t = t_{cr}$ when the first ions traverse the plasma. If the current has passed through zero one or more times before $t = t_{cr}$, the average field pressure and the resulting plasma energy are smaller than if the current remains positive during the initial implosion.

The effect of Λ_s on the normalized current is quite similar to the effect of q on the current. For $\Lambda_s \gg 1/2$, most of the energy is stored in the source inductance, resulting in small values of peak normalized current. If $\Lambda_s \ll 1/2$, the current is still high when the plasma begins to expand ($t = t_{cr}$) and thus the plasma gives up an excessive amount of energy to the field during the expansion.

As a result of numerical studies

$$\Lambda_s = \tfrac{1}{2} \tag{134}$$

and

$$q = \tfrac{4}{3} \tag{135}$$

appear to be close to the optimum values.

Two additional variables are defined here for future reference. The first is the peak current I_1 which can be evaluated by setting dI/dT = 0 in (128)

$$I_1^2 = \frac{1 - 2qz_1}{1 - z_1} \ . \tag{136}$$

Unfortunately z_1 is dependent on the time history of the current up to its peak value as is evident from (129). Hence, I_1 must be determined numerically.

The second variable z_{cr} is the position of the piston at $t = t_{cr}$. In the simple model illustrated in Fig. 4-15 the value of z_{cr} is 2/3. In the more complicated model under consideration, z_{cr} is still about 2/3 but the small variations are important to the timing of the crowbar switch. Thus z_{cr} should also be determined numerically.

Now that the current has been defined over the time period $0 < t < t_{cr}$, the peak energy of the plasma, which occurs at $t = t_{cr}$, can be related to the current I. Define W_{cr} as the average ion energy at $t = t_{cr}$

$$W_{cr} = \tfrac{1}{2} m \int v^2 f_i(v, t = t_{cr}) dv \tag{137}$$

where $f_i(v)$ is the ion velocity distribution. Since each ion is given a velocity characterized by the Alvén speed at the instant the piston strikes the ion and since the ions are collisionless, (137) can be transformed to

$$W_{cr} = \tfrac{1}{2} m v_{\alpha 1}^2 \int_{x_{cr}}^{1} \left(\frac{v_\alpha(x)}{v_{\alpha 1}}\right)^2 2x dx \tag{138}$$

where $v_{\alpha 1}$ is the maximum Alvén speed which occurs at $t = t_1$. By defining

$$\gamma \equiv 2 \int_0^{z_{cr}} \left(\frac{I}{I_1}\right)^2 (1 - z) dz \tag{139}$$

(138) becomes

$$W_{cr} = \gamma \tfrac{1}{2} m v_{\alpha 1}^2 \ . \tag{140}$$

It is apparent from (139) that $\gamma \leq 1$ where $\gamma = 1$ corresponds to the constant implosion field in Fig. 4-15. The more realistic field or current behavior of Fig. 4-16 is obviously less effective at heating the ions. As an example the γ associated with Λ_s and q = 4/3 in Fig. 4-17 is

$$\gamma = 0.628 \tag{141}$$

from numerical calculations of (139) and (128).

The peak Alvén speed $v_{\alpha 1}$ can be related to the current using (116) and (117). Substituting the result into (140) yields

$$W_{cr} = \gamma \sqrt{\frac{m}{n_0 \mu_0}} \ \frac{V_0}{2\pi b N} I_1^2 \ . \tag{142}$$

This is the desired relation between the peak ion energy and the peak current.

It is also important to relate the induced electric field $E_{\theta t}$ at the coil ($r = \bar{b}$) to W_{cr} and I_1. By defining the area A_1 inside the coil

$$A_1 \equiv \pi \left[\bar{b}^2 - a(t)\right]^2, \tag{143}$$

$E_{\theta t}$ can be written as

$$E_{\theta t} = \frac{1}{2\pi \bar{b}} \left[A_1 \frac{\partial B}{\partial t} + B \frac{\partial A_1}{\partial t}\right]. \tag{144}$$

Evaluating (144) appropriately yields

$$E_{\theta t} = \frac{b}{\bar{b}} \frac{E_\theta}{I_1^2} \left\{1 - 2qz - \frac{dI}{dT}\left[1 - \frac{\left(\frac{\bar{b}}{b}\right)^2 - 1}{\Lambda_s}\right]\right\} \tag{145}$$

where

$$E_\theta \equiv \frac{V_0}{2\pi b N} I_1^2 \tag{146}$$

[compare (146) with (142)]. When the E_θ in (145) is maximized with respect to I, the result $E_\theta|_{max}$ can be shown to be

$$E_\theta \Big|_{max} \simeq E_\theta \ . \tag{147}$$

Thus E_θ is a good measure of the peak induced electric field.

The Initial Implosion model has provided the average ion energy W_{cr} at $t = t_{cr}$ and the peak electric field E_θ as a function of circuit parameters, and the

numerically obtainable parameters γ, I_1, and z_{cr}. The equations needed to obtain these parameters are (128), (129), (136), and (139). Obviously the numerical code must track the ions to determine the time t_{cr} and position z_{cr} of the piston at which the first ions traverse the plasma. The system parameters Λ_s and q are given by (134) and (135). The value chosen for q is confirmed in the calculations of the Expansion and Reflection model. The optimum value of Λ_s is discussed in Sec. 4.3.4 where the optimum values of V_o, N, and C are calculated.

4.3.3.3 Expansion and Reflection

During the expansion and reflection of the plasma, the total flux ϕ_T is given by

$$\phi_T = \int_{A_c} \bar{B} \cdot d\bar{A} \tag{148}$$

where A_c is the sum of the effective areas of flux storage in the circuit. The indicated calculation parallels the derivation of the source inductance in Sec. 5.2.2.1.1 so only the result is presented here:

$$\phi_T = \pi b^2 B[\Phi + z(2-z)] \quad . \tag{149}$$

The normalized flux ϕ can be compared with Λ_s given by (26) in Sec. 5.2.2.1.1

$$\Phi \equiv \frac{\Delta\ell}{2\pi^2 b^2 N}\left\{\ell n\left(\frac{r_c}{b}\right) + \frac{\bar{\Delta}}{\Delta}\ell n\left(\frac{r_p}{r_c}\right) + \frac{\ell}{2b}\left(1 - \frac{\Delta}{b}\right)\right\} + \frac{2s}{b} \quad . \tag{150}$$

Evaluating (150) generates a result similar to (27) in Sec. 5.2.2.1.1

$$\Phi = \frac{\Delta}{100N}\left[2.5 - \frac{\Delta}{10}\right] + 0.14 \quad . \tag{151}$$

In fact, Φ differs from Λ_s in only two respects. The contribution from the capacitor is omitted because the crowbar shorts it out, and the first term differs by a factor of N which arises from the basic difference between flux and magnetic energy density.

The plasma energy E_p and field energy E_B are defined as the energies contained in the length ℓ of an implosion coil. An appropriate expression of the conservation of total energy is that the change in plasma and field energy between $t = t_{cr}$ and t_e is equal in magnitude but opposite in sign

$$\Delta E_B \equiv E_{Be} - E_{Bcr} \tag{152}$$

$$\Delta E_B = -(E_{pe} - E_{pcr}) \quad . \tag{153}$$

The basic purpose of this model is to determine the value of q which results in the reflection of the plasma at r = b. The requirement for reflection is that dynamic pressure balance must exist at the time of reflection. Since the plasma has not thermalized at $t = t_e$, the contribution of the electrons to the plasma pressure is ignored. The phase space distribution of the ions is not known, so the ion pressure is modeled by the thermalized pressure and a parameter ϵ which represents the degree of isotropization. The pressure balance is given by

$$\epsilon E_{pe} \Lambda_s = E_{Be} \quad . \tag{154}$$

This equation simply states that the plasma and field energy densities are equal if $\epsilon = 1$. Thus $\epsilon = 2$ for one-dimensional motion and $\epsilon = 2/3$ for complete isotropization.

The magnitude of the energy change ΔE_B is given by the amount of work done by the plasma on the field as it expands from $z = z_{cr}$ to z = 0

$$\Delta E_B = -\int_{V_{cr}}^{V_e} \frac{B^2}{2\mu_0}\, dV_B \quad . \tag{155}$$

Because ϕ_T is a constant, (155) yields

$$\Delta E_B = E_{Bcr}\, \Psi_{cr} \tag{156}$$

where

$$\Psi_{cr} \equiv \frac{1 + A_{cr}/\Phi}{1 + \Lambda_s/A_{cr}} \tag{157}$$

where

$$A_{cr} \equiv Z_{cr}(2 - z_{cr}) \quad . \tag{158}$$

One more relation is needed to solve for the five variables in (152) and (153). To establish the value of q, these energies must be related to the initial stored energy E_T

$$E_T \equiv \tfrac{1}{2} C V_0^2 \ . \qquad (159)$$

Conservation of energy requires

$$\frac{E_{ccr}}{E_T} + \frac{E_{pcr}}{E_T} + \frac{E_{Bcr}}{E_T} = 1 \qquad (160)$$

where

$$E_{ccr} \equiv \tfrac{1}{2} C V_{cr}^2 \ . \qquad (161)$$

The first ratio in (160) can be determined by use of (129), the relation between z and charge. By the time $t = t_{cr}$, the capacitor has been completely discharged and is being charged in the opposite polarity, hence

$$C(V_o + V_{cr}) = \int_o^{t_{cr}} i dt \ . \qquad (162)$$

Using (129) yields

$$CV_{cr} = 2Q_p z_2 - Q_c . \qquad (163)$$

Since the ratio of the energies is equal to the ratio of the charges squared,

$$\frac{E_{ccr}}{E_T} = (2qz_{cr} - 1)^2 \ . \qquad (164)$$

The second ratio in (160) is essentially the energy transfer efficiency to the plasma during the initial implosion. The plasma energy E_{pcr} is related to the average ion energy W_{cr} by

$$E_{pcr} = W_{cr} V_L n_o \qquad (165)$$

where V_L is the volume of the vacuum chamber of length ℓ. Recasting (140) and substituting it into (165) yields

$$\frac{E_{pcr}}{E_T} = \gamma q I_1^2 \ . \qquad (166)$$

The third ratio in (160) can be determined by using (152), (153), (154), and (156), and by modifying (159) in the following way:

$$\frac{E_{ccr}}{E_T} - \frac{E_{pcr}}{E_T}\left[1 + \frac{E_{Bcr}}{E_{pcr}}\right] = 1 \ . \qquad (167)$$

When the term E_{Bcr}/E_{pcr} is evaluated and substituted into the equation along with (164) and (165), the following constraint on q is obtained:

$$q = \frac{1}{Z_{cr}}\left\{1 - \frac{\gamma I_1^2}{4Z_{cr}}\left[1 + \frac{1}{\Omega}\right]\right\} \ . \qquad (168)$$

The value of Ω

$$\Omega \equiv \frac{1 + (1+\epsilon\Lambda_s)\Psi_{cr}}{\epsilon\Lambda_s} \qquad (169)$$

is always much greater than unity for interesting parameter values. Since the second term in the bracket of (168) is always much less than unity, it is justifiable to simplify (168) to

$$q = \frac{1}{z_{cr}}\left[1 - \frac{\gamma I_1^2}{4z_{cr}}\right] . \qquad (170)$$

Equation (170) gives the desired constraint on q. It is apparent that q is only weakly dependent on γ and I_1, and from numerical results, z_2 varies only ±5% over a wide range of parameters. As a result, q is also rather constant. To verify (135), (170) is evaluated with γ given by (141), I_1 obtained from Fig. 4-17, and z_{cr} is given by its value from the constant field model (Fig. 4-15)

$$z_{cr} = \frac{2}{3} \ . \qquad (171)$$

The result is

$$q = 1.31 \qquad (172)$$

compared with 4/3 in (135).

4.3.3.4 Isotropization and Thermalization

The purpose of this part of the model is to relate the plasma energy E_{ps} at $t = t_s$ to the peak ion energy E_{pcr} at $t = t_{cr}$. The value of x_s is also determined. Finally the relation between E_θ, x_c, and q [see (50)] is derived by relating T_s and x_s with T_c and x_c through the adiabatic law.

From experimental observation and from simple theories, it appears that the electron temperature is at least half of the ion temperature at the end of the implosion phase [see (111)]. For the purpose of this model

$$T_{es} = \frac{1}{2} T_{is} \tag{173}$$

is assumed. Even though a large portion of this energy is probably given to the electrons during the initial implosion, this energy was not included in the energy balance. The inclusion of electron pressure has two minor effects. One effect is to decrease slightly the required value of q. The second term in the brackets in (170) would be increased by 50% to account for electron heating. This lowers q by 5 to 10% and increases the required capacitance of the bank by the same percentage for a fixed filling pressure p_0.

The second effect is a result of "adding" the electron energy in the Isotropization and Thermalization model. The model assumes that the energy comes from the magnetic field after the crowbar, thus unrealistically reducing the magnetic pressure at $t = t_s$. This results in an abnormally high x_s and low T_s where

$$T_s \equiv \frac{T_{es} + T_{is}}{2} . \tag{174}$$

The adiabatic invariant $T_s x_s^{4/3}$ is in good agreement with the numerical codes so that the inaccuracies in x_s and T_s present no significant drawback to the model.

The plasma energy at $t = t_s$ is related to the temperatures by

$$E_{ps} = \frac{3}{2} n_o V_L k_B (T_{es} + T_{is}) . \tag{175}$$

Using (174), E_{ps} becomes

$$E_{ps} = 3 n_o V_L k_B T_s . \tag{176}$$

Pressure balance requires that

$$n_s k_B (T_{es} + T_{is}) = \frac{B_s^2}{2\mu_0} . \tag{177}$$

Combining (176) and (177) yields

$$E_{ps} = E_{Bs} \frac{3}{2} \left[\frac{1 - A_s}{\Lambda_s + A_s} \right] \tag{178}$$

where

$$A_s \equiv z_s(2 - z_s) . \tag{179}$$

Now that the system is described at $t = t_s$ and $t = t_e$, the change in field energy between the two times can be calculated [see (155), (156), and (157)]

$$\Delta E_{Bs} = - \int_{V_e}^{V_s} \frac{B^2}{2\mu_0} dV_B . \tag{180}$$

By assuming that the total flux ϕ_T is conserved, (180) becomes

$$\Delta E_{Bs} = - E_{Be} \Psi_s \tag{181}$$

where Ψ_s is defined by

$$\Psi_s \equiv \frac{A_s/\Lambda_s}{1 + A_s/\Phi} . \tag{182}$$

Using the pressure balance at $t = t_e$ (154), (181) becomes

$$\Delta E_{Bs} = - E_{pe} \epsilon \Lambda_s \Psi_s . \tag{183}$$

The conservation of energy requires

$$E_{ps} = E_{pe} - \Delta E_{Bs} \tag{184}$$

or by combining (183) and (184)

$$E_{ps} = E_{pe} [1 + \epsilon \Lambda_s \Psi_s] . \tag{185}$$

Equation (185) relates the plasma energies at $t = t_e$ and $t = t_s$. By a similar technique using (152), (153), (154), and (156), E_{pe} can be related to the energy at $t = t_{cr}$

$$E_{pe} = E_{pcr} \left[\frac{1 + \Psi_{cr}}{1 + (1+\epsilon\Lambda_s)\Psi_{cr}} \right] \tag{186}$$

Combining (185) and (186) yields the desired result

$$E_{ps} = E_{pcr} \left[\frac{(1+\Psi_{cr})(1+\epsilon\Lambda_s\Psi_s)}{1 + (1+\epsilon\Lambda_s)\Psi_{cr}} \right] \tag{187}$$

Equation (187) will be used later in this section to evaluate E_θ.

Even though the value of x_s [needed to evaluate (187)] can be assumed to be 0.7, it is of interest to determine the value of x_s from the code in order to compare it with numerical models. The value is readily determined by using the energy conservation law

$$E_{ps} - E_{pe} = E_{Be} - E_{Bs} \tag{188}$$

in conjunction with the two pressure balance equations (154) and (178) and the energy relation (185). The result is a quadratic equation in A_s

$$A_s^2 + C_1 A_s + C_2 = 0 \tag{189}$$

where

$$C_1 = \frac{(\frac{2}{3} + \epsilon)\ \Phi + (\frac{2}{3} - \epsilon)\Lambda_s + \frac{5}{3}\epsilon\Lambda_s\ \Phi}{\frac{2}{3} + \epsilon(\Lambda_s - \frac{1}{3}\Phi)} \tag{190}$$

and

$$C_2 = \frac{(\frac{2}{3} - \epsilon)\ \Phi\Lambda_s}{\frac{2}{3} + \epsilon(\Lambda_s - \frac{1}{3}\Phi)} \ . \tag{191}$$

If (189) and (179) are evaluated for $\epsilon = 1$, $\Delta = 2.7$ cm, and $\Lambda_s = 1/2$, then $N = 0.47$, $\Phi = 0.27$ and

$$x_s = 0.96 \tag{192}$$

which is unrealistically high as previously mentioned. If (187) is evaluated with compatible parameter values,

$$\frac{E_{ps}}{E_{pcr}} = 0.74. \tag{193}$$

Numerically it is found that

$$\gamma x_s^{4/3} \frac{E_{ps}}{E_{pcr}} \simeq 0.45 \tag{194}$$

is virtually independent of q and Λ_s. As a check on the model, use of the values in (141), (192), and (193) yields 0.44.

In addition, if the plasma were adiabatically compressed from $x_s = 0.96$ to 0.70, then T_s would increase to make (193) become

$$\frac{E_{ps}}{E_{pcr}} = 1.1 \ . \tag{195}$$

This corresponds to about a 30% decrease in total plasma energy from t_{cr} to t_s if the electron energy is added to the ion energy described by E_{pcr}. This 30% decrease agrees well with simulation code results, and the correlation adds further support to the assumption that $x_s \simeq 0.70$.

The final objective of this section is to relate the maximum induced field E_θ to the plasma parameters at $t = t_s$ and also $t = t_c$. Combining (142) and (146) yields

$$E_\theta = \sqrt{\frac{n_0\mu_0}{m}}\ \frac{W_{cr}}{\gamma} \ . \tag{196}$$

Substituting in (165) and (176) provides one of the desired results

$$E_\theta = \sqrt{\frac{n_0\mu_0}{m}} \left(\frac{E_{pcr}}{E_{ps}}\right)\frac{3}{\gamma}\ k_B T_s \ . \tag{197}$$

The electric field can be expressed in terms of compression parameters by using the adiabatic relations and (102) and (104)

$$E_\theta = \sqrt{\frac{n_0\mu_0}{m}} \left(\frac{E_{pcr}}{E_{ps}}\right) \cdot \frac{3}{\gamma}\left(\frac{x_c}{x_s}\right)^{4/3} \frac{k_B\vartheta}{\ell n\ (0.537\Theta)} \ . \tag{198}$$

Equation (198) can be evaluated by using the following parameter values:

$$m = 2.5(1.67 \times 10^{-27}\text{kg})$$

$$p_o = 4 \text{ mtorr} \qquad \text{[see (48)]}$$

$$\gamma\ x_s^{4/3}\ \frac{E_{ps}}{E_{pcr}} = 0.45 \qquad \text{[see (194)]}$$

$$\frac{k_B\Theta}{e} = 2.08 \times 10^4 \text{ ev} \qquad \text{[see (91)]}$$

$$H = \frac{\eta n_0}{x_c^2 \alpha Q_f} \quad \text{[see (101)]}$$

$$\eta = 2.5 \times 10^{-2} \ m^3/\text{neutron} \quad \text{[see (98)]}$$

$$\alpha = 0.72 \quad \text{[see (100)]}$$

$$Q_f = 1.1 \quad \text{[see (45)]}$$

The result is

$$E_\theta = 65 \, x_c^{4/3} / \ell n(5.3/x_c^2 Q_f) \ . \quad (199)$$

This is the equation used in Sec. 4.1.4.3.1 [see (50)] to motivate the minimization of x_c in Sec. 4.1.4.3.2.

This section has been devoted to the derivation of field and plasma parameters associated with the implosion system. In the next section, some of these results will be used to optimize and evaluate the implosion circuit parameters.

4.3.4 Circuit Parameterization

The parameters of the implosion circuit shown in Fig. 4-16 are determined in this section by using some of the results obtained in the previous section. The values of the source inductance L_s and the load inductance $L_p(t)$ are described in Sec. 5.2.2.1.1, including their functional dependence on the bank voltage V_o and the number of turns N on the Marshall-type implosion coil. The crowbar inductance L_c should be made as small as possible, which is about 2 to 3 nH. The sizes of N, V_o, and the bank capacitance C are dependent on the implosion-heating requirements described in Sec. 4.3.3.

The first step in determining the circuit parameters is to find the optimum value of N. In general, the optimum value of N matches the circuit impedance to the plasma so that the desired plasma heating is achieved with the minimum V_o. The best indicator for determining the required amount of implosion heating is the peak electric field E_θ. This fact can be determined from (198) with H given by (101). Equation (198) essentially states that the amount of implosion heating (parameterized by E_θ) required to achieve the goal of a given Q is uniquely related to Q. The other parameters in (198) and (101) are x_c (which is set by the m = 1 stability criteria), p_o (which is set at the minimum allowed pressure of 4 mtorr), other parameters of the compression system, constants, and a group of implosion-heating parameters

$$\gamma \, x_s^{4/3} \frac{E_{ps}}{E_{pcr}} \simeq 0.45 \quad (200)$$

[see (194)] which is found to be essentially constant within the relevant range of implosion-heating parameters. Since no parameter of the implosion circuit affects this relation between E_θ and Q, E_θ can be used as the "goal" of the implosion system.

By using E_θ as a measure of the required implosion heating, N can be optimized by minimizing V_o in the following equation

$$V_o = 2\pi b \, N \frac{E_\theta}{I_1^2} \ . \quad (201)$$

This equation comes from (146) where E_θ is defined. The variable I_1 is dependent on N through the normalized source inductance [see (122) in Sec. 4.3.3 and (26) in Sec. 5.2.2.1.1]

$$\Lambda_s \equiv \frac{L_s}{L_o} \simeq \left(\frac{1}{10N}\right)^2 \left\{2 + \Delta\left[2.5 - \frac{\Delta}{10}\right]\right\} + 0.14 \quad (202)$$

where Δ is the coil insulator thickness in centimeters.

The dependence of I_1 on Λ_s is briefly described in Sec. 4.3.3 in conjunction with Fig. 4-17. For $\Lambda_s \ll 1$, I_1 approaches unity, I_1 is only weakly dependent on Λ_s, and V_o is linearly proportional to N. This agrees with a simple circuit analog where the load inductance L_o is the dominant impedance in the circuit so that the voltage available to the plasma $2\pi b E_\theta$ is just

$$2\pi b E_\theta \simeq \frac{V_o}{N} \quad (203)$$

where N is the turns ratio of the transformer-like Marshall coil. As $\Lambda_s \rightarrow 1$ more of the voltage is dropped across L_s hence reducing $2\pi b E_\theta$. This decrease in $2\pi b E_\theta$ occurs in (201) because of the decrease in I_1 with increasing Λ_s. As Λ_s is increased toward infinity, I_1^2 goes to zero faster than N, thus forcing E_θ to zero for a finite V_o. Physically, N = 0 corresponds to a Marshall coil (see Fig. 5-11) with straight conductors (no helical twist). Such a coil cannot produce B_z or E_θ fields, which agrees with the above analysis.

Obviously, the minimum V_o for a fixed E_θ has to occur for $\Lambda_s \sim 1$. A circuit theorem states that the

maximum power to the load occurs when the source impedance equals the load impedance. This does not imply $\Lambda_s = 1$ for this system, since L_o is the empty (no plasma) load inductance, and the imploding plasma is causing $L_p(t)$ to change with time. If the load inductance in the circuit theorem were approximated by the time average of $L_p(t)$ during the implosion, then

$$\Lambda_s = \frac{1}{2} \tag{204}$$

is very close to the optimum value. Fortunately this choice of Λ_s [see (134)] agrees with numerical results. A direct analytic optimization is, unfortunately, impossible due to the complexity of (128) and (136).

Once the value of Λ_s is fixed by (204), the optimum N can be determined from (202)

$$N = \frac{[2 + \Delta\ (2.5 - \frac{\Delta}{10})]^{1/2}}{6} \quad . \tag{205}$$

However, Δ is dependent on V_o, so that (28) (from Sec. 5.2.2.1.1), (205), and (201) must be solved simultaneously. The result is

$$V_o[MV] \simeq \frac{8}{25}\ \psi\ [\psi + (\psi^2 + \tfrac{1}{2})^{1/2}] \tag{206}$$

where

$$\psi = \frac{2\pi b E_\theta}{(16 \times 10^5)\ I_1^{\,2}\ (\Lambda_s - 0.14)^{1/2}} \quad . \tag{207}$$

Using $\Lambda_s = 1/2$, b = 10 cm, $I_1 = 0.73$ from Fig. 4-16, and (77) for E_θ, to evaluate (207) yields

$$\psi = \frac{3.0}{\delta_1^{\,8/15}\ \ell n\ (70\ \delta_1)} \quad . \tag{208}$$

The dependences of V_o and N on δ_1 are plotted in Fig. 4-18 by using (208), (206), and (205) where

$$\Delta[cm] = 10\ V_o[MV]. \tag{209}$$

The result clearly indicates the advantage of using large δ_1.

The capacitance C is easily determined by using (118), (119), (120), and the values of N and V_o in Fig. 4-17. The value of q is decreased to

$$q = \frac{5}{4} \tag{210}$$

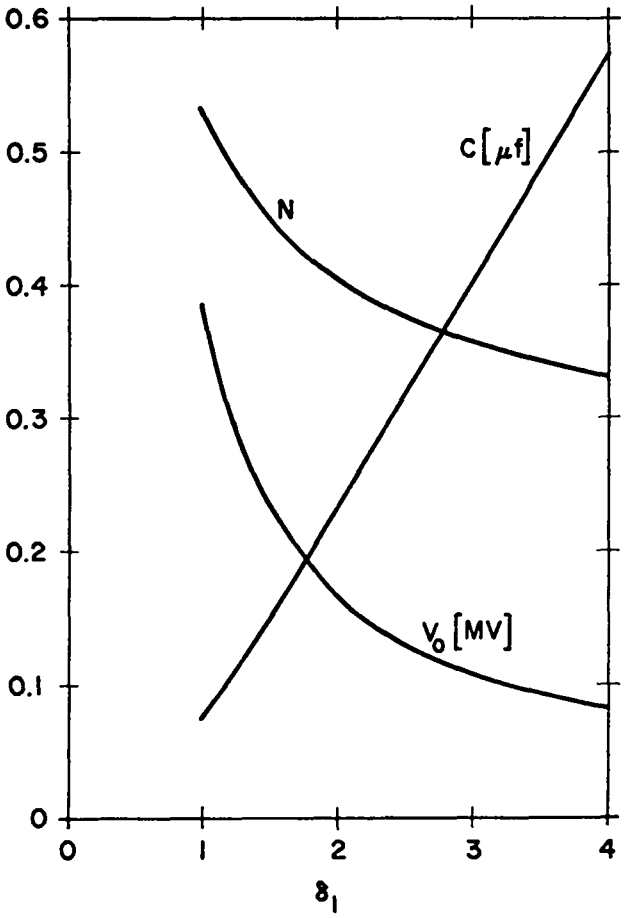

Fig. 4-18.
Effect of δ_1 on the implosion bank voltage V_o, number of turns on the implosion coil N, and the implosion bank capacitance C for a single implosion coil 20 cm long.

from the 4/3 value in (135) to allow for the electron heating as discussed in the Isotropization and Thermalization model in Sec. 4.3.3. The result is

$$C[\mu f] = \frac{1.6 \times 10^{-2}}{N\ V_o\ [MV]} \tag{211}$$

which is plotted in Fig. 4-18.

The total energy required in the implosion bank is obtained from

$$E_{TB} = (1280)\ \frac{1}{2}\ C V_o^{\,2} \tag{212}$$

where 1280 is the number of implosion coils in the system. The dependence of E_{TB} on δ_1 is plotted in Fig. 4-19.

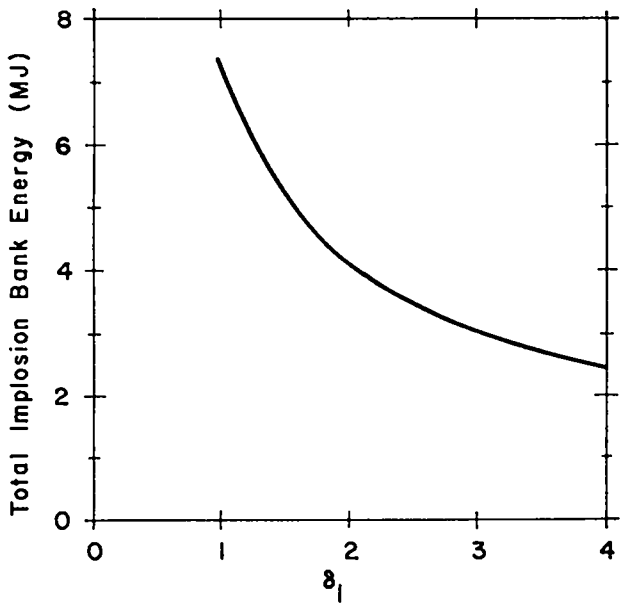

Fig. 4-19.
Dependence of the total implosion bank energy on δ_1.

The efficiency of the implosion system is estimated in Sec. 4.1.4.1.2 by using simple pressure balance and impedance matching arguments. An independent method is possible using (166), (187), and the relation

$$e_{Ti} = \frac{E_{pcr}}{E_T}\,\frac{E_{ps}}{E_{pcr}} \quad . \tag{213}$$

The result can be evaluated using Fig. 4-17, (141), (210), and (193) (hence pessimistically ignoring electron heating)

$$e_{Ti} \simeq 0.31 \quad . \tag{214}$$

This result compares favorably with the previous result in (28) or Fig. 4-5 with $x_s = 0.7$.

Two general conclusions can be made about implosion heating if experiments confirm the results of the resonant heating model. First, the method is an efficient way of preheating the plasma for the compression phase and, second, the larger δ_1 is made, the more attractive the system becomes technologically. The engineering design presented in this report is based on the pessimistic choice of $\delta_1 = 1.5$, but we hope future experiments will add to the Garching results[8] which indicate that $\delta_1 \gtrsim 3$ is an acceptable and attractive operating range.

REFERENCES (Chap. IV)

1. M. N. Rosenbluth, J. L. Johnson, J. M. Greene, and K. E. Weimer, "Stability Limitations for Stellerators with Sharp Surfaces," Phys. Fluids **12**, 726 (1969).

2. H. Grad and H. Weitzner, "Critical β from Stellerator and Scyllac Expansions," Phys. Fluids **12**, 1725 (1969).

3. F. L. Ribe, "Free-Boundary Solutions for High-Beta Stellerators of Large Aspect Ratio," Los Alamos Scientific Laboratory report LA-4098-MS (May 1969).

4. F. L. Ribe and M. N. Rosenbluth, "Feedback Stabilization of a High-β, Sharp-Boundaried Plasma Column with Helical Fields," Phys. Fluids **13**, 2572 (1970).

5. J. P. Freidberg and W. Grossmann, private communication (1974).

6. W. R. Ellis, F. C. Jahoda, R. Kristal, W. E. Quinn, F. L. Ribe, G. A. Sawyer, and R. E. Siemon, "Plasma Equilibrium and Stability in the Scyllac Toroidal Sector Experiments," Nucl. Fusion **14**, 841 (1974).

7. J. P. Freidberg, "Stability of the Straight ℓ=1 Scyllac Configuration," Phys. Fluids **14**, 2454 (1971).

8. M. Kaufmann, private communication (June 1975).

9. J. P. Freidberg, R. L. Morse, and F. L. Ribe, "Staged Theta Pinches with Implosion Heating," Symp. Technology of Controlled Thermonuclear Fusion Experiments and Engineering Aspects of Fusion Reactors, Austin, TX, Nov. 20-22, 1972.

10. R. A. Krakowski, F. L. Ribe, T. A. Coultas, and A. J. Hatch, "An Engineering Design Study of a Reference Theta-Pinch Reactor (RTPR)," Los Alamos Scientific Laboratory report LA-5336/ANL-8019 (March 1974).

11. D. Pfirsch and H. Tasso, "A Theorem on MHD-Instability of Plasmas with Resistive Walls," Nucl. Fusion 11, 259 (1971).

12. J. P. Goedbloed, D. Pfirsch, and H. Tasso, "Instability of a Pinch Surrounded by a Resistive Wall," Nucl. Fusion 12, 649 (1972).

13. E. L. Cantrell, W. R. Ellis, H. W. Harris, F. C. Jahoda, R. Kristal, M. D. Machalek, J. R. McConnell, W. E. Quinn, F. L. Ribe, G. A. Sawyer, F. T. Seibel, and R. E. Siemon, "Plasma Experiments in the Scyllac Toroidal Theta Pinch," Proc. Fifth IAEA Conf. on Plasma Physics and Controlled Nuclear Fusion Research, Tokyo, Nov. 11-15, 1974.

14. T. A. Oliphant, "Fuel Burn-Up and Direct Conversion of Energy in a D-T Plasma," Proc. BNES Conf. on Nuclear Fusion Reactors, UKAEA Culham Laboratory, Sept. 17-19, 1969, p. 309.

15. J. L. Tuck, "Thermonuclear Reaction Rates," Nucl. Fusion 1, 201 (1961).

16. A. G. Sgro and C. W. Nielson, to be published.

17. T. A. Oliphant, "A Mixed Snowplow-Bounce Model for Shock Heating in a Staged Theta Pinch," Nucl. Fusion 14, 377 (1974).

V. SYSTEM DESIGN

5.1 AN OVERVIEW

The SFTR facility can be subdivided into a number of somewhat isolated systems. This chapter describes each in detail, and this section gives an overview of their integration into the SFTR.

The electrical systems and the implosion and compression circuits provide two-stage heating of the plasma. The implosion circuit heats the ions in the preionized plasma from ~1 eV to ~3 keV. The electron heating is determined by anomalous processes in the sheath during the shock, hence we cannot calculate it. Experience from Scyllac and particle simulation codes suggests $T_e \sim 1/2\ T_i$ after implosion, so we assume that value.

The implosion circuit must produce a fast-rising magnetic field to accomplish the initial heating, and two different approaches are possible. The first is an adaptation of the Staged Theta Pinch circuit, and uses a complex circuit to program the magnetic field waveform. The field is essentially removed when the sheath is at its minimum radius, allowing it to expand freely toward the wall. Before contact, the field is reapplied to hold the plasma at a large radius. In this circuit, the plasma impedance is small compared to the circuit impedance so that the latter controls the current waveform. Figure 5.1-1 shows the circuit and field waveform of a pulse-forming network.

An alternative approach, termed resonant heating,[1] uses a simple capacitor circuit with minimum source impedance, such that the plasma impedance is comparable or larger. The plasma initially appears inductive, and the current rises as in an LC circuit. As the sheath moves off the wall, the changing inductance (which appears resistive) is the dominant plasma impedance, and the resulting RC behavior (see Fig. 4-16) resembles a crowbarred capacitor circuit. If the quarter period $\pi\sqrt{LC/2}$ is set approximately equal to the time for the sheath to reach its minimum radius (hence the term resonant heating), and the capacitor is then crowbarred, the plasma will deliver energy back to the field, increasing the circuit current (see Fig. 4-16).

The major advantages of the resonant circuit are its simplicity and its efficiency. It is efficient because the low source inductance permits more energy to be delivered to the plasma. It is simple because the capacitor switching is simultaneous as opposed to the programmed switching of the other approach. Because of these advantages we use the resonant circuit in this design.

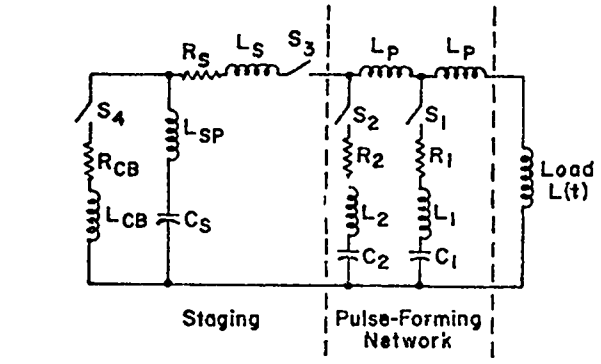

Implosion-Heating Network

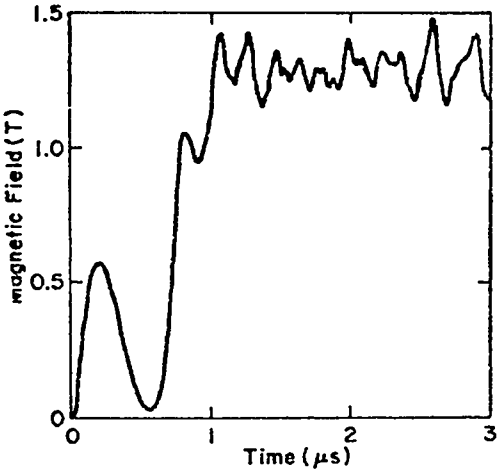

Fig. 5.1-1.
A pulse-forming network and the magnetic field waveform it produces.

The resonant approach is made possible by the Marshall coil which can be designed to have an even lower inductance than the single turn coils in present theta pinches. A separate end-fed Marshall-type implosion coil is a necessity in SFTR since a high inductance is required for the slow compression circuit. The end feed is forced by the geometry of the situation.

The implosion coils are nested inside the compression coils, and to avoid inducing high voltage on the compression coils a shorting capacitor is placed on the compression coil to force flux from the implosion coil to return in the annular region between the two

coils. This region is filled with magnetic material to reduce the energy stored in that region. The shorting capacitor allows a slow-rising compression field to rise, but shields the compression coil from the fast implosion field. The geometry is shown in Fig. 5.1-2.

Outside the compression coil there is 1/2 m of primary shield, penetrated by radial feed plates to the Marshall coil. Figure 5.1-3 shows the feed plates and supporting structure. Beyond the shield these radial plates are fed with pairs of 135-kV implosion capacitors placed on the periphery. Azimuthally spaced between the capacitors are the crowbar gaps. A cross section perpendicular to the toroidal axis is shown in Fig. 5.1-4.

A toroidal vacuum manifold runs under the main torus, with 188 connecting paths periodically placed around the torus. The ~8000-ℓ volume is pumped at 4 stations with 2000-ℓ/s pumps at each station. The vacuum and tritium handling systems are intimately connected. The tritium injection uses standard volumes and vacuum transfer methods, and the recovery is at the cryogenic vacuum pump station.

The entire vessel, from the plasma radially outward to the implosion capacitors and vacuum system, is set in a cell with 1.5-m-thick concrete walls for biological shielding. Electrical leads for energizing capacitors and coils, and for diagnostics, penetrate the wall at feedthroughs located around the cell as shown in Fig. 5.1-5, which shows a cross section of the cell. By maintaining a pressure differential of a few pounds per square inch between the cell and the outside, with the cell pressure lower, contamination of outside air is minimized in the event of a leak.

The magnetic energy transfer and storage (METS) system stores and transfers 488 MJ of energy to the pancake-type compression coils. The

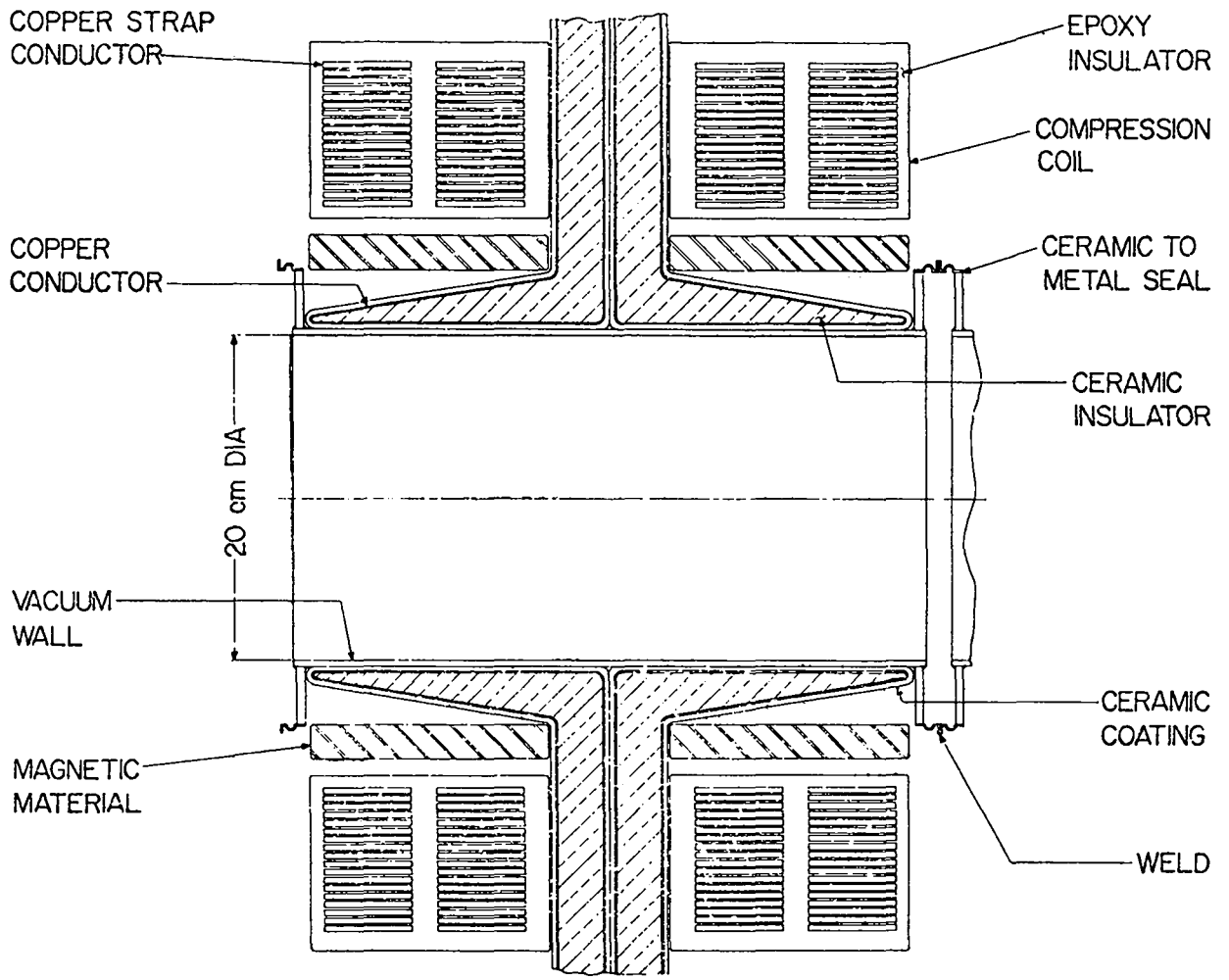

Fig. 5.1-2.
Coil assembly.

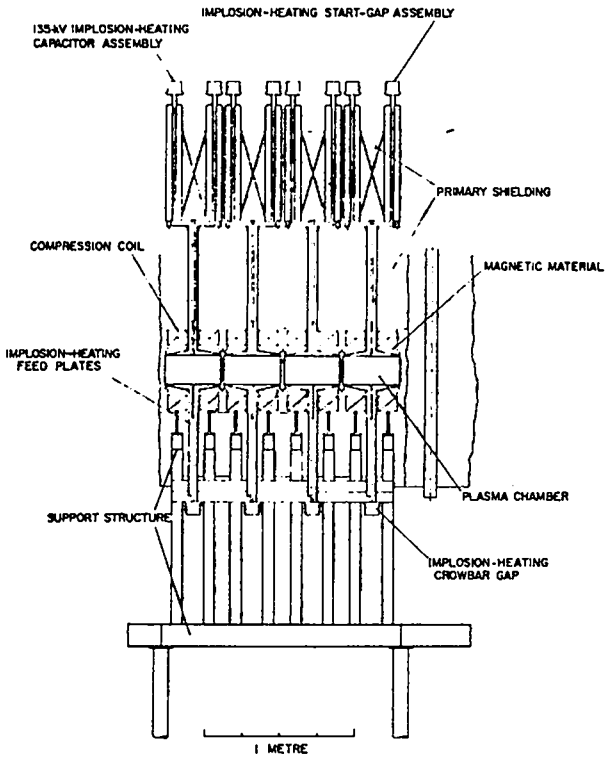

Fig. 5.1-3.
Section of the torus, showing the plasma chamber, implosion and compression coils, and physical layout of the implosion circuit components.

system is modular, with 1280 units of storage coil, interrupter, transfer capacitor bank, and compression coil. Each module has 381 kJ and energizes 20 cm of the torus. The storage coils are stacked in 128 dewars, 10 to a dewar, around the machine. The 1280 vacuum interrupter modules use 4 vacuum bottles each, 2 in series and 2 in parallel, to break 26 kA and hold 60 kV. Each transfer capacitor module has 18 series-parallel, connected capacitors storing 185 kJ. The components are located outside the cell, as in Fig. 5.1-6.

The storage coils are series charged with a 125-V, 26-kA dc supply. Each storage coil is separated by a low resistance (~10-100 nΩ) switch, which is opened to isolate the modules for parallel discharging. Energy transfer to the compression coil is initiated by opening and then counterpulsing the vacuum interrupters, forcing a momentary current zero to extinguish the arc. Energy for the counterpulse circuit (10 MJ) comes from the transfer capacitors which were charged to a few kilovolts for that purpose.

The refrigerator for the helium load liquefies 3045 kg/h, about 22 times more than any plant in operation today. The power requirement for the refrigerator and compressors is 12 MW. The heat losses include both steady-state and pulsed loads. The steady-state dewar losses are 7.6 kW, including 5.4 kW for the current leads to the dewar. The pulsed dewar losses are 8.6 kW, of which 5.5 kW are associated with the disconnect switches between storage coils. The transfer lines between components of the refrigeration system consume another 1.1 kW, for a total helium refrigeration requirement of 17.3 kW.

The cryogenic plant and tritium waste treatment facility are located on the outside of the building housing the cell. An artist's conception of the SFTR, showing the layout of the various facilities is shown in the frontispiece of this report.

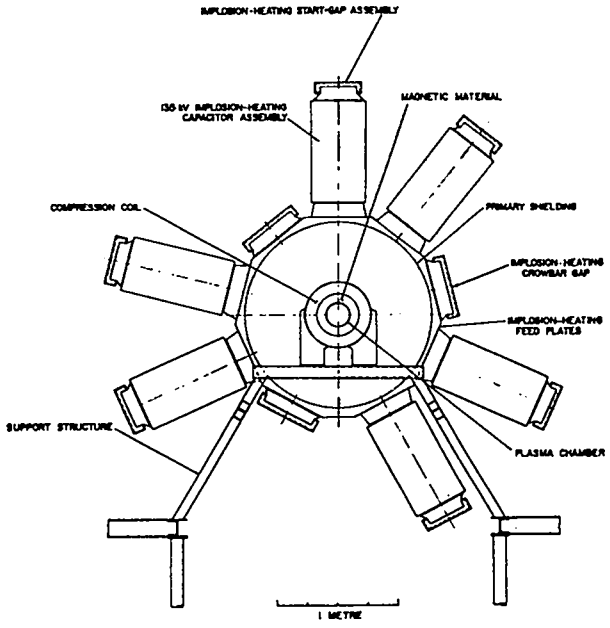

Fig. 5.1-4.
Axial view of the implosion system and coil assembly.

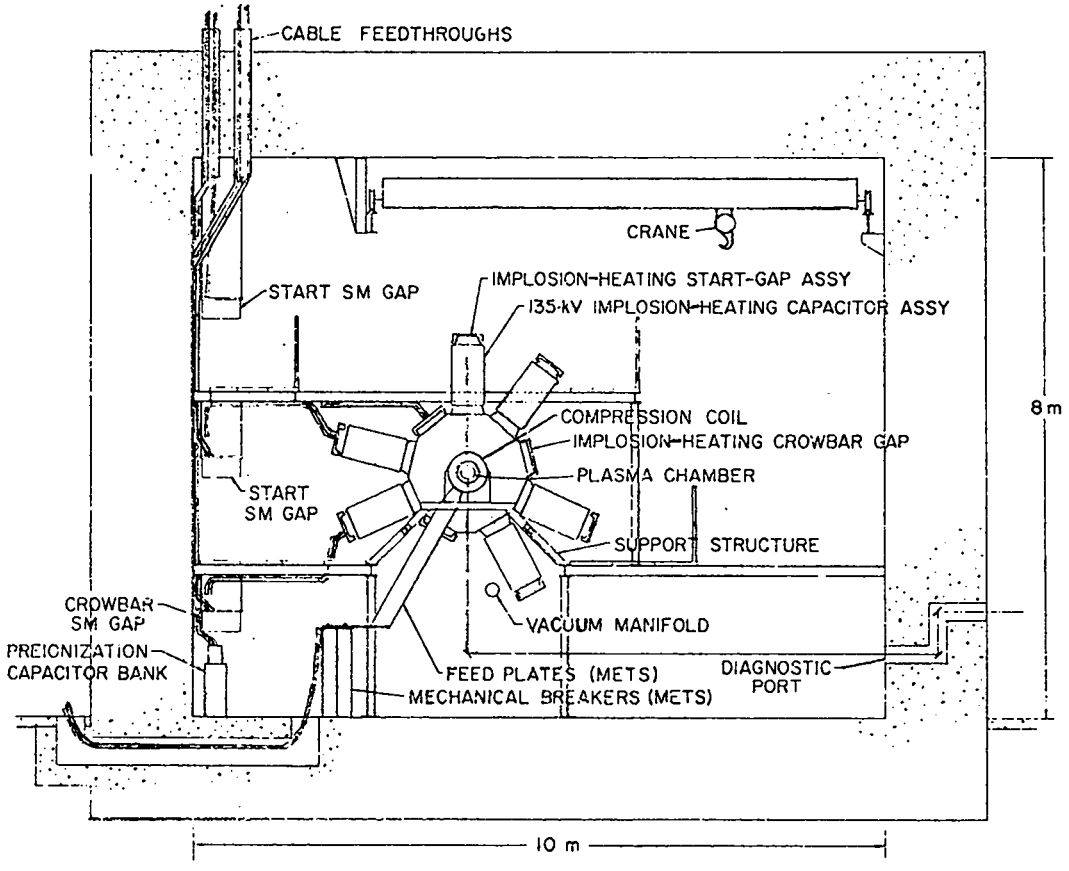

Fig. 5.1-5.
Cross section of cell with the experimental chamber, cabling, and submaster (SM) trigger gaps.

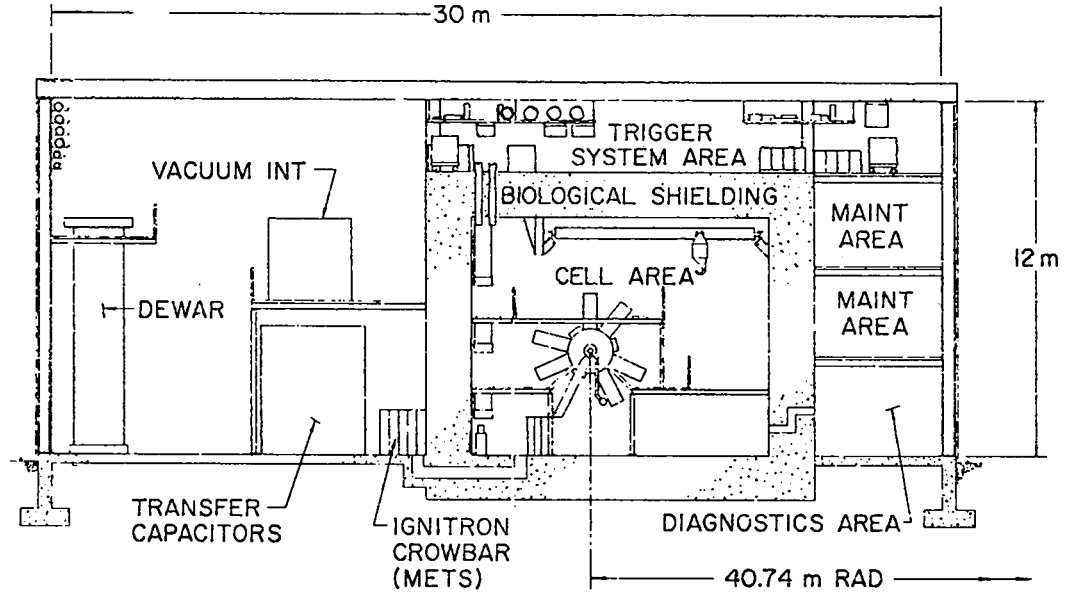

Fig. 5.1-6.
Building cross section showing location of METS components.

5.2 VESSEL DESIGN AND ANALYSIS

5.2.1 Summary

In this section the engineering design and fabrication of the containment system is described. The components include the first wall, implosion coil, magnetic material, compression coil, start and crowbar gaps, feedplates, and structural support. These components are shown in Fig. 5.1-4. In particular, we consider the electrical design, thermal and stress analyses, and the constraints imposed by the electrical and mechanical properties of materials.

The ceramic first wall and Marshall coil are both difficult components to fabricate, hence have a substantial influence on the design. The dielectric strength of the ceramic insulator in the implosion coil determines the internal inductance of the structure, hence limits the voltage for efficient energy transfer. The inductances of the coil and feed structure are computed.

The implosion coil is also subject to magnetic stresses, and both static and dynamic stresses have been calculated using a finite element code. The quasimagnetostatic fields produce a dynamic stress which is about twice the static stress but well within material limits.

The first wall is subject to neutron, particle, and photon fluxes which induce a significant thermal stress on the ceramic material. As determined here, these stresses are within limits but the margin is not large and is dependent on details of the rate of energy deposition from the plasma which are not precisely known. This rate determines the thickness of the temperature gradient region, hence the stress level.

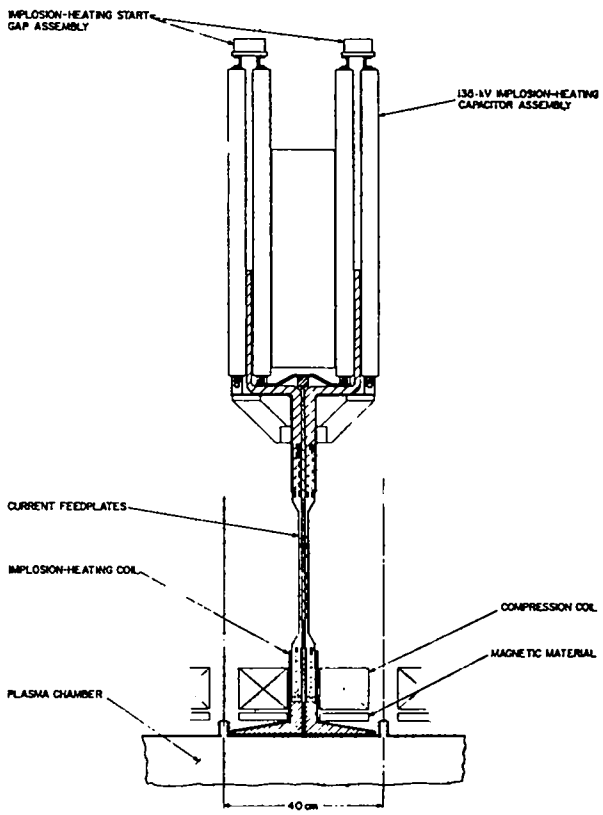

Fig. 5.2-1.
Implosion system, showing the start gaps, capacitors, transmission line, and implosion coil.

5.2.2 Engineering Design of Containment System

5.2.2.1 Electrical Aspects of Vessel Design

The electrical requirements of the implosion and compression systems strongly affect the design of the coil assembly shown in Fig. 5.1-2. Some of these aspects are discussed briefly here, while those that need more extensive explanation are discussed in the three subsections which follow.

The implosion coil must have a low inductance and be fed with a low inductance line to produce resonant heating. The implosion coil shown in Fig. 5.1-2 has the necessary low inductance, as does the parallel plate line (Fig. 5.2-1 and 5.1-4) which feeds it. The line also allows the required coaxial relation between the implosion and compression coils.

The electrical interaction between the implosion and compression coils must also be considered. A shorting capacitor can be placed across the terminals of the compression coil to prevent voltage multiplication in the multiturn compression coil when the implosion coil is energized. This shorting of the compression coil, although necessary, causes the undesirable storage of implosion field energy in the area between the coils A_2 shown in Fig. 5.2-2. If $A_1 = A_2$, and if both regions have the permeability of free space, then it is obvious from Fig. 5.2-2 that the energies stored in A_1 and A_2 will be equal.

To reduce the stored energy in A_2 without increasing the required implosion energy, magnetic material is inserted in area A_2 (see Fig. 5.1-2). If $\mu_2 \gg \mu_1$, and if $A_1 \simeq A_2$, then the implosion energy stored in A_2 will be made smaller than in A_1. In addition, the compression system will not be adversely affected.

The magnetic material not only minimizes the extra energy storage, but it also reduces the possibility of voltage breakdown inside the compression coil. Even though the compression coil terminals are shorted on the outside, flux from the implosion field

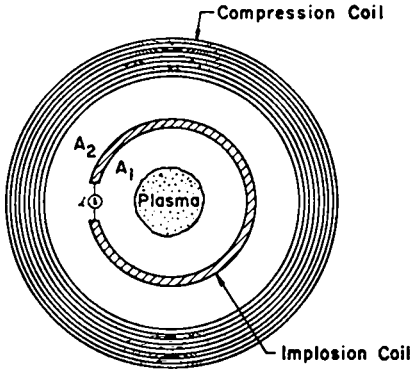

(a) Schematic Cross Section of the SFTR Module

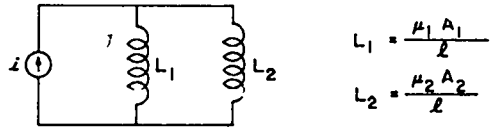

(b) Equivalent Circuit for the Implosion Coil With the Compression Coil Terminals Shorted

Fig. 5.2-2.
Schematic diagram and circuit which model the electrical interaction between the implosion and compression coils.

will still penetrate into the body of the coil. This changing flux induces an electric field which is largest between the inner two windings of the coil. The presence of the magnetic material reduces this field from the free-space condition by the ratio of μ_2/μ_0.

The magnetic material must satisfy four requirements:

1. The saturation field must be as large as possible to minimize A_2.
2. We require an effective value of $\mu_2 \gtrsim 10\ \mu_0$ (including air gaps imposed by the feedplates). Thus, the μ of the bulk material for pulsed application must exceed $30\ \mu_0$.
3. The field must be able to penetrate the material during the rise time of 100 ns.
4. The induced electric field generated by the penetrating B-field must not break the material down.

The proposed fabrication of this material is discussed in Sec. 5.2.3.2.

The first wall, or vacuum wall, must be as close to the implosion coil conductors as possible to maximize wall stabilization (see Sec. 4.1.4.2), and to minimize the source inductance of the implosion system (see Sec. 4.3.2). This implies that the vacuum wall should be made as thin as possible and still maintain mechanical integrity.

Electrical requirements of the system also impose strong constraints on the vacuum seals between adjacent vacuum wall segments. Organic materials cannot be used because of tritium contamination and radiation damage. Bolted metal flanges cannot be used because the magnetic fields cannot penetrate the massive flanges and unacceptable field distortion results. Thin welded metal joints, shown in Fig. 5.1-2, can be used only if they are at a sufficiently large radius that the implosion field (including the flux passing between segments of magnetic material) is not seriously distorted by the metal. The slowly rising compression field can diffuse through this welded seal without serious distortion. The position of the joint in Fig. 5.1-2 is the only acceptable one since the joint's radius is barely large enough to prevent serious implosion field distortion and barely small enough to allow the compression coil to slide over it.

5.2.2.1.1 Implosion-Heating Coil

A more detailed description of the coil is presented here than in the previous section. The constraints on the conductor shape and size are discussed along with insulator requirements. Finally, the fields produced by the coil are described and the coil inductance is calculated.

The current path in the coil is shown by the arrows in Fig. 5.2-3. It follows the conductive strips radially in on the transmission line, axially down the outside of the coil, helically back up the inside of the coil, and back out the transmission line. On the inside of the coil the conductor is made of strips to force the current to take the desired helical path. Elsewhere, the conductor is made of strips to allow fields to penetrate.

The 50% transparency achieved by equal conductor and gap widths insures that the implosion field, passing through the transmission line between magnetic material segments, will not be increased by more than a factor of 2. The slowly rising compression field will diffuse through the copper conductors and hence will not be greatly affected by the transmission line. The equal widths of conductor and gap do not increase the coil inductance appreciably over the solid conductor case as long as the conductor width is small compared with the insulator thickness of the transmission line.

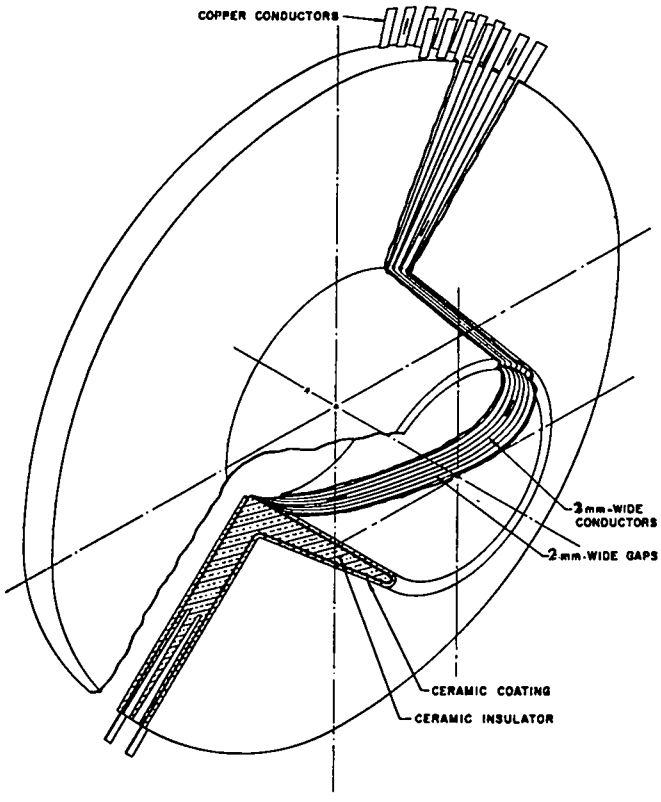

Fig. 5.2-3.
Marshall-type implosion coil.

The thickness of the conductors has been chosen to be 1.5 mm in Sec. 4.1.4.2.1 [see (21)]. The conductor is thus thick enough to allow the crowbar gap to dominate the L/R decay time of the implosion field, but thin enough so that the compression field can diffuse through the coil.

The insulator should be kept as thin as the dielectric strength will allow so that the coil inductance can be minimized. The coil thickness is tapered because the voltage across the insulator decreases linearly along the coil. For adequate reliability in a system as large as SFTR, the dielectric strength of the Al_2O_3 ceramic has been estimated at

$$E_D = 10^5 V/cm. \quad (1)$$

Additional testing is needed before a firm value can be assigned to this dielectric strength under the appropriate pulsed conditions. The ceramic coating added to the outside of the conducting layer is needed to prevent arcing between adjacent conductors. Using a maximum E_θ of 5 kV/cm (see Fig. 4-10), the maximum field between the conductors is 10 kV/cm, or 4 kV between conductors.

For the purpose of calculating the inductance of the coil, the magnetic fields can be approximated by a simple model. The field inside the ceramic insulator is in the θ (azimuthal) direction arising from the radial and z (axial) components of the current. The θ component of the current inside the coil gives rise to the axial magnetic field H_z surrounded by the coil. The H_z field outside the coil is assumed to be negligible because of the magnetic material.

The dimensions used in the inductance calculation are shown on the schematic coil cross section in Fig. 5.2-4 (compare with Fig. 5.2-1). Starting with the capacitors and working toward the coil, the best estimate of the inductance L_{cs} for the six parallel capacitor-gap combinations shown in Fig. 5.1-4 is

$$L_{cs} = 4_{nh}. \quad (2)$$

The inductance of the transmission line L_l with two thicknesses $\bar{\Delta}$ and Δ can be calculated using

$$H_\theta = \frac{i}{2\pi r} \quad (3)$$

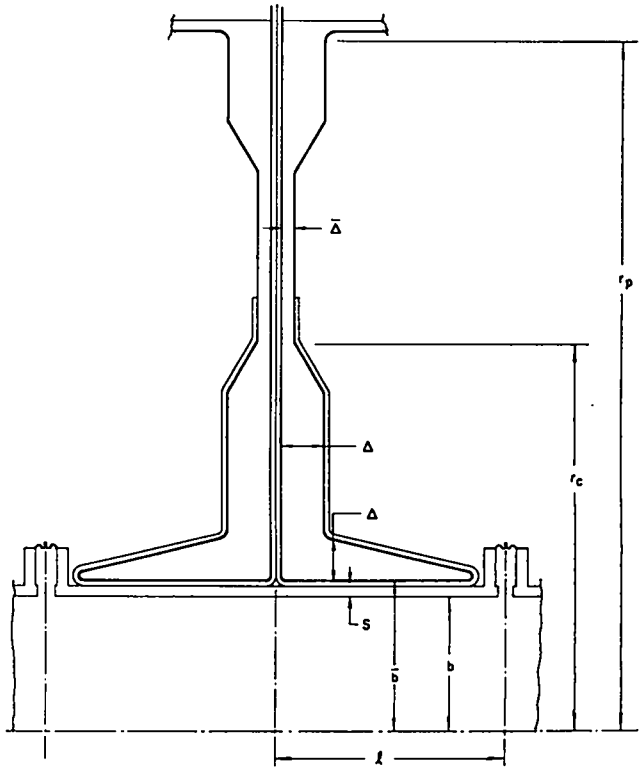

Fig. 5.2-4.
Schematic cross section of the implosion coil showing dimensions used in deriving the inductance.

and

$$L_\ell = \mu_0 \int \left(\frac{H_\theta}{i}\right)^2 dV. \tag{4}$$

The result is

$$L_\ell = \frac{\mu_0 \Delta}{2\pi} \left\{ \ell n\left(\frac{r_c}{\bar{b}}\right) + \frac{\bar{\Delta}}{\Delta} \ell n \left(\frac{r_p}{r_c}\right) \right\} . \tag{5}$$

The inductance $L_{c\theta}$ associated with the H_θ field in the coil insulator is obtained from (3) and an equation similar to (4) yielding

$$L_{c\theta} = \frac{\mu_0}{2\pi} \int_0^\ell \cdot dz \int_b^{\Delta(1 - \frac{z}{\ell}) + b} \frac{dr}{r} \tag{6}$$

and finally

$$L_{c\theta} \quad \frac{\mu_0 \ell}{2\pi} \left\{ - 1 + \left(1 + \frac{b}{\Delta}\right) \ell n \left(1 + \frac{\Delta}{b}\right) \right\} . \tag{7}$$

For $\Delta/b \ll 1$, (7) can be approximated by

$$L_{c\theta} \approx \frac{\mu_0 \Delta}{2\pi} \frac{\ell}{2b} \left(1 - \frac{\Delta}{b}\right). \tag{8}$$

The last component of inductance that is needed is the inductance L_{cz} of the coil associated with the H_z field. The derivation is simplified by defining the following areas

$$A_v \equiv \pi(b^2 - a^2) \tag{9}$$

$$A_w \equiv \pi(\bar{b}^2 - b^2) \tag{10}$$

so that

$$A_1 = A_v + A_w \tag{11}$$

(A_1 was defined in Fig. 5.2-2). In addition,

$$A_2' \equiv A_2 + \left(\frac{\mu_2}{\mu_0} - 1\right) A_m \tag{12}$$

where A_2 is the cross-sectional area between the compression coil and the implosion coil surface of $r = \bar{b}$ (see Fig. 5.2-2(a)), and A_m is the cross-sectional area of the magnetic material.

If $\mu_2 \gtrsim 10\ \mu_0$ then $A_2' \gg A_1$, and therefore the H_z field for $r > \bar{b}$ is negligible. Under this assumption the surface current K_θ in the azimuthal direction at $r = \bar{b}$ is related to the axial component K_z by

$$K_\theta = \frac{\theta \bar{b}}{\ell} K_z \tag{13}$$

where θ is the angle through which the conductors rotate from the front edge to the back edge of the coil. Since

$$K_z = \frac{i}{2\pi\bar{b}} \tag{14}$$

then

$$K_\theta = \frac{Ni}{\ell} \tag{15}$$

where

$$N \equiv \frac{\theta}{2\pi} . \tag{16}$$

From the boundary condition on H_z and (15)

$$H_z = \frac{Ni}{\ell}, \tag{17}$$

and the inductance becomes

$$L_z = \frac{\mu_0 N^2 A_1}{\ell} . \tag{18}$$

A similar but more involved derivation can be made which includes the fields in area A_2. The result is identical with (18) if A_1 is replaced by

$$A_1 \rightarrow A_1 \left\{ \frac{1}{1 + \frac{A_1}{A_2'}} \right\} . \tag{19}$$

For the SFTR design, (18) is sufficiently accurate.

For the implosion model described in Sec. 4.3, the system inductance is divided into the source inductance L_s and the load inductance L_p. The load inductance is associated only with the field inside the vacuum wall. This is given by (18) with A_1 replaced by A_v. Using (9) yields

$$L_p(t) = \frac{\mu_0 N^2 \pi (b^2 - a(t)^2)}{\ell} . \quad (20)$$

The appropriate inductance to use as a base for normalizing is the vacuum inductance

$$L_o \equiv \frac{\mu_0 N^2 \pi b^2}{\ell} . \quad (21)$$

The source inductance L_s includes all of the inductances not included in (20)

$$L_s = L_{cs} + L_\ell + L_{c\theta} + L_{wz} \quad (22)$$

where

$$L_{wz} \equiv \frac{\mu_0 N^2 A_w}{\ell} . \quad (23)$$

Since $s \ll 2b$,

$$L_{wz} \approx \frac{\mu_0 N^2 2\pi b s}{\ell} . \quad (24)$$

Substituting (5), (8), and (24) into (22) yields

$$L_s = L_{cs} + \frac{\mu_0 \Delta}{2\pi} \left\{ \ell n \left(\frac{r_c}{\bar{b}} \right) + \frac{\bar{\Delta}}{\Delta} \ell n \left(\frac{r_p}{r_c} \right) + \frac{\ell}{2b} \left(1 - \frac{\Delta}{b} \right) \right\} + \frac{\mu_0 N^2 2\pi b s}{\ell} . \quad (25)$$

Define Λ_s as L_s normalized to L_o [see (21)]

$$\Lambda_s = \frac{L_{cs}}{L_o} + \frac{\Delta \ell}{2\pi^2 N^2 b^2} \left\{ \ell n \left(\frac{r_c}{\bar{b}} \right) + \frac{\bar{\Delta}}{\Delta} \ell n \left(\frac{r_p}{r_c} \right) + \frac{\ell}{2b} \left(1 - \frac{\Delta}{b} \right) \right\} + \frac{2s}{b} . \quad (26)$$

Using (2) and SFTR dimensions yields

$$\Lambda_s = \left(\frac{1}{10N} \right)^2 \{ 2 + \Delta [2.5 - \frac{\Delta}{10}] \} + 0.14 \quad (27)$$

where Δ is in centimeters. The insulation thickness Δ is controlled by the dielectric strength E_D of the ceramic [see (1)] and the voltage V_o used to drive the coil

$$\Delta = \frac{V_o}{E_D} . \quad (28)$$

The relation between V_o and the required E_θ is derived in Sec. 4.3. For a given E_θ, V_o can be minimized by choosing the value of N which properly matches the circuit to the plasma.

5.2.2.1.2 Electrical Description of the Compression Coil

The electrical design of the compression coil is dictated by the required magnetic field strength as a function of time, the present limitations in the superconducting technology of magnetic energy storage, and finally by various constraints on the coil dimensions. The peak magnetic field is 5.5 T and the rise time for the field is 0.7 ms. At peak field the compression coils are crowbarred and the time constant of the field decay is 250 ms. Both the peak field and decay time are specified by the plasma heating and burn time requirements. The rise time is specified by the decay time of the magnetic field produced by the shock heating coils and the need for the magnetic field of the compression coils to pick up the plasma confinement before the field of the shock heating coils decays too much.

The limitations on conductor current and voltage imposed by present-day superconducting technology are uncertain, but for design purposes a peak current of 25 kA and a peak voltage of 60 kV have been selected. Beyond this, the technological problems associated with the magnetic energy storage system powering each compression coil become more difficult. The inside radius of the compression coil must be at least 17 cm to enclose the discharge tube, shock heating coils, etc. Parallel plate transmission lines feeding the shock heating coils are brought in every 40 cm along the theta-pinch's major circumference. Midway between entry points for the shock heating feeds, a 2-cm-long access space to the discharge tube must be left open for either vacuum pumping ports or diagnostic ports. Consequently, individual compression coils must fit within the 14.75-cm length between the shock heating feeds and the vacuum

pumping ports. The compression coils may extend radially to the distance required to contain the windings of the coil and its insulation. Enough copper must be included to give the compression coils a decay time of 270 ms since the bus bar and crowbar resistance will bring this down to 250 ms.

All of the above electrical requirements can be met by compression coil modules with an inside radius of 17 cm, an outside radius of 27.9 cm, and a length of 14.75 cm. These dimensions include insulation and are also average dimensions since the $\ell = 1$ and $\ell = 0$ modulations will cause small modifications of the radial dimensions. Figures 5.1-2 and 5.2-1 show these coils and their locations around the implosion coil. Each module provides field for 20 cm along the theta-pinch's major circumference. Each coil is wound with 36 turns of flat copper strap 0.38 cm thick. No further subdivision and transposition of the conductor are needed, although a single subdivision and transposition could be done with very little additional cost.

5.2.2.1.3 Current Feedplates and Structural Supports

Around the 81.48-m-diam torus, 640 machine modules are positioned. Each module is 40 cm wide and is composed of two 20-cm-wide implosion-heating coils positioned back-to-back with a common collector plate feed in the center of each module. The compression coil and magnetic material surround each implosion-heating coil. The collector plate has an inside diameter of 66 cm where the implosion-heating coil is attached and an outside diameter of 166 cm where the implosion-heating capacitor and rail-gap assemblies and crowbar rail-gap assemblies are attached. Two implosion-heating capacitor assemblies are installed side by side as shown in Fig. 5.2-1. Four additional assemblies are installed in pairs, each ±120° from the first set of implosion-heating capacitor assemblies, as shown in Fig. 5.1-4. Three implosion-heating crowbar gaps are installed, each between a pair of implosion-heating capacitor assemblies. Space at the bottom of the collector plate is reserved for diagnostic access, the vacuum system, and the METS parallel plate compression coil leads.

Each of the implosion-heating capacitor assemblies and crowbar gaps is designed to plug into the outside diameter of the collector plate with an air connection to hold off the 270-kV system voltage. The electrical connections between the collector plates and the implosion-heating coil are also made in a similar geometry. The dielectric medium between aluminum conductors in the collector-plate region will be polyethylene.

The structural supports for the implosion-heating coil and compression coil systems are an integral part of the structural platforms in the main cell area. Each of the coil systems is supported independently from a central frame geometry (as in Figs. 5.1-3 and 5.1-4) located between and below adjacent machine modules. Structural cross members tie supports together between machine modules. Each support system can be adjusted independently for positioning and alignment. Rectangular 304 stainless-steel tubing will be used for the main structural material. Four modules will be supported with one span of structure and will weigh approximately 10 000 lb. Part of this structure will remain permanently attached to the four modules for installation and removal.

Even though the implosion-heating capacitor assemblies and crowbar-gap assemblies are supported from the outside diameter of the collector plates, secondary support members to each of these assemblies from the structural platforms above and below the machine will be required.

5.2.2.2 Thermal Analysis of Containment System

As can be seen in Fig. 5.1-2, the first wall of the SFTR is formed from a 0.1-m-radius, 4.0-mm-thick alumina (Al_2O_3) tube. During a D-T burn cycle a flux of bremsstrahlung, energetic D-T ions, alpha particles, fusion neutrons, and gamma rays will be incident on the first wall. Since the neutron and gamma energy densities within the first wall material are less than 1% that of the plasma, bremsstrahlung, and alpha particles, the heat-transfer analysis reduces simply to one described by a time-dependent wall flux. The penetrability of the bremsstrahlung radiation into the first wall is on the order of 0.1 mm for Al_2O_3, and is less than the thermal diffusion distance for time scales equal to the burn time (1.0 mm at 50 ms for Al_2O_3). The bremsstrahlung source term, therefore, is also treated analytically as a heat flux rather than a volumetric heat-source term.

In view of the small ratio of wall thickness Δb to inner radius b of the first wall, the heat-transfer analysis uses a one-dimensional slab approximation. During the early stages of the burn a semi-infinite slab approximation is adequate (for times less than 0.010 s, the diffusion distance is ~0.4 mm, compared to $\Delta b = 4$ mm). For this case the temperature rise $T(x,t)$ at a distance x from the inner radius b at time t is given for a constant wall flux F_0 by[1]

$$T_{(x,t)} = \frac{2F_o}{k}\left[\sqrt{\frac{\kappa t}{\pi}}\, e^{-x^2/4\kappa t} + \frac{x}{2}\,\mathrm{erfc}\left(x/\sqrt{4\kappa t}\right)\right] . \quad (29)$$

The increase in the surface temperature is given by

$$T_{(o,t)} = \frac{2F_o}{k}\sqrt{\frac{\kappa t}{\pi}} \quad (30)$$

where k is the thermal conductivity and κ is the thermal diffusivity. Table 5.2-1 summarizes relevant thermal/mechanical properties of dense Al_2O_3.

The average heat flux F_o is assumed to occur for a time τ and is estimated as follows. If Q is the ratio of fusion neutron energy (20 MeV/n) to plasma internal energy 3/2 nkT, and f_{BR} is the fraction of the plasma internal energy emitted as bremsstrahlung radiation during the effective burn time τ, then

$$F_o(W/m^2) \simeq 3n_o \cdot kT\left[1 + 0.175\ Q + f_{BR}\right]\frac{b}{2\tau} . \quad (31)$$

The terms in the bracket correspond, respectively, to the plasma internal energy, the alpha-particle energy (3.5 MeV/alpha particle), and the bremsstrahlung energy contributions to F_o. The density n_o corresponds to the initial filling density and is related to the average plasma density n by $n_o x^2$, where x is the average plasma-to-wall radius ratio. With temperature expressed in keV and p_o (mtorr) equal to the initial filling pressure, Eq. (31) becomes

$$F_o(W/m^2) = 1.70 \times 10^4\, P_o T\left(1 + 0.175\ Q + f_{BR}\right)\frac{b}{2\tau} \quad (32)$$

$$f_{BR} = 0.0708\, P_o \tau / x^2\sqrt{T} . \quad (33)$$

For the typical SFTR conditions indicated in Table 5.2-2, $f_{BR} = 0.05$, $F_o = 0.52$ MW/m^2, and $T(o,\tau) = 10.4$ K. Using the conditions given in Table 5.2-2, the melting point of Al_2O_3 will be exceeded at the surface if τ is less than 1 μs when the only source of energy is that of the (5-keV) plasma. Under "normal" conditions, therefore, the first-wall temperature rise is modest from the viewpoint of phase change and chemical reaction. The question of thermal stress is addressed in the following sections.

Although simplistic, the above-described analytical estimate is useful for an order-of-magnitude value of the first-wall temperature excursion; the major uncertainty in this estimate is the approximation of a constant first-wall heat flux. In order to assess the thermal behavior of the SFTR first wall for a given dynamic burn case, the finite-element code AYER[2] was programmed to follow the thermal excursion as driven by first-wall energy fluxes given by the DTBURN thermonuclear burn code.[3]

Figure 5.2-5 gives the bremsstrahlung, alpha-particle, and plasma (ion/electron) first-wall energy fluxes as a function of time for a "typical" SFTR burn: the bremsstrahlung was treated as a wall flux rather than a volumetric heat source, and the plasma flux at the first wall was assumed to follow the alpha-particle flux, a classical diffusion model being used to describe the latter.[4] Neutron and gamma heating were treated as a volumetric heat source, but contribute insignificantly to the induced temperature rise. These approximations will change

TABLE 5.2-1

PHYSICAL PROPERTIES FOR (DENSE) Al_2O_3 AT 300 K

c_p(J/kgK)	Specific heat	830
k(J/m s K)	Thermal conductivity	50.0
ρ(kg/m^3)	Density	3800
κ(m^2/s)	Thermal diffusivity	1.59×10^{-5}
α(K^{-1})	Coefficient of thermal expansion	9.36×10^{-6}
E(Pa)	Young's modulus	3.1×10^{11}
$\hat{\sigma}$(Pa)	Ultimate compressive strength	7.0×10^8
$\hat{\sigma}_T$(Pa)	Ultimate tensile strength	1.0×10^8
T_{MP}(K)	Melting point	2323
ν	Poisson's ratio	0.3

TABLE 5.2-2

SFTR BURN PARAMETERS USED FOR THERMAL/MECHANICAL ANALYSES

P_o(mtorr)	Initial filling pressure	5
b(m)	First-wall radius	0.1
Q	(20 MeV) neutron-to-plasma energy ratio	1.0
τ(s)	Average burn time	0.050
T(keV)	Mean plasma temperature	5.0
x	Mean plasma-to-first wall radius ratio	0.4

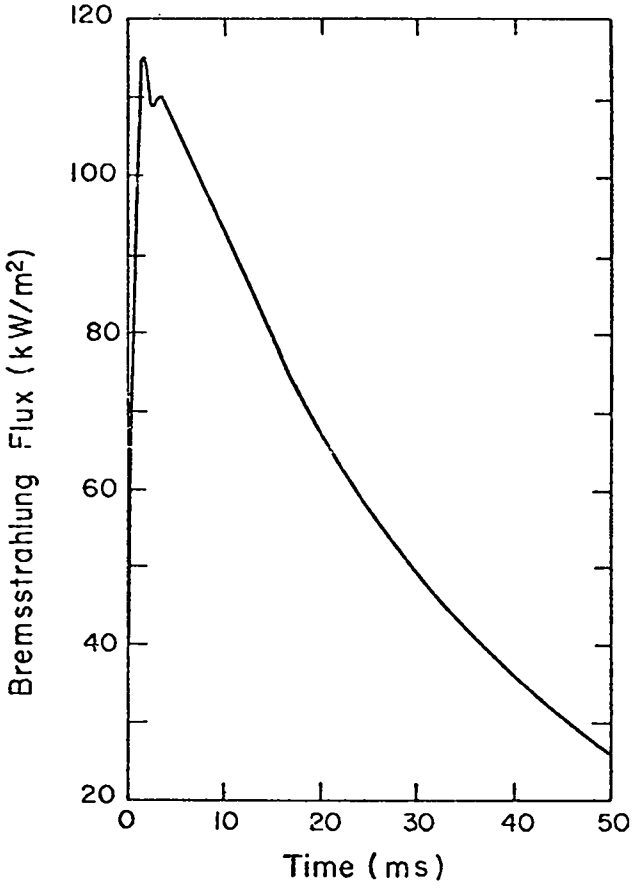

Fig. 5.2-5(a).
Bremsstrahlung energy flux at the first wall vs burn time.

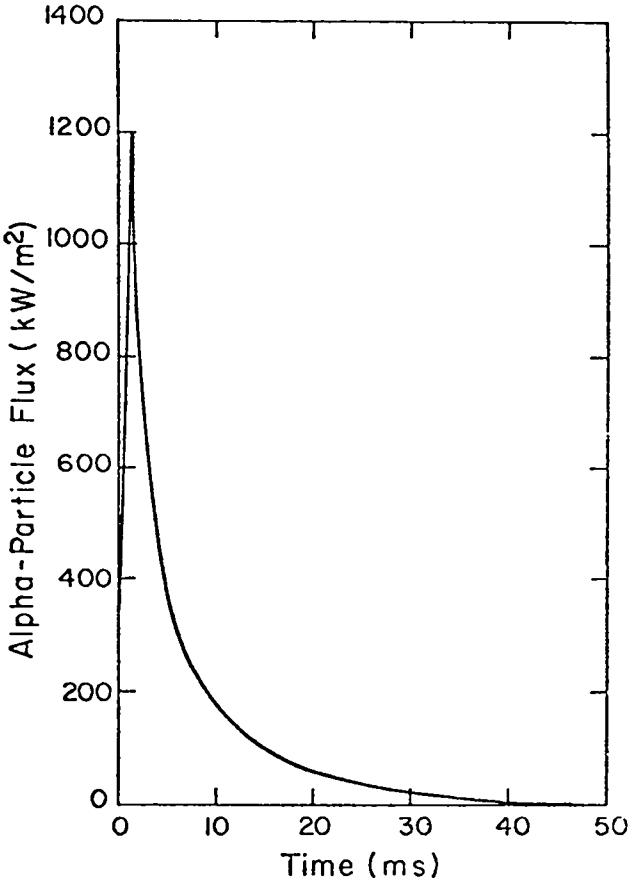

Fig. 5.2-5 (b).
Alpha-particle energy flux (3.5 MeV) at the first wall vs burn time.

by a factor of ~2 the time history and form of the computed first-wall temperature profiles, but should not significantly alter the overall temperature rise computed.

The time history of the first-wall surface temperature for these dynamic conditions is depicted in Fig. 5.2-6, whereas Fig. 5.2-7 gives the spatial dependence of the temperature vs time. The maximum temperature rise is 28 K and occurs at 5 ms into the burn cycle. The temperature rise computed by AYER is a factor of ~2 above that predicted by the analytical model, and is a result of the higher total energy deposition predicted for the plasma conditions used in the AYER computation. Hence, with the range of uncertainties in both the heat-transfer and the D-T burn models and

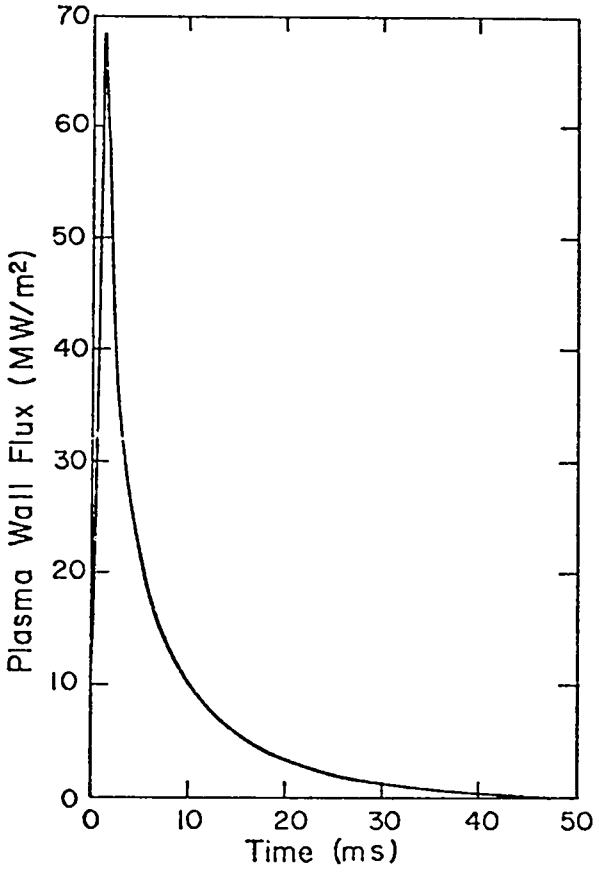

Fig. 5.2-5(c).
Plasma energy flux at the first wall vs burn time for a Q = 1 plasma.

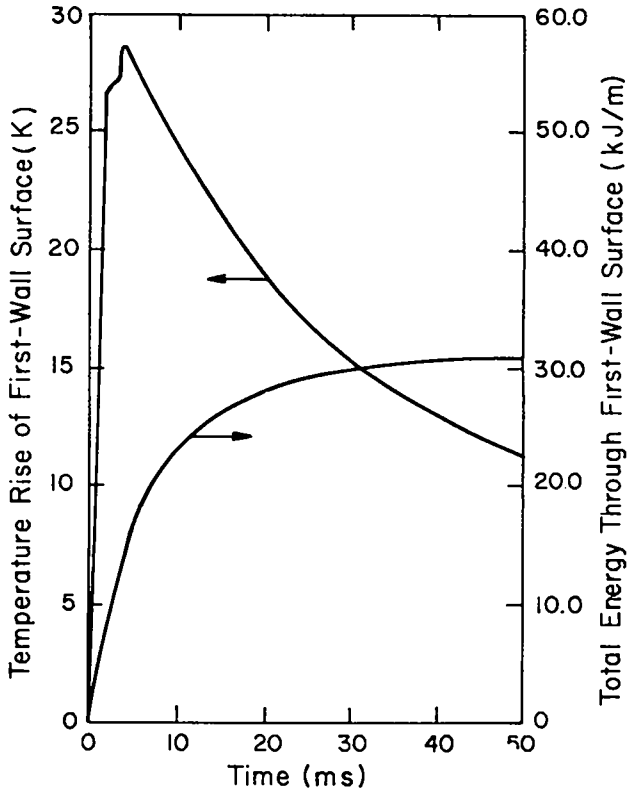

Fig. 5.2-6.
Time dependence of first-wall surface temperature and total energy deposited at the first-wall inner surface.

parameters, a first-wall temperature rise of ~10-30 K is anticipated for the SFTR. This temperature increase is caused primarily by the plasma dump and will occur, therefore, for D-D as well as D-T experiments. On the basis of both the simple analytic model and computer computation, the thermal stresses in the AlO_3 first wall will be estimated.

5.2.2.3 Stress Analyses of Containment System

The major mechanical stresses anticipated for the SFTR confinement system will be thermally driven stresses in the Al_2O_3 first wall and electromagnetically driven stresses occurring within the implosion coil and the adiabatic compression coil. Both analytical and computer estimates of these stresses are given below.

5.2.2.3.1 Thermal Stresses within the First Wall

An analytical estimate of the thermal stresses induced within the Al_2O_3 first wall can be obtained in

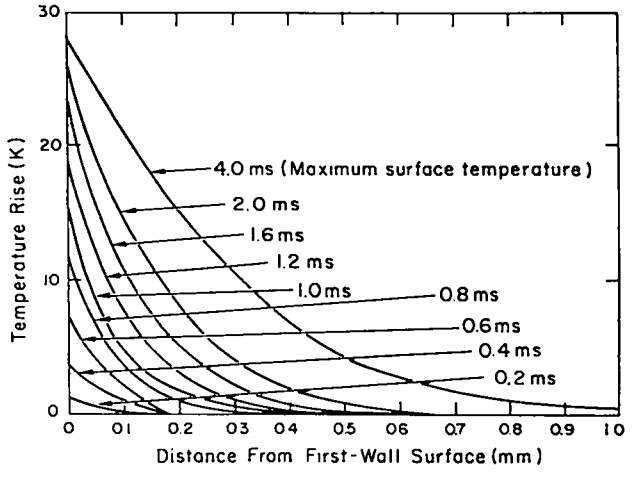

Fig. 5.2-7.
Time dependence of temperature profiles in the SFTR first wall for the conditions described in Table 5.2-1 and Fig. 5.2-5.

cylindrical geometry by solving the following equations under the plane strain approximation[5]

$$\frac{1}{r^3}\frac{d}{dr}\left(r^3\frac{d\sigma_{rr}}{dr}\right) = -\frac{2\alpha E}{1-\nu}\frac{1}{r}\left(\frac{dT}{dr}\right) \quad (34)$$

$$\frac{d\sigma_{rr}}{dr} + \frac{1}{r}\left(\sigma_{rr} - \sigma_{\theta\theta}\right) = 0. \quad (35)$$

The thermal expansivity is given by α, whereas Young's modulus and Poisson's ratio are given by E and ν, respectively (Table 5.2-1). The following approximation to the first-wall temperature distribution at any given time is used

$$T_{(r)} = T_o\, e^{-\lambda(r-b)} . \quad (36)$$

T_o is the temperature of the inner surface and $1/\lambda$ is a thermal attenuation distance, assumed here to be much shorter than the inner radius b. More realistic computer calculations verify this general behavior for small times (Fig. 5.2-7).

Using these approximations, the radial and azimuthal (hoop) stresses are given by

$$\sigma_{rr}/\sigma_o = \left[\frac{e^{-\lambda(r-b)}}{\lambda r} - \frac{1}{\lambda b}\right] + \left[\frac{e^{-\lambda(r-b)}}{(\lambda r)^2} - \frac{1}{(\lambda b)^2}\right] + \frac{C_1\lambda^2}{2}\left[\frac{1}{(\lambda r)^2} - \frac{1}{(\lambda b)^2}\right] \quad (37)$$

$$\sigma_{\theta\theta}/\sigma_o = -e^{-\lambda(r-b)}\left[1 + \frac{1}{\lambda r} + \frac{1}{(\lambda r)^2}\right] - \left[\frac{1}{(\lambda b)^2} + \frac{1}{(\lambda b)}\right] - \frac{C_1\lambda^2}{2}\left[\frac{1}{(\lambda r)^2} + \frac{1}{(\lambda b)^2}\right] \quad (38)$$

where the constants C_1 and σ_0 are given by

$$\frac{C_1\lambda^2}{2} = \frac{e^{-\lambda\Delta b}\left[\lambda b(1+\rho)+1\right] - (1+\lambda b)(1+\rho)^2}{\rho(2+\rho)} \quad (39)$$

$$\sigma_o = 2\alpha E T_o/(1-\nu) \quad (40)$$

and ρ has been defined as the ratio of wall thickness Δb to the inner radius b. The radial stresses σ_{rr} have been assumed to be zero at the inner and outer radii, b and b + Δb, respectively. For the case where $\rho \ll 1$ (thin shell) and $\lambda \gg$ b, Δb (true for most of the burn time), the hoop stress is given by

$$\sigma_{\theta\theta}(r) \simeq -\sigma_o e^{-\lambda(r-b)} \quad (41)$$

and is maximum in compression at the inner radius of the first wall. For the thermal conditions given by the analytic model in Sec. 5.2.2.2 and Tables 5.2-1 and 5.2-2, the maximum stress predicted by this approximate model amounts to 86 MPa (12.6 kpsi). The ultimate compression strength of Al_2O_3 is 700 MPa and is achieved *for the same thermal loading*, $F_o\tau$ (J/m^2), given in Sec. 5.2.2.2 when τ falls below 0.8 ms.

The simple analytical treatment given above is probably accurate to within a factor of 2. The major thermal problem appears to be related to mechanical stress rather than phase change or chemical reactions. The stress scales directly with temperature rise T_o, which in turn scales more or less directly with the burn time τ. These problems can be ameliorated for a Q = 1 plasma only by extending the time during which the plasma dump occurs. To within 10-20%, these conclusions are independent of whether or not thermonuclear burn occurs for the Q = 1 plasma described in Table 5.2-2.

To model more accurately the two-dimensional nature of the thermal-stress problem associated with the Al_2O_3 SFTR first wall, a finite element, thin-shell code, RASH,[6] was used[7] in conjunction with the temperature profiles depicted in Fig. 5.2-7. The structural properties given in Table 5.2-1 were used, and Figure 5.2-8 gives the geometric model used in the 2-D stress calculation. It should be noted that the neutral axis ξ varies in direction within regions (1) and (2).

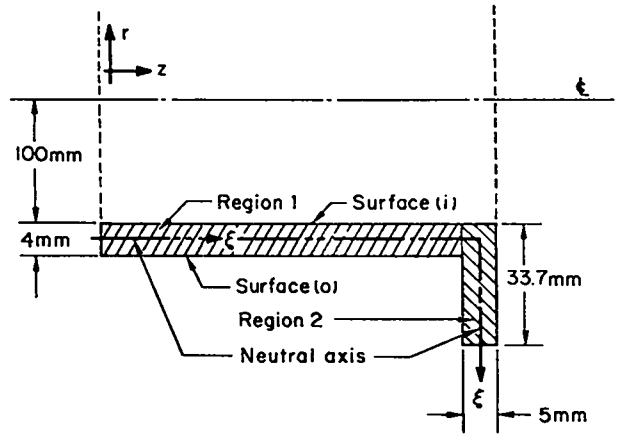

Fig. 5.2-8.
SFTR (Al_2O_3) first-wall model used for thermal stress analysis.

Figure 5.2-9 gives the time dependence of the maximum tensile and compression (hoop) $\sigma_{\theta\theta}$ stress, and Fig. 5.2-10 gives the spatial distribution of the (longitudinal) σ_{zz} and (hoop) $\sigma_{\theta\theta}$ stresses for the time

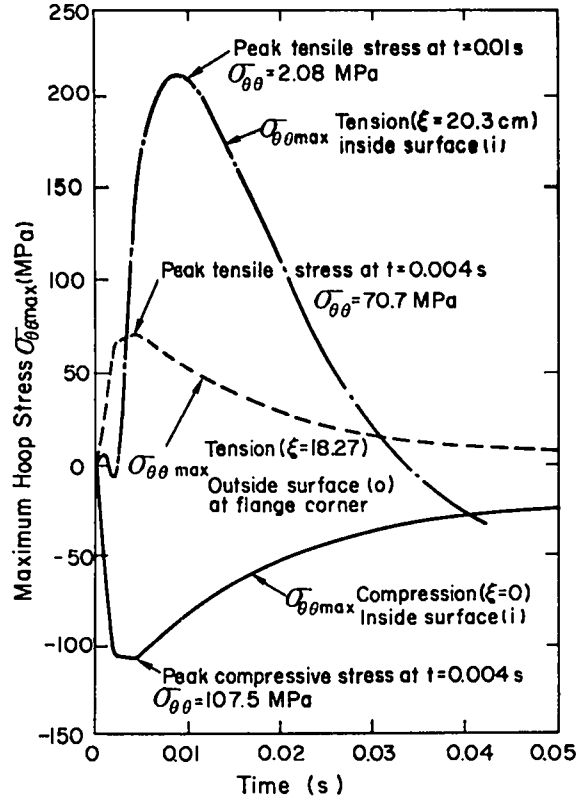

Fig. 5.2-9.
Maximum hoop stress quasi-steady thermal transient.

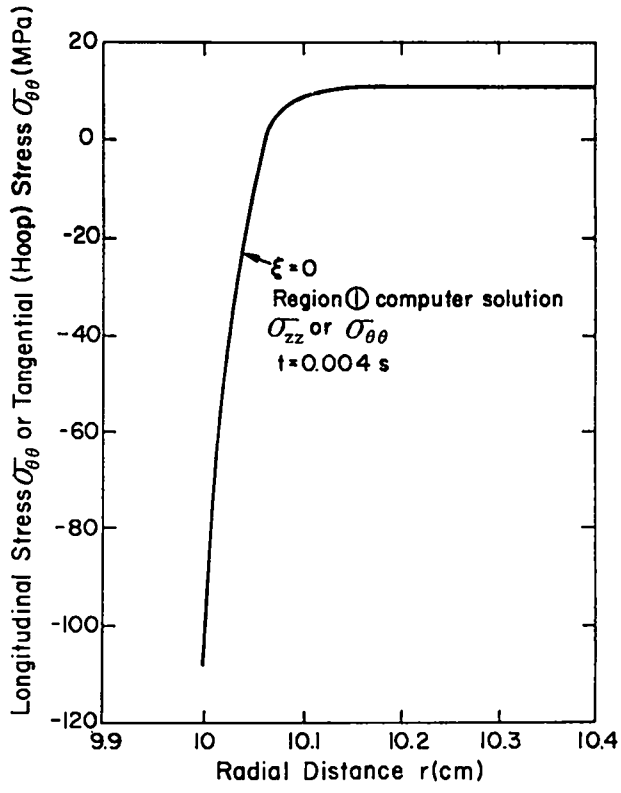

Fig. 5.2-10(a).
Computer solution radial distribution of longitudinal stress or hoop stresses at the transverse plane farthest from the end flange at time of maximum compressive stress.

(4-5 ms) when these stresses are maximum. The (radial) σ_{rr} stresses are not computed by RASH because this code is restricted by thin-shell theory. Because of the finite-difference nature of RASH, stress discontinuities exist at the common plane between regions (1) and (2); although stress gradients are steep in this region, the stress trajectories should be continuous in the actual situation. A large tensile hoop stress is predicted in the region of the flange on surface (o), and this stress amounts to 200 MPa. This stress exceeds the tensile strength (Table 5.2-1) and can be reduced by rounding both inside and outside corners of the joint between regions (1) and (2). The degree of rounding and the effectiveness of rounded edges on stress reduction in the vicinity of the joint can be determined only by more detailed, finite-element computations. The maximum compressive stress is 107 MPa and is within a factor of 7 of the ultimate compressive strength of Al_2O_3.

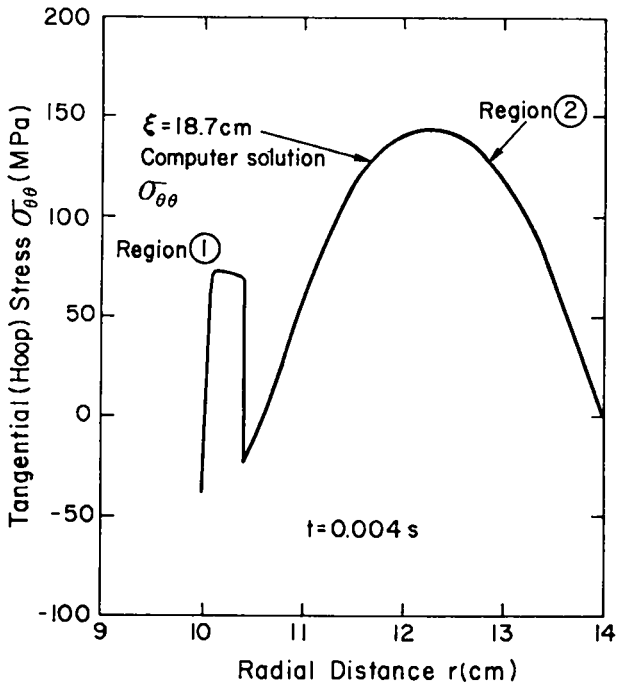

Fig. 5.2-10(b).
Computer solution radial distribution of hoop stress at the flanged end of the cylinder at time of maximum compressive stress.

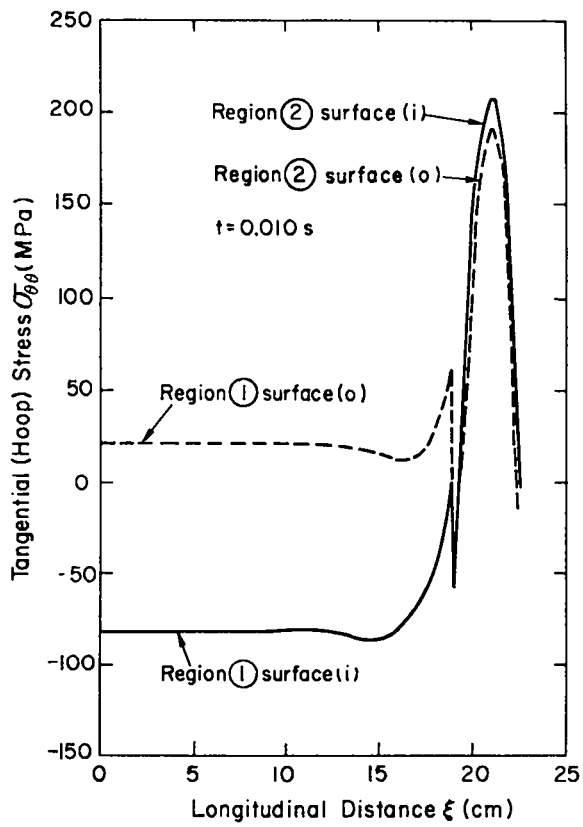

Fig. 5.2-10(c).
Computer solution longitudinal distribution of hoop stress at time of maximum stress.

The crucial problem with the Al_2O_3 first-wall structure, therefore, appears to be one of tensile failure driven by steep thermal gradients. The severity of this problem depends not only on the mode of SFTR operation and the details of the first-wall design, but also on the quality of the ceramic used to fabricate the first wall.[8] Given a high-quality, fine-grained ceramic, the primary concern is the presence of "stress-rising" flaws, which can have a stress-concentration factor of ~30. The following steps are suggested to reduce the failure via stress-rising flaws:[8]

- good surface finish (i.e., 325-grit diamond paste for final grinding),
- avoid surface damage to ceramic during fabrication and installation,
- avoid introduction of parasitic stresses during assembly,
- reduce moisture in the atmosphere around installed ceramic components to avoid chemical effects at intrinsic crack tips,
- institute a thorough system of nondestructive inspection (x-radiography) and proof testing (gas pressurization).

5.2.2.3.2 Mechanical Stresses in the Implosion and Compression Coils

Both the implosion-heating coil (IHC) and the adiabatic compression coil (ACC) will be subjected to electromagnetic force fields which are complex in both space and time. This complexity, coupled with the composite construction (insulators, metallic conductor, support structure) and the complicated geometry (short and stubby cylinder, ℓ = 1, 0 asymmetries, feedplate restraints, etc.) makes a purely analytic solution to the mechanical stress problem virtually impossible. The added complexity associated with the dynamic loading of both the coils and the support structure necessitates multidimensional, time-dependent computer calculations.

The approach used here evokes static, elastic, plane-strain theory for a preliminary estimate of mechanical loading. Separate, multidimensional computer calculations are used to model specific aspects of the problem that may appear crucial.

Representing either the IHC or the ACC as a thick-walled cylinder, and using the plane-strain theory approximately, the radial and azimuthal stress, σ_{rr} and $\sigma_{\theta\theta}$, respectively, are given below[5] for an internal pressure loading equal to $B^2/2\mu_o$.

$$\sigma_{rr} = -\frac{B^2}{2\mu_o}\frac{(1+\rho)^2}{\rho(2+\rho)}(b/r)^2 - 1/(1+\rho)^2 \quad (42)$$

$$\sigma_{\theta\theta} = \frac{B^2}{2\mu_o}\frac{(1+\rho)^2}{\rho(2+\rho)}(b/r)^2 + 1/(1+\rho)^2 \quad (43)$$

where $\rho = \Delta b/b$. The maximum stress occurs in tension for

$$\sigma_{\theta\theta} = \frac{B^2}{2\mu_o}\frac{(1+\rho)^2 + 1}{\rho(2+\rho)} . \quad (44)$$

For the IHC and ACC, respectively, b = 0.1, 0.18 m; Δb = 0.02, 0.08 m; B = 1.0, 6.0 T, and $B^2/2\mu_o$ = 0.80, 28.7 MPa. For these design conditions, $\sigma_{\theta\theta}$ (IHC) = 4.41 MPa (0.6 kpsi) and $\sigma_{\theta\theta}$ (ACC) = 82.2 MPa (12 kpsi). These preliminary estimates, therefore, indicate no severe mechanical problems with either the IHC or ACC. The unique geometry, dynamic loading, and close design tolerances associated with the IHC, however, warrant a more detailed examination of this crucial component, particularly since the ceramic support structure for the IHC will undoubtedly be placed in tension and may be required to support the mechanical load. The results of a two-dimensional, finite-element stress calculation of the IHC are summarized below.

The computer code TSAAS[9] was used[10] to estimate the static stresses in the implosion coil shown in Fig. 5.2-4. The finite-element mesh, material boundaries, and static loadings are shown in Fig. 5.2-11; the overall dimensions of this mesh are roughly scaled from Fig. 5.2-4, and most dimensions and blend radii should be considered approximate. The material properties given in Table 5.2-1 were used, and 100 000 MPa was used for the Young's modulus of copper.

To simulate the (static) electromagnetic loading, the pressure conditions were applied at the copper/insulator (Al_2O_3) interface over the straight boundary regions plus one element into the various radii. The pressures were computed as a function of average radius r(mm) at the Cu/Al_2O_3 interface by the following expressions

$$P_A = P_o\,(3/4 - 4100/r^2)$$
$$P_B = P_o\,(1/4 + 4100/r^2)$$
$$P_C = P_o\,(4100/r^2) \quad (45)$$

The coefficient P_o was taken to be $B_s^2/2\mu_o \sim 0.8$ MPa, and the pressures P_A, P_B, P_C are shown in Fig. 5.2-11. The results presented here are for a "clamped" or zero displacement boundary at the outer edge of the feedplate region (Fig. 5.2-11). A calculation which restrained only axial motion at the outer boundaries resulted in substantially the same deformations and stresses.

Figure 5.2-12 gives the radial and axial displacement contours, and the circumferential (hoop) $\sigma_{\theta\theta}$ stress contours are given in Fig. 5.2-13. The maxima of the principal (σ_{rr}, $\sigma_{\theta\theta}$, $\sigma_{r\theta}$) stresses are shown in contour on Fig. 5.2-14. The maximum tensile stresses occur at the tip of the IHC (farthest point axially from feedplate) and are hoop stresses of 6.8 MPa in the insulating coil form and 7.2 MPa in the insulation which surrounds the copper conductor. The stresses fall to very low levels around and within the feedplate region. Although placing a brittle ceramic in tension should be avoided, the low levels of the tensile loading relative to the ultimate tensile

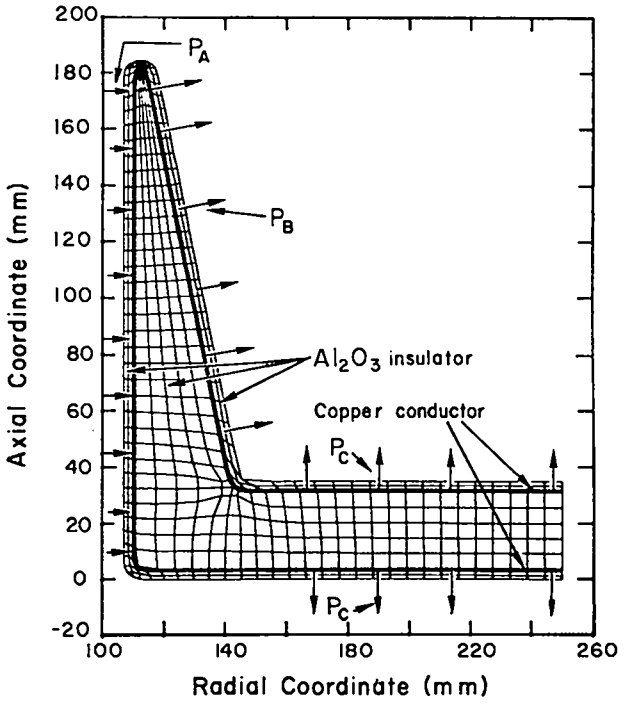

Fig. 5.2-11.
Finite-element mesh, material boundaries, and static loadings used to model static stresses in the IHC.

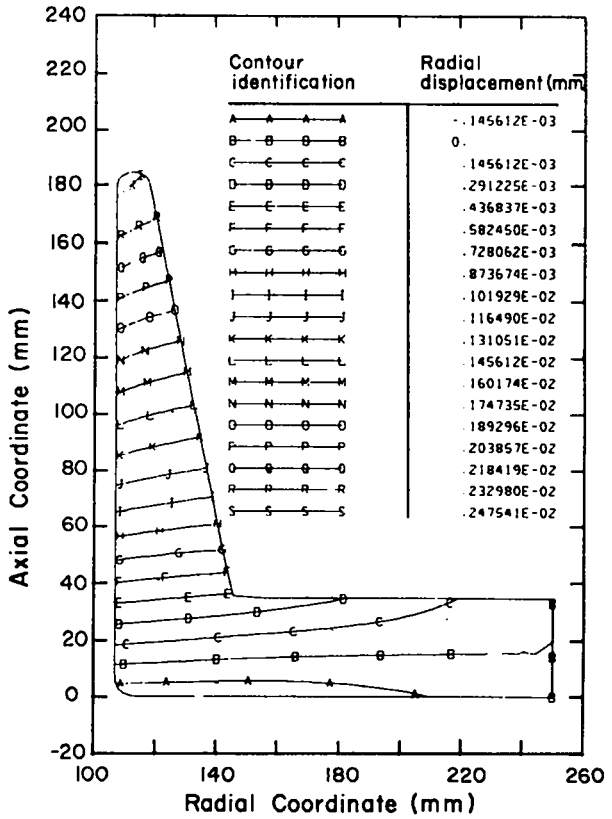

Fig. 5.2-12(a).
Radial displacement contours for the static loadings given by Eq. (45).

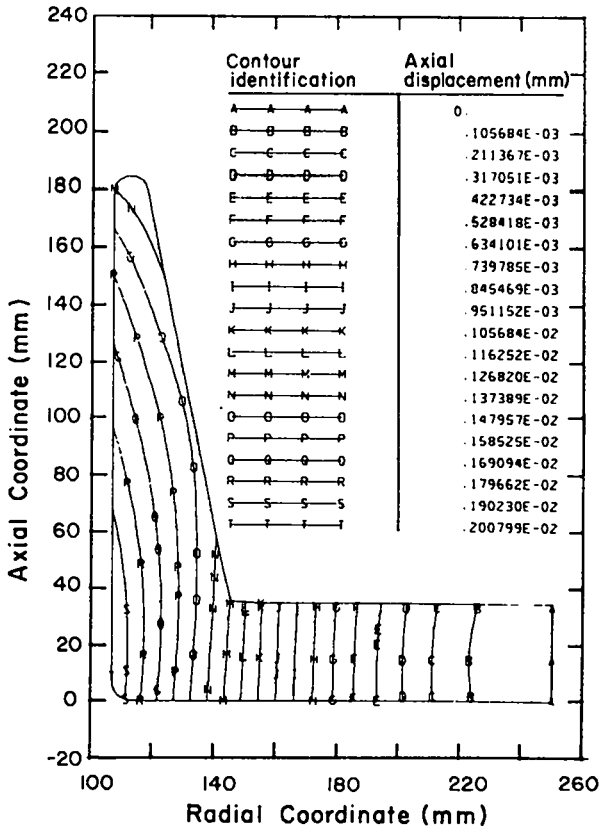

Fig. 5.2-12(b).
Axial displacement contours for the static loadings given by Eq. (45).

stress (~100 MPa) should present no serious problems; even with "stress-riser" amplification by local defects of ~30, the ultimate tensile stress should not be exceeded.

The finite-element mesh depicted in Fig. 5.2-11 and the material properties given in Table 5.2-1 were used in conjunction with an approximation to the field waveform shown in Fig. 4-16 for a dynamic analysis of the implosion-heating coil. The computer program NONSAP[11] was used and the magnetic field waveform was approximated by: (i) a linear rise from zero to the maximum value in 0.2 μs. (ii) a maximum field for 0.1 μs, and (iii) a linear decrease to half the maximum in 0.05 μs followed by a constant (one-half maximum) field. A static analysis with NONSAP verified to within 3% the previous calculations made with TSAAS.

The eigenvalue option in NONSAP was used to obtain the first five modal shapes and resonant frequencies for the IHC system. Table 5.2-3 summarizes the resonant frequencies, and indicates that a structurally significant response would probably take many tens of microseconds. The calculational time steps were checked by a series of short (0.1-μs) time steps to test for a tendency of acoustic waves to interact and to build up large stresses; longer time steps (1-2 μs) were used to examine the long-term structural response.

The largest tensile stresses were computed at the small tip of the IHC and are summarized in Table 5.2-4. The response for the (tip) element of maximum hoop stress is nearly sinusoidal with a period of ~90 μs and a peak stress of ~7.8 MPa (i.e., slightly twice the static stress with the same magnitude of pressure). Most of the deformation occurs in one mode, so the system response is nearly sinusoidal. The peak stresses from the dynamic calculation, therefore, are essentially the same as for the static calculation, and the conclusions are the same.

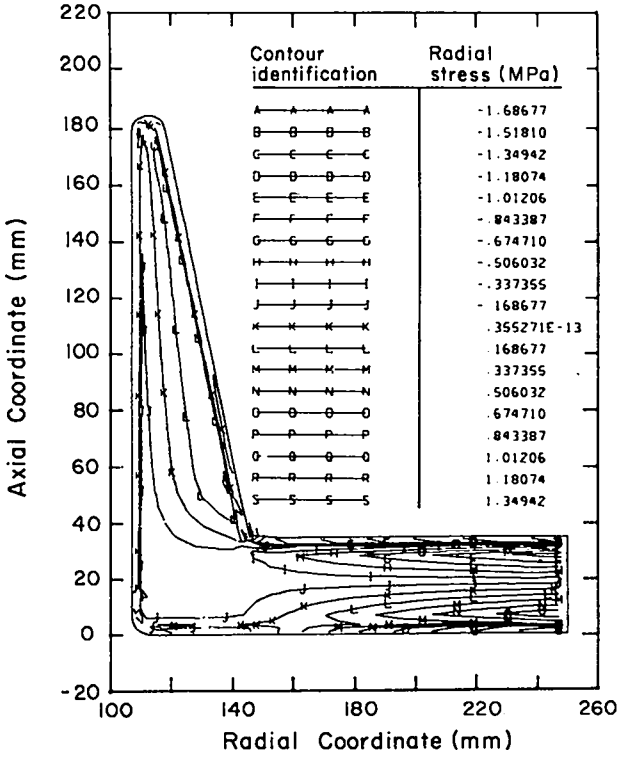

Fig. 5.2-13(a).
Radial stress contours for the static loading given by Eq. (45).

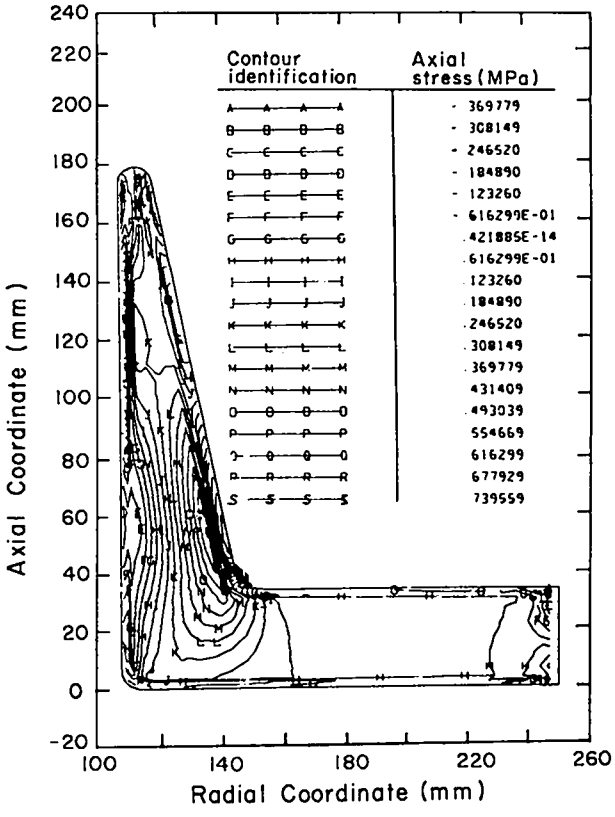

Fig. 5.2-13(b).
Axial stress contours for the static loading given by Eq. (45).

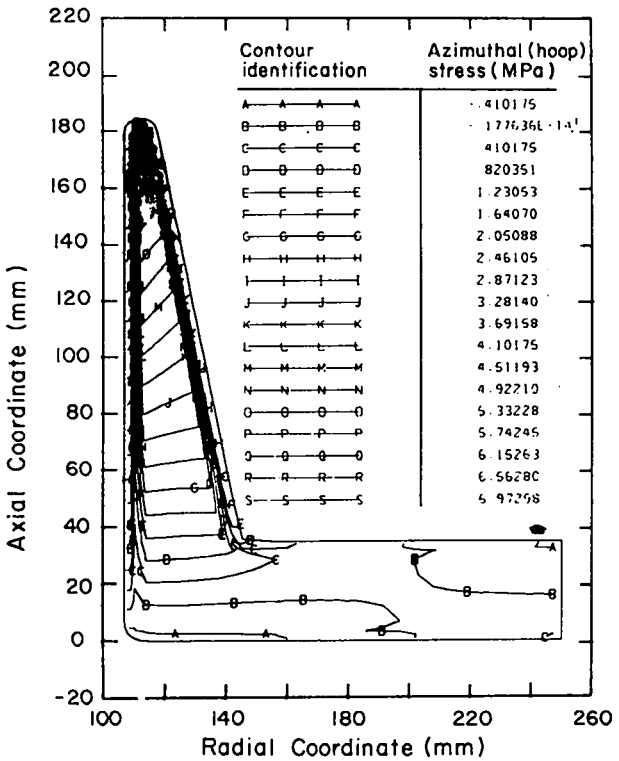

Fig. 5.2-13(c).
Azimuthal (hoop) stress contours for the static loading given by Eq. (45).

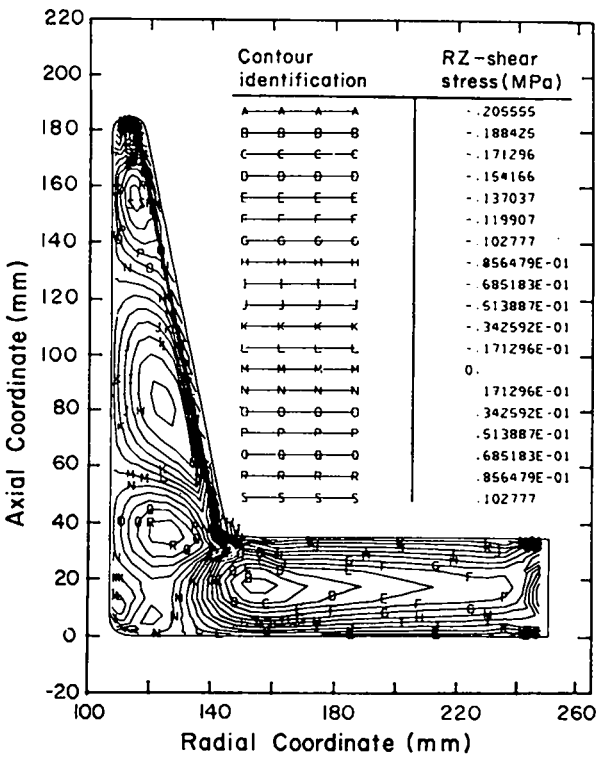

Fig. 5.2-13(d).
Radial/axial shear stress contours for the static loading given by Eq. (45).

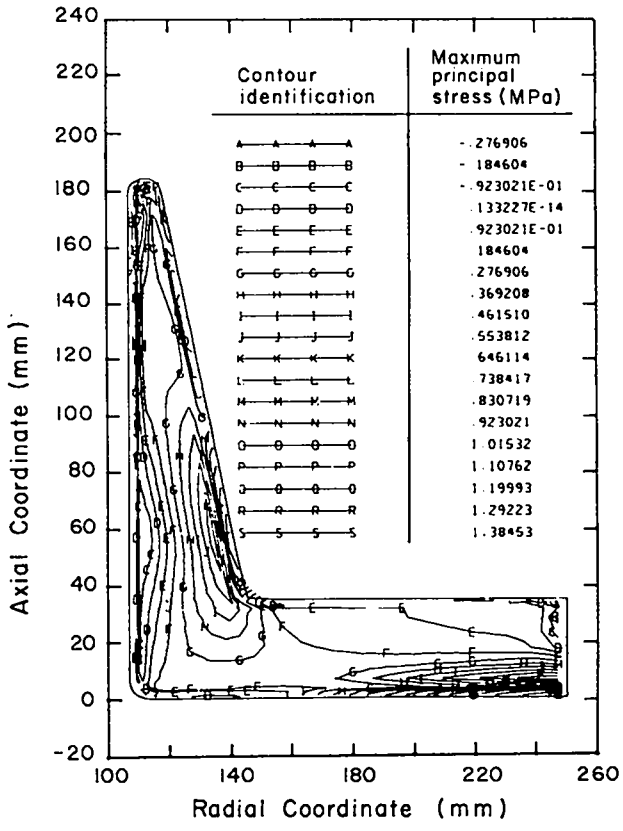

Fig. 5.2-14.
Maximum principal stress contours for the loading given by Eq. (45).

TABLE 5.2-3

MODAL FREQUENCIES OF IHC

Mode Number	Frequency (kHz)	Period (μs)
1	7.78	359
2	10.98	91
3	12.24	82
4	14.94	67
5	17.31	58

TABLE 5.2-4

PEAK TENSILE STRESSES OVER FIRST 600 μs

Material Region	Maximum Hoop Stress (MPa)	(μs)	Maximum Stress in r-z Plane (MPa)	(μs)
Ceramic Core	7.90	320	2.33	180
Copper	2.65	320	1.02	550
Outer Ceramic	8.43	320	3.67	180

5.2.3 Fabrication of Containment Vessel

5.2.3.1 Implosion-Heating Coil/Vacuum Vessel

The fabrication of the first wall and implosion (shock heating) coil for the SFTR requires a number of operations which are beyond the current state of the art. It is felt that with a concerted effort these operations can be accomplished, given sufficient lead time and resources for R&D.

Two concepts of the SFTR first wall-implosion coil assembly have been examined: (1) a unit structure with all components bonded together, and (2) a separate first-wall liner coupled with an implosion coil assembly. Because of the inherent problem of the mismatch of the thermal expansion coefficients of most ceramics and copper, the first concept presents very difficult fabrication problems. A coil based on the second concept appears to have the best chance of being successfully fabricated.

The implosion coil assembly is shaped like a wide-brimmed "top hat," as shown in Figs. 5.1-2 and 5.2-3. The current enters at the outer edge of one side of the brim and is routed over the exterior of the hat, down parallel conductors in a slow spiral pattern on the inside of the hat back to the brim, and exits on the outer edge of the brim opposite the entering point. The hat is a ceramic insulator and support structure of ~2.5-cm thickness for the ~1.5-mm-thick copper conductors, and it is coated with a ceramic insulator. The following materials have been considered for the hat: alumina bodies, electrical procelains, mica, glass-bonded mica, and glass-ceramics. At present, the most suitable material appears to be an impervious alumina body. It would have good mechanical strength and no open porosity. Much is known about its fabricability, techniques exist for depositing copper conductor patterns on its surface, and its dielectric strength is comparable to other ceramic bodies[12]; however, a fundamental problem is the assignment of a realistic and safe dielectric strength (which determines the insulation thickness) in the 200- to 300-kV region. No data exist for alumina in this voltage region for pulse-type operation and the type of geometry found in the SFTR implosion coil.

Fabrication of the insulator will be difficult. Initial forming would probably be done by slip casting followed by a considerable amount of slow diamond-grinding. This type of fabrication is technically feasible but expensive; however, if ~85% dense, high purity Al_2O_3 body can be used instead of fully dense, high purity Al_2O_3, the cost of the insulator could be reduced by a factor of ~5.

Although several techniques exist for depositing thin copper conductor patterns on alumina,[13,14] some fabrication problems remain because of the thermal expansion mismatch between alumina and copper. Current electroplating techniques tend to produce only a mechanical bond between the alumina and thin copper, and a development program is needed to perfect an electrochemical method of forming thick layers of stress-free, tightly adherent copper on alumina substrates which can withstand a moderately high (~400°C) temperature.

Once the insulator hat is formed and the copper conductor with the required pattern is deposited on the hat, the hat must be coated with electrical insulation to prevent arcing to nearby components or between adjacent current feeds. This insulating layer would be a ceramic coating. Firing techniques must be developed which will not cause the insulator to crack and yet will not exceed the ~400°C temperature limit imposed by the thermal expansion of the electroplated copper coil. An alternate method may be a flame- or arc-plasma-sprayed oxide-glass coating if sufficient coating tightness and dielectric strength can be achieved.

The first wall for the SFTR must be vacuum-tight, impermeable to tritium, fabricable, and able to withstand the plasma environment without causing erosion or contamination of the plasma. Such a material may not exist, but investigations have begun on several promising materials.

The material for a separate first-wall liner must be capable of being joined to other parts by ceramic-metal and ceramic-ceramic sealing techniques, have reasonable resistance to thermal shock, and have good mechanical strength. Both alumina and silica glass are candidates for the first-wall liner, with alumina being the first choice. Fabrication of the first-wall liner would be similar to that of the implosion coil insulator hat. Conventional ceramic-to-metal sealing techniques appear suitable; however, ceramic-to-ceramic joining techniques (low melting glass with infrared heating, a normal glazed joint utilizing a laser "brazing" operation, or a fusion joint using a laser "welding" operation) are untested and are now considered to be beyond the present state of the art. However, recent developments in laser welding technology indicate that the techniques for making such joints will be developed within the required time.

5.2.3.2 Magnetic Flux Concentrator

No commercially available material will satisfy the four requirements of the magnetic material (Sec. 5.2.2.1). However, the development of a suitable material does not appear difficult.

Oriented silicon steel seems to be the best material. It meets the requirement of $\mu/\mu_0 \gtrsim 30$, and the saturation field in a powdered or flake core is 14-15 kG. Tape-wound cores are ruled out because it is

too difficult to roll the material to a thickness less than a skin depth. The only problem with present powdered or flake oriented silicon steel cores is that the dielectric strength is marginal. Modifications are being made that may correct the problem.

The material will be manufactured into trapezoidal cross-section "logs" that will be stacked around the implosion coil to form the cylinder shown in Fig. 5.1-2.

5.2.3.3 Mechanical Design and Fabrication of the Compression Coil

Each compression coil is of split pancake design, that is, it is made of two pancake coils wound with opposite helicity and connected together electrically at the inside turns. In this way all other electrical connections can be conveniently brought to the outer radius. Insulation is made of vacuum impregnated fiber glass, and a dielectric strength of 100 V/mil is assumed. Coils can be fabricated by rolling up copper strap with a spacer of fiber glass cloth and then vacuum impregnating the composite. The paired pancake coils can be welded together at the center turn before impregnation, or the entire split pancake could be made of a continuous piece of copper with a bend between paired pancakes. The $\ell = 1$ and $\ell = 0$ modulations of the coils can be of different radii. The maximum hoop stress in the coil is well below the endurance limit of the copper strip since enough copper was used in the winding to keep the L/R time of the coil large. Dynamic hoop stress is also negligible for the same reason.

REFERENCES (Chap. V, Sec. 5.2)

1. H. S. Carslaw, J. C. Jaeger, **Conduction of Heat in Solids** (Oxford at the Clarendon Press, 2nd ed. NY, 1959).

2. R. G. Lawton, "The AYER Heat Conduction Computer Program," Los Alamos Scientific Laboratory report LA-5613-MS (1973).

3. T. A. Oliphant, personal communication (1975).

4. K. I. Thomassen and T. A. Oliphant, "First-Wall Fluxes in a Theta Pinch Feasibility/DT Experiment," J. Nucl. Mater. **53**, 48 (1974).

5. C. F. Bonilla, Ed., **Nuclear Engineering**, (McGraw-Hill Publ. Co., NY, 1975), p. 538.

6. RASH, a LASL thin-shell stress code.

7. R. J. Bartholomew, personal communication (1975).

8. F. W. Clinard, personal communication (1975).

9. R. V. Browning, D. G. Miller, and C. A. Anderson, "TSAAS: Finite Element Thermal and Stress Analysis of Axisymmetric Solids with Orthotropic Temperature-Dependent Material Properties," Los Alamos Scientific Laboratory report LA-5599-MS (May 1974).

10. R. V. Browning, personal communication (1975).

11. K. J. Bathe, E. L. Wilson, and R. H. Iding, "NONSAP—A Structural Analysis Program for Static and Dynamic Response of Nonlinear Systems," SESM Report 74-3, Dept. of Civil Engineering, University of California, Berkeley (February 1974).

12. W. S. Kingery, **Introduction to Ceramics** (John Wiley and Sons, NY, 1960), p. 726.

13. R. E. Cowan, U.S. Patent No. 3180 756.

14. G. L. Babcock et al., U.S. Patent No. 3766 634.

5.3 IMPLOSION-HEATING SYSTEM

5.3.1 General Description

The implosion-heating system provides the fast-rising magnetic field which initially heats the plasma. The basic circuit for the system is shown in Figs. 4-16 and 5.3-1. The inductance of the capacitors and start gap is L_c, L_f is the inductance of the feedplate, and L_ℓ is the inductance of the load coil. The storage capacitance is C, and S_g and S_c are, respectively, the start gap and crowbar switches. The basic operation is: (1) charge the capacitor with S_c and S_g open, (2) close S_g so that the capacitor discharges through the load coil, (3) at peak current close S_c which maintains the current in the load coil until the compression field can be raised. The implosion field must rise to 1.1 T in approximately 100 ns and be sustained for approximately 200 μs.

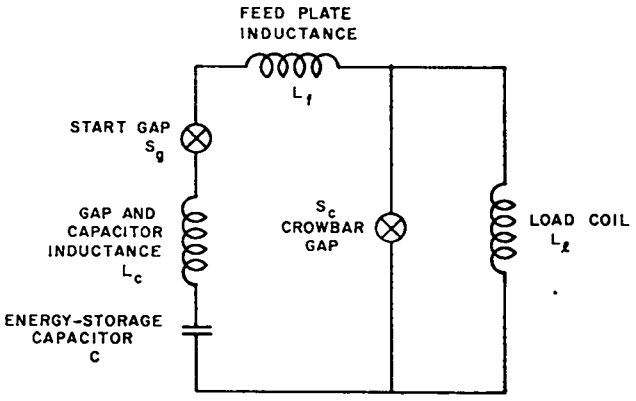

Fig. 5.3-1.
Basic circuit of the implosion-heating system.

5.3.2 Capacitor and Feedplate Design

To utilize the energy stored in the capacitor most efficiently, the source inductances L_c and L_f must be as small as possible consistent with dielectric breakdown strengths and physical dimensions. This implies that the feedplates should be as short as possible and the capacitors and start gaps should be designed for low inductance. Several capacitors and start gaps will be placed in parallel to achieve a low effective inductance of the capacitor and gap.

The approach used in the design is to configurate the feedplates as circular discs which extend from the load coil (Marshall coil) to just outside the primary radiation shield with six capacitors feeding around the periphery of the feedplates as was shown earlier in the layout of Fig. 5.1-4. Three crowbar gaps are placed between every two capacitors, with a spare being provided for the compression coil leads and the vacuum downcomers. A cross section of the feedplate and capacitor is shown in Fig. 5.2-1. The offset feedplates displace the capacitors from the neutron streaming path along the feedplates and allow space to place shielding in this streaming path.

An important feature of the design is that it allows ready access to the capacitors and gap for maintenance purposes. The radial feedplate shown in Fig. 5.2-1 is common to two adjacent Marshall coils with the outer feedplates at a common voltage of 270 kV. The center feedplate is connected to the machine ground grid. The 270 kV is achieved by connecting two 0.04-μF, 135-kV capacitors in series through a single 270-kV spark gap. The energy stored in each capacitor is 365 J. The feedplate assembly feeds two load coils which are assembled into a unit referred to as a module. The length of a module is 40 cm, and there are eight modules in a wavelength λ.

The estimated inductance of the capacitor and gap for this design is approximately 27 nH and the calculated inductance of the feedplate corresponding to one capacitor unit is 23 nH. Thus, the total source inductance for one capacitor assembly is 50 nH and with six capacitors in parallel the equivalent source inductance to the load coil is 8.3 nH. The overall electric circuit for a module is shown in Fig. 5.3-2. Each 40-cm module is made up of two load coils, six gaps, twenty-four 0.04-μF capacitors at 135 kV, and 270-kV start gaps. The preionization and pulse-charging systems also shown on the schematic are discussed in the following sections.

5.3.3 Preionization System

The preionization system consists of a capacitor and start gap connected across the load coil through a relatively large inductance. One capacitor per module will be required. The capacitor to be used will be a standard 1.85-μF, 60-kV capacitor with a standard Scyllac-type start gap.

The capacitor will be discharged through the load coil approximately 10 μs before the implosion-heating capacitors are discharged.

5.3.4 Pulse-Charge System

The pulse-charge system is used to charge the 135-kV implosion-heating capacitors. It is a relatively high-inductance system with the charge being accomplished in approximately 5 μs. The implosion-heating capacitors are pulse-charged to avoid corona problems in the implosion-heating system and to avoid the necessity of designing a start gap having the capability of withstanding 270 kV for a long period.

The basic system consists of a two-stage Marx generator which has the capability of charging half the capacitors in eight modules (one wavelength of

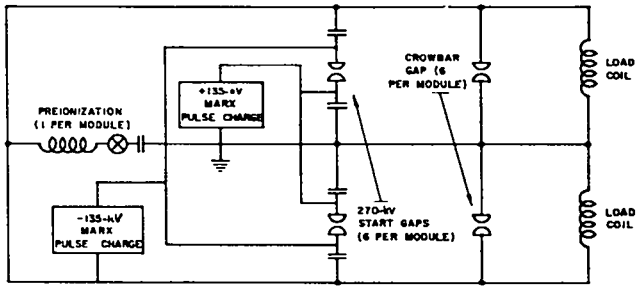

Fig. 5.3-2.
Electrical circuit of implosion-heating system module.

the plasma chamber). There are 192 capacitors in 8 modules: 96 must be charged positively and 96 negatively. Two Marx generators are required per eight modules; one for positive charging and one for negative charging.

Each Marx generator consists of two 7.7-kV, 7.7-μF capacitors connected as shown in the circuit of Fig. 5.3-3.

5.3.5 Trigger System

Independent trigger systems are required for the start gaps, the crowbar gaps, and the preionization system to allow adequate flexibility during operation. The trigger-system design follows the standard approach. An 8-kV pulser is triggered from central control; the pulser triggers a master gap which in turn triggers several submaster gaps, and so on until the actual start gaps are triggered. The synchronization of the trigger signals is controlled by maintaining proper cable lengths through the various levels of the system. The implosion-heating trigger system has been segmented into four identical systems, each of which triggers all gaps in one-fourth of the machine. For example, to trigger the start gaps, a trigger pulse is sent from the control system which triggers the 8-kV pulser at each quadrature of the machine and this in turn starts the chain of trigger pulses resulting in the triggering of the start gaps in that quadrature.

The schematic of a typical trigger-system chain is shown in Fig. 5.3-4. An important subsystem of the trigger system is the trigger-system Marx generator

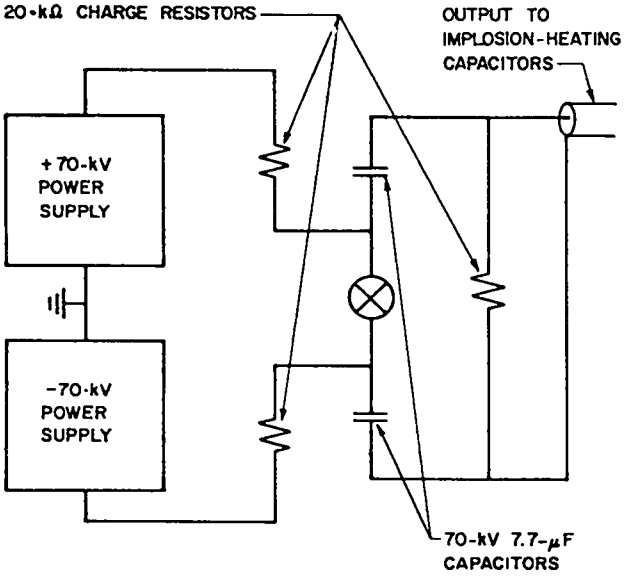

Fig. 5.3-3.
Circuit of pulse-charge Marx generator.

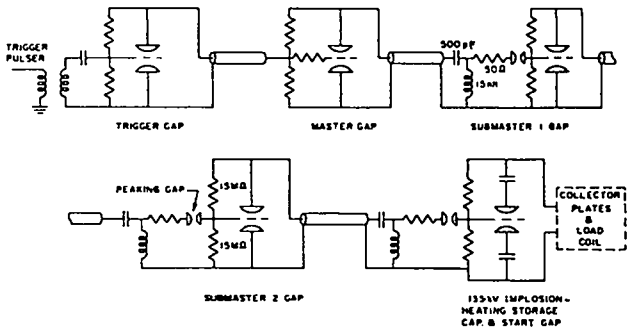

Fig. 5.3-4.
Typical trigger system schematic.

which must also be triggered from central control just before the start gaps are triggered.

5.3.5.1 Start-Gap Trigger System

The start-gap trigger system consists of four identical subsystems, each of which triggers the start gaps in a quadrature of the machine. The total number of start gaps triggered by a subsystem is 1920. Each subsystem has been designed with a master gap and two levels of submasters. The master gap triggers a submaster-one gap; each submaster-one gap triggers 16 submaster-two gaps; and each submaster-two gap triggers 12 start gaps.

Four trigger-system Marx generators are required for each of the four subsystems of the trigger system. A trigger-system Marx generator consists of four 75-kV, 7.7-μF capacitors connected as shown in the circuit of Fig. 5.3-5. Each Marx generator charges the trigger-system circuits for 40 modules, or for 480 start gaps.

The pulse-charge trigger system consists of two master gaps, each of which triggers 20 pulse-charge

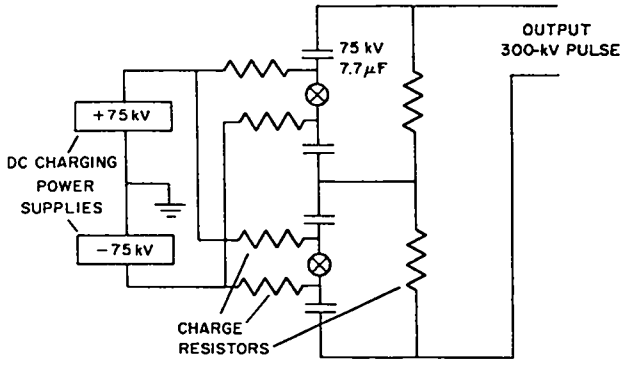

Fig. 5.3-5.
Circuit of start gap trigger system, Marx generator.

Marx generators. Each pulse-charge generator charges half the implosion-heating capacitors in a module.

A diagram of the major components in the start-gap trigger system is given in Fig. 5.3-6.

5.3.5.2 Crowbar Trigger System

The crowbar trigger system is almost identical to the start-gap trigger system. The only difference is that there are half as many crowbar gaps as start gaps. Like the start-gap trigger system, the crowbar trigger system consists of four identical subsystems, each of which triggers all the crowbar gaps in a quadrature of the machine. There are 962 crowbar gaps in a quadrature. Each subsystem consists of a master gap and two levels of submasters. The master gap triggers 5 submaster-one gaps; each submaster-one gap triggers 16 submaster-two gaps; and each submaster-two gap triggers 12 crowbar gaps.

Two trigger-system Marx generators are required for each of the four subsystems. The trigger-system Marx generators are identical to the generators discussed in Sec. 5.3.5.1 and shown in the schematic of Fig. 5.3-5.

A diagram of the major components in the crowbar trigger system is given in Fig. 5.3-7.

5.3.5.3 Pulse-Charge Trigger System

As discussed in Sec. 5.3.4, two pulse-charge Marx generators are required for each eight modules or one wavelength of the discharge chamber. There are, therefore, 40 Marx generators in a quarter of the machine, 20 positive and 20 negative. The trigger system consists of two master gaps, one triggering 20 positive Marx generators and one triggering 20 negative Marx generators. A diagram of the system is shown in Fig. 5.3-8.

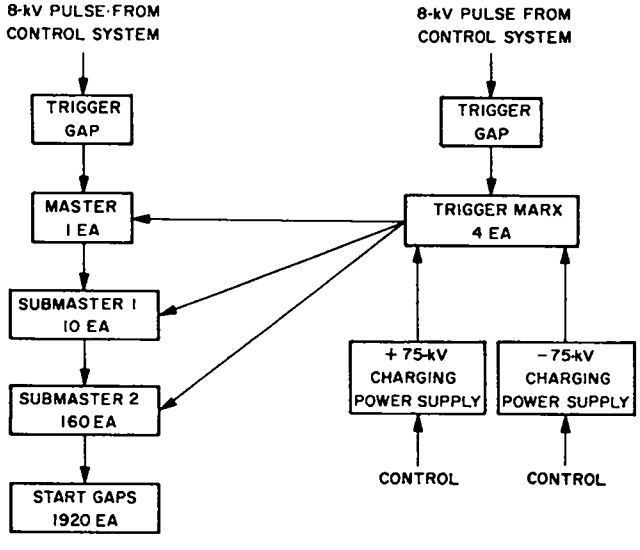

Fig. 5.3-6.
Diagram of start-gap trigger system.

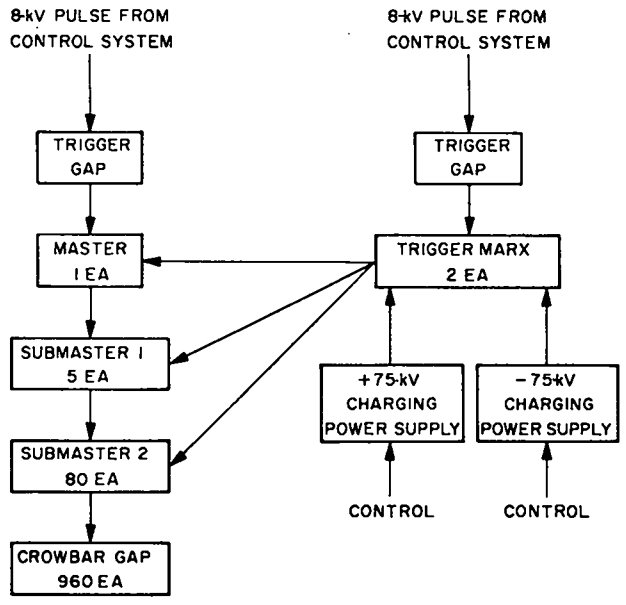

Fig. 5.3-7.
Diagram of crowbar trigger system.

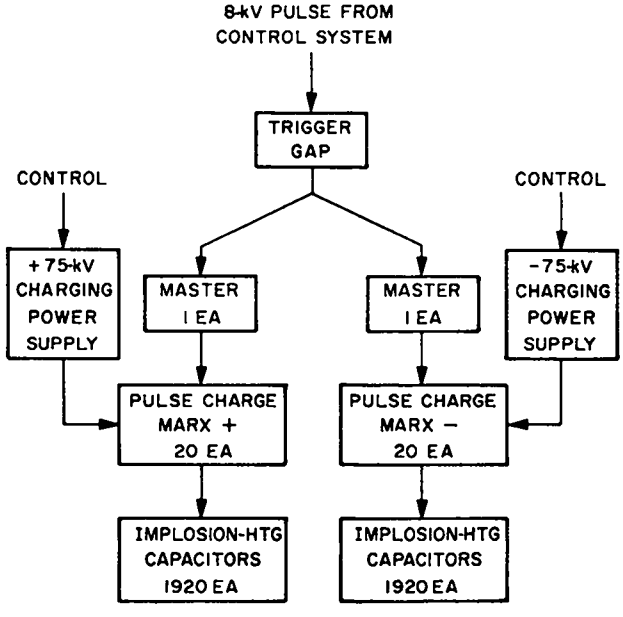

Fig. 5.3-8.
Diagram of pulse-charge trigger system.

5.3.5.4 Preionization Trigger System

The preionization system consists of one capacitor and start gap per module. Thus, there are 160 capacitors and gaps in one quadrature. The trigger system consists of a master gap which triggers 20 submasters; each submaster triggers 8 gaps. A diagram of the system is shown in Fig. 5.3-9.

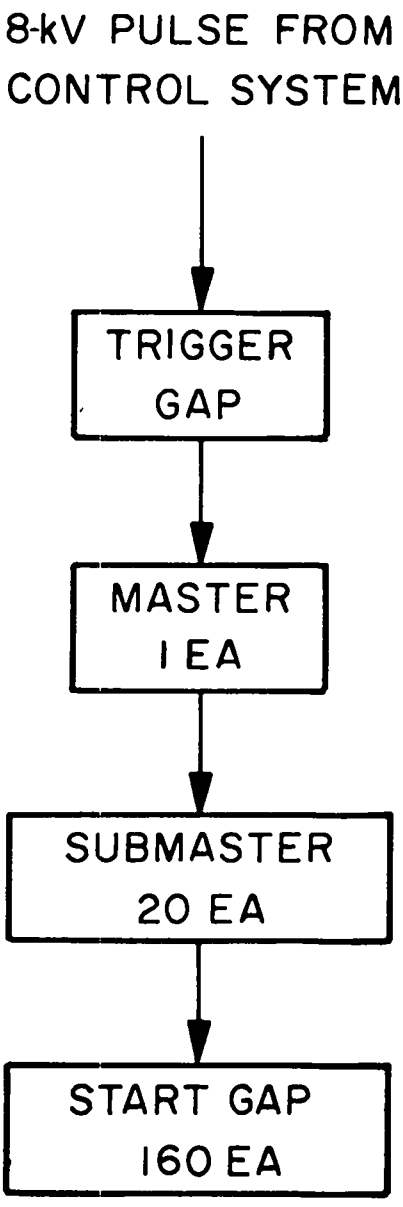

Fig. 5.3-9.
Diagram of preionization trigger system.

5.3.6 Timing and Control

The triggering of the various systems and subsystems in the implosion-heating system must be accomplished within microseconds and nanoseconds. The speed and precision of the various trigger pulses are such that a computer-type control is impractical. The control system is, therefore, designed around pulse-delay generators for generating precisely timed pulses to trigger the master gaps in the various systems. The central control computer will ensure that all systems parameters, such as pulse delays, are properly set and all slow functions accomplished, such as dc charging of the Marx generators. When the system is ready for triggering, the central control will trigger the pulse-delay generator which in turn will emit properly timed triggering pulses to the various subsystems. Timing through the system will be controlled by maintaining proper cable lengths between the various pulses and gaps.

The timing of the functions of the implosion-heating system is described below. The firing time of the implosion-heating start gaps is designated t_o.

1. $t = t_o - 30$ ms

a. Initiate charge of start-gap trigger-system Marx.

b. Initiate charge of pulse-charge system Marx.

c. Initiate charge of crowbar-trigger-system Marx.

d. Initiate charge of preionization system.

This dc charging will require approximately 30 ms.

2. $t = t_o - 10\,\mu s$

a. Trigger the start-gap trigger-system Marx.

b. Trigger the crowbar trigger-system Marx.

c. Trigger the pulse-charge system.

The 10 μs is the time required to complete the pulse-charging of the implosion-heating capacitors and the trigger systems. This is a design value of the system components and will not be changed after the machine has been constructed.

3. $t = t_o - (5 \text{ to } 10\,\mu s)$

a. Trigger the preionization system.

The range of 5 to 10 μs will be the typical operating range of the preionization system; however, the system is designed to be able to vary this time over a range as wide as necessary.

4. $t = t_o$

a. The start-gap system is triggered.

5. $t = t_o + (\sim 100 \text{ ns})$

a. The crowbar system is triggered. The timing of the triggering of this system must be flexible and must also be precise within a few nanoseconds.

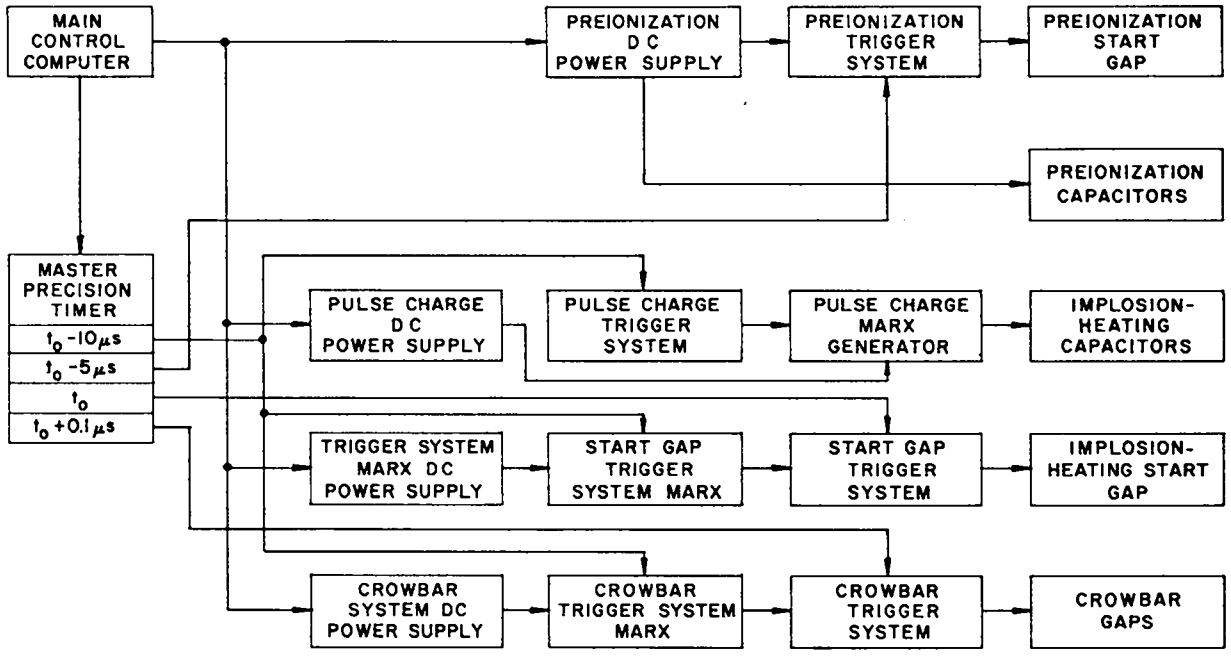

Fig. 5.3-10.
Trigger system for one quarter of the machine.

Figure 5.3-10 shows a diagram of the overall trigger system for one-fourth of the machine. Each quadrature of the machine has a system identical to that shown in Fig. 5.3-10. The central control computer and the central pulse generator are located in the machine control room, while the 8-kV pulsers and the master trigger gaps are located in the trigger-system area of the machine.

5.4 COMPRESSION SYSTEM

5.4.1 General Description

The purpose of the compression field system is to provide the necessary magnetic field to compress adiabatically the plasma for the burn cycle. A circuit diagram of a basic module of the energy-storage and transfer system is shown in Fig. 5.4-1. The energy required for the compression field is stored initially in the superconducting storage coil. The current is transferred by opening the current interrupter and allowing the current to resonate through the transfer capacitor into the load coil. At peak current in the load coil the crowbar switch is closed and the current decays with an L/R time constant.

The compression field reaches 55 kG in 700 μs and decays with a 250-ms time constant. There are 1280 compression load coils in the machine, one for each implosion load coil, with each compression coil having a crowbar switch, transfer capacitor, vacuum interrupter, and storage coil. The energy required to produce 55 kG in each compression coil is approximately 345 kJ and the energy-storage capacity of the transfer capacitor is somewhat less than half of that (185 kJ) when losses are taken into account. The 55 kG is in excess of the field required according to Fig. 4-11, but we chose to have a margin for exploration.

Although the energy for the compression field could be supplied from a capacitor bank, an inductive energy-storage system has been selected in order to advance the necessary technology required for future reactors. Although capacitor technology is presently well developed and the energy-storage requirements of the SFTR could be handled by large capacitor banks, we believe that capacitors will not

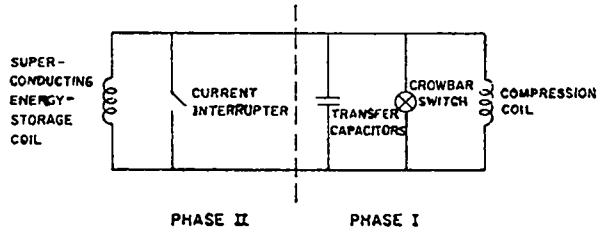

Fig. 5.4-1.
A basic module of the compressional energy supply.

be the economical choice in a reactor where approximately 1 GJ of energy storage will be required for staging between the capacitive implosion system and the homopolar compression system. The primary reasons that superconducting and inductive storage are expected to be more attractive than capacitive storage for that purpose are:

- Inductive storage has a much higher energy density from capacitors, thus, less space is required.
- Because of the higher energy density, fewer elements are required in an inductive energy-storage system, and maintenance requirements are reduced.
- An inductive energy-storage system is projected to have a lower cost per joule than a capacitive system.

For smaller experimental machines, the reduced volume requirements of the inductive system are not a major consideration; however, in a reactor the energy-storage requirements for staging systems, which must be discharged in the 1/2- to 1-ms time frame, are of the order of a gigajoule, and higher energy density becomes an important advantage for the inductive storage system. In a commercial reactor, the reliability and maintenance of the system are major considerations and the system having the fewest components consistent with acceptable reliability, such as the inductive storage system, also has the advantage. The cost of an inductive energy-storage system that would be used in a reactor can only be roughly approximated. The present cost estimate for installation of an inductive system is substantially higher than for a capacitive system. However, the technology and manufacturing capability for capacitors are well developed, and increased production of inductive storage systems will significantly reduce their cost. The cost of a capacitive storage system would be approximately 4¢/J, whereas the cost of a superconducting inductive energy-storage system would be approximately 2¢/J in a mature superconducting industry.

The compression field system will be installed in two phases. Phase I consists of the installation of the compression load coils, the crowbar switches, and the transfer capacitor bank. The experiment will be operated initially with just the transfer capacitor bank supplying the compression field. This will permit operation of the machine with a relatively reliable capacitor system similar to systems used previously in theta-pinch experiments at Los Alamos. Phase I operation will also allow more time for the development of the superconducting system. After all systems have been checked out, initial plasma experiments aimed at producing long confinment times (tens of milliseconds) will be carried out. Installation of the inductive system, or Phase II, consists of adding the superconducting energy-storage coils and current interrupters and doing ignition experiments. Under Phase I the peak magnetic field will be 39 kG with a rise time of 530 μs; under Phase II the peak magnetic field will be 55 kG with a rise time of 700 μs.

5.4.2 Capacitor Compression

5.4.2.1 General Description

The energy-storage capacity of the transfer capacitors associated with a single compression field load coil is 185 kJ. The system is designed for a peak voltage of 60 kV and would transfer energy from the inductive supply in 700 μs. Without the inductive store the transfer time is 530 μs. At 60 kV the capacitance required per module is 100 μF. Due to the large inductance of the load coil, a relatively high inductance can be tolerated in the capacitor bank. This allows the less expensive construction of connecting low voltage capacitors in series to achieve the required 60 kV. The 100-μF capacitance will be achieved by connecting four 400-μF, 15-kV "capacitors" in series in a Marx generator arrangement as illustrated in the schematic shown in Fig. 5.4-2. Each 400-μF "capacitor" consists of four 100-μF capacitors in parallel. As well as allowing the use of relatively inexpensive low voltage capacitor and ignitron start switches, the arrangement also allows the capacitor to be charged by a simple dc charging supply.

The reliability of the system has been determined by calculating the mean time between component failures, and using this to assess reliability. It was found that despite the large number of components, approximately 30 energy transfers can be expected between component failures. This analysis was based on the following assumptions:

- The prefire rate of the start switches (ignitrons) is 1 to 2000.

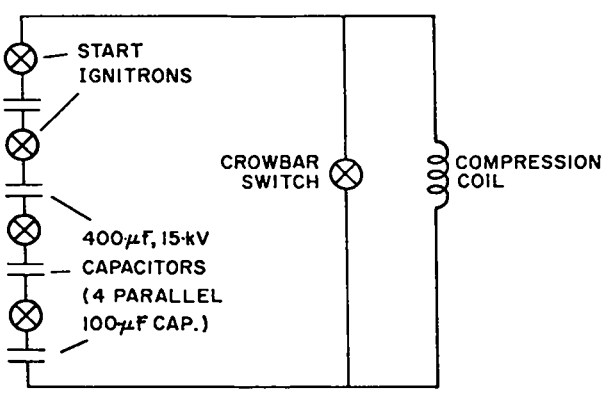

Fig. 5.4-2.
Schematic of Phase I energy-storage capacitor for one compression load coil.

• The prefire rate of the ignitrons used in the crowbar switch is 1 in 10 000. The crowbar switch consists of four size D ignitrons in series.
• Prefires do not cause component failures.
• Failure of any component terminates the shot.
• Prefire of a single ignitron does not cause a total switch prefire but a simultaneous prefire of two ignitrons in series does.
• Failure of any component does not cause failure of any other component.

This level of reliability has proved satisfactory in Scyllac, where approximately 10 shots are expected between component failures, and it is considered satisfactory in the SFTR.

5.4.2.2 Capacitor Bank

The basic capacitor used in the compression system is a 15-kV, 100-μF unit. The system is designed for minimum voltage reversal on the capacitor so that, following current practices, a relatively high energy density can be stored per unit. The total energy stored in a single capacitor is 11.2 kJ. With 3.25 J/in.^{3}, which is the approximate energy density in a standard high-density capacitor, the size of the capacitor is the same as the standard Scyllac-type unit, 24 in. x 14 in. x 11 in. For a single compression coil, 4 capacitors will be connected in parallel (to give the 400-μF, 15-kV "capacitor" in Fig. 5.4-2), with 4 groups of these parallel capacitors connected in series for a total of 16 capacitors per compression coil. The capacitors will be placed in racks just outside the concrete cell as shown in Fig. 5.1-6. Each rack contains 160 capacitors—sufficient for 10 load coils. A total of 128 racks is required for the machine.

5.4.2.3 Start Switches

The locations of the start switches are shown in the schematic in Fig. 5.4-2. Each start switch must have a peak current rating of 18 kA, be able to withstand at least 15 kV, and carry at least 6 C. Suitable commercial ignitrons have been selected for the start switch application. Ignitrons having a voltage rating of 20 kV will be employed to provide a margin of safety against prefires. The ignitrons and headers are located at one end of the capacitor racks.

5.4.2.4 Charge System

In the design of the capacitor bank charge system one must take into account not only the charging of the capacitors but also personnel safety and fault modes. The charging circuit is shown in Fig. 5.4-3. Four 100-μF capacitors are connected in parallel to a single start switch with 5-kΩ charge resistors. Fail-safe shorting balls are connected across the

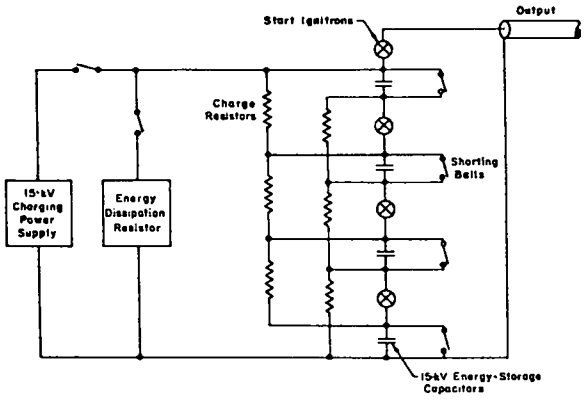

Fig. 5.4-3.
Electrical design of capacitor-bank charge system.

capacitors to ensure complete discharge of the capacitors during maintenance. A shorting switch across the bank can be closed to dump the energy into a resistor should the charge cycle ever need to be aborted.

Sixteen racks of capacitors are charged from a single controlled power supply. Eight power supplies will be required for the facility and will be located just outside the main building. Following standard Scyllac practice, the capacitor banks will be charged in 30 s; each power supply must therefore supply 128 A at a nominal 15 kV for a peak power rating of approximately 2 MW.

5.4.2.5 Trigger System

The trigger system for the 128 racks will be divided into 4 equal subsystems similar to the trigger system for the implosion-heating system. Each subsystem consists of a master pulser which triggers 320 Krytron drivers, with each driver triggering the 4 start ignitrons in a 16-capacitor unit which supplies the energy for 1 compression coil. The four master pulsers are triggered from the control computer.

An important consideration of the trigger circuit is the isolation of the start ignitrons. Since ignitrons are prone to prefire, the ratings on the four series ignitrons are chosen such that when one prefires the remaining three will hold off the voltage; two ignitrons must, therefore, prefire simultaneously for the system to malfunction, which is a much less likely event than a single prefire. However, to gain this increased protection from prefires, the trigger system must provide sufficient isolation of the trigger pulses so that a prefire in itself does not trigger the remaining ignitrons. Such a circuit is shown in Fig. 5.4-4. The pulse transformers supply the trigger pulses to the ignitrons, but when a prefire

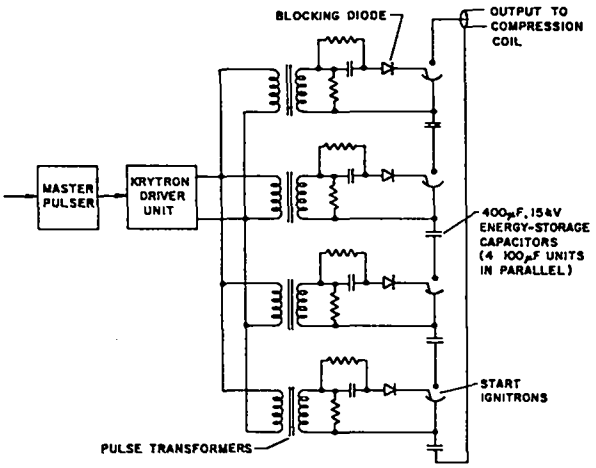

Fig. 5.4-4.
Trigger system for capacitor drive of compression coils.

occurs the blocking diode will prevent an energy pulse from feeding back through the pulse transformers to trigger the other three ignitrons. Although this circuit does not provide complete isolation, it is expected to provide a reasonable compromise between cost and performance. Should the performance of the circuit be unsatisfactory, an optical system with higher performance can be employed.

5.4.3 Magnetic Energy Storage

5.4.3.1 General Description

Energy for driving the compression coils for the adiabatic heating of the theta-pinch plasma in the SFTR is to be supplied from a superconducting magnetic energy transfer and storage (METS) system. The system has 128 cylindrical plastic dewars outside the plasma toroid, each dewar containing 10 energy-storage coils. The energy, to be pulsed into the compression coils in a 0.7-ms transfer period, is charged from a dc, low voltage power supply into a series-connected, modularized, superconducting inductive energy store. Charging is carried out over a 300-s period. The charge-discharge cycle is to be repeated every 900 s to provide for refrigeration recovery at the 4.5 K level. This 900-s cycle includes the 300-s charging time and sets the heat load cycle and size of the refrigeration plant for the system.

The refrigerator plant is capable of making liquid helium at a rate of 3045 kg/h. The refrigeration cycle will use gas turbine expanders in cascade with intermediate heat exchangers and a reciprocating expander engine in lieu of a Joule-Thomson valve in the last stage to liquefy the helium. Several principal heat loads determine the refrigeration requirements. The 4.5 K steady-state dewar heat load is 7.6 kW, 5.4 kW of which is from the 25-kA continuous duty electrical leads to each dewar; the 4.5 K pulsed heat load is 8.6 kW, 5.4 kW of which arises from the cryogenic disconnects; and the transfer lines have a steady-state, 1.1-kW heat load at 4.5 K. Half of the helium, 1517 kg/h, is returned to the refrigerator as cold gas at a temperature just above 4.5 K and the remainder as warm gas. Thus half the heat load is handled efficiently in a refrigeration cycle and the remainder is cooled and liquefied from ambient temperature as in a liquefier cycle. The liquefier-refrigerator is about 22 times larger than those in existence at present and will require 16 000 hp or 12 MW electrical power.

Components for switching and transfer of the energy from the storage coils to the compression coils are arranged in a sectionalized or modular array around the system between the plasma discharge tube and the storage coils. The sectional arrangement provides access for assembly and servicing and is sized to maintain reasonable modular interconnections between the energy-storage coils and the compression coils. Basic to this module concept are the high voltage and high current limits of 60 kV and 26 kA established for the superconducting energy-storage coils with a 2.5-T magnetic field. When these limits are considered in connection with the required 5.5-T peak plasma adiabatic compression field, the required 250-ms L/R decay time for the compression field, transfer inefficiencies, energy stored in the compression coil windings, and corrections for the applied multipole field to correct for the plasma behavior, then the storage coil module, its stored energy, and the associated switching and transfer components are defined.

The total stored energy in the 1280 superconducting coils around the torus is 488 MJ.

Switching of the energy from the superconducting energy-storage coils to the compression coils on the plasma is accomplished by disconnecting the series-connected storage coils and connecting them in parallel with the compression coils. Each storage coil is connected in parallel with a transfer capacitor. This arrangement creates an L-C-L resonant circuit with nearly 100% transfer efficiency. Once the energy is transferred into the compression coils, each coil is shorted or crowbarred so that the magnetic field is trapped in it for the plasma confinement.

Because charging of the storage coils takes a long time compared with discharge—300 s versus 0.7 ms—it is necessary to connect the storage coils in series within the liquid helium dewar. To bring the

26-kA current out of the dewar to an external series-connected switch or interrupter at each storage coil would create a prohibitive heat load from the electrical leads entering the cryogenic system and would require a very large refrigerator. A compromise arrangement is provided with groups of 10 coils in separate dewars. Thus only 128 pairs of 26-kA leads are used during the charging cycle. Within the liquid helium dewar, low resistance, cryogenic disconnects, each with dissipating peak power of less than 24 W, are used to make the series connections between coils in the separate dewars. These cryogenic disconnects are connected in parallel with HVDC vacuum interrupters external to the dewar. In the switching cycle the disconnects are opened first, bypassing the current through the HVDC interrupters which are then opened, and most of the energy dissipated in switching is outside the liquid helium system.

The switching time required for opening the cryogenic disconnect and the HVDC interrupter is of the order of 0.1 s. The subsequent 0.7-ms energy transfer period is relatively short. The electrical leads carrying the current during transfer are small since they carry a pulsed load for only 0.1 s, and their thermal conduction heat leaks and resistive electrical heat loads are small.

Switches for the HVDC interrupter bank are to be state-of-the-art vacuum breakers. Conventional counterpulse circuitry holds the current in the breakers at zero with a very low time rate of change of voltage during deionization. Crowbar switches for the compression coils will also use state-of-the-art ignitrons like those now used in the LASL-CTR program.

The transfer capacitor for the L-C-L resonant circuit for the superconducting METS system will use the capacitor bank described in Sec. 5.4.1. It will be connected to store approximately half the 488-MJ energy at 60 kV during the 0.7-ms energy transfer period.

Table 5.4-1 lists the METS-SFTR circuit components and describes their functions. The notation of Fig. 5.4-5, which is a METS-SFTR circuit diagram, locates these elements in the circuit. The following operational sequence of the system describes the energy-storage and transfer process.

In the initial state the cryogenic disconnects B_1 are closed, and the vacuum interrupters B_2 and isolating switches B_3 are open. The electrically operated line contactors B_6 are open during charge. The storage inductors are charged in series by ramping the current from the main energy supply to 26 kA in 300 s. At the same time, the counterpulse energy is supplied to the transfer capacitor bank C_1 by charging to several kilovolts. After charging, the counterpulse supply is disconnected. The high voltage vacuum interrupters are closed, the line contactors to ground are closed, and the cryogenic disconnects are opened, in that sequence. This transfers the 26 kA to the breaker circuit external to the liquid helium inductive storage coil dewar. The vacuum interrupters are then opened and draw a low voltage arc for several milliseconds until the gap spacing is sufficient to hold off the high voltage that develops during the transfer cycle. At this time, the counterpulse is triggered from the C_1 capacitor bank. The 26-kA current in the interrupter is commutated through zero at the proper rate as determined by L_3 and C_2 to allow for deionization and complete arc interruption. The current then transfers resonantly with some small cable or transmission line losses from the storage coil module through the transfer capacitor into the compression coil. At the end of the 0.7-ms transfer period the fast crowbar B_4 is closed, trapping the current and energy in the compression coil. Shortly thereafter, the slow crowbar B_5 closes, relieving the B_4 crowbar. The crowbar headers will be designed in such a way that with minor cable changes slow crowbar B_5 can be connected between the compression coils L_2, if desired. This creates a series circuit assuring equal dB/dt decay in the full plasma torus.

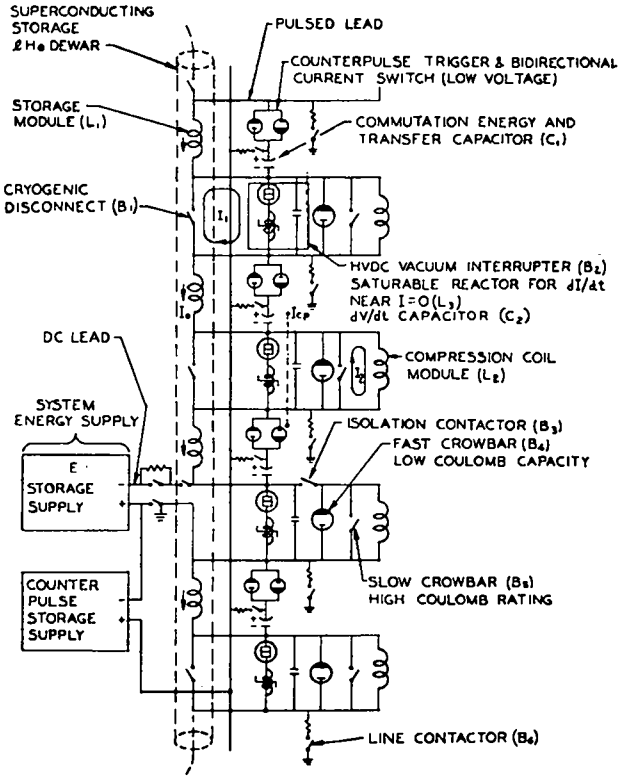

Fig. 5.4-5.
METS-SFTR circuit diagram.

TABLE 5.4-1

METS-SFTR CIRCUIT COMPONENTS

Energy Supply

Main

1-3 MW to ramp current to 26 kA in 300-s charging cycle.
Energy stored = 1280 x 381 kJ = 488 MJ. Current leads from main supply enter circuit at a point that remains at low voltage at all times.

Counterpulse

50-kW supply. It charges the transfer capacitors to several kilovolts. 10 MJ needed for counterpulse, total.

Inductors

L_1 Storage module, superconducting. $L \simeq 1.1$ mH
- E = 381 kJ at 26 kA
- V = 60 kV during 0.7-ms transfer, peak
- B = 2.5 T

L_2 Compression module, multiturn copper. $L \simeq 1.1$ mH, 14.75 cm toroidal circumference.
- B = 5.5 T in 34-cm i.d.
- L/R ≤ 270 ms
- E = 345 kJ when B = 5.5 T inside bore.

L_3 Saturable reactor to allow preferred dI/dt near I = 0 during commutation.
- Parameters to be determined.

Capacitors

C_1 Transfer capacitor sets transfer time and peak voltage during transfer. It is reverse charged to ≤ 5 kV to supply counterpulse current.

- $C_1 = 100\,\mu F$
- V = 60 kV

C_2 Transient capacitor to handle the overcurrent during commutation and limit voltage on HVDC interrupter during deionization period, several tens of microseconds. The small series damping resistor eliminates ringing.

Breakers, Contactors, Crowbars

B_1 Cryogenic disconnect within liquid helium cryostat. It carries the charging cycle current to 26 kA. It is to be designed for a power loss < 24 W at full current. Resistance $\leq 3.5\,(10)^{-8}\,\Omega$.

B_2 HVDC vacuum interrupter, or equivalent. Closes just before B_1 disconnects, current transfers into the pulsed lead ambient temperature loop to B_2.

B_3 Isolation contactor. Removes energy-storage voltage from compression coil module during charging cycle.

B_4 Fast crowbar. Crowbars compression coil module at peak current. (I = 26 C/ms.)

B_5 Slow crowbar. Relieves B_4 after several milliseconds. Voltage drop across each B_5 is insufficient to maintain B_4 conduction, extinguishing all B_4's.

B_6 Electrically operated line contactor. The series resistor provides the proper L/R to discharge the storage coil in a short time if the cryogenic disconnect B_1 fails to open.

5.4.3.2 Storage Coils

Superconducting energy-storage coils, each storing 381 kJ, form the basic element of the SFTR energy source. One thousand two hundred and eighty of these are to be located around the plasma torus, 10 each in 128 vertical axis, plastic, cylindrical dewars at a radius of 57.2 m. Separation of the coils into groups of 10 in individual dewars permits system construction and testing as well as operation by modules or by sections of a number of modules without interference with work being done on other segments of the system. Maintenance can be performed by replacement of preassembled sets of storage coils with their electrical leads, cryogenic disconnects, hydraulic actuators, etc., attached to a dewar lid. If necessary, individual dewars can also be easily replaced.

Design of these superconducting energy-storage coils considers:

1. The various components requiring energy to establish the storage requirements;
2. The technologically attainable current and voltage levels for operation of the coils;
3. The superconducting cable design and the individual superconductor strand design as they relate to the magnetic field within the coil, energy losses during charge and discharge, and the liquid helium temperature level;
4. Magnetic forces and stresses;
5. Physical dimensions and variation of the length as a function of location in the 10-coil stack;
6. Inductance matching to the compression coils;
7. Electrical insulation; and
8. Forces between coils in adjacent dewars.

The 381-kJ energy stored in each coil is based upon the four major components listed in Table 5.4-2. The largest item, 325 kJ, is the energy delivered to the compression coil to provide the 5.5-T, theta-pinch plasma adiabatic heating magnetic field and to maintain the field for a 270-ms L/R decay time for the compression coil. With the attached circuit impedance, this reduces to a 250-ms L/R time constant. The compression coil is described in detail in Sec. 5.4.3.6.

Multipole effects create both helical and sinusoidal radial modulations of the plasma along the discharge tube torus. Compression coil design to accommodate this perturbation increases the energy-storage requirement by 6%.

Transfer losses in resistances of cables, etc., but excluding the transfer interrupter losses, increase the required stored energy by 5%.

Losses in the transfer interrupters (vacuum breakers), cryogenic disconnect, and transient leads increase the energy-storage requirement by 6.3%. Descriptions of these circuit elements are given in subsequent sections.

Pulsed, short transfer period, high current-high voltage superconducting coils have been operated at LASL. This and related experience indicates that reliability of electrical components in the energy transfer circuit and the overall transfer circuit design poses rapidly increasing problems at voltages much in excess of 60 kV.

With this maximum voltage limitation, studies of superconducting METS systems indicate a broad cost minimum at storage coil fields in the 5-T range. Fields reduced to 2.5 T increase the cost by less than 2%. Because of the complex structural and electrical insulation problems at the ends of the coils for multilayer coils, a single-layer, edge-wound coil is to be used. To obtain even the low end of the 2.5-T and 5-T range for a single layer coil and to achieve an adequate ampere-turns value, the superconductor must have a 2.41:1.0 rectangular aspect ratio and carry 26 kA to have the proper energy stored with reasonable coil dimensions. This combination can be developed, given the state of the art for Nb-Ti superconductors. For these conditions, the peak transfer voltage is 60 kV.

The superconductor to carry the 26 kA is built of individual strands of twisted multifilament Nb-Ti in a complex Cu, Cu-30 Ni matrix.

Energy loss requirements for the superconductor itself during charge and discharge have been set at less than 0.3% of the stored energy. These losses arise mostly from hysteresis and eddy currents induced in the conductor during the storage coils'

TABLE 5.4-2

ENERGY REQUIREMENT FOR MAGNETIC STORAGE COILS (kJ)

Compression coil without multipole correction	324.8
Multipole correction, 6%	19.5
Transfer inefficiency, 5%	16.2
Transfer interrupter, cryogenic disconnect, and transient lead losses, 6.3%	20.5
	381.0

cyclic operation. The 0.3% criterion limits this heat load to about 10% of the 4.5 K refrigeration capacity.

In the complex Cu, Cu-Ni matrix, each Nb-Ti filament is surrounded by copper and then Cu-Ni. The copper stabilizes the superconductor, and the relatively high resistance Cu-Ni decouples the Nb-Ti filaments. The twist rate of the strands, the size of the strands; the Cu, Cu-Ni to Nb-Ti ratios, the size and number of Nb-Ti filaments, the current density at operating temperature, and the number and transposition of the strands in the superconducting cable characterize the conductor. These parameters must be carefully specified to provide for the transport current of 26 kA and to hold the energy loss below the 0.3% level. The possibility of using a low resistivity impure copper matrix conductor is not without merit. Energy losses during transfer could be low and such a conductor warrants exploration. The gross characteristics of the superconducting cable with a copper matrix are given in Table 5.4-3.

Because the energy-storage coils are arranged in groups of 10 as a solenoid, there is an appreciable field gradient at the ends of the solenoid. This gives an I x B compression force which is high in the end coils and integrates to $6.41(10)^9$ N over the central plane of the solenoid. A 3.94-cm-thick inner coil form made of a NEMA G-10 epoxy-fiber glass laminate gives an acceptable stress level of $5(10)^8$ Pa. The maximum hoop force in the conductor occurs at the center of the solenoid and a structural shell support must be added over the conductor to hold it in place. A NEMA G-10 shell of 1-cm thickness will hold the conductor with a stress level of $4(10)^8$ Pa.

Physical dimensions of the energy-storage coils are determined by the energy to be stored, the field level at which it is to be stored, and, in turn, the current level of operation. For optimum transfer of energy, the storage coil inductance must match that of the compression coil it drives. The coil volume is fixed by matching this parameter, after the field and current have been fixed, as discussed above. Because of the finite solenoid length for 10 coils, the mutual inductance of the outer coils is low. These coils are lengthened to match the inductance to the compression coils. The electrical and physical parameters of the coils are given in Table 5.4-4. Number "1" coils are the innermost pair, and the number "5" coils are the outermost of the stack of 10.

High voltage electrical insulation of the storage coils is provided in several ways. The conductor will have 0.76 mm of insulation between turns. The coil form material will be epoxy-fiber glass laminate, generally NEMA G-10, which has good insulating properties. The dielectric strength of liquid helium in which the coils are immersed is good. The electrical leads exit the coil at opposite ends. Alternate coils are reverse-wound. This permits the high voltage terminals of the adjacent coils to be close together.

Fringe fields at the plasma discharge tube for the 128 assemblies of storage coils located at a 57.2-m radius are of the order of 1 G if all coils are oriented with the same polarity and more than an order of magnitude lower if the polarity is alternated in adjacent dewars around the circle. Either arrangement is acceptable.

Forces between adjacent dewars are largest during startup and testing when energy may be stored in only two sets of solenoids. For the reversed polarity situation, the attractive force will be of the order of 3500 N, which is not excessive. Some extra structural support will be designed into the coil mounting.

TABLE 5.4-3

SUPERCONDUCTING CABLE CHARACTERISTICS

Transport current	26 kA
Operating current density	$1.41(10)^5$ A/cm^2
Short sample critical current	$2.22(10)^5$ A/cm^2
Cable cross-sectional area	2.83 cm^2
Cable thickness	1.08 cm
Insulation thickness, each face	0.076 mm
Strand filling factor	0.33
Matrix to superconductor ratio	4.0

TABLE 5.4-4

ENERGY-STORAGE COIL PARAMETERS

Energy	381 kJ
Transport current	26 kA
Maximum operating voltage	60 kV
Maximum magnetic field	2.5 T
Inductance	1.13 mH
Radius (mean)	33.64 cm
Lengths - coils 1, 2, and 3	57.9 cm
coil 4	58.9 cm
coil 5	67.4 cm

5.4.3.3 Cryogenic Disconnect

The cryogenic disconnect is a very low resistance contactor which switches the 26-kA storage coil current from its charging path through the disconnect to a low impedance path through the vacuum interrupter. After opening, the disconnect stands off the 60-kV dc pulse generated across its contacts.

The disconnect operates in liquid helium and will be located immediately outside the bore of the storage coils it serves. It will be operated by an arm connected to an actuator mounted on the lid of the storage coil dewar.

The disconnect will open fully in as short a time as practicable to minimize steady-state heating of the pulse leads. An opening time of 0.1 s or less has been selected for a design criterion. System cycling time will allow the disconnect to be open for 600 s before it begins to close. Closing will be slow, on the order of a few seconds. In the normal system cycle, the disconnect will remain closed during the storage coil charging period of 300 s. The disconnect should be capable of being cycled 5000 times without significant deterioration of performance.

From the literature[1] it appears reasonable to expect that with contact pressures on the order of 2.7 x 10^7 Pa between carefully prepared, normal conductor surfaces of the proper materials, contact interface resistances as low as 10^{-9} Ω can be obtained.

Published information on the dielectric properties of liquid helium and cold gaseous helium indicates that a 20-mm gap between the contacts should stand off 60 kV with a reasonable margin of safety.

Accordingly, a disconnect is being designed that will have a contact area approximately 8 x 10^{-3} m^2, a contact spacing greater than 20 mm when open, and will be capable of applying contact interface pressures as high as 3.8 x 10^7 Pa (5.5 x 10^3 psi). It is a toggle mechanism driving two moving contacts against two fixed contacts and is illustrated in Fig. 5.4-6.

The mechanism is designed for rolling contact between its highly loaded components during final contact closure. It will provide force amplification of approximately 10 to 1, thereby keeping the external actuator to a size compatible with rapid opening and keeping the heat leak down the actuator arm to a reasonable minimum. The mechanisms are designed to maximize actual surface areas in contact. Contact materials will be selected partly on the basis of previous work[1] and partly from results of tests now in progress here at LASL.

Initial plans are to split each contact into two regions: one of very low resistance which will open first; a second which will be connected to the first region by a very low impedance path and which will open last. Any arcing will occur only across the second region so that the contact surfaces of the first region will remain unscarred and uncontaminated. If necessary, a third contact region can be incorporated to reduce arcing. Magnetic arc quench also can be incorporated if experiments indicate the need.

With maximum contact loading, the closing force required for the disconnect is 3 x 10^4 N (6.8 x 10^3 lb). In the SFTR, 10 storage coils with their 10 disconnects are stacked vertically in each dewar. The 10 disconnects will be ganged. All 10 will be operated by a common arm which, in turn, is tied to a single actuator mounted on the dewar lid. With 10 disconnects, an actuator must develop a closing force of up to 3 x 10^5 N (6.8 x 10^4 lb). This is within a reasonable range for hydraulic actuators.

The moving parts of 10 disconnects, an actuating arm, a hydraulic piston, and a pneumatic piston are estimated to weigh 100 kg. Calculations using a cosine displacement curve show that the maximum force required to open the disconnect in 0.1 s is 3.2 x 10^3 N (14 000 lb), a force well within the range of a reasonably sized pneumatic actuator.

A hydraulic-pneumatic system for actuating 10 disconnects is shown in Fig. 5.4-7. A hydraulic actuator is used to close the disconnects, and a hydraulic buffer cushions the opening shock.

5.4.3.4 HVDC Interrupters

The HVDC current interrupter modules in the METS-SFTR system serve to disconnect the inductive energy-storage series loop, thus initiating the energy transfer pulse into the plasma compression coil. There is one interrupter module for each storage coil module, and a total of 1280 in the complete system. Ten interrupter modules are grouped into a submodule for compatibility with the system in cable runs and access for maintenance.

The interrupter module parallels the cryogenic disconnect electrically through a pair of pulsed current leads into the liquid helium dewar. During a typical energy transfer cycle, the interrupter is closed mechanically to create an electrical short circuit around the cryogenic disconnect just before the disconnect is opened. During actuation of the disconnect, the 26-kA storage current is diverted through the pulsed current leads into the external loop containing the vacuum interrupter.

When the cryogenic disconnect has separated to a gap capable of withstanding 60 kV, the counterpulse

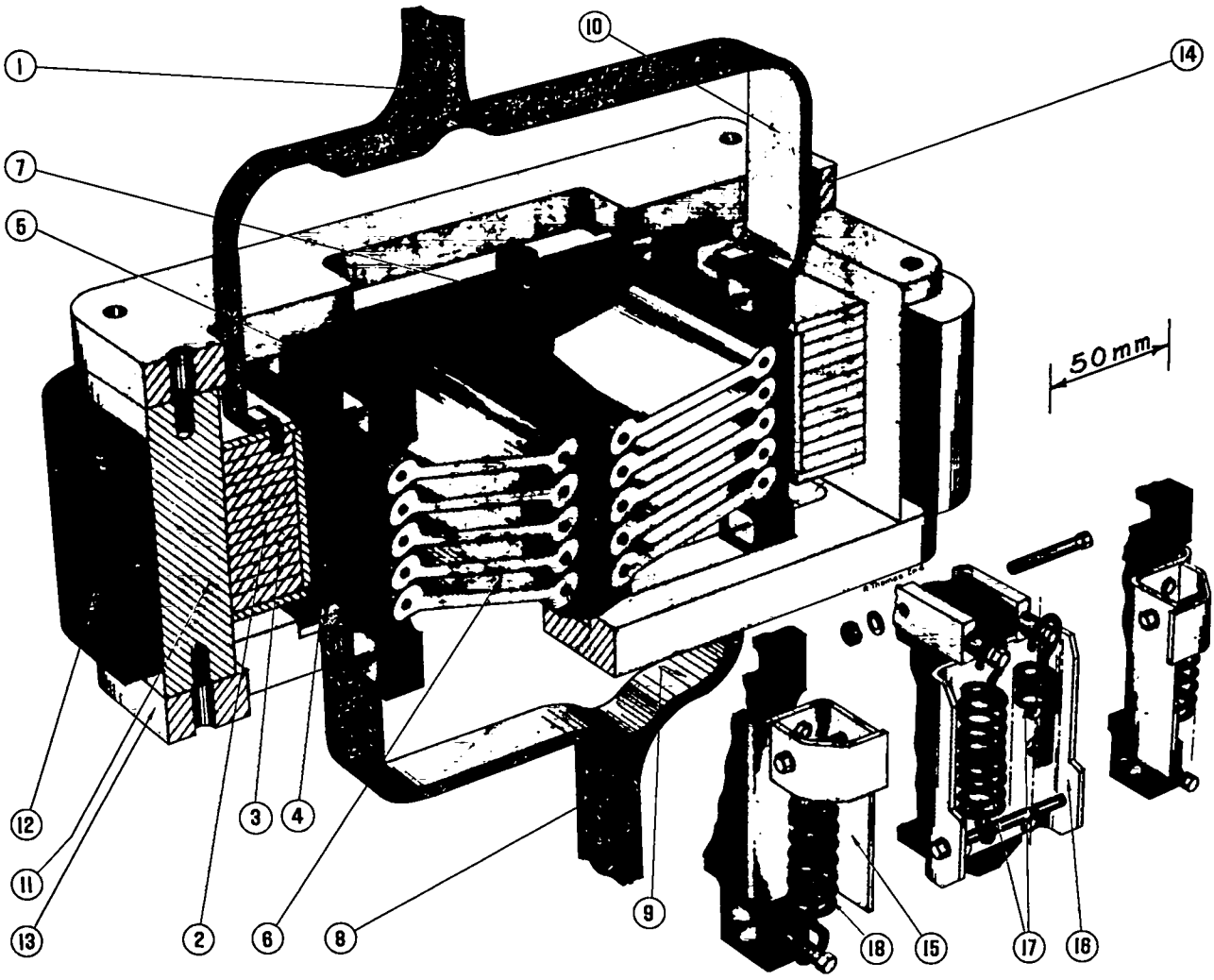

Fig. 5.4-6.
Cryogenic disconnecting switch: (1) and (10) stationary superconductors; (2) load distribution pad; (3) fixed contacts; (4) movable contacts; (5) contact slides/guides; (6) toggle bars; (7) operating arm and plate; (8) and (9) flexible superconductors; (11)-(14) structural members; (15)-(18) spring return mechanism details.

circuitry initiates fast current interruption of the vacuum breakers, presenting an open circuit to the storage coil current. The 0.7-ms energy transfer pulse begins at this point, and the interrupter completes its function.

The major components within the interrupter module are shown in Fig. 5.4-8. A vacuum interrupter of a design used in the ac power distribution industry is the interruption element. The vacuum bottle actuators are capacitor discharge solenoid drivers triggered by the submaster control. All other components are passive, with the exception of the triggerable fuse.

Each of the four vacuum interrupters conducts 13-kA current and holds off 30-kV voltage after interruption. The saturable reactor, dV/dt capacitor, and damping resistor operate when the counterpulse current is applied to off-commutate the arc current (see Sec. 5.4.3.5). The voltage grading network assures equal voltages across all interrupters during the energy transfer pulse. A vacuum breaker has already been successfully tested to a 17.0-kA, 44-kV level.

The 100-μH bucking transformer serves two important purposes in successful interrupter operation.

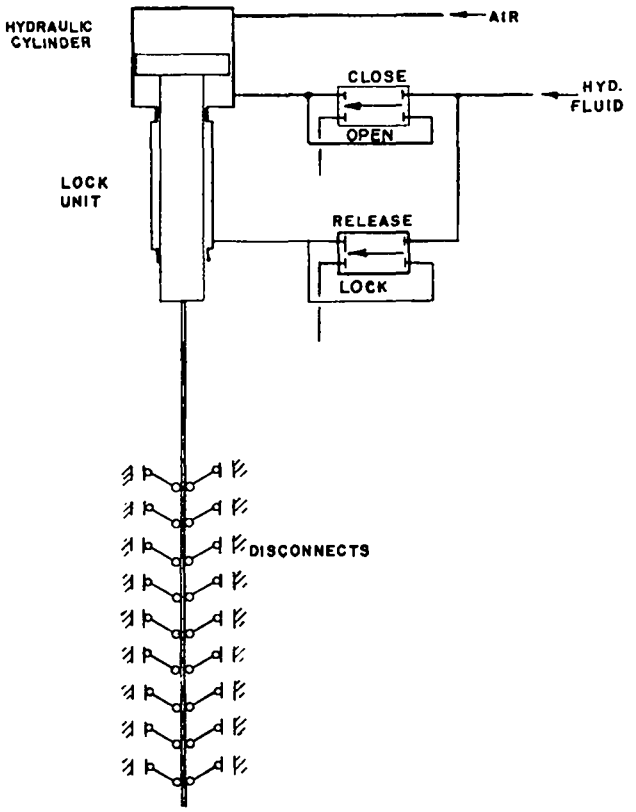

Fig. 5.4-7.
Mechanism for actuating the disconnect.

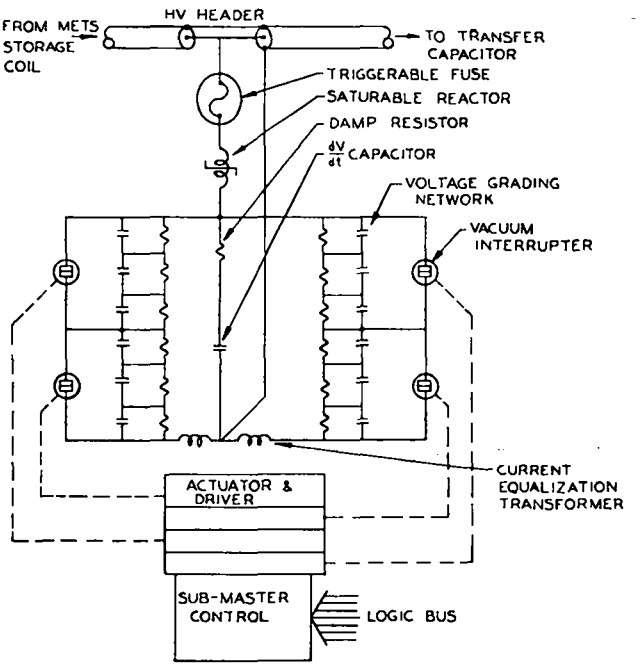

Fig. 5.4-8.
HVDC interrupter module.

First, it assures equal currents in both interrupter legs during current transfer from the cryogenic disconnect circuit, where current sharing is determined mainly by leg inductances. Joule heating starts evenly in each interrupter during the 0.1 s before the cryogenic disconnect separates. During this time, resistive stabilization through contact heating assures current sharing. All interrupters enter the contact break and arc phase with uniform contact thermal conditioning. A fraction of a millisecond jitter is to be expected in the mechanical actuation of contact breaking between interrupters. The second purpose of the transformer is to impede inductively a current outrush from one leg due to a premature arc voltage strike, and to hold the current balance within ±1 kA.

The triggerable fuse is a one-shot replaceable safety device to assure successful current interruption. Since the SFTR plasma dynamics require a fairly uniform rise in the compression magnetic field from all modules, an unsuccessful current interruption in one module leading to complete loss of field rise in its corresponding compression coil would destroy the plasma containment. The submaster control references each module's energy transfer voltage waveform to the standard waveform. Voltage lag indicates unsuccessful current interruption, and a drop or loss of voltage indicates an arc restrike. In both cases, the fuse would be opened fast enough to assure plasma containment.

An arc restrike is potentially the most troublesome failure mode of the system. However, the arc current rise is impeded during the first several microseconds by the saturable reactor, time enough to detect such a failure and trigger the fuse. A current shunt or Rogowski loop in each module may provide a much faster, more reliable failure indicator.

The mechanical layout of a 10-unit interrupter submodule is shown in Figs. 5.4-9 and 5.4-10. The high current bus runs are so located as to minimize inductance and to isolate high voltages from grounded structures. The submaster control and triggerable fuses are easily accessible. The high voltage header is located nearest the overhead cable runs. A complete module can be removed from the main enclosure and exchanged to minimize downtime during the occasional maintenance expected on interrupter bottles and actuators.

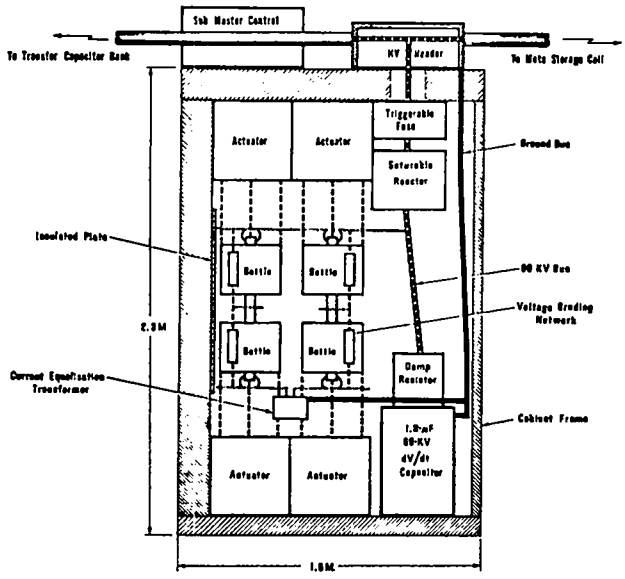

Fig. 5.4-9.
Physical layout of an interrupter module.

5.4.3.5 Interrupter Counterpulse System

A vacuum interrupter conducting a high current arc requires that the current be forced through zero to regain its high voltage vacuum dielectric strength. In the dc current circuit of METS, as opposed to an ac circuit, the current zero within the interrupter must be provided artificially by switching in a countercurrent from an external source.

The arc extinction parameters of the countercurrent required to maintain I = 0 in the interrupter during a time dt to allow arc plasma deionization and dispersal set a coulomb value Q = I dt to be met by the current source. A capacitor discharge circuit used as the current source will require minimum energy $Q^2/2C$ with maximum capacitance.

The addition of ignitron switches to each bank of transfer capacitors results in a minimum cost counterpulse circuit. No additional capacitance is needed beyond that required for the energy transfer circuit and one dV/dt capacitor per module. With

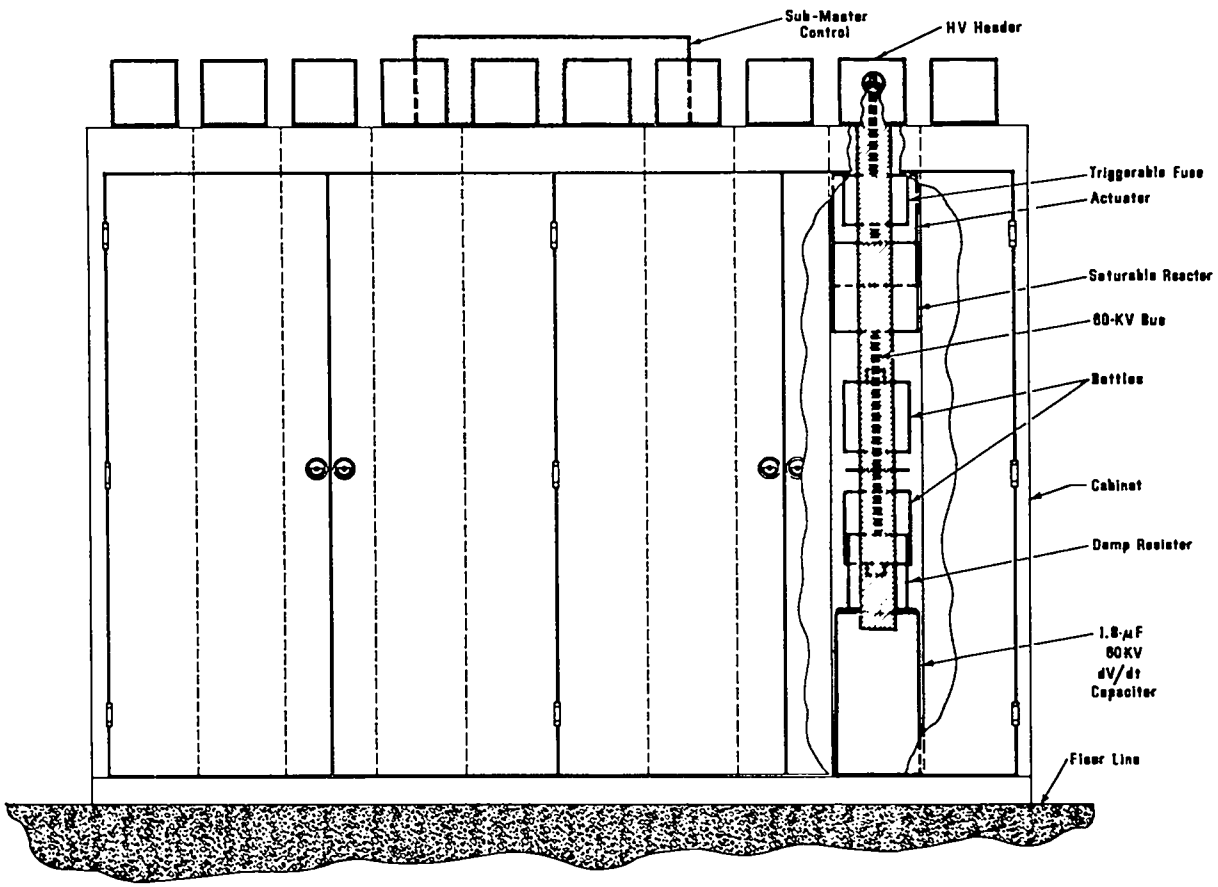

Fig. 5.4-10.
Interrupter module.

this large capacitance, a minimal counterpulse energy is required.

The transfer capacitors (Fig. 5.4-5) are reverse-charged to several kilovolts before the energy transfer cycle. The capacitor discharge ignitron switch is closed when the 26-kA storage current is flowing in the storage coil and interrupter branches of the circuit and when the interrupter has been mechanically opened and is arcing. Because the inductive impedance of the interrupter leg is negligible compared to the storage coil and compression coil branches, virtually all of the capacitor discharge current flows into the interrupter, bucking the 26-kA dc current. The interrupter current drops rapidly to the 1-kA level when the saturable reactor becomes unsaturated, forcing a lower dI/dt as the current approaches I = 0.

As the current goes through I = 0 the interrupter stops conducting. The arc begins to deionize, and ~50 μs are required to reestablish vacuum dielectric strength. During this time, large voltage transients would cause arc restrikes. A small dV/dt capacitor is placed across the interrupter to absorb the counterpulse circuit over-current following the I = 0 transition, thus limiting the reverse voltage transient. The damping resistor quenches the high frequency parasitic voltage oscillations impressed on the interrupter by the saturable reactor and dV/dt capacitor.

A saturable reactor is used instead of a standard inductor to further minimize the required counterpulse energy and, hence, the reverse voltage applied to the transfer capacitors. High values of dI/dt can be tolerated by the interrupter until close to the I = 0 interruption and deionization time. The detailed physics of the arc plasma interruption process sets limits on the dI/dt near I = 0, the quiescent recovery time, and the dV/dt following I = 0. The stray inductance of the counterpulse loop will limit dI/dt to less than 1 kA/μs until near I = 0 when the saturable reactor comes out of saturation. The large inductance of the saturable reactor at low current will limit the dI/dt to less than 100 A/μs as the current goes through zero, within the ideal range for vacuum interrupter reliability. Since the counterpulse circuit has large inductance only near I = 0, the energy required from the transfer capacitor is minimal.

Typical rates of recovery voltage for vacuum breakers are in excess of 1 kV/μs. The maximum rate of recovery voltage following interruption within the METS energy transfer circuit is 95 V/μs on each vacuum breaker. It is extremely unlikely that an arc restrike would occur with the METS voltage waveform.

The dV/dt capacitor is a standard Scyllac 60-kV capacitor of 1.8-μF value. This size represents less than 2% of the transfer capacitor size, and the capacitors are readily available. The capacitor will hold the voltage on the breaker during deionization below several kilovolts even with a 1-kA excess counterpulse current beyond I = 0.

Research on vacuum interrupters at the 12.5-kA, 30-kV level indicates that the damping resistor is not necessary. The final determination will be made by reliability testing. So far, the characteristic parasitic oscillation of 500-V amplitude has not caused a single loss of interruption.

5.4.3.6 Compression Coil

The compression coil which provides the magnetic field for adiabatic heating of the theta-pinch plasma is in the form of many small pancake coils made from copper strap insulated with layers of epoxy and fiber glass. Each pancake coil is energized by a separate module of the METS system to provide the magnetic field for 20 cm along the toroidal discharge tube. Each pancake coil is actually a so-called "split-pancake" coil, i.e., it is made of two coils, one wound clockwise and the other counterclockwise with an electrical connection at the inside turns. Thus, all other electrical connections can be conveniently brought to the surface at the outer turns of the two coils of the split pancake. Each pancake coil has 18 clockwise and 18 counterclockwise turns.

Insulation of the coils will be conservative. A thickness of 1.5 cm of epoxy-fiber glass will insulate the clockwise from the counterclockwise turns within each pancake, and 1.0 mm of epoxy will be vacuum impregnated into fiber-glass cloth between turns. The insulation thickness along the outside radius and along the side of the pancake containing the high voltage terminal will be 1.5 cm, whereas insulation thickness on the inside radius and low voltage side need be only 0.75 cm to stand off half the peak voltage.

Radiation damage effects to the insulation after several years of operation under pessimistic dose rates are still well within the levels found tolerable for use in high-energy particle accelerators. The average hoop stress on the coil at 5.5 T, including dynamic stress, is only $4.82(10)^7$ Pa (7 kpsi), which puts half-hard OFHC copper below the fatigue endurance limit by at least a factor of 2. Additional support will be provided from the epoxy-fiber glass insulation.

Average dimensions of a completed pancake coil with epoxy-fiber glass insulation are 34 cm i.d., 55.7 cm o.d., and 14.8 cm length. The copper strap used in the conductor is 3.8 mm thick and 5.5 cm wide. Energy stored in each compression coil amounts to 345 kJ, including the field energy stored outside the bore in the windings and gaps between coils.

The compression coil must be shaped to follow the dimensional variations of the shock heating coils which themselves are shaped to provide the multipole fields for plasma equilibrium. These multipole fields will alter the plasma surface while still maintaining its cross section as a circle. The center of this circle describes a helix along the toroidal discharge tube, with a wavelength of 3.2 m. Relationships between the flux surfaces at the plasma edge and the inner surface of the compression coils have been derived.[2,3]

For the present choice of plasma parameters, the amplitude of the radial modulation δ_0 of the flux surface at the compression coil is 0.7 cm, while the radius of the helical modulation δ_1 is 3.1 cm. Incorporation of these spatial modulations into the compression coil complicates its construction only minimally. Several mandrels of different sizes will be needed for winding the pancake coils, and each successive pancake will need to be offset radially from its neighbor by about 7.0 mm.

Table 5.4-5 is a summary of the compression coil design parameters.

TABLE 5.4-5

SUMMARY DESCRIPTION
OF COMPRESSION COIL DESIGN

Parameters of Pancake Coils	
Type of coil	Split pancake
Mean outside diameter	55.8 cm
Mean inside diameter	34.0 cm
Length	14.8 cm
Number of turns	36
Magnetic field	5.5 T
Peak voltage	60 kV
Peak current	24.3 kA
Total inductance	1.10 mH
L/R decay time	0.27 s*
Amplitude of δ_0 modulation	0.7 cm
Amplitude of δ_1 modulation	3.1 cm
Copper conductor width	5.5 cm
Conductor thickness	3.8 mm
Stored energy	345 kJ
Materials Required	
Total number of pancake coils	1280
Copper for each coil	92.6 kg
Epoxy for each coil	9.84 ℓ
Total mass of copper	1.18×10^5 kg
Total volume of epoxy	$1.25(10)^4$ ℓ

*0.25 ms when connected to crowbar circuit.

5.4.3.7 Fast and Slow Compression Coil Crowbar Switches

The crowbar switches used in the system transform the L-C-L METS transfer circuit to an L-R circuit with an L/R ≥ 250 m. This is accomplished by shorting (crowbarring) the compression coil at time of peak current in the compression coil with a dual ignitron, metal-to-metal switch design. The ignitrons are arranged to carry the initial current (fast compression coil crowbar switch) and a metal-to-metal type switch to carry the final total current (slow compression coil switch). An attempt is being made at LASL to increase the coulomb rating of the commercial-size D ignitron so that the ignitrons will be able to withstand the maximum coulomb load possible during the L/R decay cycle.

The critical operating parameters of the crowbar ignitron are to maintain 26 kA for a 10-ms L/R time, which is equivalent to 250 C, and to withstand a pulse voltage of 60 kV. Single ignitrons have been tested as 400-C, 15-kV, 2-mΩ switches; hence, a series arrangement of ignitrons will suffice to provide the necessary crowbar switch. Each compression coil module will have four ignitrons arranged in series and installed to fire automatically through solid state rectifiers in series with each of the ignitron igniters. The header will be designed so that the crowbar can be applied directly across the compression coil for single coil operation; and, with minor reconnection, the crowbar can connect the compression coils in a series or loop mode if this proves to be the desired circuit. The metal-to-metal crowbar will be a commercially available switch capable of closing within 10 ms, withstanding the SFTR 60-kV pulse voltage, and carrying the 25-kA current with a contact resistance of 100 μΩ.

5.4.3.8 Charging Power Supply for Storage Coils

The METS storage coils will be charged to 26 kA in 300 s by using a 125-V, 26-kA, dc power supply. The power supply probably will consist of a 13.2-kV/480-V distribution transformer, 480-V contactor, 6-ϕ Y-Y transformer and three modules, 125 V and 9 kA SCR each. The duty cycle will consist of 300 s charge and 600 s off in the most optimistic mode. The control system shall permit remote operation from a central control area and shall provide current and voltage regulation in a flexible manner so that maximum current output and rate of charging each storage coil can be monitored and adjusted. The power supply is to be connected to the storage coil through a normally open charging switch. The charging switch is to be connected in parallel with an

electrolytic dump resistor capable of absorbing the stored energy in the event of a power failure or a desire to dump the stored energy. The normally open switch would be closed while the system is being charged, and would open only under emergency situations.

As is characteristic of charging superconducting storage coils, the circuit resistance is a low value consisting primarily of dc bus resistance and some lead resistance. The load inductance is quite high with L storage = 1.4 H, and the maximum voltage rating is determined by the rate of change of load current and load inductance; therefore $\dot{I}$ = 26 kA/300 s = 86.7 A/s and V = L$\dot{I}$ = 1.4 x 86.7 = 121 V. A power supply rated at 125 V and 26 kA will supply the requirements with some spare capacity and the total 121 V x 26 kA = 3.1 MW peak will not exceed the power distribution system capabilities. In addition, typical charging characteristics of superconducting systems call for a higher $\dot{I}$ initially, with a decrease in $\dot{I}$ at the end of the charging period. This will permit a substantial decrease in the peak current power, particularly if the power supply is designed to have a voltage rating as high as 200 V for the early charge period.

The operating sequence of the power supply consists of closing the contactor and energizing the rectifier with an input voltage determined by the preset charge rate and maximum loadsettings. While the load coil current increases, the controller will automatically decrease output voltage until the preset current level is achieved. At that time the power supply output voltage will be only a few volts—enough to offset the IR drop of bus and lead resistances. The charge complete signal will be transmitted upon achieving the preset current level and within 10 s the firing sequence will be initiated. After a normal shot the contactors will open and the power supply and controller will be reset for the next shot. In the event of a delayed test, the current can continue to circulate in the charging loop for many hours, limited to the L/R decay time (15 h) of the charge loop. As mentioned previously, the system energy can be dumped more rapidly by opening the charging switch, thereby inserting the dump resistor in series with the storage coils.

5.4.3.9 Counterpulse Storage Power Supply

The counterpulse storage power supply consists of one or two capacitor charging supplies carried over from the Phase I system as described in Sec. 5.4.1.

Approximately 10 MJ total energy must be supplied to the transfer capacitor banks for the counterpulse energy. The energy is delivered in 300 s during the same period that the superconducting energy-storage system is charged. Whenever a fault occurs during the energy-storage ramp and a fast dump is required, the counterpulse circuit is set with the proper reverse voltage for current interruption.

A 50-kW power supply with 10-kV rating at 5 A is adequate to charge all transfer capacitor banks in parallel. Remote programming will be required to make the charging voltage follow the energy-storage current.

5.4.3.10 Capacitor Transfer Bank

The METS capacitor transfer bank is used primarily to provide for efficient energy transfer from the METS storage coils to the load coils. The bank serves the secondary purpose of providing an energy source for the counterpulse circuit (see Sec. 5.4.3.5). A description of the bank is given in Sec. 5.4.1. The main difference between Phase I, where the transfer bank is the primary energy source, and Phase II, where the METS storage coil is the primary energy source, is the connection scheme of the capacitors. Utilized as the transfer bank with total C = 0.13 F, energy = 230 MJ, each of the 1280 capacitor modules consists of 16 each, 15-kV, 100-μF capacitors with a total C = 100 μF per module. The capacitors are arranged in a 4 series by 4-parallel array and the module is connected to the transfer circuit through the counterpulse trigger and bidirectional current switch. The capacitor module is charged by the storage coil during the 0.7-ms energy transfer pulse from storage coil to load coil. The module is charged to a maximum of 60 kV during that pulse and the peak energy stored is 180 kJ. Energy-storage capacitor banks have been used successfully for many years in LASL's CTR program, and experience with relatively large banks has shown that the total energy required per module is well within state-of-the-art techniques.

5.4.3.11 Electrical Leads

Two basic types of electrical leads will be required in the METS system: 128 pairs of 26-kA continuous duty leads and 1280 coaxial-type 26-kA pulse leads. The 26-kA continuous duty leads will connect the bus of the storage coil charging power supply (see Sec. 5.4.3.8) to the storage coils and provide interconnection between storage coils and their adjacent dewars. To carry the rated 26 kA in a continuous mode, the leads will necessarily be rather large. The 26-kA coaxial pulse leads are much smaller; however, the relatively large number of pulse leads required for the complete system introduces a significant source of heat load. The pulse leads connect each storage coil module with coaxial cables to

the corresponding HVDC interrupter. An additional lead complication for the system is the fact that the pulse leads will be required to withstand a 60-kV, 0.7-ms pulse during the discharge sequence. This high voltage pulse introduces dielectric problems that are considered in the lead design.

A. 26-kA Continuous Duty Lead: These leads will be similar to commercially available leads to 10-kA current ratings. Each consists of a cylindrical conductor with a number of small-diameter cooling channels running the length of the conductor. The bottoms of the cooling channels are located above the liquid helium level and the helium gas is directed upward through the channels and out the top of the lead where it is collected and returned to the refrigerator system. The heat load of these leads is 43 W per pair at the liquid helium level. A computer program has been used in the design of these leads to consider the steady-state heat transfer and fluid flow for evaluating the temperature and pressure profiles.

B. 26-kA, 60-kV Pulse Leads: These leads will be coaxial to limit the number of dewar penetrations and to limit the amount of mechanical stress present with conventional parallel leads. Figure 5.4-11 is a representation of the pulse lead. Note that the center portion of the lead carries the 60-kV pulse and that it is cooled by helium gas flowing through the center of the lead. It is surrounded by a dielectric medium that prevents voltage arcing to the outside return lead. Consideration must also be given to possible voltage tracking across the dielectric both at the lower end of the lead in the helium gas and at the upper end; therefore, special attention is given to providing a rather lengthy tracking path between the two leads. Any frost problem will be eliminated by adequate insulation in the upper region. The outer lead is cooled by passing helium gas around its outside through the channel between the outer lead and outer membrane. The upper portion of the lead is designed to connect to an adjacent coaxial header for direct coaxial cable routing to the dc interrupter.

The refrigeration heat load from each of these leads is calculated to be 0.5 W at the liquid helium level. Most of the heat load results from the fact that the lead is connected to the storage coil permanently, and the heat conduction along the lead from room temperature to the liquid helium is far greater than any joule heating experienced during pulsed operation.

A computer program has also been used in the design of the pulse leads to consider the transient heat transfer and fluid flow to determine the transient temperature profiles.

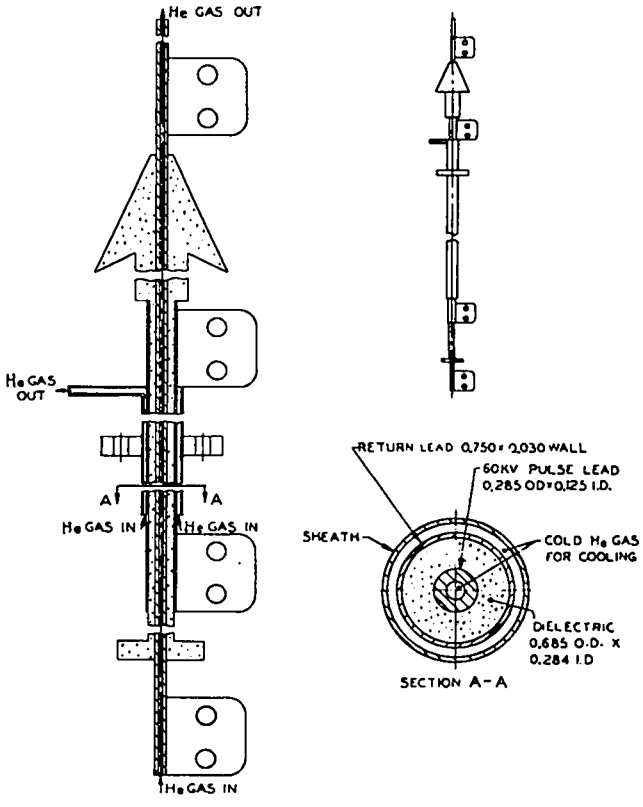

Fig. 5.4-11.
A 60-kV, 26-kA coaxial pulse lead.

5.4.3.12 Component Connections and Cabling

Most of the interconnections to be made in the METS system from the storage coil through the compression coil will be accomplished by the use of high voltage, pulsed-type coaxial cable. The types of coaxial cables proposed were developed for use in the LASL CTR program and consist of RG 17/14 and RG 19 cable. Bus-type interconnections will be used only on the dc charging system connecting the METS power supply with the storage coil modules and the final connections of slow crowbar to compression coil.

The entire METS circuit can be separated into five primary interconnection modes: (1) storage coil to HVDC interrupter, (2) HVDC interrupter to transfer capacitor bank, (3) transfer capacitor bank to fast crowbar switches, (4) fast crowbar switches to slow crowbar switches, and (5) slow crowbar switch to compression coil. The schematic of Fig. 5.4-5 shows that each of the five interconnections has a different purpose and duty cycle.

1. Storage coil to HVDC interrupter: The cabling required for this connection must necessarily be of

low resistance and inductance because the energy dissipated in the arc that is initiated during the opening of the cryogenic disconnect is a function of the resistance and inductance in the storage coil to interrupter loop. These cables are also in series with the pulsed leads and must ordinarily be able to carry a 26-kA, 100-ms pulse without appreciable temperature rise. The most practical, lowest inductance 60-kV pulsed cable is RG 17/14. A total of 17 parallel RG 17/14 cables per storage coil is required to prevent a temperature rise per charge cycle of more than 15°C.

2. HVDC interrupter to transfer capacitor bank: This connection requires a minimum amount of cabling in terms of current-carrying capacity. Under normal operating conditions, current will be carried for the relatively short transfer time of 0.7 ms. These cables must also carry the counterpulse current of 26 kA for 100 μs. Thus the 26 kA for 0.7 ms is the controlling requirement and can be handled by four RG 17/14 cables. The use of RG 17/14 cables is proposed because of their unique fusing characteristics. Under fault conditions they can be used as a fuse to protect the circuit.

3. Transfer capacitor bank to fast crowbar switches: The conductor function is similar to that described in the previous section except that it does not carry any counterpulse current.

4. Fast crowbar switches to slow crowbar switches: The cabling for this section must have a large L/R ratio to provide for the longest possible decay in the crowbarred compression coil loop. In addition, the cable must be capable of providing satisfactory current terminating characteristics for the large coulomb capacity of the crowbarred section. The RG 19 cable has these capabilities. The RG 19 cable with an L/R ratio = 8.87×10^{-5} is approximately two and one-half times better than RG 17/14 with an L/R ratio = 3.64×10^{-5}. Only eight RG 19 cables are required for the crowbar section; consequently, fewer cell wall penetrations are needed.

5. Slow crowbar switches to compression coil: This connection will be accomplished with a commercial aluminum bus, 0.5 cm x 25 cm x 4.6 m long, to provide for a negligible L/R decay factor when compared to the L/R of the compression coil itself. For each of the 1280 runs, L = 45 nH and R = 0.2 mΩ.

Table 5.4-6 summarizes cable requirements for each section.

TABLE 5.4-6

INTERCONNECTION MODE PER COMPRESSION COIL MODULE

Item	Storage Coil to HVDC Interrupter	HVDC Interr. to Transfer Capacitor Bank	Transfer Capacitor Bank to Slow Crowbar	Fast Crowbar to Slow Crowbar
Type of cable	RG 17/14	RG 17/14	RG 17/14	RG 19
Load requirement	26 kA-100 ms	26 kA-1 ms	26 kA-1 ms	26 kA-10 ms
Number of parallel cables	17	4	4	8
Temperature rise per pulse (°C)	15	2.7	2.7	6.8
Fusing time for 26 kA (s)	3.6	0.2	0.2	3.9
Total length of cable per module (m)	18.3	4.9	3.7	3.7
Resistance and inductance equivalent of run	3.9 mΩ 141 nH	4.4 mΩ 160 nH	3.3 mΩ 160 nH	1.46 mΩ 129 nH
Total length of cable for entire METS system (m)(excluding the capacitor intercapacitor cabling	438 000	27 500	20 600	41 200

5.4.3.13 Dewars

A series of 128 cylindrical, epoxy-fiber glass dewars will provide the 4.5 K environment for the superconducting magnetic energy-storage coils and the associated cryogenic disconnects. The dewars will be located at a major radius of 57.2 m and will accommodate 1280 coil-cryogenic disconnect pairs (10 pairs per dewar). Each dewar will have a pressure rating of 5 atm.

The details of a storage coil dewar are shown in Fig. 5.4-12. The dewar walls and lid are constructed of fiber glass-reinforced epoxy. The selection of a specific resin system and a specific reinforcement configuration depends to some extent upon the process used to manufacture the structure, which in this case is filament winding. There are other structural material requirements such as the dewar lids and vacuum pumpout ports, the construction of which is not amenable to the filament winding technique. These parts will be machined from flat laminates (NEMA G-10) made of epoxy-fiber glass cloth. The resin system (see Table 5.4-7) chosen for filament winding of the cylindrical dewar vessels was developed by Soffer and Malho[4] and modified by Westinghouse.[5]

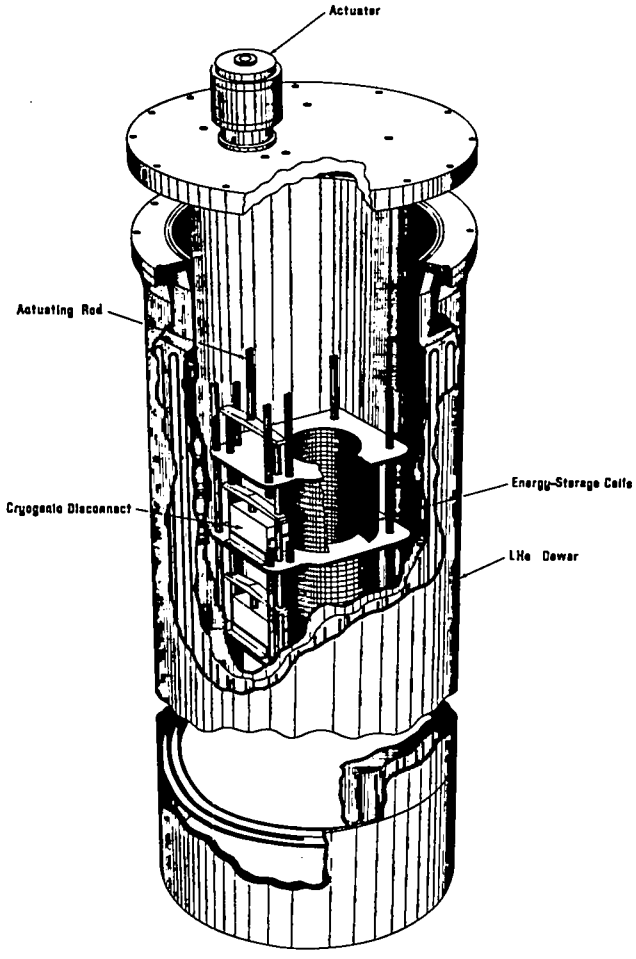

Fig. 5.4-12.
A 10-coil dewar assembly.

The two types of glass fibers that may be considered for use in this application are E-glass and S-glass. S-glass has about 30% higher strength and 20% higher modulus than E-glass. S-glass is used for critical aerospace applications, is made under highly controlled conditions, and is, therefore, about 3 to 4 times as expensive as E-glass. A commercial version of S-glass known as S-2 glass is also available but is not manufactured under the exacting quality control conditions of S-glass; nor does it have the high performance finish of the S-glass.

The glass chosen for this application is S-904. It has a high performance finish which acts as a wetting agent for the epoxy and which is neither temperature nor humidity sensitive. It is particularly useful for slow winding operations.

The basic dimensions of each dewar are 1.07-m i.d. by 6.96-m depth. The depth of liquid helium above the top coil is regulated to 0.1 ± 0.025 m and the ullage space is 0.61 m in depth. Several phenolic shields are placed in the ullage volume to disrupt natural convection currents between the liquid helium surface and the warm lid and to act as thermal radiation barriers. The 10 coils in each dewar will be placed over an epoxy cylinder which will be an integral part of the inner shell. This cylinder will reduce the helium inventory.

An 80 K shield is located between the inner and outer vacuum walls. It is tied thermally to the inner shell at a point 0.3 m from the top and consists of several layers of etched conductor on a plastic substrate. The layers are separated to prevent field coupling and eddy current losses during coil pulsing. Three layers of overlapping but not continuous superinsulation (0.00635-mm-thick Mylar aluminized on one side) are placed on the outside of the inner vessel to improve the emissivity and to minimize the radiation heat load from 80 to 4.5 K.

Two levels of heat interception are available: one at 80 K by gaseous helium and the other at 4.5 K by liquid helium. The 80 K steady-state heat loads in the dewars are summarized in Table 5.4-8.

The 4.5 K steady-state heat loads to the liquid helium in the dewars are summarized in Table 5.4-9.

In addition to the steady-state heat loads, load factors result from the pulsed operation of the system at the 4.5 K refrigeration level. To determine these loads, it was assumed that one charge and discharge cycle occurred every 900 s and that each cryogenic disconnect had a power loss of 24 W when carrying 26 kA. Table 5.4-10 summarizes the pulsed 4.5 K refrigeration requirements. The heat loads in the table have been averaged over the 900-s cycle

TABLE 5.4-7

DEWAR RESIN SYSTEM

Constituent	Supplier	Composition of Constituent Parts by Weight	Function
DER 322	Dow Chemical Co.	100.00	Base epoxy resin: diglycidyl ether of bisphenol-A
Dodecanyl Succinic Anhydride	Allied Chemical Corp.	115.9	High molecular weight curing agent
Empol 1041	Energy Industries, Inc.	20.0	For flexibility: trimer acid
Benzyldimethylamine	Miller-Stephenson Co.	1.0	Catalyst

TABLE 5.4-8

80 K STEADY-STATE DEWAR REFRIGERATION REQUIREMENTS

	Single Dewar (W)	128 Dewars (W)
Radiation from the warm walls and lid	273	34 944
Transfer lines	0	318
Total	273	35 262

TABLE 5.4-9

4.5 K STEADY-STATE DEWAR REFRIGERATION REQUIREMENTS

	Single Dewar (W)	128 Dewars (W)
Wall conduction 80 to 4.5 K	1.8	226
Radiation from the walls 80 to 4.5 K	1.0	128
Radiation from the lid	6.0	768
Continuous leads conduction	42.5	5440
Instrumentation	0.6	77
Support structures	0.3	38
Fill, blowdown, and vent lines	2.6	333
Pulsed leads	4.8	614
Total	59.6	7624

TABLE 5.4-10

4.5 K PULSED REFRIGERATION REQUIREMENTS

	Single Dewar (W)	128 Dewars (W)
Pulsed leads above liquid surface	9.8	1254
Pulsed leads below liquid surface	1.8	230
Continuous leads joule heating	0.08	10
Cryogenic disconnect joule heating	26.2	3354
Cryogenic disconnect opening losses	16.7	2138
0.3% electromagnetic losses	12.7	1627
Total	67.3	8613

time and have assumed 10 coil-cryogenic disconnect pairs per dewar. The pulsed leads are coaxial, with one per coil.

The liquid helium evaporated at the 4.5 K level is a valuable contributor to refrigeration because of the high value of $C_p \Delta T$ between 4.5 K and 300 K, i.e., 1486 J/g, as compared to its heat of vaporization of 20.4 J/g. It is, therefore, used to cool the continuous and pulsed leads. The total heat deposited in a pulsed lead during a pulse is 60 500 J maximum. The average power over the 900-s cycle period is 68 W. The system is designed so that 90% of this power is absorbed by warming helium gas as it passes through the leads, and 10% of this power manifests itself as an additional 4.5 K refrigeration requirement.

All items placed within the dewar are to be mounted from the lid to facilitate assembly. The major components are the coils and cryogenic disconnects. NEMA G-10 epoxy-fiber glass is to be used for support structure for these items. The pulsed electrical leads will be coaxial and superconducting below the liquid helium level. Each will terminate opposite the coil to which it attaches.

Each dewar will be provided with a 0.33-m vent sized to handle the helium gas evolved from the failure mode in which all 10 of the storage coils go normal and deposit their full 3.9 x 10^6 J of stored energy in the liquid helium. Other penetrations through the lid include the pulsed and continuous leads, liquid helium fill line, instrumentation feedthroughs, and the actuator drive mechanism for the cryogenic disconnects.

Each dewar is equipped with appropriate safety relief valves and/or rupture discs on both the liquid and vacuum spaces.

5.4.3.14 Liquid and Gas Distribution Systems

Liquid helium must be provided to each of the 128 coil dewars. In addition, a helium recovery and purification system is required. Liquid helium storage dewars will provide a total capacity of 500 000 *l*—equal to the total capacity of the coil dewars—and will be used to maintain the helium inventory as described in Sec. 5.4.3.17.

The liquid helium will flow through vacuum-jacketed, 38.1-mm-i.d. transfer lines through individual dewar control valves and into the dewars. The liquid level in the individual dewars will be controlled by carbon resistor level sensors whose output will control the position of the feed valves. The 4.5 K transfer line refrigeration requirements are summarized in Table 5.4-11.

Evacuation and backfill purges will be used to reduce the size of the required gas purification system. With this procedure the purification system will have to accommodate only the small leakage of

TABLE 5.4-11

4.5 K TRANSFER LINE REFRIGERATION REQUIREMENTS

Item	Heat Load (W)
Line radiation	314
Joints, valves	717
Refrigerator in-line liquid helium storage	33
Total	1064

impurities into the helium system during normal operation.

A summary of the transfer line parameters is given in Table 5.4-12.

5.4.3.15 Application of Refrigeration

To apply the refrigeration from the helium refrigerators to the storage coil dewars under steady-state conditions is routine and typical of standard practice in the cryogenic industry. However, the transient heat loads arising from heat generation in the pulsed leads, from operation of the cryogenic disconnects, and from the 0.3% electromagnetic losses complicate the system.

Varying the rate of refrigeration in the refrigerators would be undesirable and difficult to execute. The pulses should be accommodated with as little disturbance as possible to either the refrigerator or the dewar refrigeration balance.

A large reservoir for absorbing the pulsed heat load exists in the liquid helium inventory within the dewars. The liquid inventory per dewar at operating conditions is 3900 *l*. If, during a pulse, the liquid is permitted to warm to a temperature of 5.16 K (2.2 atm) from 4.22 K (1 atm), 6 MJ would be absorbed without vaporization. This compares to 0.06 MJ generated in each pulse and 3.8 MJ that would be released should all 10 coils in a dewar go normal and release all of their stored energy to the liquid helium. The probability of the coils releasing all of their stored energy to the liquid helium is very small because a safety circuit will pulse the stored energy to an external load if any coil begins to go normal.

In this analysis it is assumed that most of the heat generated in the pulses results in the immediate vaporization of liquid helium because bubbles of gaseous helium will rise through the liquid with little condensation. Approximately 20% of this heat is assumed to remain in the coil and surrounding liquid and will be withdrawn as vaporized helium before the next pulse. Because most of the gas is generated rapidly, it will not absorb much heat as it passes out of the dewar, and thus it will be returned cold to the appropriate heat exchanger in the refrigerator through the vacuum-jacketed transfer lines.

TABLE 5.4-12

TRANSFER LINE PARAMETERS

Purpose	Insulation	Pipe Size (mm i.d.)	Total Length (m)
1. Liquid helium from the refrigerator to the coil dewars:			
Main distribution	LN_2 traced, vacuum	38.1	371
Feeders to each dewar	LN_2 traced, vacuum	12.7	117
2. 5 K gaseous helium return line to refrigerator:			
Feeders from dewars	LN_2 traced, vacuum	12.7	117
Collection header	LN_2 traced, vacuum	63.5	371
Header to surge tank	LN_2 traced, vacuum	63.5	5.3
Surge tank to refrigerator	LN_2 traced, vacuum	38.1	8.0
3. 300 K gaseous helium return line:			
Feeders from dewars	none	12.7	117
Collection header	none	101.6	371
Header to refrigerator	none	127.0	10.6

5.4.3.16 Refrigerator Design

The helium liquefier refrigerator will provide 3045 kg/h of liquid helium. All of the helium vaporized as a result of the steady-state heat load will be returned as warm gas to the compressors, and in this respect the unit will operate as a liquefier. The gas evolved as a result of the current pulse will be returned to an intermediate heat exchanger at a temperature of 25 K or less.

The refrigerator for this application is much larger than any equipment in existence. At present, the largest systems are liquefiers with a capacity of 1000 *l* of liquid helium per hour.

When designing a liquefier-refrigerator of this size, it is important to use commercially available components, the three most important of which are the compressors, expanders, and heat exchangers.

The *compressors* chosen are three-stage, nonlubricated, reciprocating machines with balanced horizontally opposed cylinders. Each cylinder is equipped with a double rod seal to reduce the leakage of helium gas from the machine and to return this gas through a small purification system to the main process stream. The total required compressor input power is 12 MW. One backup compressor will be installed to permit maintenance on the other compressors while maintaining full refrigerator capacity.

The *expansion engines* used in the refrigerators will be centripetal, gas bearing turbines. In these machines half of the enthalpy drop of the gas occurs in the nozzles and the other half in the wheel. The machines are designed such that the velocity of the gas at the exit of the nozzle does not exceed the speed of sound. For steady-state operation with pulsing once every 900 s, expanders 1 and 2 (Fig. 5.4-13) will be operating at a pressure ratio of approximately 2.8, well below the theoretical maximum value of 5.6 calculated from ideal gas considerations. Expander 3 will be operating near the maximum pressure ratio value and its operation will not be optimum. At reduced output the machines will operate at decreased efficiency. Under certain conditions it may also be possible to bypass one of the expanders.

The heat exchangers are not large by commercial standards and will be of the plate-fin type shown in Fig. 5.4-14. They are considerably cheaper than any other type of heat exchanger that might be used.

The basic refrigeration process is shown in Fig. 5.4-13. The process points with significant fluid properties are listed in Table 5.4-13. The following points should be noted.

1. Liquid nitrogen is used to provide refrigeration at the 80 K level.

2. Refrigeration generated by expanders 1 and 2 can be varied by changing the pressure ratio across the expanders. This is done by varying the speed of each machine.

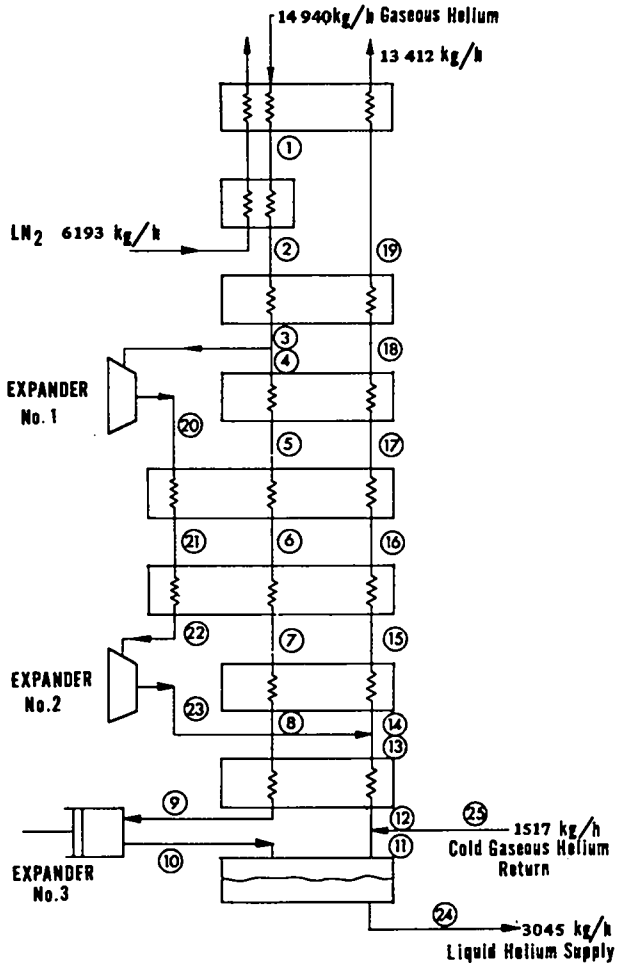

Fig. 5.4-13.
Schematic of refrigerator.

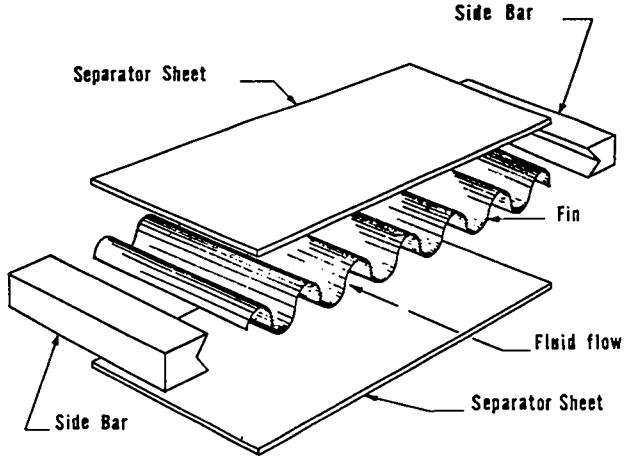

Fig. 5.4-14.
Plate-fin type heat exchanger.

TABLE 5.4-13

REFRIGERATION PROCESS POINTS

	Flowrate (kg/h)	P (atm)	T (K)	Enthalpy (J/g)
1	14 940	12.4	91.0	491.1
2	14 940	12.4	81.4	413.7
3	14 940	12.3	36.9	204.7
4	7082	12.3	36.9	204.7
5	7082	12.2	31.7	177.4
6	7082	12.1	23.6	132.6
7	7082	12.1	14.2	77.0
8	7082	12.0	12.3	64.8
9	7082	12.0	7.9	31.4
10	7082	---	---	---
11	4037	1.40	4.6	29.6
12	5554	1.40	4.6	29.6
13	5554	1.38	11.5	72.1
14	13 412	1.38	11.5	72.1
15	13 412	1.34	12.6	78.6
16	13 412	1.32	23.6	136.6
17	13 412	1.31	31.5	177.9
18	13 412	1.28	34.2	192.3
19	13 412	1.25	79.1	425.2
20	7858	4.05	31.5	177.6
21	7858	4.03	24.3	140.4
22	7858	4.01	15.5	91.5
23	7858	1.38	11.5	72.1
24	3045	1.40	4.6	11.9
25	1517	1.40	4.6	29.6

3. Expander 3 is shown as a reciprocating expander; however, fluid conditions at the inlet and discharge are such that a turbine expander would be suitable.

5.4.3.17 Utilities, Cryogen, and Gas Supplies

Electrical Requirements. The electrical power required to produce full refrigeration capacity is estimated to be 11 965 kW, as shown in Table 5.4-14.

In addition to the normal unit electric power cost of approximately $0.0085/kWh, a special monthly demand charge of $2.55/kW will be levied. Therefore, if the facility is run only one day in a billing month, the additional demand charge will be $30 510. To avoid this extra levy, it would be practical to establish a demand monitoring and indicator meter so that operators could limit the power level.

Cooling Water Requirements. A cooling water system will be necessary to reject the heat generated by the helium compressors and other auxiliary equipment. A cooling water system was sized by using two prepackaged mechanical draft cooling towers as shown in Fig. 5.4-15. These towers are constructed of galvanized steel and induce flow from the bottom to the top of the tower, counter to the water flow. These modular units meet normal fireproof ratings and are shipped in modular form, which minimizes field fabrication time. Each modular cell is equipped with a 37.3-kW, 50-hp fan and has an integral pump.

TABLE 5.4-14

ELECTRICAL POWER REQUIREMENTS FOR FULL REFRIGERATION

	(hp)	(kW)
Helium refrigerator compressors	15 600	11 633
Cooling water system	350	261
Purification system	30	22.2
Miscellaneous	65	48.5
Total	16 045	11 964.7

The units required for this installation were sized to accommodate a 11.1°C (20°F) temperature rise for 44.4°C (80°F) water with a wet bulb temperature of 36.7°C (66°F), which corresponds to summertime conditions in Los Alamos. Two 18 925-//min (5000-gpm) pumps would be required to attain the maximum capacity of the tower modules. Thus the power requirements for this system would include 149.6 kW (200 hp) for the fans and another 112.0 kW

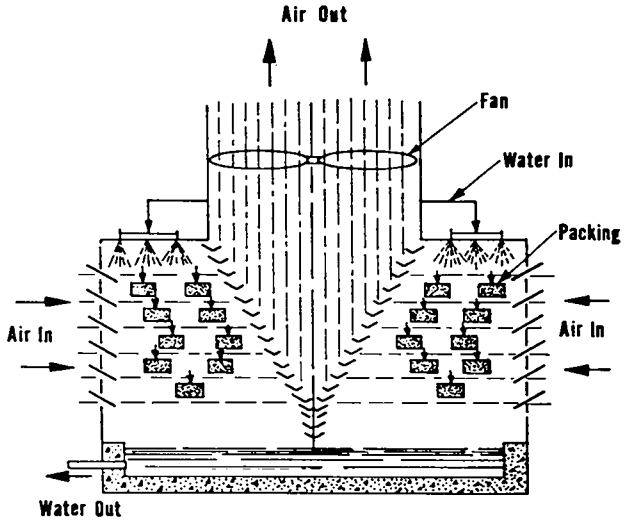

Fig. 5.4-15.
Cross flow cooling tower.

(150 hp) for the circulating pump, for a total of 261.6 kW (350 hp).

Makeup water will be required to replace that lost by evaporation, from drift, and by blowdown. The periodic draining (blowdown) of water from a cooling tower is necessary to prevent buildup of insoluble minerals and chemicals that eventually coat the tube walls and cause corrosion in heat exchangers of the tower basin. At the minimum heat load, the total water makeup will be approximately 511.0 //min (135 gpm).

Nitrogen System. Large quantities of liquid nitrogen will be required for the helium refrigerators and incidental quantities for the purifiers, helium storage tanks, and primary dewar. The highest consumption will occur during plant cooldown and coil pulsing.

The maximum usage rate, 7733 //h (2043 gph), can be met by either on-site production or direct purchase of nitrogen from large industrial gas producers.

Liquid nitrogen is produced concurrently with oxygen in air separation plants, few of which produce more than 120 tons/day. Most have committed at least 80% of their capacities and usually can only meet short-duration demands by careful advance scheduling.

Liquid nitrogen is transported by railcars of 39 364-/ (10 400-gal) capacity or by over-the-road tankers capable of hauling up to 22 710 / (6000 gal). For our purposes, tankers would probably be the preferred carrier.

To obtain the maximum desired quantity of 7733 //h (2043 gph) the following logistics must be considered. Assuming that a tanker requires at least 32 h for a round trip, five tankers would have to unload every 24 h to supply 185 592 //day (49 034 gal/day), and the supplier would have to commit at least 10 tankers to the job. Also, because of the uncertain timing of the tests, it is unreasonable to expect a supplier to stand by for delivery of such large quantities.

The alternative is to purchase the product in more conventional quantities and store enough to make a complete test run. On two weeks' notice, a delivery rate of 60 tons/day would be reasonable to expect. Therefore, two 378 500-/ (100 000-gal) tanks would store enough nitrogen for 4 to 5 days of normal operation. Three types of liquid nitrogen storage tanks are available: shop-fabricated units with capacities up to 189 250 / (50 000 gal), field-erected flat-bottomed tanks, and field-erected spherical or pressure tanks. The most economical tank would be a flat-bottomed field-erected tank provided by concerns such as Chicago Bridge and Iron Co. or Graver Tank.

Instead of buying liquid nitrogen, one can recover and reliquefy warm nitrogen gas by using a system consisting of a 2982.8-kW (4000-hp) compressor, a 223.7-kW (300-hp) Freon system, a cold box 2.438 m (8 ft) by 2.438 m (8 ft), and 12.192 m (40 ft) high, and a 151 400-/ (40 000-gal) storage tank. The installation cost for such a system, exclusive of the storage tank, would be approximately $1M. The operational cost would be in the range of $0.0052// ($0.02/gal) without considering the power demand. If the system were run only 1 wk a month, the cost would increase to $0.0079// ($0.03/gal) because of the premium for higher power demand.

In today's market, liquid nitrogen can be purchased for $0.049// ($0.19/gal), delivered; consequently, on-site production of liquid nitrogen would save approximately $0.044// ($0.17/gal), exclusive of investment costs. In addition, on-site storage capacity could be decreased from 757 000 to 151 400 / (200 000 to 40 000 gal), so the net additional investment would be $900 000. In other words, the nitrogen reliquefier would have to be run for 115 days before it became economical: Purchased liquid nitrogen costs/day = $0.19/gal x 49 034 gal/day = $9316/day. On-site liquefaction costs/day = $0.03/gal x 49 034 gal/day = $1471/day. So,

$$\frac{\$900\,000}{\$9316 - \$1471} = 115 \text{ days of operation}.$$

Under the criterion of 100 to 1000 maximum pulses, there is little justification for on-site production of liquid nitrogen.

Helium Supply. Helium for the initial charge and normal makeup requirements will be supplied by liquid-carrying tankers, each capable of transporting 37 850 / (10 000 gal). Tube trailers are impractical because of the large quantities of helium required and the distance from the production plants. Hauling charges for a tanker and a gas-carrying trailer are the same, but the larger capacity of the tanker decreases the unit transportation cost by a factor of 8. Helium comes from one or more of three commercial liquid helium plants in Kansas. Our requirements of 499 200 / (132 000 gal) represent a 33-day output from a plant.

Once the system is operating, replacement helium will be required. Losses will occur along the shafts and seals of the compressors, through valve stems and packing glands, and through flanges and other mechanical joints. Losses will also occur during safety valve releases and during equipment maintenance.

The helium inventory required for the proposed system is about three times that required for 1000-MW gas-cooled nuclear reactors now under design. Inventory losses for nuclear reactors range from 0.03 to 0.5%/day which implies an inventory of 136 to 2271 //day (36.0 to 600 gal/day) for the proposed system. However, the short-duration runs and the pulsing in the proposed system will probably result in losses closer to 1%, or 4996 //day (1320 gal/day).

The lost helium could be replaced from a 37 850-ℓ (10 000-gal) on-site tanker. If losses are 1%, each tanker load would last one week.

The cost for liquid helium in the required quantities would be approximately $1.06/ℓ ($4.11/gal), f.o.b. the production plant. Freight charges would increase the cost to approximately $1.11/ℓ ($4.20/gal). Total cost for the helium required to charge the system should be approximately $554 000.

Liquid helium would be unloaded into on-site storage tanks near the periphery of the experimental area, except during operation. From there, it could be vaporized into the compressor suction lines by the compressor housing as necessary.

Liquid will be transferred from the cold storage dewar to the storage coil dewars by pressurizing the cold storage dewars. By the reverse process one can empty the storage coil dewars. Very little pressure is required for these transfers.

Provision must be made to contain all the helium even when the experimental facility is not operating. One way would be to operate the refrigeration system continuously, storing the liquid helium in four 151 400-ℓ (40 000-gal) dewars. However, that may not be economically feasible when the research facility is not operating, and certainly there will be times when the refrigeration plant will need maintenance or repairs. This suggests a need for a helium gas storage system. Such a system could be assembled from six surplus LASL high pressure gas storage tanks. The tanks would cost nothing, but there would be installation costs for the tanks as well as the cost of a compressor to complete the system.

Adequate tankage is available for 17 275 000 ℓ (610 000 scf) of helium gas at a pressure of 2 812 400 kg/m^2 (4000 psi). A 1%/day dewar boiloff, if pumped into gas bottles, permits approximately 5 days of refrigeration system downtime, and most repairs can be completed in that time.

To run the refrigeration system with 5-day downcycles saves electrical power, but is practical only when the research facility is to be shut down for an extended period or when the refrigeration system is in need of maintenance or repairs.

As long as dewar boiloff is being pumped into gas storage bottles, the dewar itself is venting at constant pressure and there is very little temperature rise in the liquid helium stored in the dewar. Additional downtime can be obtained by closing off the dewar vent line when the storage tanks are full, thereby allowing the dewar pressure to build up. By setting the upper pressure limit at the critical pressure of helium, assuming a heat leak equivalent to 1%/day boiloff, and estimating a 50% efficiency from mixing in the dewar (some baffling would be required), the helium can be contained for 5 to 10 additional days. However, at the end of that time, a large fraction of the helium has become a saturated vapor. Also, the temperature of the remaining liquid has increased to approximately 5.2 K. Consequently, after the refrigeration system has been restarted, some running time is required to reduce the dewar temperature to 4.5 K. This is a worst-case situation and would arise only when the refrigeration system had been off for more than 5 days.

5.4.3.18 Cryogenic System Operation

A flow sheet (Fig. 5.4-16) shows the interaction of the various system components and helps in developing instrumentation control philosophy.

All components of the refrigeration system—individual coil storage dewars, helium storage tanks, surge tanks, and all lines—will be purged by evacuation and gas flushing to minimize the purification required.

For startup, one of the liquid helium storage tanks will be cooled by circulating cold helium from the refrigerator through the tank. As the system cools, liquid helium will collect in the dewar to the desired level.

Individual coil dewars will be cooled by circulating gaseous helium from the refrigerator through the main storage space of the dewars. Liquid helium will then be transferred from the storage tanks to the coil dewars at a rate limited by the capacity of the refrigerator compressors to recompress the vaporized helium. To cool the 89 600-kg total mass to 4.5 K will require the removal of 7.2 x 10^9 J. Cooldown time is calculated to be 72 h.

Once the dewars are cooled, filled with liquid helium, and stabilized, little attention will be required. If the refrigerator is liquefying more helium than is required, the liquid inventory in the storage tanks will increase and the amount of vapor leaving the coil dewars will decrease. The recycle valve on the refrigerator compressors will then open and the helium flowrate of the refrigerator will be lowered.

The amount of expander flow is determined by the refrigeration requirements and will increase or decrease as necessary to maintain the temperature of the first expander. This is accomplished by opening or closing the adjustable nozzles on the turbines. The nozzles provide a way to decrease the flow through the expanders without decreasing efficiency. The cross-sectional area of the nozzles is changed so that the pressure of the gas at the expander wheel is constant at all flowrates.

Once the pulsing has begun, the increased flow from the dewar will increase the compressor suction pressure and cause the recycle valve to close and

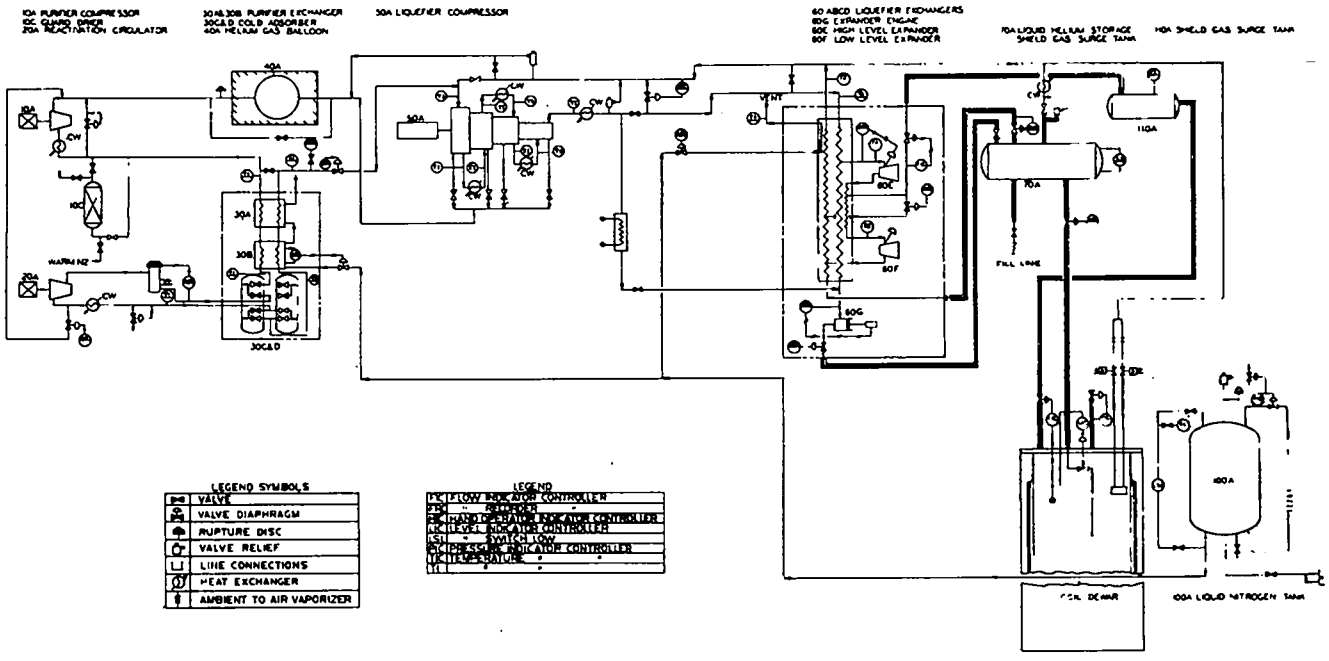

Fig. 5.4-16.
Schematic of SFTR cryogenic system.

deliver more flow to the refrigerator. The compressor discharge pressure will increase and cause the expanders to speed up.

For warmup, the liquid helium will be transferred from the coil dewars to the storage tanks by pressurizing the dewars. During the transfer the refrigerator must liquefy both the helium vaporized during the transfer and the cold gas displaced from the storage tanks. The coil dewars could be emptied in approximately 40 h. Circulating helium gas would be used to warm up the individual coil dewars. At a flowrate of 14 900 kg/h the warming period would be about 3 days.

5.4.3.19 Assembly Area

Practically all METS components will be preassembled into modules for installation in the SFTR building. Some of these modules will be assembled by vendors under LASL contracts; others will be assembled by LASL personnel. Regardless of where the modules are assembled, some testing and calibration work will be required. This work will be done in a small test facility to be constructed early in the assembly program and to be used for adjusting and testing complete modules. Faults may be detected in some modules during testing. Minor faults will be corrected while the units are in the checkout stand; more complex problems may require rebuilding of the modules.

All of this work can be done in the assembly area—a bay providing 929 m^2 (10 000 ft^2) of work space. A 9072-kg (10-ton) traveling bridge crane will be available for moving dewar modules and heavy transfer capacitor banks. Test fixtures, stands, and facilities such as vacuum pumping stations will be provided in the bay for the necessary assembly and maintenance work on the METS components.

For separation of assemblies, clearance is needed in an amount equivalent to twice the height of a dewar, and a pit area will therefore be included. The pit area will include two hydraulic lift platforms for storage coil assembly. These lifts will be used to position coil assemblies so the working area along the assembly is always at floor height, thus eliminating the need for elevated platforms and attendant safety equipment.

Spare modular coil assemblies will be stored in the assembly area, ready for immediate installation in the main facility if component failures occur. This capability is essential to minimize machine downtime.

Some office space will be provided in the assembly area for a mechanical engineer, an electrical engineer, a cryogenic engineer, draftsman, and building foreman. These individuals, along with

several technicians, will be responsible for the assembly, checkout, and installation of all METS components in the main facility. They will also have the primary responsibility for the operation and maintenance of the METS refrigeration and gas storage systems located adjacent to the assembly area.

5.4.3.20 System Cost Analysis

In this section, additional costs of the METS-SFTR system are presented, exclusive of the costs of the Phase I, capacitor-driven system described in Sec. 5.4.1. Some Phase I components are to be rearranged or reconnected for the Phase II system; however, since such changes are considered operating expenses, no cost factor is included here. Thus the costs for the following components are *not* included here:

1. Interrupter counterpulse system (Sec. 5.4.3.5)
2. Fast and slow compression coil crowbar switches (Sec. 5.4.3.7)
3. Counterpulse storage power supply (Sec. 5.4.3.9)
4. Capacitance transfer bank (Sec. 5.4.3.10).

Connections and cabling between components will be the same or will use the same material to some degree in both phases. The cabling costs given here are separated for the Phase I and Phase II systems.

Details of the costs are given in Tables 5.4-15 through 5.4-25 and are summarized in Table 5.4-26. Not included are field overhead, contractors' fees, engineering fees, and site preparation.

REFERENCES (Chap. V, Sec. 5.4)

1. Jacob L. Zar, "Electrical Switch Contact Resistance at 4.2 K," Avco Everett Research Laboratory report AMP 234 (July 1967).

2. F. L. Ribe, "Free-Boundary Solutions for High-Beta Stellerators of Large Aspect Ratio," Los Alamos Scientific Laboratory report LA-4098 (May 1969).

3. F. L. Ribe, W. H. Borkenhagen, W. R. Ellis, and K. S. Hanks, "Initial Equilibrium Configuration of the Scyllac 5-Meter Toroidal-Sector Experiment," Los Alamos Scientific Laboratory report LA-4597-MS (February 1971).

4. L. M. Soffer and L. Malho, "Cryogenic Resins for Glass-Filament-Wound Composites," NASA-CR-72114 (1967).

5. E. Mullan, "Design and Fabrication of 300 kJ Superconducting Energy Storage Coil," Westinghouse Electric Corp., Cheswick, PA, report E.M. 4617 (1974).

TABLE 5.4-15

STORAGE COIL COSTS

Superconductor	$ 5.6(10)^6
Coil material, manufacturer, and test	16.9
Total	$22.5(10)^6

TABLE 5.4-16

CRYOGENIC DISCONNECT COSTS

Disconnects (1280)	$3.9(10)^6
Actuators and hydraulic system	0.9
Total	$4.8(10)^6

TABLE 5.4-17

HVDC INTERRUPTER COSTS PER MODULE, 1280-MODULE SYSTEM, 10 MODULES PER CABINET UNIT

4 actuators + 4 breaker bottles + driver electronics ($300/actuator + $500/bottle + $400 electronics)	$3600
Voltage grading network	25
1.8-μF, 60-kV capacitor (7c/J installed)	225
Damping resistor	150
Saturable reactor and equalization transformer (20 lb iron + several turns copper + labor)	100
Fuse	200
H.V. header (open design with corona shields)	100
Bus bar	50
Support framework	75
H.V. insulation	50
H.V. monitors, current monitor	300
Control logic	100
Per Module Subtotal	$4 975
10 modules/unit	$49 750
Cabinet	500
10-Module Subtotal	$50 250
128-Unit Total	$6,432 000
Cabling, logic main controls	50 000
Total	$6.48(10)^6

TABLE 5.4-18

COMPRESSION COIL COSTS

Material/coil	$ 411
Labor/coil	708
Material for 1280 coils	526 000
Labor for 1280 coils	906 000
Total	$1 432 000

TABLE 5.4-19

CHARGING POWER SUPPLY FOR STORAGE COILS, COSTS

Rectifier power supply, 26 kA, 125 V	$145 000
Switch gear	10 000
Bus	17 000
Direct current interrupter	5 000
Resistor	3 000
Total	$180 000

TABLE 5.4-20

ELECTRICAL LEAD COSTS

Continuous, 26 kA, 128 pairs	$ 512 000
Pulsed, 26 kA, 60 kV, 1280 pairs	512 000
Total	$1 024 000

TABLE 5.4-21

COMPONENT CONNECTIONS AND CABLING COSTS

	Material	Labor
Phase I		
Transfer capacitor bank to fast crowbar	$ 68 000	$ 64 000
Fast crowbar to slow crowbar	135 000	128 000
Slow crowbar to compression coil	54 000	27 000
Subtotals	$257 000	$219 000
Total	$476 000	
Phase II		
Storage coil to interrupter	$1 437 000	$272 000
Interrupter to capacitor bank	90 200	64 000
Subtotals	$1 527 200	$336 000
Total	$1 863 200	

TABLE 5.4-22

Storage Coil Dewar Costs	$3.2(10)^6$

TABLE 5.4-23

LIQUID AND GAS DISTRIBUTION COSTS

Cryogenic piping	$890 000
Warm gas piping	25 000
Total	$915 000

TABLE 5.4-24

REFRIGERATOR SYSTEM AND CRYOGENIC STORAGE COSTS

Refrigerator cold box and compressors	$5.24(10)^6$
/He storage, 5-30 000 gal	1.25
/N_2 storage, 1-100 000 gal	0.25
Purification system	0.08
Controls, valves, instrumentation	0.38
Vacuum pumps	0.28
Total	$7.48(10)^6$

TABLE 5.4-25

Cooling tower costs (installed)	$68 000

TABLE 5.4-26

SUMMARY OF COSTS

Storage coils	$22.50(10)^6$
Cryogenic disconnects	4.80
HVDC interrupters	6.48
Compression coils	1.43
Charging power supply	0.18
Electrical leads	1.02
Isolation contactors	0.32
Component connections and cabling (Phase II)	1.86
Storage coil dewars	3.20
Liquid and gas distribution	0.92
Refrigerator and cryogenic storage	7.48
Cooling towers	0.07
Total	$50.26(10)^6$

5.5 SHIELDING DESIGN

5.5.1 Design Objectives

Several radiation protection criteria must be met during operation of the SFTR. These include permissible neutron and gamma-ray doses to the public and to site workers, control of radioactive effluents in air and water, disposal of radioactive wastes, and prevention of excessive radiation damage to electrical insulators. Preliminary design calculations have been performed to specify biological shielding (via the concrete cell wall) which will reduce dose rates to levels below values anticipated to be allowable in the 1980's. Activation of magnet coils, capacitors, and other structures in the cell was found to be excessively high if no primary shield were placed around the coils. Thus, a primary shield, 0.5 m thick, was designed to allow access to the cell shortly after a pulse, to reduce air activation in the cell, and to reduce radiation damage in capacitor insulation.

5.5.1.1 Biological Shield Design Criteria

Present ERDA radiation protection standards[1] allow an occupational dose equivalent (DE) limit, usually called simply "dose," of 3 rem/quarter, with a practical yearly limit of 5 rem. Legally, the latter limit can be relaxed to an accumulated dose of (N-18) 5 rem, where N is the employee's age, but this limit is not meaningful for shield design purposes. Consultation with health physics personnel revealed that current ERDA "as low as practical" requirements have been translated into a design criterion of <1 rem/yr for recently constructed ERDA facilities. Informal inquiries from ERDA have suggested more stringent limits of 0.5 rem/quarter. Considering this trend, we have selected a conservative occupational exposure limit from direct neutron and gamma-ray doses of 0.5 rem/yr in this design. This does not include doses from activated components. Such additional doses might be received during maintenance operations in the cell or during handling of activated components. Also, the 0.5-rem/yr direct dose will be a maximum at any point on the outer surface of the concrete secondary shield; most exposures will be less.

Because the maximum potential dose will be delivered in $\sim 10^3$ instantaneous pulses, rather than in a continuous exposure, more leeway exists in which to notify personnel of anticipated pulses. Thus, further dosage reduction can be achieved during the pulse if personnel are stationed in locations of minimum dosage consistent with their work assignments. Dose rate criteria for long-term low-level exposure are clearly not applicable for pulsed operations. However, radiation biologists were consulted to verify that high dose *rates* (as during a very short pulse) would not significantly change the biological effects to be expected when the same total dose is delivered slowly over a long period with a low dose rate. At the extremely low allowable dose (0.5 rem/yr) it is difficult to detect any somatic effects, and dose *rate* effects are unobservable.

Doses to the general public must be kept to less than 5 mrem/yr, and no problems are expected in this regard. However, quantitative predictions must await detailed facility design and location, fence locations, and other administrative control procedures.

5.5.1.2 Activation and Radiation Damage Criteria

Air activation is limited by the allowable release of activity into the airshed, and is ultimately determined by allowable exposure to the public. Specific quantitative criteria for allowable airborne radioactive materials are given in Ref. 1 as maximum permissible concentrations (MPC's) for a long list of isotopes. At the low total neutron fluences from the SFTR this will pose no problem. Calculations reveal that air activities in the cell are within occupational breathing tolerances several seconds after a pulse.

Design criteria for biological doses to personnel from activated components are much more complex. They must take into account factors such as time of access to the cell after a pulse, dose rate falloff as a function of time, length of time required for maintenance or other operation, location of the exposed person relative to numerous activated components. Simplifications were therefore necessary to reduce the problem to tractable proportions. The quantitative criteria for radiation protection of personnel are then given by the ERDA standards for occupational dose limits as discussed in the previous section.

Design limits for physical radiation doses to coil and capacitor insulation are difficult to establish due to lack of experimental data. Since the primary shield must be placed outside the magnet coils, shielding can do little to alleviate radiation damage to organic insulation in the coils; radiation-resistant materials must be selected. For example, doses of 9×10^5 gray (9×10^7 rad) will cause 25% elongation in polyethylene.[2] Further complicating the problem are gamma-ray doses, which will be of comparable

magnitude to the neutron doses. The addition of a primary shield will probably aggravate the problem slightly by reflecting more neutrons back to the coils and radiating gamma rays back to the coils. However, the primary shield is designed to reduce physical doses to the capacitors to levels below those which cause any significant damage in liquid organics. Using as criteria the gas evolution and viscosity increase due to radiation,[2] one finds that doses of $\sim 10^6$ Gy (10^8 rad) cause gas evolution rates of ~0.1 to 10 cm^3 (STP) of gas per cubic centimeter of liquid, which may well be unacceptable for off-the-shelf capacitors. Due to a lack of data on radiation effects to the capacitors, a conservative criterion was adopted. The maximum allowable physical dose to the capacitors is limited to 10^3 Gy/yr, which should cause barely detectable radiation effects in the castor oil insulation.

5.5.2 Shielding Concept and Layout

To identify approximate shielding requirements to satisfy the above-mentioned criteria, preliminary scoping calculations were performed. The toroidal source of 14-MeV D-T neutrons was treated as an equivalent line source with strength 1.78×10^{16} neutrons/m per pulse. Excluding all shields and using empirical removal cross sections for coils, insulation, and structures, a total dose of $\sim 1 \times 10^6$ rem/yr was calculated at 4 m distance from the plasma centerline. Thus, to achieve the first design objective of 0.5 rem/yr, shielding must be introduced which provides an effective dose attenuation factor of 5×10^{-7}. This attenuation could be obtained by an ordinary concrete shield of approximately 2-m thickness.[5] However, to meet the activation and radiation damage criteria it is necessary to employ some shielding as close to the plasma as possible. These requirements lead to the concept of a close-in primary shield in addition to a biological shield farther out from the plasma. The positioning of such a primary shield is dictated primarily by the requirements of the plasma containment system (i.e., the coil design). To minimize interference of the primary shield with the magnetic flux paths of implosion and compression coils, the closest possible location to the plasma is just outside the compression coil at a radius $R > 28$ cm. Access requirements to the coils limit the primary shield thickness to about 50 cm. This, in turn, reduces the thickness of the secondary shield to about 1.5 m of ordinary concrete. To further identify specifications for the primary and secondary shield components, it was necessary to perform more detailed calculations and also to assess additional design limitations.

5.5.2.1 The Primary Shield

First, the dose rate at ~1 m from the coils was computed from radionuclides in the coils and Fe-Ni alloy only, assuming no primary shield is provided. Unacceptably high doses (>1 rem/h) at 1 day after a pulse immediately led to the requirement for a primary shield around the coils. This shield serves multiple purposes, as discussed below, including the reduction of activation dose rates in the cell to the order of a few mrem/h. The shield keeps gamma radiation from the coil structure (vessel) and reduces capacitor and structural activation.

Minimizing activation and radiation damage of the capacitors and structure is the principal function of the primary shield. There is no way to shield the implosion and compression coils from the 14-MeV neutrons, so radiation-resistant insulators must be chosen for this application. However, reflected, low energy neutrons from the primary shield can be suppressed to some extent by judicious choice of shield materials. For example, boron-impregnated graphite and polyethylene will suppress thermal and epithermal neutron fluxes, and these materials were included in the primary shield. Suppression of low energy fluxes also reduces activation of the coils, and cell maintenance operations are thereby simplified. Incorporated in the primary shield design is a commercial lead-impregnated polyethylene which reduces dose rates in the cell from the activated coils to ≤1 mrem/h. Only when the primary shield is removed or streaming paths are created through the shield (e.g., through the optical ports) do the activated coils contribute significantly to the dose rate in the cell.

Once the necessity for a primary shield was established, a conceptual design was evolved to satisfy several design criteria. Some requirements for the materials of the primary shield are:

1. Low conductivity of the shield material located within the first few centimeters immediately outboard of the compression coil so as not to interfere with the magnetic flux paths.
2. Radiation resistance of the shield material with respect to dimensional stability, gas evolution, etc.
3. Reasonable cost and fabricability, i.e., commercially available materials which can be formed with standard machining and construction methods.
4. Effective gamma-ray attenuating properties for activation gamma rays from the vessel.
5. High cross section for neutron slowing down and absorption.
6. Minimum reflection of neutrons back to the coils, and minimum prompt gamma-ray production (radiating to coils).

7. Low potential for activation within the shield materials of long-lived gamma-ray emitters and radiologically hazardous isotopes (for waste disposal considerations).

The application of these criteria is reflected in the final primary shield design described in Table 5.5-1.

Graphite was selected for the first lamination in the shield principally for the following properties:

1. Low conductivity can be built in if desired (~5000 $\mu\Omega$-cm);
2. Negligible activation and moderate gamma-ray production;
3. High resistance to radiation, especially as opposed to polyethylene;
4. Moderately good neutron attenuating properties; and
5. Excellent structural properties and machinability.

Boron at 1 wt% was added to the graphite to suppress thermal (and epithermal to some extent) neutron return to the vessel, which return could result in subsequent activation of the copper, nickel, and iron. Aluminum structure was placed in two shells to support the shield and tie the laminations together, yet not activate significantly itself. Because of its high conductivity, the nearest aluminum shell was located about 26 cm outboard of the compression coil. Finally, borated and leaded polyethylene were used in places where neutron fluxes would be sufficiently attenuated by the graphite and aluminum to preclude excessive radiation damage to the polyethylene. The graphite and aluminum also shield the polyethylene somewhat from capture gamma rays in the coils. Leaded polyethylene was selected as the outermost lamination in order to shield against prompt gamma rays,

TABLE 5.5-1

PRIMARY SHIELD DESIGN AND COMPOSITION

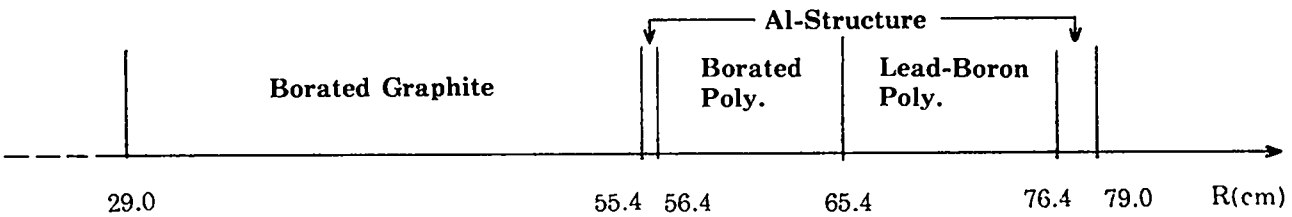

Zone Description	Density (g/cm^3)	Composition	Number-Density (atoms/barn·cm)
Borated Graphite	1.6	99 wt% Carbon	C: 0.07943
		1 wt% Boron	B-10: 0.000191
			B-11: 0.000702
Al-Structure	2.7	100% Aluminum	Al: 0.06027
Borated Polyethylene	0.94	95 wt% Polyethylene	H: 0.06515
			C: 0.02884
		5 wt% Boron	B-10: 0.00056
			B-11: 0.00206
		Impurities	O: 0.00785
Lead-Boron-Polyethylene	4.4	80 wt% Lead	Pb: 0.01023
		12.5 wt% Polyethylene	C: 0.02363
			H: 0.04706
		1 wt% Boron	B-10: 0.000524
			B-11: 0.00193
		6.5 wt% Mortar	O: 0.00696
			Si: 0.00125
			Al: 0.00665

and more important, activation gamma rays during access to the cell after a pulse.

5.5.2.2 The Secondary, Biological Shield

Initial shielding studies concentrated on sizing the concrete cell walls and ceiling which serve as the biological shield. Ordinary concrete was chosen on the basis of several considerations, including structural requirements, cost, and extensive experience with its use in conventional fission power plants. A schematic of the cell cross section and its concrete biological shield is shown in Fig. 5.5-1.

Calculations were first performed without a primary shield, and with only the coils between the plasma and the concrete walls (i.e., streaming paths which do not intersect capacitors or structure were assumed for the sake of conservatism). Biological doses per pulse from neutrons were calculated assuming that the concrete secondary shield extended from r = 397 to 500 cm. It was found that this amount of concrete would not be an adequate biological shield because the calculated neutron dose outside the wall was ~0.6 rem/pulse, or 600 rem/yr. The gamma-ray dose would be a comparable value. No attempt was made at this stage to size the secondary shield; however, it could be inferred that a 50-cm-thick primary shield would reduce the neutron dose outside the secondary shield to ~6 rem/yr. Under current guidelines for occupational doses (cf. Sec. 5.5.1.1) another ~40 cm of concrete (i.e., 143 cm total) would be required in addition to a 50-cm primary shield if access to the concrete wall is desired during a pulse. The 40-cm estimate assumes that the gamma dose is approximately equal to the neutron dose, a conservative assumption in this case.

A 1.5-m-thick secondary shield was thus maintained throughout several iterations on the primary shield design, coil material, thickness choices, etc.

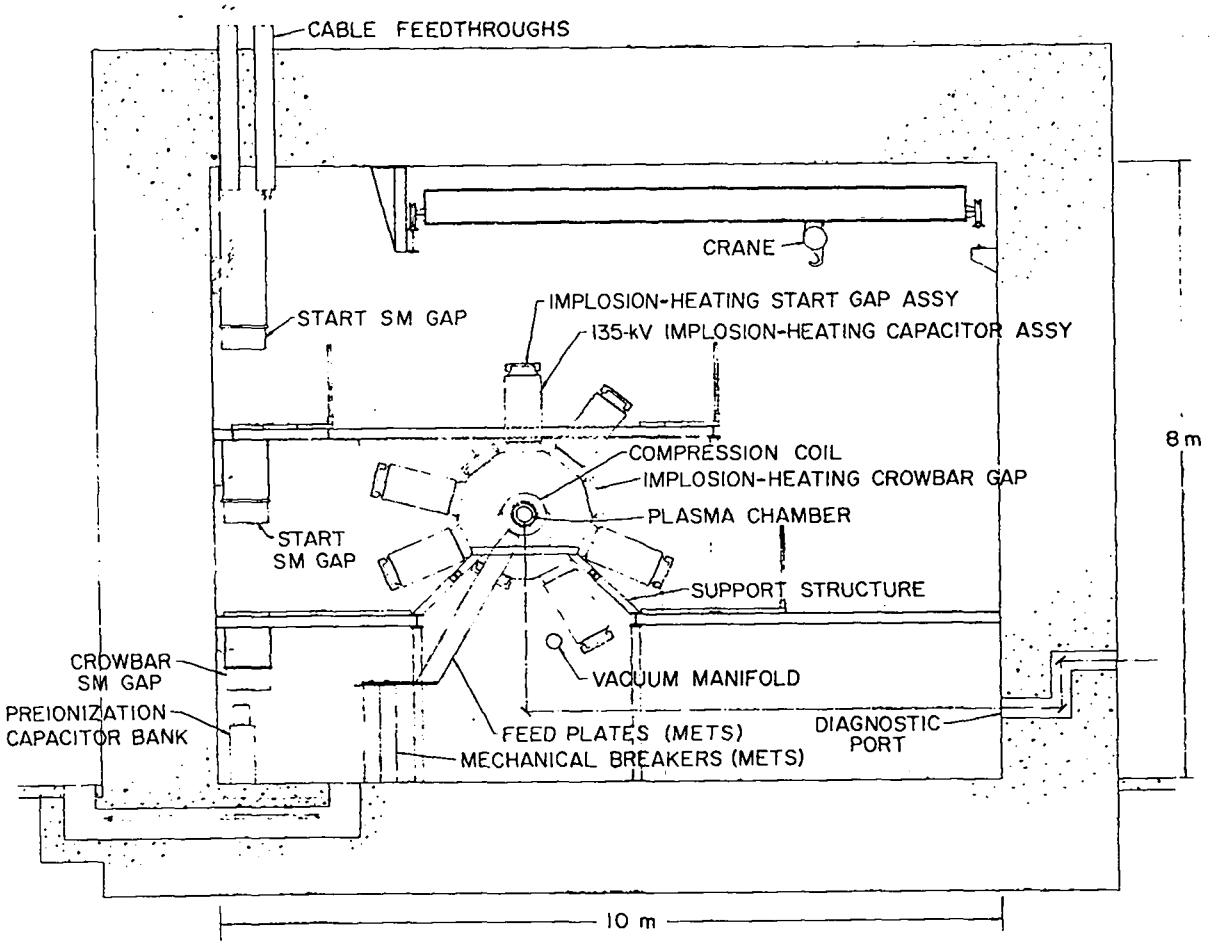

Fig. 5.5-1.
Cross section through SFTR cell.

After the current reference vessel module, feedplate, and capacitor designs were selected, a complete and comprehensive shield analysis was performed. Since the capacitors outside the primary shield do not form a closed ring around the torus, their shielding effect for biological dose calculations outside the concrete is very limited. Therefore, to maintain conservatism in the dose calculation through the biological shield, only streaming paths which circumvent the capacitors were considered.

Although calculational models assume a monolithic concrete secondary shield, there obviously will be many penetrations for optical ports, cables, etc. Some thought has been given, for example, to shadow-shielding major penetrations to avoid direct streaming of neutrons from the vessel to the penetration entrance. Also, penetrations are made as normal to the streaming line as possible, and ducts are bent or offset where possible. On the basis of fission reactor experience, these measures should prove adequate. However, at the detailed design stage, precise calculations of neutron and gamma-ray streaming and scattering will need to be performed.

5.5.3 Radiation Transport Analysis and Results

On the basis of the shielding concept and layout discussed in Sec. 5.5.2, detailed radiation transport calculations were performed to confirm the required performance of both primary and secondary shields. The methods and data applied for this analysis are described below. In presenting the results of the computations we will often incorporate results of calculations that do not include the primary shield for purposes of easy comparison and to justify the necessity of a primary shield structure.

5.5.3.1 Method of Analysis and Nuclear Data

All radiation transport calculations are performed with codes available in the LASL CTR Nuclear Analysis System described in detail elsewhere.[3] Transport and activation cross sections, together with other nuclear data, are retrieved from the LASL CTR library,[4] which is based on most recent ENDF/B evaluations, and the LASL TD library. The 100-group neutron cross-section sets in the CTR library are collapsed to 25 groups for the final shield design analysis. All transport calculations are performed in one-dimensional cylindrical geometry from the plasma centerline outward along radial traverses. Such one-dimensional computational models are considered adequate at this stage of the SFTR design. The application of two- or three-dimensional transport methods is not warranted until a later design stage, because the numerous geometric complexities which can be incorporated into multidimensional calculations will undoubtedly have to undergo several additional design iterations before they can be firmly established. The consideration of such complex geometric structures at this conceptual design stage would only complicate the shield analysis disproportionately and handicap the interpretation of the results.

Figure 5.5-2 shows an R-Z cross section through the magnet coils, primary shield, and capacitors, extending radially from the plasma centerline to the outer edge of the capacitors and axially over two 40-cm modules. It can be seen that many streaming paths exist which allow radiation to circumvent coils, primary shield, and capacitors. Whenever possible, design solutions were sought to block or eliminate such radiation streaming paths. For example, the line-of-sight penetrations required through the primary shield so that the aluminum feedplates can reach the coils inside the shield are blocked by shield sections between adjacent capacitors. An

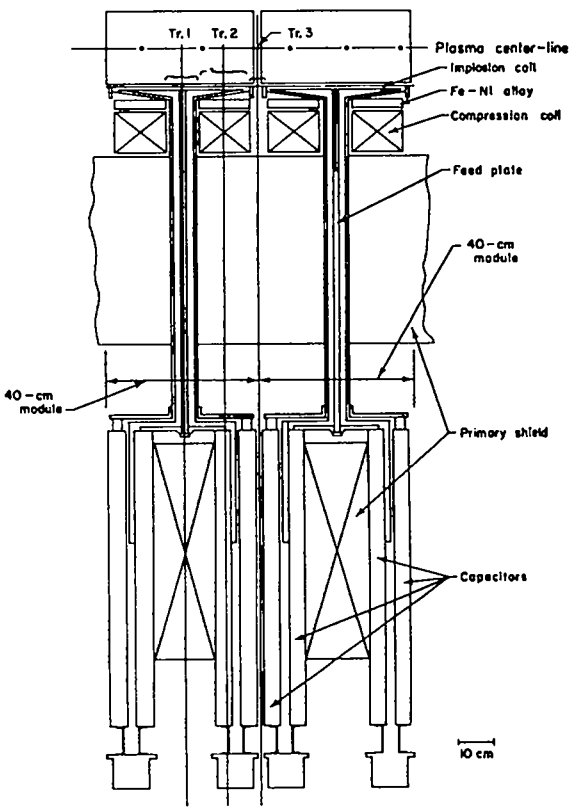

Fig. 5.5.2.
Cross section through two adjacent SFTR modules including coils, primary shield, and capacitors.

attempt was made to incorporate the effects of the remaining streaming paths into our computational analysis by selecting several radial traverses for the cylindrical model calculations. As indicated in Fig. 5.5-2, for the computation of air activation and radiation effects to the capacitors, we considered three different traverses, Tr. 1, Tr. 2, and Tr. 3, for which separate radiation transport calculations were performed. The calculated neutron flux spectra ϕ_1, ϕ_2, ϕ_3 were then linearly combined to calculate the radiation effects of interest. The coefficients a_i for this linear combination are determined from the fraction of first-wall area per module associated with each traverse; $a_i = A_i/(A_1 + A_2 + A_3)$. For the three traverses shown in Fig. 5.5-2 we obtain

$$\phi = 0.66875\phi_1 + 0.20625\phi_2 + 0.125\phi_3.$$

The integral effects of interest are then calculated from

$$R = \langle \Sigma_R, \phi \rangle ,$$

where Σ_R stands for the macroscopic response cross section and the symbol<,> indicates integrations over all energies and the spatial zones of interest.

5.5.3.2 Computational Results

All transport calculations performed with the DTF-IV code were originally normalized to a source strength of one 14-MeV neutron emitted per centimeter of torus. The flux distributions resulting from these computations were then processed through a post-processor code, TR3, which performs the linear combinations for streaming corrections together with the energy and spatial integrations described above, and renormalizes the source strength as desired. Usually, results are presented per pulse assuming a neutron source strength of 1.78 x 10^{14} neutrons/cm-pulse. For time-integrated effects a total of 1000 pulses/yr is assumed. In some instances it is convenient to quote equivalent time-averaged quantities per second which may be obtained by multiplying the results per pulse by 3.17 x 10^{-5} pulses/s, or assuming an equivalent time-averaged neutron source strength of 5.64 x 10^9 neutrons/cm s.

5.5.3.2.1 Neutron Flux Distribution Inside SFTR Cell

The radial distribution of the neutron fluence per pulse is shown in Fig. 5.5-3 for positions inside the SFTR cell. In addition to the total neutron fluence (integrated over all energies), the fast neutron fluence is also plotted for neutron energies above 10 MeV. This high-energy radiation component may be of special interest in estimating threshold activation reactions which may not be specifically quoted in this report.

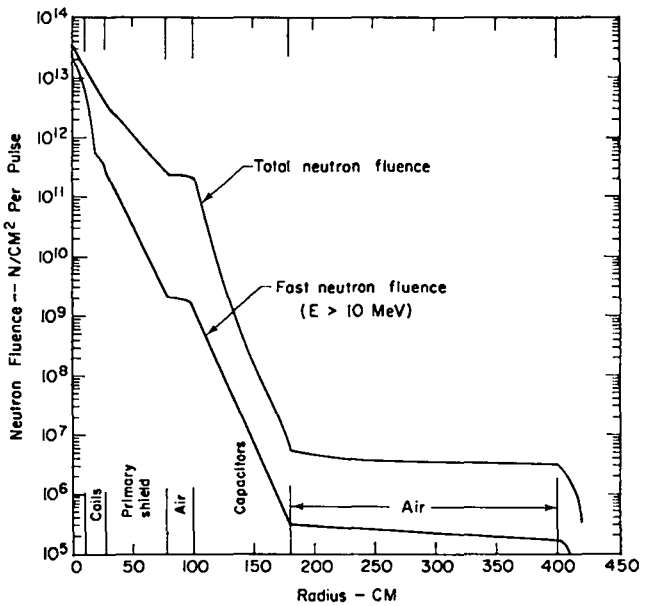

Fig. 5.5-3.
Radial distribution of total and fast neutron fluence per pulse inside SFTR cell.

5.5.3.2.2 Biological Dose Distribution

The radial distribution of the neutron dose per pulse delivered at any point within 5.5 m of the plasma is given in Fig. 5.5-4. A conservative assumption has been made for this computation: the shielding effectiveness of the capacitors is totally neglected and the space between the primary shield and the concrete cell wall is assumed to be air. Even with this stringent assumption the calculated neutron dose at the outer surface of the concrete wall meets the biological shield design criterion of 0.5 rem/yr (equivalent to 0.5 mrem/pulse), as seen from Fig. 5.5-4. This calculation also confirms that the 1.5-m-thick biological shield, together with the 50-cm-thick primary shield, is sufficient to meet radiation exposure limits for personnel access areas outside the SFTR cell. This conclusion holds even for the extreme case in which personnel are present during all 1000 (assumed) pulses per year, immediately outside the concrete cell wall and at the maximum dose location.

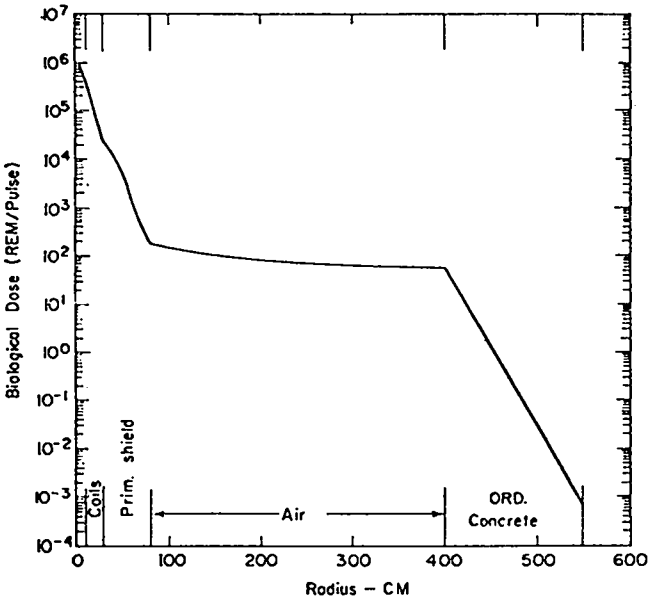

Fig. 5.5-4.
Radial distribution of biological dose per pulse.

5.5.3.2.3 Air Activation in the SFTR Cell

Table 5.5-2 presents a summary of the radioactivity generated in the air inside the SFTR cell per pulse and per year. The air circulating in the cell is assumed to be well filtered so that activation of dust particles need not be considered. Unless removed, the activated isotopes in the cell air will eventually be released into the containment atmosphere and into the environment. Therefore, Table 5.5-2 also lists the total annual radiological impact from air activation, assuming 1000 pulses/yr. For the short-lived isotopes (N-13 and N-16) the radioactive decay will in itself reduce the generated activity to negligible values between pulses. However, the environmental impact of the isotopes with longer half-lives must be considered. Therefore, the MPC's for occupational exposure as defined in Ref. 1 are also given in Table 5.5-2. No MPC is given in Ref. 1 for ^{39}Ar; it was calculated assuming the lens of the eye and the skin to be the most critical organs and therefore represents a conservative limit. Defining a RBH (relative biological hazard) as

$$RBH = \frac{A(Ci/m^3)}{MPC(Ci/m^3)}$$

where A is the calculated specific activity per pulse, it can be seen that for all isotopes the RBH is less than 1.0. This indicates that even if the activated air from the SFTR cell were released immediately after each pulse, its activity would not create any biological hazard. This conclusion is true, even if no dilution of the cell air is assumed. Due to the long half-lives of ^{39}Ar and ^{14}C isotopes, their activity will be cumulative for multiple pulses. But even after 1000 pulses/yr with the same cell air environment, RBH $\ll$ 1. To express the radiological impact of the long-lived isotopes in air more quantitatively we define an IHP (integrated hazard potential) as

TABLE 5.5-2

SFTR AIR ACTIVATION, EXCLUDING DUST

Isotope	Production Reaction	Half-Life ($T_{1/2}$)	Mean-Life (τ(s))	Principal Radiation (type; MeV)	MPC (Ci/m^3)	Spec. Act. per Pulse (Ci/m^3)	Tot. Act. per Pulse (Ci)	Tot. Act. per Year (Ci/yr)	RBH (1)	IHP (s)
^{13}N	$^{14}N(n,2n)$	9.9 min	8.6E+2	β^+1.2	---	1.03E-5	1.08E-1	---	---	---
^{16}N	$^{16}O(n,p)$	7.1 s	1.02E+1	β^-4.3, 10.4 γ6.1, 7.1	---	1.62E-3	1.68E+1	---	---	---
^{14}C	$^{14}N(n,p)$	5730 yr	2.6E+11	β^-0.16	4.0E-6	2.9E-11	3.0E-7	3.0E-4	7.3E-6	1.9E+6
^{39}Ar	$^{40}Ar(n,2n)$	269 yr	1.2E+10	β^-0.56	1.0E-4	4.3E-13	4.5E-9	4.5E-6	4.3E-9	5.2E+1
^{41}Ar	$^{40}Ar(n,\gamma)$	1.8 h	9.5E+3	β^-1.2, 2.5 γ1.3....	2.0E-6	1.7E-6	1.8E-2	---	0.85	8.1E+3

Note: 8.6E+2 means $8.6 \times 10^{+2}$.

$$IHP = RBH \int_0^{\infty} e^{-\lambda t}\, dt$$

$$= RBH \cdot \tau,$$

where τ is the mean-life of the isotope in seconds ($\tau = 1/\lambda = T_{1/2}/\ln 2$). These values are also given in Table 5.5-2.

A comparison of the activities given in Table 5.5-2 with values calculated without a primary shield confirms the effectiveness of this shield. The unshielded air activities are approximately a factor of 100 higher than the values in Table 5.5-2.

5.5.3.2.4 Activation of Coils, Structures, and Capacitors

Seventy different nuclear reactions of neutrons with materials surrounding the plasma were considered for our activation analysis. In the process of selecting the most important radioactive isotopes generated in the SFTR cell we dismissed a number of production mechanisms on the basis of (a) very small activation cross section, (b) very low abundance of parent-isotope in natural element, or (c) pure beta emission of product isotope. The remaining activation reactions are listed in Table 5.5-3 for materials expected to be present in the magnet coils, the primary shield structure, and the capacitors. Isotopic production rates, P_{ij}, as the number of product isotopes, j, generated per parent isotope, i, per pulse, are given at various locations in the cell for every activation reaction considered relevant for the SFTR. The table is organized according to increasing half-lives of the product isotopes. Potential activation reactions with ^{59}Co are also included because cobalt is expected to be contained in nickel as an impurity with 0.3-0.5 vol%. From the production rates given in Table 5.5-2 it is easy to calculate specific as well as total activities for certain integral components inside the cell:

$$A_{spec.,j}(r) = K \cdot \lambda_j \sum_i N_i\, P_{ij}(r)$$

$$A_{tot} = \sum_j \int_V A_{spec.,j}(r)\, dV$$

$$= V \cdot \sum_j \overline{A}_{spec.,j}$$

where

$A_{spec.,j}(r)$ = specific activity per pulse from product isotope j at location r, $Ci/cm^3 \cdot pulse$

A_{tot} = total activity per pulse, Ci/pulse

K = conversion factor 2.7×10^{-11} Ci/(disintegrations/s)

N_i = number density of parent isotopes i, = parent isotopes/cm^3

λ_j = decay constant for product isotope j, (disintegrations/s)(product isotope)

$P_{ij}(r)$ = production rate of isotope j from isotope i, at location r per pulse, product isotopes/parent isotope · pulse

V = volume of material containing parent isotopes at density N_i, cm^3.

In evaluating the number densities N_i, the abundance of the particular isotope of interest in the naturally occurring element must be considered, as well as the volume fraction of that element when a chemical compound or physical mixture is considered:

$$N_i = \frac{N \rho_i}{A_i}\, a_i\, f_i$$

where

N = Avogadro's number = 0.60225×10^{24} atoms/mol

ρ_i = mixture density, g/cm^3

A_i = atomic weight of element i, g/mol

a_i = volume fraction of element i in mix

f_i = fraction of isotopic abundance of specific isotope in element i.

The above formulas are given intentionally in this much detail to allow the designer to estimate induced activities in the process of future design iterations, and to provide the basis for determination of possible activations of instruments located throughout the SFTR cell but not shown in the present design drawings.

The so-calculated activities per pulse are the basis for determining (a) safe access of personnel to the cell, (b) potential biological exposures during maintenance and repair inside the cell, and (c) requirements for the handling and disposal of activated components. These criteria are discussed in Chapter VII.

TABLE 5.5-3

PRODUCTION RATE OF RADIOACTIVE ISOTOPES PER PULSE

Product Isotope (j)	Production Mechanism (i(react.)j)	$T_{1/2}$	Production Rate P_{ij} (product-isotope/parent-isotope pulse) at Distance R(cm) from Plasma							
			I.C 10.52	Fe-Ni 13.77	Comp. Coil 17.55	Comp. Coil 27.45	Sh. 55.65	Capacitors 101.0	Capacitors 141.0	Capacitors 179.0
Cu-66	Cu65(n,γ)	5.1 min	1.3 −12	1.2 −12	1.8 −12	8.1 −13	2.1 −13	2.5 −13	5.7 −16	6.2 −18
Cu-62	Cu63(n,2n)	9.8 min	2.2 −12	9.9 −13	5.0 −13	1.7 −13	6.9 −15	4.5 −16	5.2 −18	7.7 −20
Co-62	Cu65(n,α)	13.9 min	1.9 −13	8.7 −14	4.4 −14	1.6 −14	8.8 −16	6.3 −17	9.4 −19	1.6 −20
Mg-27	Al27(n,p)	9.5 min	4.3 −13	2.0 −13	1.0 −13	3.9 −14	2.5 −15	1.9 −16	2.9 −18	5.3 −20
Al-28	Al27(n,γ)	23.0 min	3.7 −14	3.5 −14	3.1 −14	1.4 −14	4.3 −15	7.9 −16	3.7 −19	2.7 −21
Ni-65	Cu65(n,p)	2.6 h	1.1 −13	5.0 −14	2.6 −14	9.2 −15	5.1 −16	3.7 −17	5.4 −19	9.4 −21
Mn-56	Fe56(n,p)	2.6 h	5.4 −13	2.5 −13	1.3 −13	4.5 −14	2.4 −15	1.7 −16	2.5 −18	4.2 −20
Mn-56	Mn55(n,γ)	2.6 h	6.7 −12	6.4 −12	1.0 −11	4.5 −12	1.2 −12	1.5 −12	3.5 −15	3.8 −17
Mn-56	Co59(n,α)	2.6 h	1.4 −13	6.6 −14	3.4 −14	1.2 −14	6.1 −16	4.3 −17	6.2 −19	1.0 −20
Cu-64	Cu63(n,γ)	12.7 h	2.9 −12	2.7 −12	4.0 −12	1.8 −12	4.8 −13	5.2 −13	1.2 −15	1.3 −17
Cu-64	Cu65(n,2n)	12.7 h	4.5 −12	2.0 −12	1.0 −12	3.5 −13	1.6 −14	1.1 −15	1.3 −17	2.1 −19
Na-24	Al27(n,α)	15 h	6.3 −13	2.9 −13	1.5 −13	5.2 −14	2.7 −15	1.9 −16	2.8 −18	4.8 −20
Ni-57	Ni58(n,2n)	36 h	1.0 −13	4.6 −14	2.3 −14	8.0 −15	3.0 −16	1.9 −17	2.0 −19	2.9 −21
Cu-51	Fe54(n,α)	28 days	7.3 −13	3.3 −13	1.7 −13	6.0 −14	2.9 −15	2.1 −16	2.9 −18	4.8 −20
Cr-51	Cr52(n,2n)	28 days	1.2 −12	5.2 −13	2.6 −13	9.1 −14	3.4 −15	2.2 −16	2.3 −18	3.2 −20
Fe-59	Ni62(n,α)	45 days	9.4 −14	4.3 −14	2.2 −14	7.5 −15	3.5 −16	2.4 −17	3.2 −19	5.2 −21
Fe-59	Fe58(n,γ)	45 days	1.3 −12	1.0 −12	1.2 −12	5.2 −13	1.3 −13	1.5 −13	3.4 −16	3.7 −18
Fe-59	Co59(n,p)	45 days	3.8 −13	1.7 −13	8.9 −14	3.2 −14	1.7 −15	1.2 −16	1.8 −18	3.0 −20
Co-58	Co59(n,2n)	71 days	2.7 −12	1.2 −12	6.0 −13	2.1 −13	8.8 −15	5.9 −16	7.1 −18	1.1 −19
Co-58	Ni58(n,p)	71 days	2.6 −12	1.3 −12	6.9 −13	2.7 −13	2.1 −14	1.5 −15	2.4 −17	4.4 −19
Co-57	Ni58(n,np)	271 days	7.1 −13	3.2 −13	1.6 −13	5.6 −14	2.5 −15	1.7 −16	2.2 −18	3.5 −20
Mn-54	Fe54(n,p)	313 days	2.4 −12	1.2 −12	6.4 −13	2.5 −13	1.9 −14	1.4 −15	2.2 −17	4.1 −19
Mn-54	Mn55(n,2n)	313 days	4.6 −12	2.0 −12	1.0 −12	3.6 −13	1.6 −14	1.1 −15	1.3 −17	2.0 −19
Co-60	Ni60(n,p)	5.2 yr	7.8 −13	3.6 −13	1.8 −13	6.6 −14	3.6 −15	2.6 −16	3.8 −18	6.5 −20
Co-60	Co59(n,γ)	5.2 yr	2.6 −11	2.5 −11	3.6 −11	1.5 −11	4.1 −12	4.5 −12	9.7 −15	1.1 −16
Co-60	Cu63(n,α)	5.2 yr	1.9 −13	8.6 −14	4.4 −14	1.6 −14	8.8 −16	6.3 −17	9.4 −19	1.6 −20
Al-26	Al27(n,2n)	7.3×10^5 yr	1.6 −13	6.8 −14	3.5 −14	1.2 −14	4.1 −16	2.6 −17	2.5 −19	3.3 −21

Note: 1.3 −12 means 1.3×10^{-12}

5.5.3.2.5 Radiation Effects to Coils and Capacitors

Radiation effects which may change mechanical or chemical properties of materials are considered in this section. Most of these effects can be quantitatively related to the physical dose absorbed in such material and which can be expressed in units of Gy (1 Gy ≡ 1 gray = 100 rads) or as an energy production density in units of erg/g or MJ/m^3 (1 Gy = 10^4 erg/g).

Energy production densities from neutron and gamma-ray deposition are everywhere less than 1 MJ/m^3 per pulse, causing only negligible radiation heating rates so that temperature rises caused by nuclear heating are <1 K per pulse at any location inside the SFTR cell. Likewise, the time-averaged 14-MeV neutron wall loading on the first wall is only 2×10^{-6} MW/m^2, so radiation damage to metals is inconsequential. Due to the small neutron fluence levels, the transmutation effects at any location are below 1 ppm/yr and cause no noticeable changes of mechanical or electrical properties in the copper coils or the Fe-Ni alloy. Also, maximum atom displacements in the iron, nickel, or copper are $\sim 2 \times 10^{-8}$ displacements/atom/pulse or 2×10^{-5} displacements/atom/yr, which are negligible values. The only remaining radiation effect that may impose a significant burden on the SFTR design is the radiation damage to organic materials being used as insulating and shielding materials.

The radial distribution of the neutron physical dose absorbed in organics per pulse is shown in Fig. 5.5-5. Organic insulation may be used in the Fe-Ni alloy as well as in the compression coil and the capacitors. The maximum dose to an organic insulator in the Fe-Ni alloy at r = 13.6 cm is 5×10^2 Gy/pulse; to the compression coil insulator at t = 17 cm it is 3×10^2 Gy/pulse. These doses may cause significant damage and impair the insulating properties of organic materials if used as insulators in these locations. However, no information exists to identify a limiting damage mechanism (e.g., gas generation, sludge formation, dimensional growth) and no firm design criterion has been established. The polyethylene in the primary shield is subject to a maximum physical dose of ~10 Gy/pulse at its location closest to the plasma. However, since there are no other than shielding requirements established for these polyethylene regions, an absorbed dose of 10 Gy/pulse is of no concern.

The maximum physical dose to the capacitor insulation is 1.5 Gy/pulse at R = 100 cm and falls off by about 4 decades to 8×10^{-5} Gy/pulse at R = 180 cm. Comparing this maximum dose of 1.5 Gy/pulse with the radiation damage criterion established in

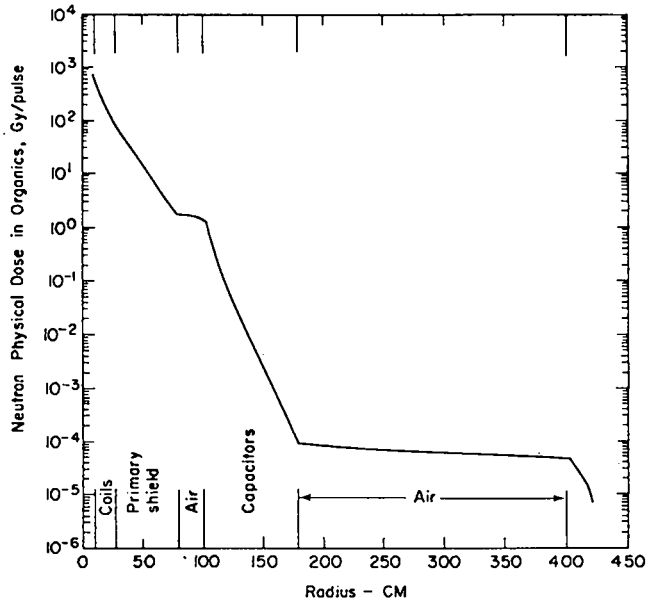

Fig. 5.5-5.
Radial distribution of neutron physical dose absorbed in organic material (1 Gy = 100 rads).

Sec. 5.5.2.1 for the capacitors, 10^3 Gy/yr, it is seen that this conservative criterion is almost met, even for the maximum value. We therefore conclude that radiation damage to the capacitors is not expected to be a problem, but the presence of the primary shield is absolutely necessary to meet this objective.

REFERENCES (Chap. V, Sec. 5.5)

1. "Standards for Radiation Protection, Rules and Regulations," Title 10, Part 20, U.S. Atomic Energy Commission (1970).

2. Harold Etherington (Ed.), **Nuclear Engineering Handbook** (McGraw-Hill, New York, 1958), pp. 10-136 ff.

3. Donald J. Dudziak, "Fusion Reactor Nuclear Analysis Methods and Applications," Proc. 8th Symp. on Fusion Technology, Noordwijkerhout, The Netherlands, 17-21 June 1974.

4. D. W. Muir et al., "Nuclear Data for the Controlled Fusion Program," in Applied Nuclear Data R&D Quarterly Progress Report, July 1 through Sept. 30, 1974, Los Alamos Scientific Laboratory report LA-5804-PR (Dec. 1974).

5. P. N. Stevens and D. K. Trubey, "Methods for Calculating Neutron and Gamma-Ray Attenuation," Chapter 3 in Weapons Radiation Shielding Handbook, DNA-1892-3, Rev. 1 (1972).

5.6 TRITIUM HANDLING SYSTEM

5.6.1 Overview of Tritium Handling System Function, Design Requirements, and Layout

The major functions of the tritium handling system are: (i) to inject precisely measured $(D,T)_2$ mixtures into the SFTR discharge tube in preparation for a D-T discharge; (ii) to recover and/or to account for all unburned tritium after a D-T discharge; (iii) to provide safe storage of gram quantities of tritium; (iv) to monitor and to control the chronic release of tritium and, (v) to present safeguards and cleanup capabilities in the event of a significant accidental release of tritium. The major subsystems that make up the tritium handling system are:

- Passive Storage Facility or Vault (PSF)
- Tritium Injection System (TIS)
- Tritium Recovery System (TRS)
- Vacuum System
- Tritium Waste Treatment (TWT) Facility
- Cell Cleanup Facility (CCF).

Figure 5.6-1 depicts schematically the interrelationship of components of the tritium handling system. In addition to the more obvious functions of storage, injection, and recovery, the SFTR vacuum system, $(D,T)_2$ impurity control, and postdischarge gas analyses are considered important portions of the tritium handling system.

The interactions between these subsystems may be multifarious and/or diffuse; for instance, the vacuum system per se plays important roles in both tritium injection and recovery and to some extent impinges upon the design of the TWT and CCF.

Tritium injection will be made by the use of standard volumes and vacuum transfer techniques. A uranium bed will supply clean tritium to the injection system. Recovery of used $(D,T)_2$ gas will occur at the cryogenic vacuum pump station, and the $(D,T)_2$ so collected will be stored on a second uranium bed. In addition to metal hydride storage of tritium, a vault-like structure will be used for a more permanent, secure storage of gaseous tritium. Chronic tritium releases are expected to occur at the vacuum pump stations (four stations are located within the SFTR cell) and at the locations of major tritium handling components (cleanup units, uranium beds, etc.) Such components will be located in ventilation hoods, and tritium released

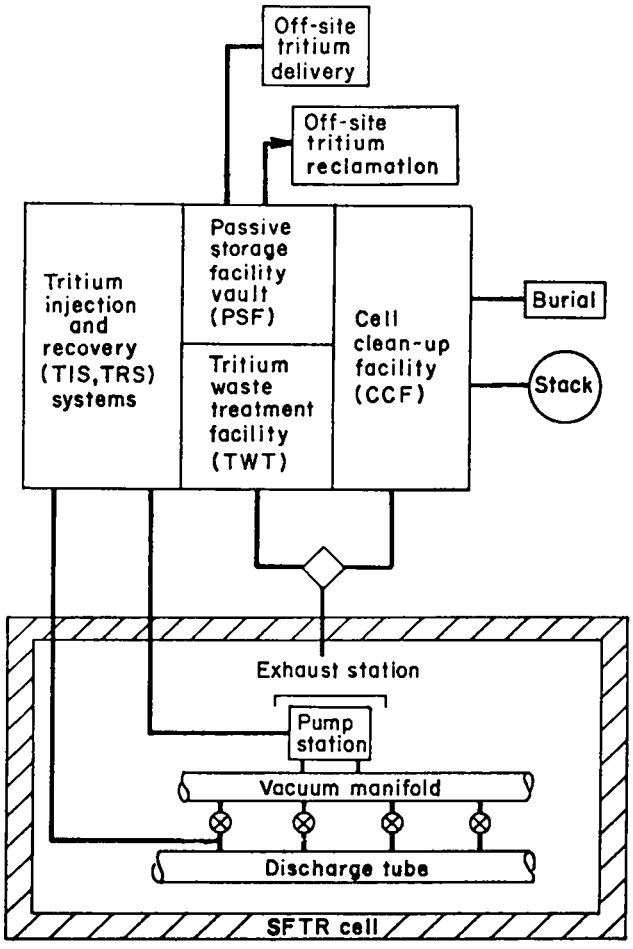

Fig. 5.6-1.
Schematic of tritium handling system.

during routine maintenance of these components will be carried in flowing air to a small 7-//s (15-cfm) cleanup unit. A larger 4700-//s (10-kcfm) cleanup unit will be provided to remove tritium from the recirculating air in the SFTR cell in the event the discharge tube fails during a D-T discharge; the larger cleanup facility will be available for nonscheduled action associated with the failure of other components of the tritium handling system.

The system described above is designed to provide for 1000 D-T discharges/yr, each discharge requiring on the average 15 mg of T_2. On the basis of 20 D-T discharges/week, a total tritium supply of 3 g is anticipated; 0.3 g (one week's supply) will be stored as uranium tritide and 2.7 g (two months' supply) will be in gaseous form.

In many respects the design for the tritium handling system presented here is very conservative in view of the low inventory of tritium on-site (3 g, or a

maximum of 7 g including that tritium not yet sent off-site for recovery) and the relatively small number of D-T discharges (4/day or 1000/yr). Nonetheless, a total release to the SFTR cell ($\sim 2.5 \times 10^4$ m^3) of tritium associated with a D-T discharge ($\sim$15 mg) would result in 6000-μCi/m^3 air concentration; MPC for T_2O or HTO in air[1] is 5 μCi/m^3. Although a total release of the tritium to the cell seems highly unlikely for any disruption short of a total demolition of the SFTR discharge tube (i.e., the vacuum system should collect the major portion of the tritium before the $\sim$8-m^3 discharge tube reaches atmospheric pressure),* incorporation of a 4700-ℓ/s cleanup unit in the CCF provides a capability of a $\sim$1.5-h turnover time for the cell atmosphere in the event of a total release of the 15 mg of tritium. The similarly conservative design of the vacuum system dictates a 1-s time constant to assure (i) rapid recovery of tritium within the discharge tube, (ii) a discharge cycle time of 15 min, and (iii) a base pressure low enough to restrict impurity levels in the $(D,T)_2$ gas to below 0.1 at.% for a relatively high outgassing rate and 10 s between isolation of the discharge tube and the occurrence of the plasma discharge. Assumptions of a similarly conservative nature have been made in other subsystem designs as well as in proposed monitoring, control, and maintenance procedures. The freedom to select conservative parameters is in part afforded by the preliminary, conservative nature of the SFTR design; ultimately, however, the cost vs benefit relationship must be examined in more detail.

5.6.2 Physical, Chemical, and Radiological Nature of Tritium[1,2,3]

Tritium is a radioactive hydrogen isotope of mass three. It decays by emission of a β^- particle forming three-helium. The emitted β^- particle has a maximum energy of 18.6 keV and an average energy of 5.6 keV. The half-life of tritium is $\sim$12.3 yr. Chemically, tritium undergoes the same reactions as normal hydrogen.[3]

The radiological hazards associated with tritium are related to the fact that tritium gas will oxidize to form tritiated water.[4] Tritium will also undergo an isotopic exchange reaction with water:[5]

$$T_2 + H_2O \rightarrow HT + HTO \quad . \qquad (1)$$

This water mixes rapidly with body water and is then rapidly eliminated from the body. The biological half-life of tritium in oxide form is 6-14 days.[3]

The maximum permissible concentration[6] of tritium as T_2O or HTO in air (MPC_a) in controlled areas is 5 μCi/m^3. In practice this number is used in lieu of the number of 2000 μCi/m^3 for T_2 when the chemical form of the tritium is not known with certainty. The occupational maximum permissible body burden for individuals is 1 mCi.[6]

In uncontrolled areas the MPC_a for tritium as the oxide is 0.2 μCi/m^3, which is the maximum 24-h average concentration that will exist in the SFTR stack. For individuals in controlled or uncontrolled areas, the maximum dose equivalent resulting from operation of the SFTR facility will not exceed the then-current government limits.

Evidence[7-13] exists that tritium entering the body as the oxide slowly exchanges with the hydrogen of the organic molecules. Tritium from tritiated water is known to be assimilated in the organic constituents of other forms of plant and animal life.[13] Should tritiated proteins enter the human body in vegetable, dairy, or meat products, the in-body residence time for tritium in human tissues might be increased considerably. As a result, the decay of tritium so incorporated in biologically active substances could conceivably result in increased somatic and genetic (e.g., tritium in thymidine[3]) damage to body tissue. Clearly, further experimental work is needed on the effects of low levels of tritium on biological systems.

Releases of tritium to the environment must be sufficiently low that tritium concentrations in man or his food chains do not increase to critical levels. The maximum permissible water and air concentrations listed in Table 5.6-1 reflect this concern. Since tritium appears in the environment predominantly as tritiated water (HTO), the related radiation dose to man is strongly dependent on the local hydrologic cycle. An atmospheric source of tritium may contaminate a local landscape either by direct deposition of moisture or by exchange of tritiated water molecules of the atmosphere with ordinary water of soils, plant, animals, and surface waters. Once contaminated, soils, plants, and animals can carry tritium to man through the food

To insure a reliable vacuum cleanup of tritium in event of a local rupture of the discharge tube, the gettering of $(D,T)_2$ along with any air which ingresses must be done by the LN_2-cooled roughing pump. Therefore, the roughing pump must be maintained at LN_2 temperatures during the D-T experiment, and the cost of this readiness may be high.

TABLE 5.6-1

SUMMARY OF IMPORTANT RADIOLOGICAL, BIOLOGICAL, AND CHEMICAL CHARACTERISTICS OF TRITIUM

Mode of decay	$^3H \rightarrow {}^3He + \beta^-$
Radiological half-life (yr)[14]	12.26
Decay rate (%/day)[14]	0.01548
Average beta energy (keV)[15]	5.593
Specific activity (Ci/m^3)	2.6×10^6 (9670 Ci/g)
Decay energy density (W/g)	0.3206
Max permissible body burden (mCi)[6]	1.0 (23 μCi// body water)[a]
Biological half-life (days)[3]	6-14
MPC_a as HTO or T_2O in air ($\mu Ci/m^3$)[1]	5.0[b], 0.2[c]
MPC_w tritium in water ($\mu Ci/cm^3$)[1]	0.1[b], 0.003[c]
$^{30}LD_{50}$ lethal dose (Ci)[16]	4.5
Explosion limits at 1 atm in air, %[17]	4.0-74.2

[a] *For radiation workers.*

[b] *Concentrations in a controlled area.*

[c] *For public.*

chain. An example of such a pathway is the soil-plant-cow-milk-man food chain. The total dose to man from such a pathway depends on the turnover and replacement rate of tritium in each link of the pathway. In general, the overall turnover rate in a given ecopathway depends on the rate of the slowest transport mechanism. Tritiated soil water has turnover times ranging from 24 days in the tropics to 1.7 yr in the desert. In temperate zones, turnover time for soil water in the rooting zone of plants may vary from 30 to 120 days, depending on location, soil type, and season of the year. Intrinsic turnover rates in plants, animals, and man are much faster.

Table 5.6-1 summarizes those characteristics of tritium which will have a direct impact on the SFTR design. An ever-present problem associated with routine tritium handling is the tendency toward isotopic exchange with normal hydrogen in any hydrogenous material. Subsequent to isotopic exchange, the hydrogenous materials will undergo self-irradiation and thereby suffer radiation damage.[3] Also the daughter ^3He resulting from decay will tend to collect in the material. The low solubility of helium in most materials generally causes extreme property changes (swelling, embrittlement, etc.). Oils and plastics are particularly susceptible to these problems. It is therefore highly advisable to design tritium facilities so that the use of organic materials is minimized.[18] This means using metal gaskets on flanges and connectors, using all-metal valves and fittings whenever possible, and employing oil-free vacuum systems. In essence, all components used in a tritium facility must be carefully scrutinized with respect to possible tritium pickup either by isotopic exchange or by tritium adsorption on surfaces.[18]

Hydrogen embrittlement is an additional concern in systems handling hydrogen gas and, in particular, tritium gas. To avoid this problem the low 300-series stainless steels or copper are recommended for use in tritium systems. There is evidence that the presence of tritium can lead to enhanced hydrogen embrittlement,[19] but systems can be easily designed to avoid this problem. The primary mechanism for enhanced hydrogen embrittlement by tritium is the reduction of oxide films on the metal. Such films retard the diffusion of hydrogen by acting as a protective layer in which the diffusion of hydrogen is molecular and hence slow. A second factor results from the helium formed by decay of the tritium dissolved in the metal. (The helium is insoluble and has a low permeability constant in metals.[20]) Also, gaseous hydrogen and, in particular, tritium, will tend to leach carbon from stainless steels thus forming tritiated methane. This reaction is more probable with SS-304 than with SS-316. The use of SS-316 throughout the tritium handling facility is therefore recommended.

The intent of this summary is to present the major constraints associated with the use of gram quantities of tritium. Detailed descriptions of significant, specific experiences associated with handling gram quantities of tritium can be found elsewhere.[18] The problems associated with tritium containment are widespread, particularly for high-temperature applications. But the SFTR is a room temperature device and many of the containment problems can be alleviated by proper design and anticipated maintenance procedures, so tritium containment (e.g., against low chronic releases) should not be difficult in the SFTR.

5.6.3 Description of Subsystems

The primary functions of the tritium handling system are the storage injection and recovery of tritium gas. Cleanup and waste treatment functions are identified as either routine or nonscheduled. The following sections describe the operation (storage, injection, recovery) as well as the cleanup function of tritium handling.

Figure 5.6-2 illustrates the fueling/recovery aspects of the tritium handling system. Gaseous tritium from a passive storage vault is transferred weekly to a uranium bed in ~0.3-g quantities. The quantity of tritium gas required for a daily series of D-T discharges (typically 4 discharges/day at ~15 mg/discharge) is transferred from the uranium bed to a preinjection space, where measurements and sampling occur. An amount of gas desired for a given discharge is metered and mixed with D_2 and transferred to four holding volumes located at each of four vacuum pumping stations within the SFTR cell. The vacuum system is isolated from the SFTR discharge tube, the $(D,T)_2$ gas at each of the four staging areas is injected into the discharge tube, and the discharge is triggered. The spent $(D,T)_2$ gas [~0.01-0.03% burnup, $(H,D,T)_2O$ contaminated] is collected at the cryogenic pumping stations, which have been open to the discharge tube subsequent to the discharge. The collected $(D,T)_2$ gas undergoes a vacuum transfer via a cryogenic pump to a second uranium bed and is stored thereon for one week; samples of spent $(D,T)_2$ are easily retrieved for postdischarge diagnostics (Sec. 5.6.4.3). After a week of operation the ~0.3 g of tritium that was initially absorbed in the uranium bed used for tritium supply now is absorbed in the recovery bed. Each week the tritium in the recovery bed is transferred and stored in the passive storage facility vault and a clean, 0.3-g tritium supply is transferred to the tritium supply bed. Approximately every 2 months the tritium in the vault (~3 g) is exchanged for a new tritium supply obtained from an off-site source.

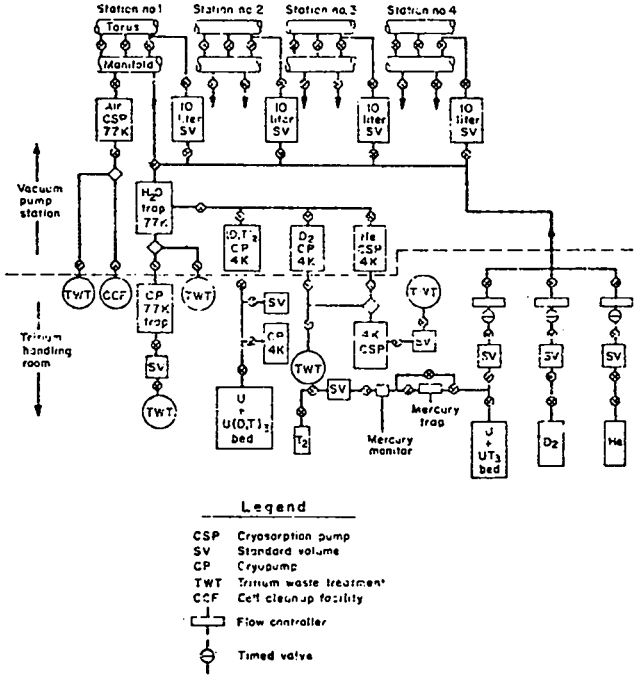

Fig. 5.6-2.
Schematic diagram of tritium fueling/recovery system.

The tritium cleanup scheme operates at two levels: a low-flow cleanup (7 ℓ/s) Tritium Waste Treatment (TWT) system for routine and chronic tritium release and a high flow cleanup 4700-ℓ/s Cell Cleanup Facility (CCF) for accidental releases. In both systems the tritium is first oxidized in the flowing air stream and then dried. All tritium handling equipment is located in hooded chambers which ventilate to the TWT. The air within the SFTR cell is continually replaced and monitored for tritium and other activities. The tritium concentration within the exhaust air is continually monitored to determine whether cleanup in the CCF is required before stacking.

5.6.3.1 Tritium Storage Facility

The tritium storage facility comprises two major components: a passive storage vault for secure storage of gaseous tritium, and an active tritium supply which enables tritium to be stored on a uranium-uranium tritide bed. Tritium gas will be desorbed from the uranium bed on demand to provide gas for the SFTR injector system, whereas reserve or spent tritium will be kept in the vault.

Tritium gas will be received from the ERDA supplier as gas in DOT-approved tanks and will be stored in the vault. A portion of this gas (~300 mg) will be absorbed in the uranium bed each week, and the tank with its contained gaseous tritium will be returned to the vault. The vault is secured with fireproof and blastproof walls and security door. This vault will permit close control over access to the bulk of the 7-g maximum of tritium expected to be on-site at any given time. When the bulk of the tritium is stored in this area, it will not be subject to release in any credible accident.

The vault (Fig. 5.6-3) will have a ventilation system (~7 ℓ/s) so the air in the vault can be processed by the TWT or CCF if necessary. For instance, if a tritium tank should develop a leak, the tritium can

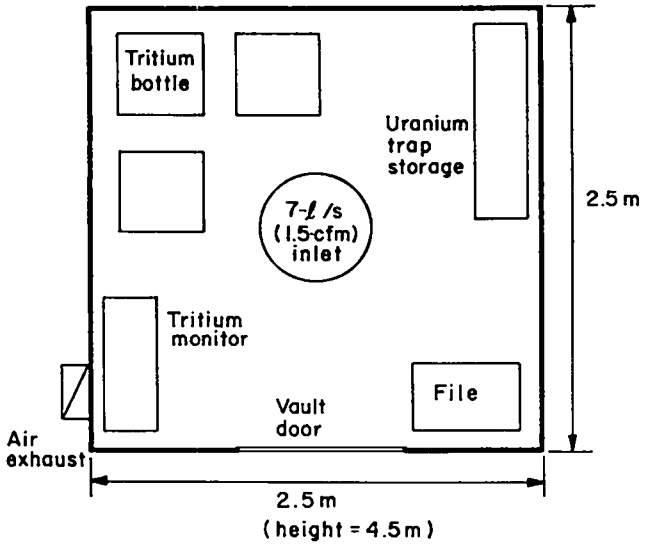

Fig. 5.6-3.
Layout of tritium vault.

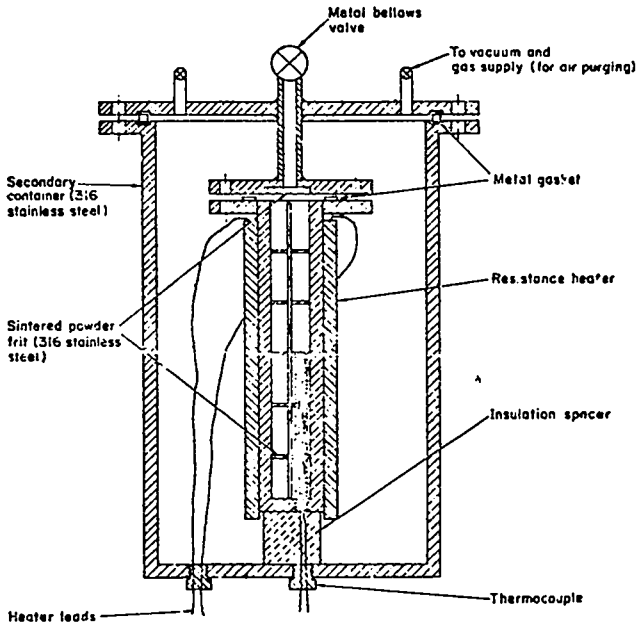

Fig. 5.6-4.
Detail view of uranium bed.

be isolated in the vault by appropriate valve closures, and the air in the room processed at a slow rate to remove all tritium before release to the atmosphere. The vault air will be continuously monitored for tritium.

The active storage facility consists of an all-welded, SS-316 uranium bed on which a 1-wk supply (~0.3 g) of tritium can be stored as the tritide. The details of the uranium bed are shown in Fig. 5.6-4. The uranium bed will contain ~50 g of uranium, which can absorb about 2 g of tritium, although the bed will not be charged with more than the 1-wk supply (~0.3 g).

Tritium will be reacted with the uranium bed as follows. A tank containing gaseous tritium will be removed from the vault, connected to the uranium bed, and the gas lines evacuated. Tritium gas will then be admitted to the calibrated volume on the inlet line until the pressure in that volume corresponds to a tritium charge of 0.3 g. After equilibrium is reached in the calibrated volume, the pressure readings will be recorded and the gas composition determined by a mass spectrometric analysis. The tritium within the standard volume will then be admitted to the uranium bed at a rate such that no significant temperature rise occurs in the uranium bed. This charging process will occur each week, and careful records will be maintained on the quantity of tritium added to the uranium bed at each charging.

Each day the uranium-uranium tritide bed will be heated (623-673 K) to decompose the uranium tritide to produce the daily tritium requirement. The dissociation pressure of tritium vs uranium is 101.33 kPa and 19.98 kPa, respectively, at 665 and 595 K. The equilibrium dissociation pressure of tritium vs uranium is given by the equation

$$\log P_{atm} = \frac{-3372.6}{T} + 4.974$$

for the temperature range 393 to 623 K and by

$$\log P_{atm} = \frac{-4038.2}{T} + 6.074$$

in the temperature range 623 to 845 K.[21] The tritium gas desorbed from the uranium bed will be essentially free of ^3He formed by tritium decay. Included in the uranium bed heater circuit will be a thermal over-ride switch set at ~700 K so that all electrical power to the bed heaters will be cut off in event of a thermal excursion.

The uranium bed will be heated once a day, at which time an amount of tritium adequate for all anticipated D-T shots for that day is desorbed. This tritium gas will pass directly into the thermostated, calibrated volume in the injector system.

As with other major components that handle tritium, the uranium bed will be redundant, and one bed will always be available. The uranium beds will be connected to the gas lines by compression fittings

using metal-to-metal seals such as the Cajon UCR[22] Haskel 'K'[23] types, both of which use metal gaskets. A standard purge system with valves on both sides of the connectors will be used. The valves will be of the metal bellows variety (similar to the Nupro U series).[24] These valves will operate effectively at the temperatures and pressures involved. The gas pressure in the system will be measured by an electronic capacitance manometer such as the Baratron system made by MKS Instruments, Inc.[25]

The entire active storage system will be enclosed in a hood that will also enclose the main portion of the tritium injector system. The hood can be isolated from the room air, permitting the processing of hood air through the 7-ℓ/s TWT system. The hood air can also be sent directly to the larger cell cleanup system in case a (large) tritium spill dictates rapid cleanup of the air. However, during routine maintenance and equipment replacement the 7-ℓ/s system is anticipated to adequately remove tritium from the hood air.

A sequence of events must be considered which would result in the release to the hood of all of the tritium on the uranium bed. Such a release would correspond to a maximum of 0.3 g, if it were to occur immediately after the uranium bed had been charged. If the spill bypassed the hood and entered the tritium handling room,the larger cell cleanup system would be used to remove tritium from the air. However, the spill could be expected to be confined to the hood area, and the smaller TWT would be used to remove the tritium. This 0.3 g or 3000 Ci would go to the 7-ℓ/s TWT ballast tank where it would be mixed with some 2 m^3 of air at ~2.5% relative humidity. The tritium concentration would then be 1500 Ci/m^3. At the exhaust from the TWT the concentration would have been reduced by a factor of 10^6 to give a concentration of 1500 μCi/m^3. This air from the 7-ℓ/s unit would then be mixed with the stack air to give a momentary concentration of 2.2 μCi/m^3. The integrated stack release after several minutes would amount to 3 mCi, and would be far below the daily tolerance of 86 mCi. Except for the 3 mCi the entire 3000-Ci release would be contained within the TWT on the molecular sieve bed.

5.6.3.2 Tritium Injection System

The tritium injection system will be supplied with tritium gas from the uranium-uranium tritide bed; deuterium and helium will be provided directly from gas bottles. The primary function of the injection system is to feed a predetermined amount of the appropriate gas mixture into the discharge tube. Schematic drawings of the flow pattern and operation of the injector system are given in Figs. 5.6-2 and 5.6-5.

The discharge tube, on the average, will be filled to a pressure of 10^{-2} torr for each shot. The torus volume is 7.89 m^3, so each shot wil require 104 cm^3 (STP) of $(D,T)_2$ gas or 13.8 mg of T_2. Although most discharges will be with pure D_2, about four shots each day will be $(D,T)_2$. Occasionally the injection gas may be a deuterium-helium mixture. The tritium gas will be supplied from the uranium bed. Each day a quantity of tritium gas sufficient to fuel all planned D-T discharges for that day will be thermally desorbed from the uranium bed and collected in the thermostated, calibrated volume shown in Fig. 5.6-5. Typically, each discharge will require 15 mg of T_2, including auxiliary systems; hence, four shots will require 60 mg or 226 cm^3 (STP) of T_2. These figures do not include the gas which must be supplied to the standard volume to provide a sufficient pressure gradient for the gas to flow from the standard volume into the injector system. Also, some gas must be left in the injector system after injection, but this quantity is a small fraction of the total amount. Therefore some 250-400 cm^3 (STP) of T_2 will have to be collected in the standard volume at the start of each day. After the gas has been collected in the standard volume, time will be allowed for the gas to reach thermal equilibrium, and the temperature and pressure will be recorded. As indicated on Fig. 5.6-5, an electronic capacitance manometer will be used to monitor pressure.

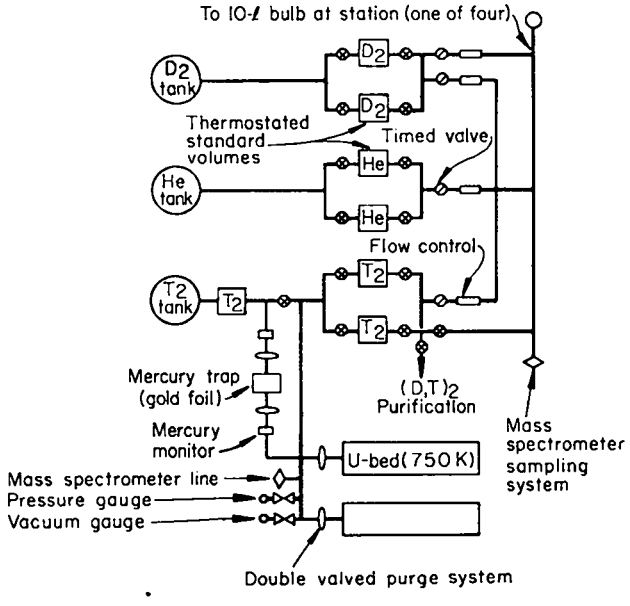

Fig. 5.6-5.
Tritium injection system.

Deuterium gas from a gas tank will be collected similarly in a calibrated volume on the deuterium inlet line and the temperature and pressure recorded. At a predetermined time before a discharge the electronically controlled timing valve on the deuterium line will open, and deuterium gas will flow through the timed valve to the flow controller. The flow controller will be similar to the Series 8240 Brooks Thermal Mass Flow Controller,[26] and will permit a predetermined flow rate of gas to flow through the controller into the lines leading to 10-ℓ gas mixing bulbs located at four pumping stations adjacent to the discharge tube. The timed valve will shut automatically when the mass of gas flowing through the controller corresponds to the amount of deuterium desired for the shot.

Tritium gas from the standard volume also will be admitted to a common gas line according to the above-mentioned sequence. The deuterium and tritium will then flow simultaneously through the common gas line into the 10-ℓ injection bulbs. In this way the deuterium and tritium will be mixed, and additional mixing will occur in the 10-ℓ bulb before injection into the discharge tube. Pressures and temperatures will be recorded routinely once equilibrium is obtained in the 10-ℓ bulbs, and the option to perform mass spectrometric analysis will be available at that time. Once the gas mixture is in the 10-ℓ gas bulb, fast-acting valves located on the vacuum downcomers (Fig. 5.6-2) immediately adjacent to each pump station will close, thereby isolating the vacuum system manifold from the discharge tube. A fast valve on the bulb will then open, allowing the gas mixture to flow into the discharge tube. During the period after closure of the vacuum valves and before discharge of the next plasma, the first wall will outgas water at an unknown rate. The goal is to have less than 0.10 at.% water in the $(D,T)_2$ gas mixture at the time of discharge. Therefore, the shot must occur as soon as possible ($<$10 s) after the gas mixture is introduced into the discharge tube. After the valve on the injection system is closed and as soon as the gas pressure in the discharge tube stabilizes, the machine will be fired. Immediately after the shot the vacuum valves will open and the vacuum system will begin to evacuate the discharge tube. At the same time the 10-ℓ bulbs will be opened to the $(D,T)_2$ cryopump to evacuate the bulbs and associated gas lines (Fig. 5.6-2). A cryosorption pump will then be used to remove the traces of ^4He from the D-T reaction, the ^3He from tritium decay, and ^3He from D-D reactions. Numerical estimates of maximum allowable outgassing rates, injection equilibration times, and vacuum time constants are given in Sec. 5.6.3.3. At the end of the day any tritium gas remaining in the standard volume will be reabsorbed in the uranium bed and the volume evacuated to remove the traces of helium.

All transfer lines on the gas injector system will be stainless-steel or ETP copper tubing.[27] The construction of the transfer lines will be such that all permanent joints will be welded. Joints that might have to be opened with any frequency will have metal gasket connectors. The standard purge system will be installed at each connector so the line can be opened with a minimum exposure to personnel. The 10-ℓ bulbs will be of stainless-steel construction with all-welded joints, and the bulbs will be carefully calibrated so that accurate PVT measurements can be performed. Capacitance manometers will be used for measuring pressures in these bulbs.

These 10-ℓ injection bulbs will be located at each of four vacuum stations to minimize pressure equilibration times after the $(D,T)_2$ injection. This scheme will require considerable piping to transfer the gas from the flow controller in the injection hood to the four stations spaced around the discharge tube (see Fig. 5.6-2). In addition, these measurements will be recorded on the deuterium and tritium standard volumes once the timed valves have closed and the gas has flowed into the injector bulbs. This procedure will provide an additional check on the amount of gas transferred to the discharge tube on each shot.

As with the storage system, all major components of the injector system will be redundant and will be fitted to the system by a standard purge system which uses double valving across all removable joints. All manual valves in the system will be metal bellows valves similar to the Nupro U series.[24]

The maximum credible release of tritium from the injector system (exclusive of the uranium bed) would be the 1-day supply stored in the standard volume. This corresponds to some 250-400 cm^3 (STP) or a maximum of 1 kCi of tritium gas. The injector system will be enclosed in the same hood as the uranium bed. The action to be taken in the event of a spill in the hood is described in more detail in Sec. 5.6.3.5. The tubing leading to the 10-ℓ injector bulbs at the vacuum stations will not be in hooded areas, but in all cases will be in the SFTR cell or in rooms where the air can be processed through the cell cleanup system and where the air is continuously monitored for tritium. The injector bulbs will be located in the hoods at each of four vacuum stations where the air circulating through the hood is directed either to the tritium waste treatment or to the cell cleanup system. The transfer tubing from the 10-ℓ bulbs to the discharge tube will be inside the

SFTR cell so that any leak in this tubing will be contained inside the SFTR cell, and the tritium can be scrubbed from this air by the cell cleanup system (Sec. 5.6.3.5).

At this point the insulator material for the first wall has not been defined, although a ceramic/glass composite is a prime candidate from a fabrication viewpoint. Hence, the amount of outgassing to be expected from the discharge tube is uncertain. Also, the rate at which the unburned D and T atoms from the plasma will react with the wall to form water is not known. If subsequent experience shows that this reaction rate is high, then the outgassing from the first wall will be correspondingly high, and the vacuum system or the discharge tube may have to be redesigned to meet the goal of ≤0.1 at.% water in the $(D,T)_2$ mixture. Also, if this outgassing rate is substantial, the water formed uniformly along the discharge tube may be swept along by the gas front when the fuel is injected into the discharge tube at the four pumping stations. This phenomenon can result in potentially severe concentration gradients of water within the discharge tube, thereby affecting the homogeneity of the final plasma. In any case, the goal will be to initiate the discharge as soon as possible after the gas is injected.

The flow rate of gas from the flow controllers to the 10-ℓ injector bulbs may be quite low through the ~200 m of small-diameter tubing; this question must be more extensively investigated. In any event, sufficient time must be allowed for the gas mixture to reach thermal equilibrium in the injector bulbs before the pressure-temperature measurements are made.

5.6.3.3 SFTR Vacuum System

Although the fundamental modes of operation for the tritium injection and recovery systems have been qualitatively discussed in other sections, the vacuum system is basic to tritium injection and recovery. Also, outgassing phenomena, pumping efficiencies and time constants, and tritium injection rates are strongly dependent upon the peculiarities of the vacuum system design. Ultimately, the success of a given plasma discharge will be dependent on the time required between tritium injection and the plasma discharge; outgassing rates and vacuum time constants play a significant role in this respect.

The following sections give an outgassing criterion by which the gross pumping schemes are considered, and a detailed description of a pumping station is presented. For the vacuum system selected, an estimate of the tritium injection time is made.

General Requirements

The essential elements of the SFTR vacuum system are shown in Fig. 5.6-6. In the simplest terms, a tube of radius R_1 and length L_1 must be evacuated by a pump of speed S (cm^3/s) under conditions where the tube is outgassing at rate G (cm^3 torr/cm^2 s).* The high aspect ratio of the SFTR discharge tube ($R_o/R_1 \sim 400$) suggests two evacuation schemes, shown schematically in Figs. 5.6-6(A) and 5.6-6(B). Figure 5.6-6(A) illustrates a discrete pumping system, whereby N independent pumping stations operate on n downcomers, which are separated by a minimum distance $L_o \sim 0.4$ m. The alternative system, illustrated in Fig. 5.6-6(B), envisions a continuous system wherein n downcomers are evenly spaced around the discharge tube at a distance L_2 equal to a multiple of the minimum distance L_o. The downcomers are attached to a continuous toroidal manifold of minor radius R_2 onto which are affixed N pumping stations. For both schemes the distance $L_1 = 2\pi R_o/N$. The minimum distance L_o is fixed by the SFTR module length, as indicated schematically in Fig. 5.6-7.

*1 cm^3 torr = 3.22 x 10^{17} H_2 molecules at 300 K.

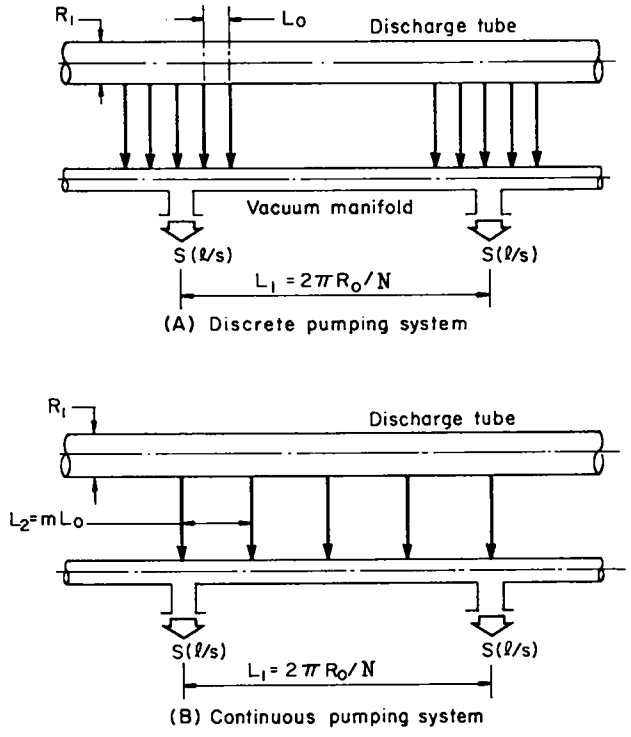

Fig. 5.6-6.
Essential elements of the SFTR vacuum system.

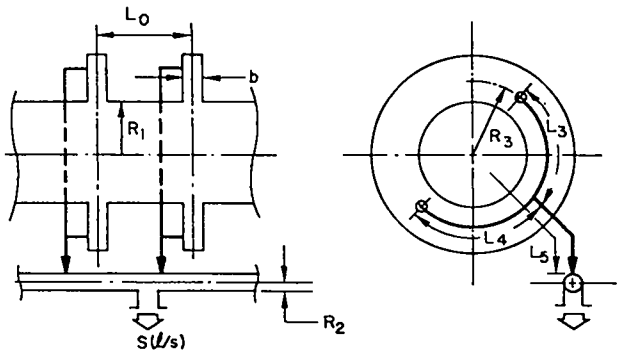

Fig. 5.6-7.
Schematic of a vacuum downcomer and its associated dimensions (b = 2 cm; $R_1 = R_2$ = 10 cm; R_3 = 30 cm; L_0 = 40 cm; L_3 = 34 cm; $L_4 = L_5$ = 60 cm).

The following design criteria and system functions must be met by the SFTR vacuum system:

- The SFTR must be capable of a 15-m duty cycle; hence the pumping time constants must be on the order of 1 to 10 s for a practical (i.e., outgassing) vacuum system.
- The use of ceramic or glass discharge tubes in conjunction with $(H,D,T)_2$ portends a serious outgassing problem. The pump speed selected for the system must produce an ultimate vacuum [i.e., $(H,D,T)_2O$ pressure] commensurate with 0.1% impurity in the $(D,T)_2$ gas just before a discharge and after the vacuum pumps have been isolated from the discharge tube for ~10 s. The discrete scheme depicted in Fig. 5.6-6(A) involves a lower total volume than the continuous scheme, although a higher vacuum conductance is associated with the shorter tube length L_1 for the continuous system. A steady-state impurity level will exist along the constantly outgassing discharge tube for the discrete scheme. The pressure gradient associated with large values of L_1 is considerably reduced by the continuous scheme of Fig. 5.6-6(B), although the added manifold volume may be a disadvantage. When the design criteria are satisfied, the choice between the two schemes must be based on relative simplicity, determined by the system with a minimum number of downcomers, n, for a given number of pumping stations, N, as well as the complexity of the plenum or manifold.

Before the system is determined, a qualitative estimate of the overall pumping requirements must be made. If S (cm^3/s) is the total pumping speed required for the system which is outgassing at a rate G (cm^3 torr/cm^2 s), the time response of the pressure in the generalized system shown in Fig. 5.6-6(A) can be described by

$$(\pi R_1^2 L_1)\, dP/dt = -SP + (2\pi R_1 L_1)G . \qquad (2)$$

At equilibrium the pressure is given by $P_{EQ} = 2\pi R_1 L_1 G/S$. If the outgassing rate continues once the vacuum pump is isolated from the discharge tube, the pressure at some time t after the valve closure is given by

$$P(t) = (2/R_1)G[\tau_p + t] , \qquad (3)$$

where $\tau_p = (\pi R_1^2 L_1)/S$ is defined as a pumping time constant.

If P_o represents the $(D,T)_2$ filling pressure and $f = P(t_B)/P_o$ represents the fractional impurity level allowable at the time t_B when discharge occurs, Eq. (3) can be used to estimate τ_p, given the outgassing rate G. For instance, if the fraction f_R of the $(D,T)_2$ injected during a previous discharge reacts with the discharge tube to form $(D,T)_2O$, which is subsequently adsorbed onto the tube wall, then the mean outgassing rate established at equilibrium for a pumpout time t_p between discharges is given by

$$G = (R_1/2)\, f_R P_o/t_p . \qquad (4)$$

Substituting Eq. (4) into Eq. (3) and rearranging yields the following expression for τ_p

$$\tau_p = (f/f_R)t_p - t_B . \qquad (5)$$

Hence, for t_B = 10 s, t_p = 600 s, $f = 1.0 \times 10^{-3}$, and $f_R = 5.5 \times 10^{-2}$, τ_p = 1 s. Since the volume of the SFTR discharge tube is $(\pi R_1^2)(2\pi R_o) = 7.89 \times 10^6$ cm^3, the total pumping speed should be at least 7.89×10^6 cm^3/s (7900 ℓ/s). For this minimum value of pumping speed, the base pressure in the discharge tube would be 1.83×10^{-6} torr and the mean outgassing rate would be 9.17×10^{-7} cm^3 torr/cm^2 s (2.95×10^{10} molecules/cm^2 s) for a filling pressure P_o of 10^{-2} torr.

Because of the simplifying assumptions upon which Eq. (2) and the estimate of G are based, the above numerical results are probably accurate within an order of magnitude. The chemistry of water formation, adsorption, and desorption is complex and not well understood for the conditions anticipated for the SFTR vacuum wall. Furthermore, the distributed vacuum conductance represented by the model given in Fig. 5.6-6(A) will lead to pressure gradients at equilibrium when the wall is outgassing. For the latter case Eq.(2) must be replaced by

$$(FL_1/\pi R_1^2)(d^2P/dx^2) = - (2\pi R_1 L_1 G)/\pi R_1^2 L_1) + (dP/dt) , \qquad (6)$$

where F (cm^3/s) is the vacuum conductance of the discharge tube,[20]

$$F = 3638 \sqrt{T/M}\, \pi R_1^2\, \kappa(R_1/L_1) \tag{7}$$

$$\kappa(R_1/L_1) \simeq 1/(1 + 3L_1/8R_1) \tag{8}$$

and x is the distance along the tube. If P_i represents the initially uniform pressure and P_s represents the (low) pressure at the pump stations the solution to Eq. (6) is[28]

$$\frac{P_{(x,t)} - P_{(x,\infty)}}{P_i - P_s} = \sum_{n=1}^{\infty} \left(\frac{4}{\beta_n}\right) \cdot \left[1 - \alpha/(\pi\beta_n)^2\right] e^{-\beta_n^2 \tau} \sin(\beta_n \xi), \tag{9}$$

where

$$\alpha = 2\pi R_1 L_1 G/P_i F$$

$$\beta_n = (2n + 1)\pi/2$$

$$\xi = x/L_1$$

$$\tau = (F/\pi R_1^2 L_1)t$$

$$P_{(x,\infty)} = P_s + (\alpha/2)\,\xi(1 - \xi).$$

Defining an average pressure within the tube,

$$\langle P \rangle \equiv \int_0^{L_1} P(x,t)\,dx/L_1$$

$$\frac{\langle P\rangle_\tau - \langle P\rangle_\infty}{P_i - P_s} = \sum_{n=1}^{\infty} \frac{8}{\beta_n^2}\left[1 - \frac{\alpha}{(\pi\beta_n)^2}\right] e^{-\beta_n^2\tau} \tag{10}$$

$$\langle P\rangle_\infty = P_s + (\alpha/12)(P_i - P_s). \tag{11}$$

At equilibrium, $\langle P\rangle_\infty = \pi R_1 L_1 G/6F$, which equals $S/12F \sim 1/[12\kappa(R_1/L_1)]$ times P_∞ obtained from Eq. (2). For $R_1/L_1 \ll 1$, this difference amounts to $\sim L_1/32R_1$. Furthermore, the maximum value of pressure at equilibrium equals $\pi R_1 L_1 G/4F$, or $P_{MAX}/\langle P\rangle = 3/2$. These differences tend to underestimate pump sizes and time constants predicted by Eq. (2). The assumed ~5% reaction of $(D,T)_2$ to form water is undoubtedly high, and the overestimation of G will compensate the nonconservative errors introduced by the use of Eq. (2). Furthermore, the major outgassing problem will probably occur during the thermonuclear burn as a result of bremsstrahlung and ion irradiation of the vacuum wall.

Determination of Manifolding Scheme and Pumping Requirements

The calculations and results of the previous section give the gross vacuum requirements based on a relatively conservative outgassing restriction. Whether a 1-s time constant can be achieved with 8000 ℓ/s of total pumping must be determined by calculations which pertain to a specific arrangement of pumping stations and downcomers. As indicated in Figs. 5.6-6(A) and 5.6-6(B), the possibility exists of either discretely or continuously manifolding the downcomers from a module to the pumping station. The system with the minimum number of downcomers per pumping station, n, and the minimum number of pumping stations, N, is obviously preferred.

Since a fast-acting isolation valve is associated with each downcomer, maintenance and reliability requirements dictate as few downcomers as possible. Each pumping station, described in the following section, must be rated at ~8000/N (ℓ/s) and will function as a separate, self-contained unit that can be separately removed and replaced. The desirability of minimizing the tritium injection/recovery function and the cryogenic (liquid helium and liquid nitrogen) requirements associated with each pump station provide a strong motivation for minimizing N. On the basis of the latter logistical considerations, N is fixed at 4, giving S = 2000 ℓ/s for each pump station.

By neglecting the vacuum conductance associated with the length L_2 of discharge and manifolding between downcomers, an optimistic upper limit can be placed on n. Since the maximum number of downcomers equals $2\pi R_o/2L_o = 314$ (L_o = 40 cm, R_o = 40 m), the fraction of modules with downcomers, f_{DC}, equals

$$f_{DC} = (S/F_{DC})(L_o/\pi R_o) \tag{12}$$

where F_{DC} is the downcomer conductance and S is the pumping speed of a pump. Figure 5.6-7 illustrates the downcomer geometry and nominal dimensions. The vacuum conductance of the "brim" of the "top hat" was estimated using a square duct geometry[20] with dimensions a = $\pi(R_1 + R_3)$, b, and c = $(R_1 - R_3)$. Standard tabulations[20,29] were used for the conductances of elbows and tubing. In this way the downcomer conductance F_{DC} from the discharge tube to the vacuum manifold was estimated to be ~80 ℓ/s for the dimensions given in Fig. 5.6-7. Introduction of two high conductance valves (130 ℓ/s) into the downcomer reduces F_{DC} to ~50 ℓ/s. By plumbing both sides of a given "top hat," F_{DC} in principle can be increased to ~73 ℓ/s. For F_{DC} = 50 ℓ/s, the fraction of modules with downcomers given by optimistic predictions of Eq. (12) is 51%; if F_{DC} = 73 ℓ/s, then f_{DC} becomes 36%.

These preliminary estimates neglect the conductance of the discharge tube and vacuum manifolding located between downcomers, and indicate that under the most optimistic conductions ~110 downcomers will be required to achieve the 1-s time constant. With N = 4 pump stations, L_1 = 62.8 m of torus are evacuated by each pump station, and 28 downcomers/station would be required. The discrete pumping scheme would require 22.4 m of manifolding for each quadrant of the discharge tube, whereas for the continuous scheme one downcomer would be required for every ~4 modules (L_2 = 2.4 m).

To account for toroidal vacuum conductance and the vacuum dynamics, the NET-2 computer code[30] was used to solve the equivalent electrical circuit depicted in Fig. 5.6-8 for the continuous and discrete schemes depicted in Fig. 5.6-6. The effective toroidal conductances between downcomers (F_T or F_M) were obtained by using mean pressures, differentiation of Eq. (10) after the higher harmonics have decayed, and identification of an effective conductance. The effective conductance equals the conductance of a tube of length L and radius R [Eq. (7)], increased by the factor π^2. Figure 5.6-9 gives the dependence of the pumping time constant, τ, on f_{DC} for N = 4 and equal discharge-tube and manifold radii ($R_1 = R_2$ = 10 cm) for the two manifold schemes considered and for three values of F_{DC} (50, 75, 100 ℓ/s).

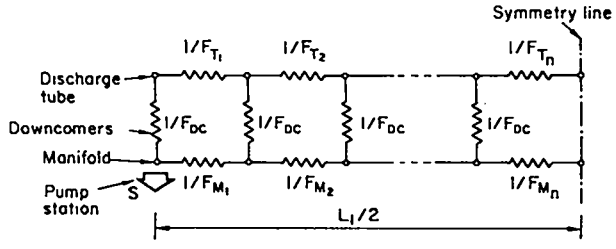

Fig. 5.6-8.
Electrical analogue used to model the SFTR vacuum system with the NET-2 computer code.[30]

As with the sizing of most complex vacuum systems, the numerical results presented here must be considered approximate. Although theoretically sound, these computations often give results which are invalidated when the physical constraints of assembly and the outgassing of real surfaces occur in the actual system. The Scyllac experiment[31] provides a vacuum experience with which to relate the foregoing computations. Table 5.6-2 compares the vacuum characteristics of Scyllac with those computed for the SFTR.

For all cases considered, the discrete manifolding scheme offers the potential for smaller vacuum time constants when compared to the continuous manifolding scheme for similar values of f_{DC} (total number of downcomers), nF_{DC} (downcomer vacuum conductance). For F_{DC} = 100 ℓ/s the desired 1-s time constant can be achieved with f_{DC} ~ 60% (nN = 188 downcomers). For each quadrant ($L_1 = 2\pi R_o/N$ = 62.75 m) 37.6 m of the torus are occupied by downcomers; the toroidal distance between extreme downcomers, therefore, is 25.15 m. As noted previously, the maximum pressure at the center of an outgassing tube of length L and radius R is given by $\pi RLG/4F$, where G (cm^3 torr/cm^2 s) is the constant outgassing rate and F is the tube conductance [Eq. (7)]. Using the maximum allowable value of G (9.17×10^{-7}) previously determined, and equating L and R to 2515 cm and 10 cm, respectively, an estimate of the maximum pressure differential can be obtained. The $(D,T)_2O$ pressure between

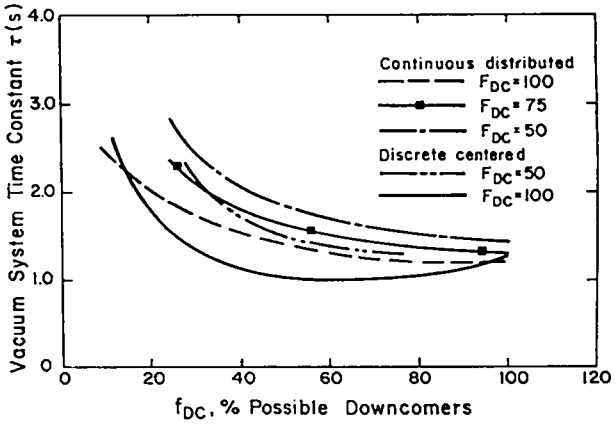

Fig. 5.6-9.
Dependence of the vacuum time constant on f_{DC} for 4 pumping stations and F_{DC} = 50, 75, and 100 ℓ/s. A comparison between continuous and discrete pumping schemes is shown.

TABLE 5.6-2

COMPARISON OF SFTR VACUUM DESIGN WITH SCYLLAC

Parameter	Scyllac[31]	SFTR
Major radius, R_o(m)	4	40
Minor radius (vacuum), R_1(cm)	4.4	10
Volume, V(ℓ)	153	7900
Discharge tube surface area, A(m^2)	6.9	160
Circumference, C(m)	25.1	251
Downcomer conductance, F_{DC}(ℓ/s)	10-12[a]	50-73
Number of pumping stations, N	3	4
Number of downcomers/station, n	3.3	47
Total number of downcomers, nN	10	188
Pumping speed/station, S(ℓ/s)	260	2000
Total pumping speed, NS(ℓ/s)	780	8000
Distance between pump stations, L_1 (m) = $2\pi R_o/N$	8.73	62.8
Distance between downcomers, L_2 (m) = L_1/n	2.51	1.34 (av)
Vacuum time constant, τ(s)	1	1

[a] *F_{DC} for Scyllac is limited by a perforated plate which is placed in the throat of the downcomer for first-wall continuity and is not limited by tubular conductances. The need for such a plate is obviated by the SFTR design.*

pump stations will be approximately twice the latter value. Since previous estimates indicate that a base pressure of ~1.86 x 10^{-6} torr would be adequate for the above value of G and a 0.1% impurity level in the predischarge $(D,T)_2$ gas, the pressure difference of the order of 1.25 x 10^{-6} torr should present no problems.

In summary, the design for a 1-s time constant and ~5%/shot $(D,T)_2$ reaction with the wall presents a conservative system; this design will probably give the desired preshot purity and the facility for rapid (15-min) discharge rate. The major cost of these design restrictions and conservatism is embodied in the large number of isolation valves and downcomers (f_{DC} = 60%, nN = 188) required. By either decreasing the requirements on τ or increasing F_{DC}, N can be decreased and the cost reduced. In view of the uncertainties associated with vacuum wall outgassing and reaction rates, the conservatism built into the above results is warranted in the absence of definitive experimental results.

Estimation of $(D,T)_2$ Injection Time Constant

As discussed in Sec. 5.6.3.2, the premeasured $(D,T)_2$ volume will be injected into the SFTR discharge tube through 4 downcomer sets located at each pumping station. The last stage of the injector volume, V_I, and the preinjection pressure, P_I, within this volume is such that P_IV_I equals 1/N = 0.25 of the $(D,T)_2$ gas requirement for a given shot (i.e., $2P_oR_o(\pi R_1^2)/N$. Although flow in the vicinity of a given injector downcomer will be first turbulent and then viscous, the estimate of the injection time given below is based solely on free molecular flow and should, therefore, give conservative results.

The geometry used for the estimation is depicted in Fig. 5.6-10 where the distance between pump stations is $L_1 = 2\pi R_o/N$ (31.4 m). After the discharge tube is evacuated to a low pressure (10^{-6} to 10^{-7} torr), all nN downcomers are isolated from the vacuum manifold, and four prefilled volumes, V_I, of $(D,T)_2$ are opened through a high conductance line and valved to the evacuated discharge tube. The $(D,T)_2$ filling gas is discharged through the primary conductances F_L and F_{DC}. The pressure within the discharge tube at the injection point, P (x = $\pm L_1/2$, t), is assumed to be described by

$$P(x = \pm L_1/2, t) = P_o(1 - e^{-t/\tau_I}), \quad (13)$$

where P_o is the final $(D,T)_2$ filling pressure and τ_I is the injector time constant, assumed here to equal V_I/F_{DC}. Neglecting outgassing during the $(D,T)_2$ injection stage, the pressure within the discharge tube at a nondimensional position $\xi = 2x/L_1$ and time $\tau = (2F_L/\pi R_1^2 L_1)t$ is given by a solution to

$$d^2P/d\xi^2 = dP/d\tau \ . \qquad (14)$$

Equation (13) gives the boundary conditions, and a zero pressure initial condition is assumed. The solution of Eq. (14) is,[28]

$$P(x,t)/P_o = 1 - \frac{\cos(\rho^{1/2}\xi)}{\cos(\rho^{1/2}/2)}\, e^{-\rho\tau} - 4\rho \sum_{n=0}^{\infty} \frac{(-1)^n e^{-\beta_n^2 \tau}(\cos \beta_n \xi)}{\beta_n(\rho - \beta_n^2)} \qquad (15)$$

where

$$\rho = \tau_L/\tau_I$$

$$\tau_L = \pi R_1^2 L_1/2F_L$$

$$\tau_I = V_I/F_{DC}$$

$$\beta_n = \pi(2n + 1) \ .$$

The total amount of gas injected into a quadrant of the discharge tube at time t equals

$$M(t) = \pi R_1^2 \int_{-L_1/2}^{+L_1/2} P(x,t)\, dx = V \langle P \rangle_t ,$$

where $\langle P \rangle_t$ is the spatially averaged pressure at a given time. Integration of Eq. (15) gives

$$M(t)/VP_o = 1 - (2/\rho^{1/2}) \cdot \tan(\rho^{1/2}/2) e^{-\rho\tau} + 8 \sum_{n=1}^{\infty} \frac{e^{-\beta_n^2 \tau}}{\beta_n^2 (1 - \beta_n^2/\rho)} \ . \qquad (16)$$

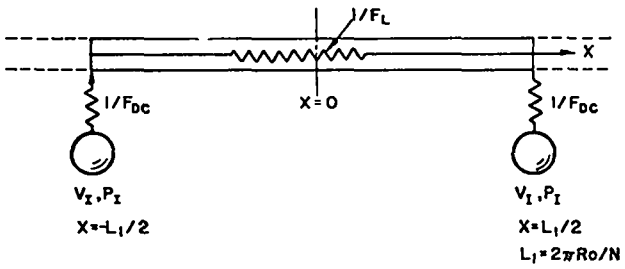

Fig. 5.6-10.
Schematic of model used to estimate DT injection time.

The dependence of $M(t)/M(\infty)$ on time and $\rho = \tau_L/\tau_I$ is given[28] in Fig. 5.6-11. Using Eq. (7) for F_L (~75 ℓ/s), τ_L is estimated to be 13.2 s. If f_I is the volume ratio $\pi R_1^2 L_1/2V_I$, then $\tau_I/\tau_L = (F_L/F_{DC}/f_I)$. Since F_{DC} equals 50-75 ℓ/s, the ratio τ_L/τ_I is approximately equal to f_I, which in turn is 16.5-25. For these system parameters pressure equilibrium is expected to occur for $2(t/\tau_L)^{1/2}$ ~1.5, or $t/\tau_L = 0.56$ and t ~ 7.4 s. The 7.4-s value is within the 10-s period allocated between the isolation of the discharge tube and the actual plasma discharge.

Description of Pumping Stations

Four pumping stations will be equally spaced around the torus. After a shot, gas will be pumped from the discharge tube via downcomers that connect the discharge tube to a pump manifold. The manifold may circle the discharge tube.

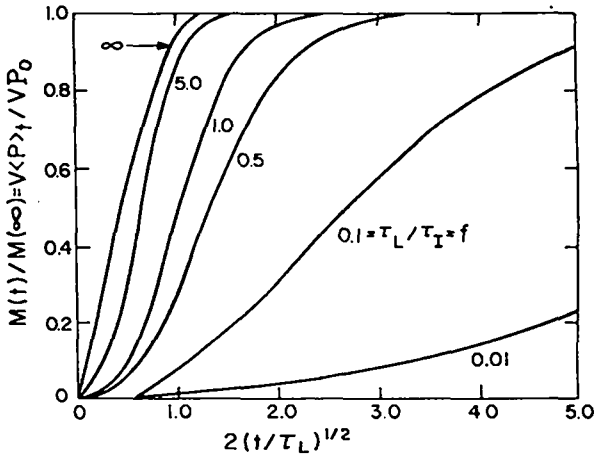

Fig. 5.6-11.
Dependence of D-T injection time on injector time constant and vacuum time constant of the discharge tube.[28]

Since the D_2 or $(D,T)_2$ gas is dissociated, reaction of atomic hydrogen with the discharge tube wall is certain to take place[32,33] to a degree that depends on the life of the atomic hydrogen, the nature of the inner wall, and the time of contact. Further, the $(D,T)_2O$ that is formed will be adsorbed on the wall to an extent determined by the pressure of the $(D,T)_2O$, the nature of the wall, and the adsorption time. Thus, to minimize the introduction of $(D,T)_2O$ impurity in a subsequent gas charge, the time between firing and gas evacuation should be minimized. Also, as discussed in Sec. 5.6.3.2, the time between cessation of pumping and the firing of a charge should be minimized. These considerations indicate the desirability of using fast-acting valves on the evacuation ports.

Accordingly, each downcomer will be equipped with a pneumatically operated fast-acting valve with effective opening and closing times of 1 s or less. Because valve seat replacement may be frequent, a second valve will be located between the first valve and the discharge tube pump-out disc to allow isolation of the discharge tube during such periods. This second valve serves the same function during valve seat replacement in fast-acting injection valves. The "through" leak rate of these valves is not critical, and can be as high as 10^{-5} and 10^{-2} ℓ/s for the inlet and all exhaust valves, respectively.

The manifold(s) connected to the valved downcomers is joined to a pumping station that serves to remove the gas rapidly from the discharge tube. In addition, the station serves to separate the components of the gas to allow better recovery and analysis of the $(D,T)_2$, analysis of the amount of wall reaction, and a PVT analysis of the degree of burn in the D-T reaction. A drawing of the pumping station is shown in Fig. 5.6-12. The station is surrounded by a ventilated hood to isolate accidental tritium leaks in the injection and evacuation lines and to provide protection for personnel during maintenance on these lines. Figure 5.6-13 gives a schematic layout of the SFTR vacuum system.

Redundancy in the pumping stations is provided by four pumping stations (this number was selected for other reasons, namely, to increase the speed of evacuation to a predetermined value, as discussed in Sec. 5.6.3.3). Also some redundancy is provided in the station itself.

The evacuated gas is assumed to have a pressure of 10^{-3} torr at the traps and pumps to assure effective separations of gas components. Final plans may possibly require a short-term use of a throttling valve during a given pump-down to achieve this pressure.

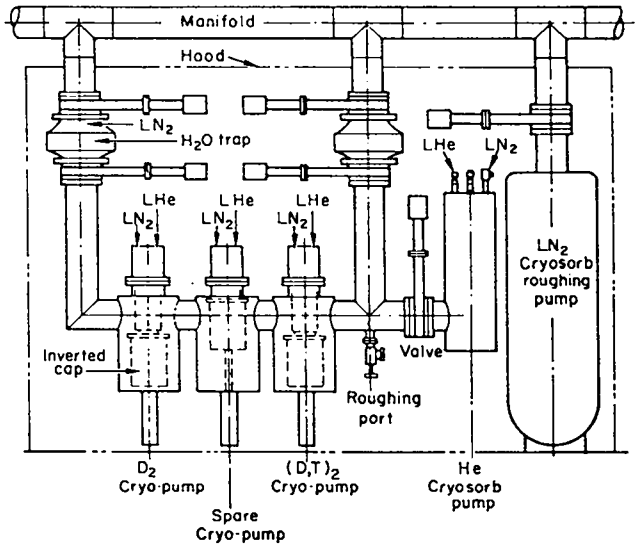

Fig. 5.6-12.
Isometric drawing of one of four SFTR pumping stations.

The pumping system of the SFTR is completely cryogenic, with cryogenic separation of most of the components of the gas. At each station the $(D,T)_2$, together with any O_2 or N_2 is pumped by a Balser[34] (or equivalent) liquid helium cryopump with a 2000-ℓ/s pumping speed. The $(D,T)_2O$ is trapped by a

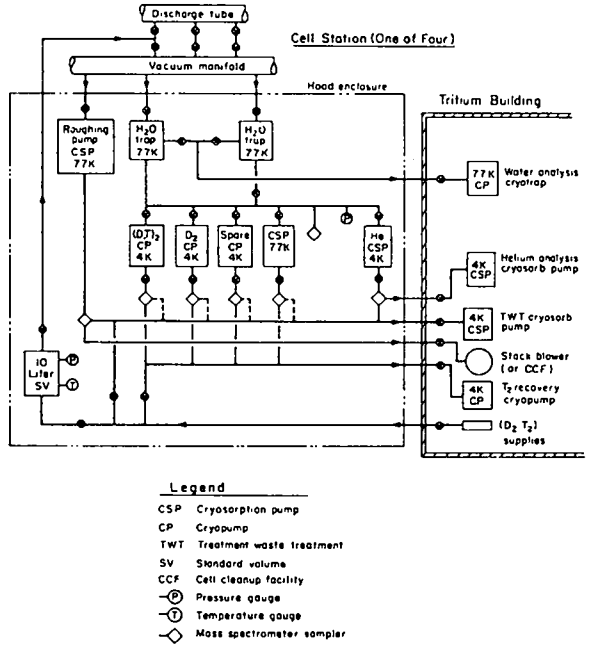

Fig. 5.6-13.
Detailed layout of SFTR pumping station and associated plumbing.

liquid nitrogen Varian cryotrap[35] with similar capacity. (A spare trap is also provided.) After the pressure is constant, the ^4He is pumped with a 1000-ℓ/s Excaliber liquid helium cryosorb pump.[36] (This pump uses a bonded molecular sieve on the cryopanels.) The time needed to pump the ^4He is about 1 min of the 10-min evacuation time between runs.

A feature of the Balser cryopumps not apparent in the drawing is a type of construction that gives an economy of space, a minimization of the increased pumping resistance usually associated with pumps, and a dual role in that it also serves as a valve. An inverted cap is pneumatically raised to close off the cryogenic pumping surface (within the pumping system) and effect a seal against the flange on the pump. The core of the pump can than be removed for cleaning without affecting the vacuum, or the condensate can be exhausted.

The $(D,T)_2O$ trap is isolated at the end of the day (or sooner, if desired) with pneumatically operated valves, the trap is warmed, and the water is transferred cryogenically to the tritium handling facility for measurement, decomposition, and possible $(D,T)_2$ recovery.

The helium that is collected during D_2 and $(D,T)_2$ runs will normally be evacuated daily from the warmed pump. On D-T shots, the helium can be expanded from the warmed pump, separated from any $(D,T)_2$, and PVT-measured in a thermostated container for a determination of the percent burn.

The D_2 also will normally be evacuated from the warmed pump on a daily basis. It will be cryosorb-pumped to the 7-ℓ/s waste treatment system. The mixture of $(D,T)_2$ will be evacuated after each run, and PVT and mass spectrometer measurements will give an approximate accounting of tritium. The $(D,T)_2$ will then be absorbed on a uranium trap, which will allow subsequent recovery (by ERDA, elsewhere) of the $(D,T)_2$ free from N_2 and O_2. Weight changes of the uranium container, together with both the known (assuming a known mix) $(D,T)_2$ content and a possible subsequent analysis, can give the oxygen content. This together with the measured water content gives the extent of the atomic D and T reaction with the discharge tube. Finally, the uranium container will be of a standard size that is commonly calorimetered for an independent measurement of the tritium content.

An independent requirement of the pumping station is the evacuation of the discharge tube from atmospheric pressure. An Excalibur[36] or equivalent cryosorb pump with an appropriate capacity (18-in. x 5-ft size) and a speed of 1000 ℓ/s (2000 cfm) will be used. A separate cryosorption pump,[37] attached to the flange shown in Fig. 5.6-12, will be used for outgassing purposes during nonworking hours. In this case, the outgassing of $(H,D,T)_2$ may be sufficiently high to require liquid helium cooling. No recovery or tritium measurements are planned here unless monitoring equipment during waste processing indicates a high tritium content.

Gauges to measure pressures from 10^{-7} torr to 1 atm will be required at various points on the vacuum system. Some temperature measurements will also be required.

Routine operation of the vacuum system will be automatic, with automatic recording of temperature and pressures, together with mass spectrometer or residual gas analyzer analyses. Special operations, usually once a day with D-T runs, will be manual. All operations will be remote-controlled except for maintenance operations during nonoperating periods of the fusion experiments.

Selection of relatively large volume enclosures for the cryopumps is planned to allow the daily collection of deuterium with oxygen (from the decomposition of and outgassing from the discharge tube inner wall by particle bombardment) without danger resulting from a shock-induced explosion of the solid mixture. The volume of the container should be about a factor of 7 larger than the volume (STP) of, for example, a two to one hydrogen to oxygen mixture. Air leakage would cause the greatest hazard; if a massive leak of air is assumed, the combined volume of the enclosure should be about a factor of 10 larger than the 2 ℓ of deuterium to provide reasonable safety. In the case of the $(D,T)_2$ mixtures, the 0.08 ℓ will be processed after each run and can in no case present a problem.

5.6.3.4 Tritium Recovery System

A strong effort is being made to recover the purest possible $(D,T)_2$ from the plasma ash. The use of cryogenic pumping and the reaction of the spent plasma gas with a uranium bed allows the recovery of $(D,T)_2$ with protium as the only likely impurity. This separation method should operate with relative ease and high efficiency. A further benefit is the separation and recovery of the helium to provide an additional and simple means of measuring the degree of burn of the D-T plasma.

Part of the discharge tube exhaust gas will be $(D,T)_2O$ from the reaction of atomic D and T with the inner wall. Although this will constitute a major portion of the tritium waste handled by the 7-ℓ/s tritium waste treatment unit, the value of the tritium will amount to only a few dollars per day. Tritium from mass spectrometer samples will be a

second major source of waste tritium. Again the quantity is small and also will be discharged into the waste treatment system. In this case the daily discharge is marginally accountable. The $(D,T)_2$ from the mass spectrometer and the $(D,T)_2O$ analysis gas will be cryosorption-pumped to the tritium waste treatment system. If desired, the $(D,T)_2O$ from these sources could be recovered by the addition of a hot bed of copper turnings [for removing oxygen from the $(D,T)_2O$] and minor piping revisions.

The final major source of waste tritium may be $(D,T)_2$ in collected helium. Should this be appreciable, it could be piped directly to the tritium recovery uranium bed.

Primary tritium recovery will handle the $(D,T)_2$ that has been collected in the cryopump, together with traces of nitrogen from outgassing and perhaps a few tenths of a percent of oxygen from the first-wall decomposition. The cryopump will be allowed to warm up, and the pressure and temperature of the gas in the previously calibrated volume will be measured. The quantity of gas will be determined with an accuracy of a few percent. A mass spectrometer analysis will determine the purity of the gas. The gas will then be reacted with a uranium bed, Fig. 5.6-14. The uranium trap will be of a standard size for precise calorimetric determination of the tritium content. Not only the mass spectrometer analyses but also weight changes in the trap could be useful for crude oxygen determination if wall decomposition is large. Alternatively, a cryotrap (with an additional valve), cooled with helium at 20 K and located between the liquid nitrogen trap and the cryopumps, could be used to collect the oxygen for subsequent PVT measurements. Scyllac measurements could be devised to measure oxide decomposition, at least for one type of inner wall.

The uranium beds normally would be shipped elsewhere. Alternatively, they could be heated to regenerate the $(D,T)_2$ gas for collection in standard tritium gas shipping containers or for direct reuse in the SFTR. Nitrogen and oxygen would not be released during this heating, so the uranium bed acts to purify the $(D,T)_2$ gas. The operation of the uranium beds in the recovery operation is like that used for fuel injection, except that twice as much gas would be absorbed (but to give the same tritium content), as discussed in Sec. 5.3.

5.6.3.5 SFTR Cleanup Systems

The design of a facility to clean up tritium waste incurred during routine and abnormal operations is made difficult by the disparity between the required flow rates anticipated for the two cases. The cleanup

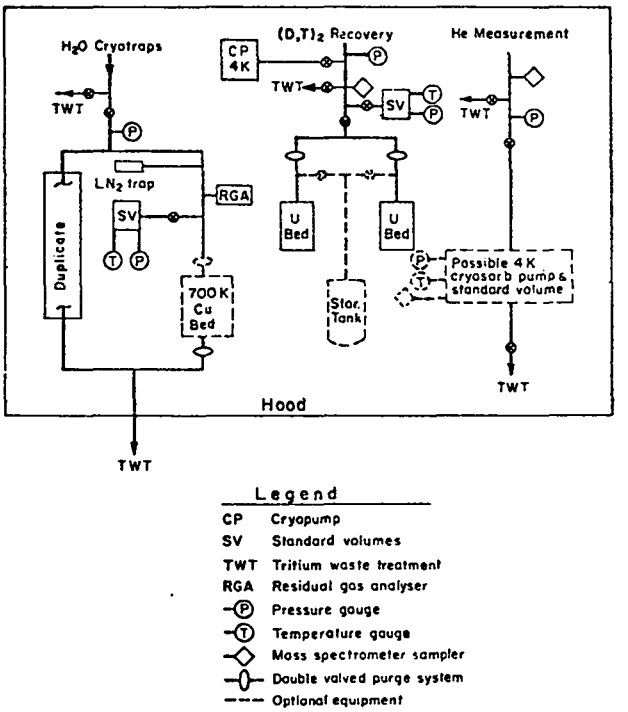

Fig. 5.6-14.
Analysis and D-T recovery system.

of routine waste associated with equipment maintenance, intentional leaks (Sec. 5.6.3.4), $(D,T)_2$ diffusion through walls of process equipment, loss from contaminated surfaces, and accidental leaks can be made by means of a relatively small unit (7 *l*/s) used in conjunction with a ballast or storage tank and proper scheduling. This approach is useless, of course in event of a rapid, large release to the SFTR cell or tritium handling area. Cleanup of the latter release must be reasonably rapid and large volumes of air must be treated. Two cleanup systems, therefore, are anticipated: routine waste will be treated by a small capacity TWT system, with a 7-*l*/s capacity, whereas large spills will be subjected to cleanup by a large 4700-*l*/s unit. For cases such as an accidental spill in the vault, the TWT system could still be employed over a period of days. If, however, the SFTR cell atmosphere suddenly becomes contaminated with tritium, the 4700-*l*/s cleanup unit must be used to effect a rapid cleanup of a large volume of air. This section describes both the 7-*l*/s TWT and the 4700-*l*/s CCF. Operation of these two systems in conjunction with a monitoring system under accident-type conditions is described below. The Engelhard Corp. manufactures similar but simpler systems.[38]

Cleanup System for Scheduled Tritium Releases (TWT)

The TWT system is an automatically actuated tritium removal system based on a precious metal catalytic recombiner which converts all hydrogen isotopes in air to water, and organic materials to water and carbon dioxide. The water is then adsorbed on molecular sieve drying towers. This system will handle otherwise noncollectable residues and effluents from the vacuum systems, injector system, purge system, uranium beds, mass spectrometer system, and the relatively low air flows through the hoods associated with these systems during maintenance periods. Air circulating through these hoods will flow into the ventilation ducts and can be automatically diverted into the TWT, in event of minor tritium spill in these areas. Figure 5.6-15 is a flow diagram of the TWT and its relationship to the larger cell cleanup facility described in the following section. The TWT described here is similar to a system which is operational at LASL.[39]

Gas from the various above-mentioned sources will first flow into a large storage and ballast tank. The oxygen, hydrogen isotope, and water concentrations in the tank air will be continuously monitored and maintained at a level sufficient to provide enough oxygen to convert catalytically all of the hydrogen isotopes to water; the oxygen and hydrogen are controlled to levels below the explosive limits; and the water is kept to 2.5% relative humidity, minimum, to effect dilution of the $(D,T)_2O$ without unnecessary loading of the dryer with water.

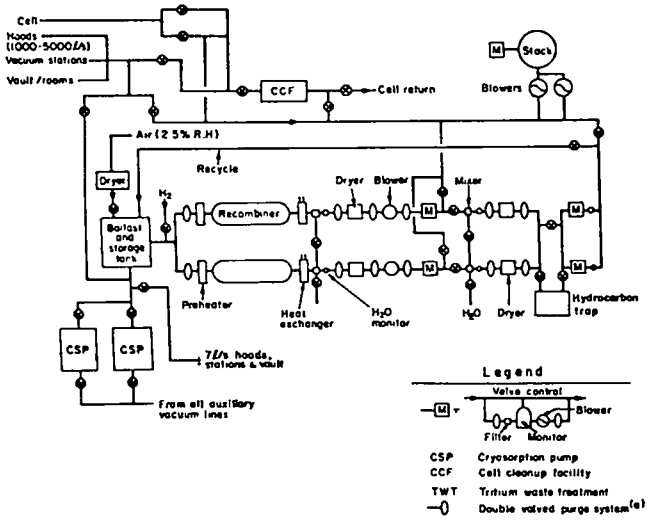

Fig. 5.6-15.
Flow diagram of the tritium waste treatment system.

(Tritiated water is removed with greater efficiency with an increase in the number of dryers and a decrease in the amount of water injection.) The pressure in the ballast tank will be maintained between 27.6 and 68.9 kPa by electrical valves. When the pressure in the tank reaches a preset upper limit (~70 kPa) the valves will open and the circulation blower on the system will come on and pull gas out of the tank through the TWT. The gas flow through the TWT will continue until the pressure in the ballast tank falls to the lower pressure limit (~28 kPa) at which time the automatic valve on the tank closes and the 7-ℓ/s blower is turned off.

The recombiner/preheater arrangement and flow pattern are shown in more detail in Fig. 5.6-16. The catalytic recombiner contains a precious metal (platinum-based) catalyst distributed on the substrate of a high surface area (100-200 m^2/g) alumina support material.[40] The bed operates at a temperature of ~450 K. The gas leaves the recombiner and passes through a water-cooled heat exchanger to reduce the temperature to ~295 K before the gas enters the molecular sieve drying tower. At this point all but ~1 ppb of the hydrogen isotopes will have been converted to water. The gas exiting from the drying tower will contain ~1 ppm water. This gas must then pass through ion chamber tritium monitors to determine the extent of tritium contamination in this exit gas stream. At this point the TWT logic system will route the gas to one of two possible paths depending on the tritium level still present in the exit gas. If the tritium level is acceptably low, the gas will go directly to the 30-m stack. If the tritium level is high, the gas will go to a second dryer. If the tritium level is now low enough, the gas will be stacked. If the tritium is too high and the

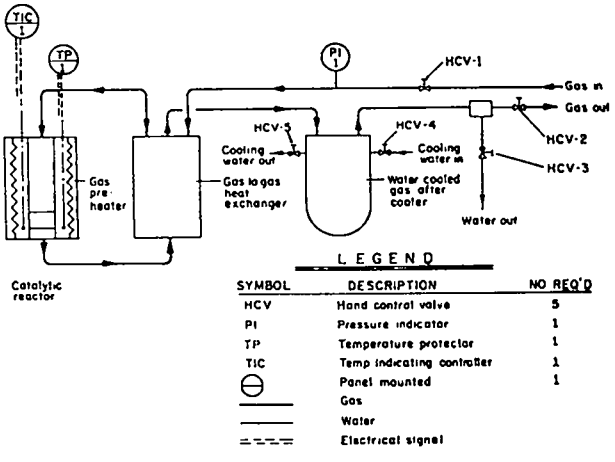

Fig. 5.6-16.
Flow diagram for the tritium recombiner/preheater.

water level low, the gas will then be recycled, going back to the ballast tank, or if necessary, transferred to the second line. Also, if the tritium level is high and the water concentration is correspondingly high, the gas will flow through the second set of recombiners, drying towers, and ion chambers. At this point the gas will go one of two routes. If the tritium level is sufficiently low, the gas goes up the stack. If tritium still remains in the gas stream, the flow is directed back to the ballast tank. At this point more efficient tritiated-hydrocarbon removal (by a 13X dryer[38]) or longer recirculation may be required. The system will be designed with an automated alarm system such that operating personnel will be immediately alerted if the system goes into a recycle mode. The activation of the alarm will be indicative of a system problem requiring immediate attention.

The drying towers will have redundant beds containing regenerable molecular sieve similar or equal to the Linde 4-A product.[40] These molecular sieves are very effective for water adsorption. The redundancy in drying towers will permit regeneration of a saturated tower while the TWT system continues to operate with a second processing line. The molecular sieve bed can be regenerated by heating the bed to 450 K and flowing a dry purge gas (argon) over the sieve bed. This regeneration function sweeps out the adsorbed water, which can then be condensed from the purge gas and collected in a container approved for off-site disposal. The container may be shipped to an approved recovery laboratory or it may be shipped to an approved burial site.

Both the recombiners and the drying towers will have heaters. The recombiner operates at elevated temperature (~450 K) and the drying towers must be heated to ~450 K for regeneration. These units will be designed so that the heaters are external and can be replaced without opening the active beds to the outside air. This design eliminates the need for personnel exposure to tritium during heater changeout, which could conceivably occur with some frequency. These units will be equipped with overtemperature thermostats that will shut off all electrical power to the unit in the event of a thermal excursion. These units will also be built such that the active material, either catalyst or molecular sieve, can be changed in situ. Each unit will have removal ports at the bottom of the columns and fill ports at the top. A second option is the complete replacement of the unit since the tritiated water in the unit would be well contained and in a solid form.

The blowers to be used in the system will be oilless compressors. The main compressor providing the 7-*l*/s gas flow will be an oilless, sealed compressor. A unit of this type provides adequate gas flow, suffers relatively little radiation damage, and does not introduce any organic materials into the system. A pair of these compressors will be used in the TWT system; one compressor will be in use and the other will be a standby unit that can quickly be placed online. All components in the TWT system will have to be specially designed or modified to insure that they are gastight (leak rate $\leq 10^{-4}$ cm^3 torr/s). The equipment will be in an isolated room, but any tirtium leakage to the open room will be a potential hazard.

All equipment will be connected to the TWT by means of a standard purge system described in Sec. 5.6.4.4. The piping within the TWT will be either copper or stainless-steel tubing. Wherever possible, the joints will be permanent, e.g., soldered or welded. Flanges which require gaskets will use "Grafoil" gaskets. Where possible the nonpermanent joints will be made with Cajon-type metal gasket connectors. The use of elastomers as gasket material will be avoided. The manual valves on the low-pressure side of the compressor will be quarter-turn stainless-steel ball valves with a Teflon seat. On the high-pressure side of the compressor, metal-bellows valves such as the Nupro or Hoke packless bellows valves will be used.

Cleanup System for Accidental Tritium Releases

In the event of a significant release of tritium to the SFTR cell or to one of the tritium handling rooms, a rapid cleanup of a large volume of air will be required. A 4700-*l*/s cleanup system will be used for this purpose; the most likely function of this unit will be to remove rapidly tritium which has been released to the SFTR cell as a result of a large-scale failure of the SFTR discharge tube during a D-T plasma pulse. The unit proposed for this purpose is similar to a system available commercially from the Engelhard Corp.,[38] and is probably conservatively safe, even for a massive discharge tube failure during a D-T shot.

This facility will be activated in any of the following cases: an accidental tritium spill in the cell surrounding the discharge tube, as a backup for the handling of a large spill in the hoods, or tritium handling rooms, or possibly for the emergency handling of a major spill in the vault. Figure 5.6-17 gives a flow diagram for the cell cleanup facility.

This facility has a low probability of use because:

(1) The discharge tube, vacuum system, and most other components of the injection, recovery, and postdischarge gas diagnosis systems are normally under a partial vacuum, so that all leaks would be into the system.

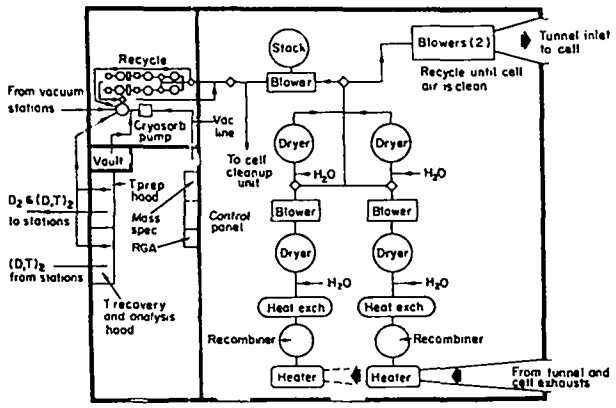

Fig. 5.6-17.
Tritium facility floor plan and cell cleanup facility.

(2) Only minor quantities of tritium are involved in the SFTR (no breeding).

(3) Should a large break occur in the discharge tube, the enclosed gas could be evacuated immediately into the four cryosorb pumps (Sec. 5.6.3.3) which have a capacity of several thousand liters (STP) and a speed of 1000 *l*/s. Continual operation of these pumps might not be economical.

(4) Long gas lines which carry tritium will be of copper to reduce the permeation of tritium; SS-316 is another option.[19]

(5) In the operation of the hoods, which are normally closed, a low flow of gas exhausts into the 7-*l*/s unit described in the previous section. Thus, accidental leaks would be well confined.

(6) A large spill in the vault could be handled by the 7-*l*/s unit.

The accidental release that would be the most difficult to handle would be a massive rupture of an appreciable fraction of the discharge tube to release about 150 Ci of tritium. Only 10% of the runs, however, will involve tritium. This release would probably be into an undamaged cell, the volume of which is 25 000 m^3. The resulting average tritium concentration would be 6 mCi/m^3, or a volume fraction of 3×10^{-9}. The volume fraction of T_2O in air suitable for public release is 0.2 $\mu Ci/m^3$ or a fraction of 10^{-13}. It follows that a dilution of about 30 000 would be required before the gas could be stacked.

The safest method of cleaning such an enclosure is on a "once-through" basis with an inlet of fresh air, a processing of the air to remove tritium, and a final external exhaust of the cleaned air. In this case, however, the processing of ~280 m^3/min (10 000 cfm or 4×10^5 m^3/day) of air at 25°C and 100% humidity would produce 11 tons of tritiated water per day with attendant water handling problems, frequent dryer regeneration, long dryer regeneration times, and a requirement for massive dryers. Accordingly, it is planned to recirculate the treated gas. The flow pattern of the 4700-*l*/s unit is shown in Fig. 5.6-17.

Tritium removal in the TWT and CCF is based on the conversion of T_2 to T_2O in air on a high surface area material impregnated with precious metal catalyst, dilution of the T_2O with H_2O, and removal of the tritiated water with one or more dryers, with H_2O addition between dryers. Most catalysts for the T_2-O_2 reaction are proprietary products formulated to give reproducibly high catalytic activity under selected conditions of temperature, pressure, and flow.

Since the cost of the CCF will be high (~3×10^6 dollars), alternative operational modes might well be considered for the final design. As a guide to the final plant design and to operational procedures, basic principles of the operation are examined in detail:

1. The catalyst bed or "recombiner" is assumed to be of the Engelhard type.[38] At the recommended sizes, temperature, and air flow rates, the volume fraction of T unconverted to T_2O amounts to 1 ppm. For a 150-Ci release of T_2 into a cell volume of 2.5×10^4 m^3, the ultimate release of the 150 μCi of unconverted T_2 (assuming the removal of the T_2O) by the 4.7-m^3/s CCF unit would be well within the daily tolerance of 82 mCi. On the other hand a massive tritium release in the tritium handling room or vault would require recirculation through the recombiner and dryers before it is exhausted. In all cases, the tritium concentration in the air would be reduced to tolerance levels before exhausting. Although a spare recombiner has been incorporated in the present plans, any need for it is remote since the presence of leaks, poisoning of the catalyst, or breakdown of any heaters or heat exchangers seems unlikely.

The effectiveness and adaptability of the recombiner merit further examination. For a given flow, temperature, and bed volume, the fractional conversion of T_2 to T_2O should be independent of the T_2 and T_2O concentrations. First, ignoring isotopic effects, the equilibrium ratio of T_2 to T_2O (or H_2 to H_2O) in the presence of 0.2 atm of O_2 is $<10^{-7}$ at temperatures below 960°C.[41] Thus the back-reaction rate (T_2O decomposition) can be neglected except for high tritium concentrations where some beta decomposition of T_2O might occur. Second, the fractional rate of conversion should also be unaffected by concentration if the rate controlling step is the diffusion of T_2 through a boundary layer of air surrounding the catalyst. Garber and Peebles[42]

found this to be the case for H_2 at somewhat elevated temperatures. (Of course, for high hydrogen concentrations, some increase in rate would be caused by the change in composition of the boundary layer.)

2. Some Engelhard recombiners can be operated over a range of temperatures[38] but reaction rates are not given for their catalysts. Since the CCF unit is used only for standby, continuous heating of the massive recombiner and preheater would be onerous, and room temperature operation should be considered.

If the reaction rate is controlled by diffusion through a gas layer, the rate should be approximately proportional to the square of the absolute temperature.[20] Experiments by Garber and Peebles[42] at temperatures of 230 to 500°C on their (unspecified, but probably similar) catalyst agreed with this functional dependence. Accordingly, a 20% increase in the volume of catalyst might allow operation at room temperature with no loss in the assumed fractional reduction of a factor of 10^6. Experimental confirmation of this effect would be desirable.

3. Operation of the recombiner at room temperature and the omission of a 13X molecular sieve in the CCF could allow tritiated hydrocarbons to escape in the exhaust. This situation could arise if the operation of the CCF were delayed after an accident. This problem probably should be reassessed as the SFTR plans become final.

4. Provision has been made for the addition of hydrogen to the contaminated air that enters the recombiner. This might be useful to (a) increase the rate of reaction due to the temperature rise that would be associated with H_2-O_2 reaction, (b) increase this rate markedly if the catalyst is sufficiently poisoned to give a reaction rate that is concentration-dependent, (c) heat the catalyst to drive off accidentally condensed water, and (d) reactivate a poisoned catalyst. Although the need for this capability is remote, the cost is small.

5. The dryers constitute the most expensive part of the CCF, and various schemes for their operation might be considered. There is, however, a potential limitation that has not been adequately assessed, but which could probably be studied at LASL in time to be useful for the final CCF plans. The problem relates to the rate at which water from the bed of the dryer exchanges with the water in the processed air. For example, a dryer that is highly contaminated with tritiated water might well add tritium to a gas having a low level of tritium contamination. This exchange should be studied using fresh, cryogenically dried air in beds containing various water fractions.

If this exchange rate is high, one must be very careful to limit the tritium contamination of the final dryer to low levels. On the other hand, if the rate is exceedingly low, one might elect to use only two or three dryers. This saving, combined with the use of only one recombiner could reduce equipment, building, and maintenance costs by perhaps a million dollars. The option to recirculate the air, using "batch" processing, is also attractive but would increase the processing time.

It has been assumed that the air entering each dryer would have a water content of 1000 ppm, corresponding to a relative humidity of 2.5% at 25°C and 600 torr, and that the exit would have a content of 1 ppm. The water content entering each dryer would be adjusted to this value by mixing with a continuous water (or steam) spray. Thus each dryer would reduce the tritium content by a factor of 10^3. This cleaning technique can be extended to give air with a tritium level equal to the natural background level of about three parts of T_2O in 10^{18} of H_2O.[2] (Air saturated with T_2O would require six such dryers in series. If the inlet air to each dryer were brought to 100% relative humidity, only four dryers would be required.) Thus the choice of 1000 ppm H_2O in the inlet is arbitrary. An increase in the inlet humidity would reduce the number of dryers, the number of recirculations, the space requirements, and the pressure drop, but would increase the volume of tritiated water collected and frequency of dryer regeneration. As a further example, the use of both 25% relative humidity for the inlet water concentration and two dryers, a purification factor of 10^8 would be achieved. Alternatively, using 2.5% relative humidity and three dryers, a purification factor of 10^9 would be obtained with only 15% as much waste water being collected, and there would be a corresponding reduction in the need for the regeneration of the dryers.

The proposed operating procedure is as follows:

1. The cell air, ideally of low humidity, is processed through a recombiner to convert the $(D,T)_2$ to $(D,T)_2O$. The relative humidity is controlled at more than 2.5%.

2. The air is passed through a molecular sieve dryer.

3. Water is sprayed into the exhaust to give a relative humidity of about 2.5%.

4. The gas is passed through a second dryer and then into the cell. (Appropriate sensing and control devices are implied.)

5. Occasionally the dryers are regenerated, the water is collected in cans on an absorbent, and the product buried in doubly sealed containers. For the case assumed, the tritium content would be 150 Ci per major accident.

Although present plans call for a 4700-//s processing unit, commercial units of 2800 //s, maximum, have been built by Engelhard.[38] In either case a flow of 0.5 m/s (100 ft/min) in a 1-m-high bed of Linde molecular sieve 4A[40] in each of two dryers in series would be used. The pressure drop across the two beds would be 8 kPa (1.2 psi). Four drying units would be required to provide redundancy. Weight and size comparisons of the 2800- and 4700-//s units are shown in Table 5.6-3.

About 500 m^2 (5000 ft^2) of floor space would be required for handling and installation of the four large drying units, for the two recombiners, the blowers and stack(s), and for the 7-//s tritium waste treatment unit.

5.6.4 Instrumentation, Control, and Operational Procedures

The instrumentation, control, and operational aspects of each subsystem defining the tritium handling system have been described in previous sections. This section treats specifically four aspects of the tritium handling system which interface with more than one of the tritium handling subsystems: tritium monitoring, nonscheduled action, postdischarge diagnosis of gases, and maintenance procedures.

5.6.4.1 Tritium Monitoring

Permanent flow-through ionization-chamber-type tritium air monitors for personnel protection will be located in the SFTR cell and in the tritium handling room. These will be rate instruments, giving concentrations directly. Figure 5.6-18 gives the flow patterns and monitor stations. A cell monitor will be located at each of the two cell entrances, and readouts will be available at both entrances and at the SFTR control room. These monitors will sample

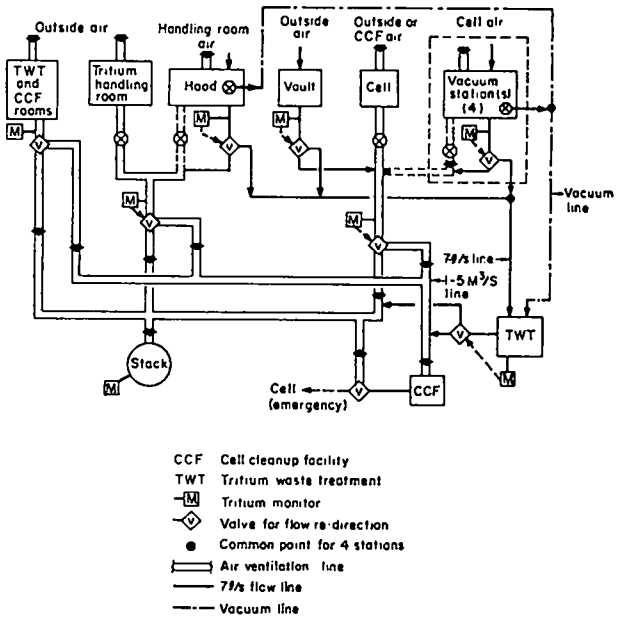

Fig. 5.6-18.
Tritium flow and monitoring system for SFTR.

the air at selected points in the cell sequentially and automatically through sampling hoses. The monitor in the tritium handling room will also have readouts located locally and in the control room. The five hoods will also be monitored with rate instruments with local readouts in addition to those in the control room. These air monitors will have sampling hoses to enable the person working with the equipment inside the hood, sometimes through glove ports, to monitor any part of the equipment inside.

The vault and rooms where the two tritium recovery systems (TWT and CCF) are located will be monitored only as needed with portable or semiportable air monitors. However, the exhausts of these rooms will be continuously monitored with ionization-chamber-type integrating air monitors which will route the exhausts to one of the recovery systems if the tritium being exhausted past a particular monitor exceeds 20 mCi/day. This and similar action by the other integrating monitors (except the stack monitor) will assure that the concentration in the stack is kept below the maximum permissible concentration of tritium in air (0.2 $\mu Ci/m^3$) averaged over 24 h. This stack concentration monitored for a day corresponds to a release of 82 mCi.

Integrating monitors will also be located in the exhaust ducts of the cell and the five hoods. Similar monitors will also be used in the recovery systems to check their performance and route the air to redundant, backup components as necessary to keep the

TABLE 5.6-3

COMPARISON OF
2800- AND 4700-//s DRYERS

	2800 //s Dryer	4700 //s Dryer
Area of bed, m^2	6 (60 ft^2)	10 (100 ft^2)
Diameter of bed, m	2.7 (8 ft)	3.4 (11 ft)
Weight of bed, Mg	4 (4 tons)	7 (7 tons)

concentration at the exhaust of the recovery systems within design levels.

The normal flow through the five hoods and the vault will be kept at less than 7 ℓ/s so that spills in these places can be handled by the smaller 7-ℓ/s TWT. Toward this end, flexible ducts will be used in the hoods to increase ventilation near any highly contaminated parts being handled when glove ports cannot be used. The larger 4700-ℓ/s CCF system will back up the TWT and handle any released tritium that cannot be handled by the TWT. Figure 5.6-18 shows the ventilation system for the SFTR cell and the tritium rooms and indicates the location of the various air monitors.

Monitoring of low-level tritium in the presence of activated air produced by neutrons during a D-T pulse or in the presence of a high natural radon background can present some problems. For a discussion of these and of tritium monitoring in general at the SFTR facility, see Sec. 7.3.1.1.

5.6.4.2 Nonscheduled Action

Section 5.6.4.1 outlines the purposes of the tritium monitoring equipment and refers to the ventilation and tritium cleanup systems to which the equipment is connected. Accidental releases of tritium will normally be trapped and only insignificant quantities will be released to the environment (<82 mCi/day).

Should a release occur in a room where personnel are present, the room will be evacuated and reentry permitted only after the concentration has dropped to an acceptable level. Supplied-air suits[43] will be worn if reentry is required sooner than would otherwise be allowed. Tritium is stored not only in the vault and the tritium recovery systems, but in hoods at each pumping station. A release in any of these will not require evacuation but only assurance that the hood doors are closed. Action will be taken whenever possible to minimize the amount of tritium released to the ventilation system.

In case of failure of the discharge tube during a D-T pulse, ~10-15 mg of tritium at most would be released in the unoccupied cell and automatically exhausted to the 4700-ℓ/s CCF. A potential tritium release in the event of a minor failure of the discharge tube could be handled by having the downcomer and cryosorb roughing pump valves open immediately, directing most of the tritium into the cryosorb pumps (refer to footnote in Sec. 5.6.1); only a small fraction of the tritium inventory within the discharge tube would be expected to escape into the cell in this case.

Unless a fire or explosion is directly involved, the tritium in most of the significant releases would be in the form of the gas, which is orders of magnitude less toxic than the oxide. Normal conversion of the gas to the oxide by oxidation or exchange is very slow and this release can be neglected. However, all safety guides will assume that tritium measured by the monitors is in the oxide form.

5.6.4.3 Postshot Diagnosis

The cryogenic-type SFTR pumping system is admirably suited for aiding in postshot analysis of the fuel ash. First, the system itself introduces no impurities into the exhaust gas, except possibly for trace amounts of outgassed material, so that neither is protium introduced into the gas nor are (D,T) substituted methanes (or other organics) introduced that might cause ambiguity in the water (or oxygen) contents in mass spectrometric analyses. Further, a cryogenic pump can be used not only for evacuating but also for transferring gas at atmospheric pressure. Finally, by suitable design, cryogenic pumping can be used to separate gas components. The degree of separation depends on pumping rates, gas pressures, relative concentrations of components, temperature control, and gas solubilities in the condensed solids. For the system considered here, evidence for effective separation is strong, except possibly in the case of helium.

Some of the postshot diagnostics that would be useful follow:

1. A determination of the amount of oxygen formed in a run would show the extent of decomposition of the wall material or the magnitude of leaks. Such oxygen might be formed by a combination of alpha, deuteron, and triton bombardment, neutron sputtering, and bremsstrahlung and other high intensity radiation. The extent of this formation is expected to be of minor significance. Outgassing of oxygen is also of minor concern, given the planned injection and evacuation schedule. Of major imortance is the early detection (and repair) of leaks.

2. The determination of the amount of water in the ash is critical. The amount of water in the ash could be quite large (perhaps a few percent) since the inner wall will almost certainly be an oxide, and since existing thermodynamic data,[32,33] indicate that all oxides are unstable in the presence of the anticipated pressures of atomic hydrogen. The reaction is kinetically controlled, and the yield might well be governed by the relative rates of reactions such as: $D + D (+ \text{wall}) \rightarrow D_2$, and $D + D + \text{oxide} \rightarrow D_2O$ + metal, suboxide, oxyhydroxide, etc. The relative rates of these two reactions will certainly depend on the ceramic used and on additives that might purposely be used in the ceramic. A selection for the inner wall material would be based on research on

ceramics tailored to minimize water formation and still give the required electrical conductivity, thermal stability, etc.

The rate of corrosion of the inner wall by atomic hydrogen attack should be extremely low (less than 30 μm/yr) unless nonuniform attack or pitting of the coat by preferential reaction should occur.

The critical problem with water formation is that the water formed will most likely be adsorbed on the oxide wall and will then slowly outgas to contaminate the subsequent plasma gas charge. Since heavy-ion contamination of the plasma significantly lowers its temperature by bremsstrahlung radiation, it is imperative that the oxygen impurity content of the plasma be kept low. A steady state will be obtained if shot intervals, injection times, and evacuation times are constant, to give an amount of outgassed water during evacuation that is equal to the amount formed during a shot. Thus, the measurement of the $(D,T)_2O$ content of the plasma ash can be used to calculate the amount of water contamination in the plasma. If a constant outgassing rate is assumed, the calculated contamination would tend to be too large. If the differential outgassing rate during the evacuation period is measured, then a more accurate knowledge of the actual contamination would be obtained. Since the wall temperature would be expected to drop during evacuation, a knowledge of the change in outgassing rate during this period is clearly advisable.

3. The helium content of the ash gives the D-T burnup of the fuel. A helium measurement thus allows a direct determination of the degree of burn of the D-T reaction in a particular run as a check against other diagnostic methods. It is assumed that such measurements will be made only occasionally.

4. The measurement of other impurities by mass spectrometer and/or quadrupole mass spectrometer residual gas analyzer will be made to

(a) Determine protium contents to estimate not only the protium content of the plasma but also to give information on the purity of the plasma charges and $(D,T)_2$ recovered gas,

(b) Measure the tritium and deuterium contents of the injected gas (to check the volumetric measurements) and of recovered tritium,

(c) Estimate the amount of contaminants, such as CO, CO_2, N_2, in the exhaust (from outgassing). Such measurement will be of particular use after the discharge tube has been exposed to air and the first few runs have been made. Of major importance is the detection of leaks, in conjunction with oxygen determination discussed in item 1.

(d) Assist in the determination of helium in the exhaust gas. Such determinations are not unambiguous since HD interferes with any ^3He determination but, of far more importance, the presence of D_2 in large quantities negates the usefulness of a ^4He determination. However the $(D,T)_2$ can be oxidized to $(D,T)_2O$ and easily separated from the helium.

Figure 5.6-14 shows a schematic of the postshot diagnosis apparatus. Mass spectrometer or RGA samples will be taken where shown and also at the pumping stations (Fig. 5.6-13). Details of the mass spectrometer analytical techniques have not been selected. A Nier-type and an RGA-type spectrometer are to be located in the tritium handling room.

Cryotrapped $(D,T)_2O$ will be transferred, at least every day, to a liquid nitrogen trap.[29] After warming, the gas will be expanded into a calibrated thermostated standard volume for PVT measurements. The water will then be transferred via a liquid helium cryosorption pump to the TWT, as shown in Fig. 5.6-15. As knowledge is gained on normal water contents of the ash, water determinations will be made by expanding water directly into a calibrated volume at ambient temperature for PVT measurements. (It should be noted that such expansions must be handled carefully to avoid the extremely slow sublimation that occurs from ice.) If water contents are low or well known, the water can be expanded directly to the TWT. If the $(D,T)_2O$ content is sufficiently high, it might be desirable to pass the vapor over hot copper for recovery of the $(D,T)_2$. Indeed, such a technique might be used as the analytical method for obtaining average water contents. This could be obtained by measuring weight changes in the copper (or hopcalite tube. This option is also shown in Fig. 5.6-14.

Initially, it is planned to make helium PVT measurements in a calibrated volume at ambient temperature as shown in Fig. 5.6-14. Assuming a need for an accurate measurement of the helium, a standard thermostated volume and an additional cryosorb pump would be added, as shown in Fig. 5.6-14. In both cases, mass spectrometer analyses would be required. If $(D,T)_2$ contamination is significant, the $(D,T)_2$ would be converted to $(D,T)_2O$ and removed as indicated above. Helium from D_2 runs could be measured the same way, but since the quantity of gas is so small, PVT measurements will be made only occasionally in a calibrated volume at ambient temperature. More extensive measurements would require an additional liquid helium cryosorption pump at the pumping stations.

Finally, ~1-in.-diam tubing for gas transfers will be located in the cell. Having four pumping stations allows the use of only one station for a given analysis, with a rotation of sampling points to speed operating

times. Alternatively, specific products from the four stations can be combined for analysis.

5.6.4.4 Maintenance of Tritium Handling Equipment

The entire tritium handling facility is designed with the goal of minimizing routine maintenance. For this reason organic materials will not be used in those sections of the system with which tritium might come in contact. The cryogenic pumping system will eliminate vacuum pump oils from the system and will provide a clean, fast, and efficient mode of evacuation.

Wherever possible the tritium lines will be of welded construction to eliminate as many joints as possible. Where it is necessary to have joints, the connectors or flanges used in the joints will have metal gaskets. Where flanges and connectors must be used in TWT and CCF areas and where a hard vacuum is not required, the use of Grafoil gasketing material[44] will be specified. This all-graphite material will not absorb tritium by isotopic exchange; furthermore, it will suffer relatively little radiation damage. Grafoil is currently in use at the LASL tritium facility.[39] Throughout the tritium system considerable redundancy has been incorporated into those major components that might present frequent maintenance problems. This procedure was adopted so that a standby unit would always be available in event of a critical component failure. Also, this procedure allows routine maintenance to be performed on a component without shutting down the entire system.

The components of the tritium storage, injector, and vacuum systems will be enclosed in hoods. These hoods are designed such that during routine maintenance and component change-out, the air flowing through the hoods can go to either the 7-//s TWT or the 4700-//s CCF for removal of any released tritium before stacking. If the tritium release during these operations can be kept low enough the air will, of course, go directly to the stack rather than be processed. This routing of the air will be automatically determined by the ventilation logic system once the air has been monitored for tritium (Fig. 5.6-18).

The tritium handling system has been designed so that all major components can be isolated by a set of valves. This procedure leads to the use of many valves but means greater personnel protection against tritium-contaminated air and surfaces during maintenance. Each component in the system will be joined to the main tritium system by a double-valved, purge system as illustrated in Fig. 5.6-19. When a component has to be changed, valves

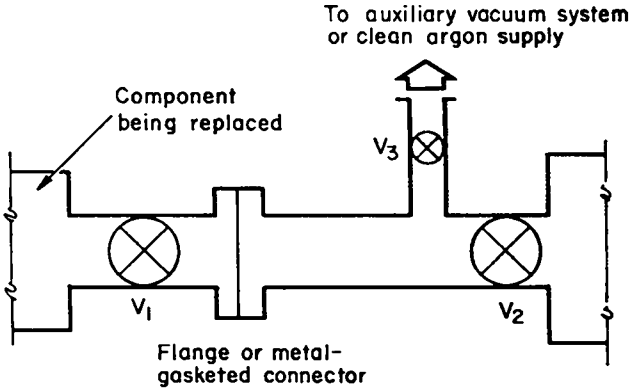

Fig. 5.6-19.
Typical double-valved purge system to be used throughout SFTR tritium handling system.

V_1 and V_2 will be closed and valve V_3 opened to the auxiliary vacuum system. When the volume between V_1 and V_2 has been evacuated, this volume will be back-filled with clean argon. The same sequence of events will occur at all other joints leading into or out of the component. The joints can then be opened with a minimum hazard to personnel, and the maintenance and/or change-out can proceed. This procedure has the added advantage of keeping the remainder of the system isolated so that working vacuum or pressure can be maintained. After the maintenance is finished, the component can be easily rejoined to the system. The auxiliary vacuum system will then be used to evacuate the room air from the volume defined by valves V_1 and V_2, valve V_3 will be closed, and valves V_1 and V_2 can be opened to bring the system back to operating condition. This purge system is being used in the LASL tritium facility[39] with great success (reduced personnel exposure, tritium releases to the atmosphere, and maintenance times).

The four vacuum stations located around the discharge tube will be situated in semimobile hoods. These hoods are designed in such a way that the vacuum station will be assembled in the hood at a remote assembly station in the tritium handling area. The hood will then be transported to the working location in the SFTR cell. Here the hood will be connected to the ventilation system ductwork and the vacuum system connected to the vacuum manifold leading to the discharge tube. Conversely, when major overhaul of a vacuum station is necessary, the vacuum system and hood can be isolated and the hood moved out of the cell to a more favorable working area in the tritium facility for performance of the necessary maintenance. Here again the hood will be connected to the main ventilation

system so an adequate supply of fresh air will be pulled through the hood. In this scheme the air can be processed by a cleanup system in the event of a tritium release during the maintenance operation. During this maintenance the remaining three vacuum stations will be adequate to keep the SFTR operating. It will be desirable however to have a spare hood and vacuum assembly readied for installation. Once the required maintenance is complete, this system will be available as the standby unit. It must be emphasized that replacement of an entire vacuum station would occur only in the event of major maintenance requirements. Most maintenance and the replacement of cryogenic heads, valve seats, and molecular sieve should be done in situ. During maintenance the air in the area will be carefully monitored to assure personnel safety. When maintenance is being performed in situ on any part of the tritium handling facility the maintenance personnel will work in supplied-air bubble suits. These suits and the associated air supply will be similar to those described by Mound Laboratory.[43]

Components of other portions of the tritium handling system, (e.g., the injector system, TWT system, etc.) will be interconnected with the standard purge system illustrated in Fig. 5.6-2. The tritium storage, injection, recovery, and diagnostic systems will be enclosed in a hood that will have air flows from front to back to pull the air away from working personnel. The hoods will be relatively shallow so that a person working at the face of the hood can easily reach all components. Provision will be made at each hood for attachment of a small flexible duct through which air can be pulled on its way to the TWT for tritium removal. This will allow one to hold the duct next to the working area, thereby giving a more positive air replacement in the critical area. A plastic covering containing gloves will be used over the door opening in some cases to reduce the air flow sufficiently for the TWT to be used.

The fast-acting pneumatic valves on the injection line and downcomers will require periodic maintenance. Because these valves are not located in the vacuum station hoods, provision must be made for the safe handling of tritium released during the maintenance. Once again, flexible ducting from the vacuum station hood will be run to the valve area and positioned next to the valve during maintenance. The backup valves at the injection station will permit closure and isolation of tritium-contaminated surfaces, thereby exposing a minimum of contaminated area.

REFERENCES (Chap. V, Sec. 5.6)

1. Federal Register, Title 10, Part 20 (10CFR20), "Standards for Protection Against Radiation" (1968).

2. D. G. Jacobs, "Sources of Tritium and Its Behavior Upon Release to the Environment," USAEC report TID-24635 (September 1971).

3. E. A. Evans, **Tritium and Its Compounds** (van Nostrand Co., Inc., Princeton, NJ, 1966).

4. G. J. Casaletto, L. H. Gevantman, and J. B. Nash, "The Self-Radiation Oxidation of Tritium in Oxygen and Air," U.S. Naval Radiological Defense Laboratory report USNRDL-TR-565, San Francisco, CA (May 1972).

5. J. Y. Yang and L. H. Gavantman, "Tritium β Radiation-Induced Isotopic Exchange in the T_2-H_2O System," U.S. Naval Radiological Defense Laboratory report USNRDL-TR-471, San Francisco, CA (September 1960).

6. **Maximum Permissible Body Burdens and Maximum Permissible Concentrations of Radionuclides in Air and Water for Occupational Exposure**, NBS Handbook 69, K. Z. Morgan, Chairman (Superintendent of U.S. Documents, U.S. Gov. Printing Office, Washington, DC, (June 1959).

7. A. G. Evans, "New Dose Estimates from Chronic Tritium Exposures," Health Phys. **16**, 57 (1969).

8. W. Minder, "Interne Kontamination mit Tritium," Strahlentherapie **137**, 700 (1969).

9. W. S. Snyder, B. R. Fish, S. R. Bernard, M. R. Ford, and J. R. Muir, "Urinary Excretion of Tritium Following Exposure of Man to HTO—A Two Exponential Model," Phys. Med. Biol. **13**, 547 (1968).

10. B. E. Lambert, H. B. A. Sharpe, and K. B. Dawson, "An Accidental Intake of Tritium Water," J. Am. Ind. Hyg. Assoc. **32**, 682 (1971).

11. S. M. Sanders and W. C. Reinig, "Diagnosis and Treatment of Deposited Radionuclides," **Excerpta Medica Foundation** (1968), p. 534.

12. A. A. Moghissi, M. W. Carter, and R. Lieberman, "Long-Term Evaluation of Biological Half-Life of Tritium," Health Phys. **21**, 57 (1971).

13. J. J. Koranda, "Residual Tritium at Sedan Crater," USAEC report UCRL-70292 (April 1967).

14. W. M. Jones, "Half-Life of Tritium," Phys. Rev. **100**, 124 (1955).

15. G. H. Jenks, F. H. Sweeton, and J. A. Gormley, " A Precise Determination of the Half-Life and Average Energy of Tritium Decay," Phys. Rev. **80**, 990 (1950).

16. Subcommittee on Permissible Exposure to Radiation in an Emergency Condition, G. V. LeRoy, Chairman, " Exposure to Radiation in an Emergency," Report No. 29, National Committee on Radiation Protection and Measurements, Univ. of Chicago, Chicago, IL (January 1962).

17. R. C. Weast, S. M. Selby, and C. D. Hodgman, Eds. **Handbook of Chemistry and Physics,** 46th Ed. (The Chemical Rubber Co., Cleveland, OH, 1965-1966).

18. T. B. Rhinehammer, P. H. Lamberger, Eds., "Tritium Control Technology," USAEC report WASH-1269, Mound Laboratory, Miamisburg, OH (December 1973).

19. R. M. Alire, Los Alamos Scientific Laboratory, personal communication, October 1974.

20. S. Dushman, J. M. Lafferty, **Scientific Foundations of Vacuum Technique** (J. Wiley and Sons, Inc., New York, 1962).

21. R. S. Carlson, Mound Laboratory, Miamisburg, OH, personal communication, October 1974.

22. Cajon Vacuum Products, Cat. No. CA-1171, Cajon Co., Cleveland, OH (1972).

23. Haskel Engineering and Supply Co., Bulletin S-6, Burbank, CA, 1966.

24. Nupro Manually Operated Bellows Valves, Bulletin N-473, Nupro Co., Cleveland, OH (1973).

25. MKS Instruments, Inc., Applications Note No. 1 MKS Instruments, Inc., Burlington MA (1973).

26. Matheson Gas Products Engineering Report G-131, Matheson Gas Products, East Rutherford, NM (1973).

27. "Properties of Copper and Copper Alloys," **Metals Handbook**, Vol. I, Am. Soc. Metals, Metals Park, OH (1961), pp. 1007-1010.

28. J. Crank, **The Mathematics of Diffusion** (Oxford at the Clarendon Press, 1967).

29. D. H. Davis, "Monte Carlo Calculation of Molecular Flow Rates through a Cylindrical Elbow and Pipes of Other Shapes," J. Appl. Phys. **31**, 1169 (1960).

30. Net 2 - A. F. Malmberg "Users Manual Net-2, Network Analysis Program," Release No. 9, HDL-050-1, Harry Diamond Laboratories, Washington, DC, September 1973.

31. W. E. Quinn, Los Alamos Scientific Laboratory, personal communication, September 1974.

32. J. W. Tester, R. C. Feber, and C. C. Herrick, "Heat Transfer and Chemical Stability Calculations for Controlled Thermonuclear Reactors (CTR)," Los Alamos Scientific Laboratory report LA-5328-MS (July 1973).

33. J. P. Coughlin, **Contributions to the Data on Theoretical Metallurgy, XII. Heats and Free Energies of Formation of Inorganic Oxides**, Bureau of Mines Bulletin 542 (U.S. Gov. Printing Office, Washington, DC, 1954).

34. Balsers Bulletin P31-14-7102c, Balsers High Vacuum Corp., Santa Ana, CA (~1973).

35. Varian Bulletin VAC-1025, "NRC 316 Series Circular Chevron Cryotraps, Varian Vacuum Division, NRC Operation, Lexington, MA (~1973).

36. The Excalibur Corp. bulletins 3-750-01 and "Cryo-Vacuum Pumps Excalibur series CVR-1100," The Excalibur Corp., Los Altos, CA (November 1973).

37. The Excalibur Corp., private communication, 1974. Pump description: Linde Cryosorption pump (4000 *l* capacity); Linde bulletin F2891 "Linde SN-150 Cryosorption Vacuum Roughing Pump," Union Carbide Corp., Linde Division, New York (~1973).

38. H. M. Rogers and R. Michalek, "Tritium Removal Systems," bulletin EM 10054, Engelhard Industries Division, Engelhard Minerals and Chemical Corp., East Newark, NJ (~1972).

39. J. L. Anderson, personal communication, Los Alamos Scientific Laboratory, September 1974.

40. Linde Co. Bulletin F1026B, The Linde Co., New York (1962).

41. D. R. Stull and H. Prophet, Project Directors, **JANAF Thermochemical Tables,** 2nd Ed., NSRDS-NBS 37 (Superintendent of Documents, U.S. Government Printing Office, Washington, DC, 1971).

42. J. H. Garber and F. N. Peebles, "The Combination of Hydrogen and Oxygen in Platinum Catalyzed Flow Reactors," Oak Ridge National Laboratory report ORNL 1796 (October 1954).

43. G. L. Phillabaum and P. C. Adams, "The Development of the Mound Laboratory Supplied-Air Bubble Suit," Mound Laboratory Report MLM-2008 (February 1973).

44. Carbon Products Div. Bulletin 524-203ha, Union Carbide Corp., N.Y., NY, 1971.

5.7 DIAGNOSTICS

5.7.1 Introduction

5.7.1.1 Experience at Los Alamos

Progress in controlled thermonuclear research has been inextricably tied to the development of plasma diagnostics. Researchers at Los Alamos have an expertise in diagnostics accumulated from many years of experimental work and are uniquely qualified for the task of instrumenting and diagnosing the SFTR.

The original Scylla experiments pioneered the use of streak cameras and neutron detectors.[1,2] The results were excellent, and very nearly the same techniques are in use as standard methods today. Careful studies of x-ray emissions from Scylla established the electron temperature, impurity levels, and other plasma features.[3-6] The double-foil or two-absorber technique[7] for electron temperature measurements grew out of the work and was the standard method until the advent of Thomson scattering. During this same early period, work on the Perhapsatron S-4 involved elaborate visible and ultraviolet spectroscopy for determination of impurity levels and energy losses due to radiation.[8]

Significant improvement in diagnostics was made possible with the use of lasers. Their brightness and nonperturbing interaction with a plasma led to a host of applications. One of the first and most impressive applications at LASL was the use of a ruby laser as an illumination source in a Mach-Zehnder interferometer on Scylla IV.[9] The resulting interferograms showed the density profile in a striking manner—both qualitatively and quantitatively. The method was later combined with a He-Ne laser measurement of Faraday rotation to obtain the magnetic field internal to the plasma.[10]

One of the next laser techniques developed was the coupled-cavity interferometer (using the 3.39-μ wavelength of a He-Ne laser) which is fairly easy to align and offers significantly greater response to plasma than does visible radiation.[11] Examples of results using this method are found in the Scylla III experiment[12,13] and Scyllac.[14]

Many other interferometric methods have been used, such as a Mach-Zehnder on a linear Z-pinch,[15] a coupled-cavity with a CO_2 laser,[16] a Michelson interferometer with a CO_2 laser,[17] and a Mach-Zehnder interferometer using a pulsed CO_2 laser.[18]

At the same time that lasers were being used, refinements were sought in other measurements. Plasma luminosity was made more quantitative by the use of fiber optics and photomultipliers. Combined measurements of luminosity and magnetic excluded flux determined the plasma beta in theta pinches.[12,14] External field measurements have also been applied to the Columba Z-pinch to determine internal current characteristics.[19]

Interferometry with a Mach-Zehnder, while extremely useful, is a difficult technique because of practical requirements of alignment and mechanical stability. Due to the pioneering effort at Los Alamos,[20,21] essentially the same data are now obtained routinely and much more easily by the use of double-exposure holographic interferometry. The technique has been used on Scylla IV-3, a 3-m theta pinch,[22] using in some cases as many as three lasers for three time intervals;[23,24] on the 5-m linear Scyllac;[25] and implosion studies on Scylla I-B.[26] The method has also been extended to CO_2 pulsed laser light,[27] and recently to HF laser radiation at 3.39 μ, which permits side-on density profile measurements in Scyllac.[28]

In recent years Thomson scattering has become one of the favored plasma diagnostic schemes because of its highly localized and fundamental nature. On Scylla III the cooperative scattering phenomena were studied;[29,30] 90° Thomson scattering was used on the linear 5-m Scyllac;[25] the electron temperature was measured with a unique technique on the Scyllac toroidal experiment;[14,31] and on ZT-1 the electron temperature was measured.[32]

5.7.1.2 Importance of Diagnostics

In the thinking and planning for this experiment it was clear that elaborate diagnostics would be needed. This need comes from the level of uncertainty in predicting the results, and a realization that only by careful instrumentation and observation can one effectively identify the inevitable problems.

The proper role of diagnosticians is to test hypotheses advanced to predict plasma behavior. Experience shows that first interpretations can change completely when sufficient data are examined. Since much time and expense are involved in modifying a device the size of SFTR, careful diagnostics greatly facilitate the process of defining problems and seeking their solutions. In so doing, the effort and expense of thorough instrumentation are more than repaid.

5.7.1.3 Increased Role of Automatic Data Processing and Its Significance

In recent years, many of the improvements in diagnostic methods consist of better data acquisition and analysis by the use of computers. Previously, the standard approach for taking data had been to use oscilloscopes with cameras and Polaroid film. As soon as fast (submicrosecond intervals) analog-to-digital converters became commercially available, it was possible to acquire data and transfer them to a small dedicated computer immediately (a second or less) after an experimental discharge. The implications of this technique are many and far-reaching. The computer can be programmed to display results in an intelligible manner. Data analyses can range from simple tasks such as scaling to more substantial feats such as curve fitting.

Consider, for example, the data obtained from a coupled-cavity interferometer. On an oscilloscope, one sees essentially a sine wave of voltage representing the optical path length vs time. To express the signal as plasma density vs time, one compares the phase timing with and without plasma. The difference is proportional to plasma density and is virtually impossible to see by simply looking at an oscilloscope trace, but it does show up when digitally recorded data are put through a straightforward computer operation. After every discharge, one immediately sees the plasma density at the preionization time and after main bank time. Any change from the expected values is immediately noted and can be investigated. In the older mode of taking data, it might happen, for example, that abrupt changes in preionization conditions would go unnoticed since analysis was time-consuming and attention was directed elsewhere. Clearly, it is possible to waste effort, lose valuable operating time, and temporarily misinterpret results while certain data await analysis. Such problems are largely avoided by automatic data acquisition and on-line computing.

Table 5.7-1 lists some comparisons between conventional and computer-oriented data acquisition. Overall, the automated data acquisition provides a more organized and fail-safe system with sophisticated feedback to the experimenter, permitting him to direct the experiment more intelligently.

Under development at the present time is automated digitization of optical information such as streak-camera results, Thomson scattering, interferograms, etc. The tremendous quantity of information in such two-dimensional displays of intensity have heretofore been largely unused because of practical constraints. By the use of dedicated minicomputers and modern television tube technology, this situation should change dramatically.

The present revolution in technique is fortunate, even essential, for a large device such as the SFTR. Conventional methods would be difficult if not impossible to extrapolate to such a large experiment with so many channels of information. Consequently all planning for diagnostics assumes the use of digital acquisition and computer control.

5.7.2 Basic Measurements and Equipment Required

5.7.2.1 Plasma Luminosity for Profile and Location of Density

A hot deuterium or D-T plasma (Te $\gtrsim$ 100 eV) emits radiation in the visible portion of the spectrum, which for the most part is free of lines and varies as $1/\lambda^2$. The intensity can be estimated as that due to bremsstrahlung although small amounts of impurities inevitably increase the level. The estimate for a deuterium plasma integrated from 4000 to 7000 Å is[33]

$$P_{Brem} = 6.4 \times 10^{-34} \frac{n_e^2}{T_e^{1/2}} \ (W/cm^3) \quad (1)$$

(n_e, cm^{-3}; T_e, keV). The relatively stronger dependence of emitted power upon density than upon temperature is the basis for using visible light to determine density profiles.

In the SFTR experiment, we expect substantially lower density and higher temperatures than in

TABLE 5.7-1

COMPARISON OF DIAGNOSTIC PROCEDURES USING CONVENTIONAL MEANS (WITHOUT COMPUTER) AND MODERN MEANS (WITH COMPUTER)

Step in Diagnostics	Procedure without Computer	Procedure with Computer
1. Prepare instruments for data collection	Generally easier because interfacing with an oscilloscope is easy.	Generally harder but improvements are constantly being made in A/D equipment. See below.
2. Calibrate response	Done on occasion depending upon attention of experimenter.	Typically done on every discharge by computer control, May require complications in the instrumentation.
3. Record data with plasma	Use oscilloscope. Accuracy is fair.	Use analog-to-digital device. Accuracy can vary to suit the experiment and be better than oscilloscopes if needed,
4. Make preliminary check of proper recording after each discharge	Look at photographs of oscilloscope traces.	Program computer to perform tests and display information to guide the experimenter.
5. Recheck calibrations	Done according to need as determined by experience.	Done either on every shot or intermittently with the aid of the computer.
6. Analyze data	Normally done one or more days after the event.	Done within seconds or minutes and displayed.
7. Re-analyze or further analyze in light of questions raised by study of the results	Often requires returning to original data, Process is usually tedious.	Original data is archived and analysis can be performed by programming.

previous experiments, but the level of intensity is still readily detectable. Section 5.7.4 gives some typical numbers based on the above formula. Image intensifiers are required in front of conventional streak cameras to record the expected level of luminosity. Furthermore, the time required to obtain enough photoelectrons to form an image of the plasma will limit the timing resolution to about 1 μs unless the plasma is much brighter because of impurities.

At present, an image-converter streak camera with intensifier and digital readout is under development. Such a device satisfies all the requirements of luminosity measurements in the SFTR. It offers the same type of quantitative information as the present luminosity apparatus (using fiber optics, photomultipliers, and analog-to-digital converters on each photomultiplier output). The new approach is less bulky, less expensive, and potentially more accurate because of greater spatial resolution.

We therefore propose to use such cameras at a variety of locations around the torus to observe the time history of the density profile. Any variations in the equilibrium around the torus will be detectable.

Instabilities of any type affecting the density profile and its evolution in time will also be detectable. Just as conventional streak cameras have been so useful heretofore, plasma luminosity is expected to be a basic diagnostic in the SFTR.

Special purpose instruments also can be readily designed. Position detectors for feedback and a framing camera to observe many slits simultaneously for mode structure have been used in the past. Because of the large time scale involved, we plan to develop a special television camera with instant replay features for qualitative observations. A single line of TV information can be scanned in 50 μs. If that line is parallel to the image of plasma through a slit, the resulting video signal stored with a recorder contains the same information as a conventional streak camera would, except that the time resolution is limited to the 50-μs framing time. Nearly standard video recorders can be used in this manner as inexpensive monitors of luminosity time history.

5.7.2.2 Neutron Detectors for Ion Temperature

The neutron flux will, of course, depend upon whether or not the filling gas includes tritium. In either case, the expected temperature and density are such that the neutron flux will be substantially higher than in previous experiments.

In many experiments the temperature derived from neutrons has been suspect because the time scale of the experiment did not appreciably exceed the "self-collision time" as given by Spitzer.[34] Some typical values are given in Table 5.7-2.

In the SFTR, the time scale will be sufficiently long that the ion velocity distribution should be truly Maxwellian; thus, the neutron emission rate should provide a reasonable measure of temperature. The reaction rates and cross sections are given by Glasstone and Lovberg[35]

$$R = 1/4\ n_D^2\ (\overline{\sigma v})_{DD}$$

(neutrons emitted/cm^3-s from D-D),

or

$$R = n_D\ n_T\ (\overline{\sigma v})_{DT}$$

(neutrons emitted/cm^3-s from D-T),

where

TABLE 5.7-2

ION-ION SELF-COLLISION TIME FOR DEUTERONS

Temperature (keV)	Density 10^{15} cm^{-3}	Density 10^{16} cm^{-3}
1	50 μs	5μs
4	400 μs	40 μs

$$(\overline{\sigma v})_{DD} = \frac{2.33 \times 10^{-14}}{T^{2/3}} \cdot \exp\ -\frac{18.76}{T^{1/3}}\ \text{cm}^3/\text{s},$$

$$(\overline{\sigma v})_{DT} = \frac{3.68 \times 10^{-12}}{T^{2/3}} \cdot \exp\ -\frac{19.94}{T^{1/3}}\ \text{cm}^3/\text{s},$$

with T in keV.

The temperature dependence is very strong; at 4 keV the neutron flux is 400 times greater than at 1 keV. Furthermore, the D-T cross section is approximately 75 times larger than the D-D cross section. Thus, we expect SFTR neutron fluxes to be 10^2 to 10^4 times larger than in previous experiments with time integrated yields 10^8 times larger because of the longer time scale.

The experimental apparatus for this diagnostic consists of scintillators and photomultipliers to determine the time history of the neutron emission and silver foils with counters to determine activation and thus total yield.

Spatial resolution, although clearly limited, is not as bad as one might think. Since the solid angle of neutron collection falls as $1/r^2$, the effective length of plasma column providing the signal is only a few times greater than the distance from the detector to the plasma axis. For example, a detector 1 m from the axis receives 99.9% of its signal from 3 m of length along the column.

5.7.2.3 Interferometry for Plasma Density

The basic interferometry method for plasma density measurement consists of measuring the change

in optical path length caused by the presence of plasma electrons. Taking p as the number of fringe shifts due to plasma (i.e., phase shift of light divided by 2π), n_e as the electron density along a ray of light (cm^{-3}), we have[36]

$$p = 4.5 \times 10^{-18} \lambda \int n_e d\ell \text{ (fringes)}$$

where λ is in microns and length is in centimeters. For example,

$$\int n_e \, d\ell = (2 \times 10^{15} \text{ cm}^{-3}) \times (6 \text{ cm})$$

$$= 1.2 \times 10^{16} \text{ cm}^{-2},$$

$$\lambda = 3.4 \, \mu,$$

$$p = 0.18 \text{ fringes.}$$

This may be too small for a holographic interferometer using HF laser light, but it is an adequate signal level for a coupled-cavity interferometer or similar device. It is reasonable to seek 1/100 fringe resolution using a He-Ne coupled-cavity interferometer operating at 3.39 μ. Normally one measures $\int n_e \, d\ell$ as a function of time along a single line, e.g., a chord through the center of the discharge tube. However, techniques are being developed to permit more than one chord to be scanned simultaneously, thus permitting density profiles to be measured.

5.7.2.4 Light Scattering for Temperature and Density Profile

Present techniques of Thomson scattering used on Scyllac should be directly applicable to SFTR. The scattered intensity for Thomson scattering is well known: at 90°, using a ruby laser, we have[37]

$$P_s \, d\lambda d\Omega dV = 4.48 \times 10^{-26} P_i \, n_e \cdot \frac{e^{-(\Delta\lambda/\lambda_o)^2}}{\lambda_o} \, d\lambda d\Omega dV \quad (W)$$

where

P_s = scattered power ($W/Å\text{-ster-cm}^3$)
P_i = incident power (W/cm^2)
n_e = electron density (cm^{-3})
λ_o = $19.4\sqrt{T_e}$ (Å) with T_e in electron volts.
$\Delta\lambda$ = wavelength shift from 6943Å.

In Sec. 5.7.5 we show that the intensity of the scattered light can be measured using reasonable parameters. By resolving the scattered light in space as well as wavelength, we obtain from a single laser pulse the density profile from the intensity of scattered light as well as the electron temperature profile from the spectral distribution of the scattered light. This is indeed a powerful diagnostic.

In principle, the density measurement can be calibrated absolutely by using Rayleigh scattering, but for the calibration one needs a much smaller level of stray light than is necessary to measure the spectrally shifted Thomson scattered light. By combining the interferometry data for absolute density with Thomson scattering for relative density, Rayleigh scattering calibrations are unnecessary.

For the time scale of SFTR, the electron and ion temperatures will be nearly equal if energy losses and energy exchange between the two species are classical. Ion temperature measurements using neutrons, excluded flux measurements, and electron temperature measurements will permit a study of the actual energy confinement.

5.7.2.5 Excluded Flux Loops

The significant feature of excluded flux measurements in SFTR is the very large signal available compared with standard theta pinches. Because of the large plasma radius, the excluded flux will be on the order of 10% of the flux through a loop around the plasma, rather than 1% as in present-day experiments. For this reason, the measurements should be significantly more accurate.

By combining excluded flux with an independent estimate of the relative pressure profile, the aboslute level of plasma pressure, or beta, can be determined. The relative pressure profile can be determined from luminosity as a function of time and checked by Thomson scattering at one instant of time. Plasma beta is an important parameter in all theories of equilibrium and stability.

5.7.2.6 Diagnostic Apparatus and Cost

Two levels of resolution are required in SFTR. Important phenomena surely occur within the basic helical wavelength, and these require a concentration of diagnostics within a single wavelength. Other variations can be expected over many wavelengths and thus require diagnostics periodically placed around the torus. The diagnostic apparatus described in Table 5.7-3 assumes that two distinct regions will be instrumented in as detailed a way as possible,

TABLE 5.7-3

LIST OF DIAGNOSTICS AND REQUIRED EQUIPMENT

Diagnostics	Required Equipment	Systems Needed	Estimated Cost
Digital streak camera	Image-intensified, conventional streak camera, digital TV systems, minicomputer.	4	$4 x 70K
Plasma luminosity TV monitor	LLTV camera, video recorder, display system.	80	80 x 15K
Neutron scintillators	Scintillator, photomultiplier, A/D converter.	80	80 x 1.0K
Neutron counters	Silver foil, Geiger tube, counter with digital output.	20	20 x 0.5K
Coupled-cavity interferometer	He-Ne laser, optics, detector, fast A/D converter.	4	4 x 20K
Thomson scattering	Ruby laser, optics, 3-grating polychrometer, image intensifier, digital TV system, minicomputer.	4	4 x 100K
Excluded flux	Loops, probes, A/D converter.	80	80 x 2K
		Total	$2210K

while the remainder of the torus will be monitored at equal intervals using relatively less expensive diagnostics.

In addition to equipment costs, there is a substantial development cost for a large and sophisticated system. Approximately 20 man-years would be needed for testing and calibration of prototypes. The total cost for instrumentation of SFTR is, therefore, estimated to be $3.21M. In addition, an estimated $1.0M would be used for advanced development (see below) so the total cost for diagnostics is estimated to be $4.2M.

5.7.3 Advanced Techniques for Development

5.7.3.1 Light Scattering at 10.2 Microns

Light scattering measurements in the cooperative regime (Salpeter parameter $\alpha \equiv (\Delta k \lambda_D)^{-1} \approx 1$) can be used to measure ion temperature and/or plasma turbulence. For the SFTR parameters, a CO_2 laser at 10.6 μ can be used at a scattering angle of about 10° for such a measurement. The technique has been applied elsewhere[38] and should be applicable to SFTR if windows for the CO_2 wavelength are carefully incorporated into the vacuum system.

The measurement would establish the level of turbulence at wavelengths close to the Debye length and might be important to transport processes. In the absence of turbulence, the measurement would provide a localized determination of ion temperature.

5.7.3.2 Determination of Wall Interaction

A difficult but important question concerns the plasma/gas conditions outside the main column and near the wall. Appropriate diagnostics are unknown because little can be predicted about the conditions to be found. Spectroscopy, specialized Thomson scattering, wall pressure and temperature sensors, and magnetic field probe measurements come to mind. Such measurements will be carefully planned and refined as experience is obtained.

5.7.3.3 Neutron Measurements

The increased flux of neutrons will doubtless allow a number of refinements in neutron measurements. For example, significant improvements in spatial resolution may be possible.

An interesting technique for temperature measurements using neutron activation of materials has been discussed at LASL by Group T-2.[39] The energy spread of emitted neutrons is significantly increased by the thermal motion of the interacting ions. Using the $^{9}Be(n,p)^{9}Li$ reaction, which has a threshold of 14.26 MeV, it is possible to determine the ion temperature at 5 keV with a statistical uncertainty of 2%. This new approach should be tried and may prove very valuable.

5.7.4 Predicted Bremsstrahlung Level of Luminous Radiation in SFTR

Using Eq. (1) in Sec. 5.7.2.1 we can estimate the effective surface brightness by using expected plasma parameters. Present-day theta pinches radiate 10 to 50 times this estimated level because of small levels of impurities, but we will not include this factor because the higher temperature and longer time scale of SFTR may give different results. Assuming,

$$n_e = 2 \times 10^{15}\ cm^{-3},$$

$$T_e = 4.0\ keV$$

$$R_{plasma} = 4\ cm,$$

we estimate a source brightness of

$$B = (P_{Brem}/4\pi) \times R_{plasma} = 0.4\ mW/cm^2\text{-ster}.$$

For example, if one uses an image of the 20-cm discharge tube on a 2-cm photocathode (magnification = 0.1), and the lens aperture is f/1.6 (f/16 in the plasma), the light flux F on the cathode is

$$\text{Solid angle} = \frac{\pi}{4f^2} = \frac{\pi}{4(1.6)^2} = 0.307$$

$$F = B \times \text{solid angle} = 0.123\ mW/cm^2.$$

Typical cathodes give 50 mA/W so the electron flux from the cathode is 6.1 $\mu A/cm^2$. If we seek spatial resolution of 0.01 cm on the cathode (0.1 cm in the plasma), we must detect 0.61 nA per picture element.

This current corresponds to one photoelectron every 0.25 ns. A good image requires about 1000 photoelectrons per picture element so the time resolution is limited to about 0.25 μs. This is not expected to be an important limitation, but working at such a low level of intensity does require more gain than is offered by conventional streak cameras. Various types of image intensifiers are available to permit operation at the limit of quantum statistics so we see no fundamental difficulty in the measurement.

5.7.5 Predicted Intensity for Thomson Scattering

Assuming that a two-dimensional detector is used to obtain spatial resolution as well as wavelength resolution, we estimate the signal level at the first photocathode of the detector. The intensity of light per unit area may be increased by demagnification of the image until either the necessary lens aperture becomes impractical or the spatial resolution becomes unacceptable. For this numerical example, we assume collection at f/8, magnification of 1/5, spatial resolution of 2.5 mm in the plasma (0.5 mm on the cathode), and wavelength resolution of 100 Å (200 Å/mm linear dispersion on the cathode). We write ϕ, the flux of light per unit area on the cathode, as

$$\phi = gm^{-2}\, P_s\, d\Omega \left(\frac{d\lambda}{dy}\right)\left(\frac{dy}{dx}\right)$$

where

g	= efficiency of optical system,
m	= magnification from plasma to cathode,
$d\lambda/dy$	= linear wavelength dispersion on cathode (Å/cm)
dV/dx	= A, the area of the incident laser beam (cm^2),
P_s	= scattered power (W/cm^3-Å-ster),
$d\Omega$	= solid angle of collection (ster).

Taking

$P_i A$	= 500 MW
n_e	= $10^{15} cm^{-3}$
$e^{-(\Delta\lambda/\lambda_0)^2}$	= 1/2
T_e	= 4000 eV
λ_0	= 1200 Å
$d\Omega$	= 0.0123
m	= 0.2
$d\lambda/dy$	= 2000 Å/cm
g	= 0.05

and using the equation in Sec. 5.7.2.4, we obtain

$$\phi = 0.89\ mW/cm^2$$

This assumes that an image of the incident laser beam is as small as the entrance slit of a grating polychrometer. Assuming we use an S-20 photocathode with 20-mA/W sensitivity, we would expect a 20-ns laser pulse to give N photoelectrons in each resolution element (1/2 mm x 1/2 mm)

$$N = \left(\frac{0.02\ A/W}{1.6 \times 10^{-19}\ C/e} \right) \phi A t$$

$$= 5600\ p.e.$$

This signal level is adequate with regard to statistical fluctuations (1%) and detectability using image intensifiers.

REFERENCES (Chap. V, Sec. 5.7)

1. K. Boyer, W. C. Elmore, E. M. Little, W. E. Quinn, and J. L. Tuck, Phys. Rev. **119**, 831 (1960).

2. E. M. Little, W. E. Quinn, and F. L. Ribe, Phys. Fluids **4**, 711 (1961).

3. K. Boyer, E. M. Little, W. E. Quinn, G. A. Sawyer, and T. F. Stratton, Phys. Rev. Lett. **2**, 279 (1959).

4. F. C. Jahoda, E. M. Little, W. E. Quinn, G. A. Sawyer, and T. F. Stratton, Phys. Rev. **119**, 843 (1960).

5. A. J. Bearden, F. L. Ribe, G. A. Sawyer, and T. F. Stratton, Phys. Rev. Lett. **6**, 257 (1961).

6. G. A. Sawyer, A. J. Bearden, I. Henins, F. C. Jahoda, and F. L. Ribe, Phys. Rev. **131**, 1891 (1963).

7. E. M. Little, W. E. Quinn, F. L. Ribe, and G. A. Sawyer, Nuclear Fusion: 1962 Supplement, Part 2, p. 497.

8. H. J. Karr, E. A. Knapp, and J. E. Osher, Phys. Fluids **4**, 424 (1961).

9. F. C. Jahoda, E. M. Little, W. E. Quinn, F. L. Ribe, and G. A. Sawyer, J. Appl. Phys. **35**, 2351 (1964).

10. R. F. Gribble, E. M. Little, R. L. Morse, and W. E. Quinn, Phys. Fluids **11**, 1221 (1968).

11. D. A. Baker, J. E. Hammel, and F. C. Jahoda, Rev. Sci. Instrum. **36**, 395 (1965).

12. G. A. Sawyer, V. A. Finlayson, F. C. Jahoda, and K. S. Thomas, Phys. Fluids **10**, 1564 (1967).

13. K. S. Thomas, Phys. Fluids **11**, 1125 (1968).

14. W. R. Ellis, F. C. Jahoda, R. Kristal, W. E. Quinn, F. L. Ribe, G. A. Sawyer, and R. E. Siemon, Nucl. Fusion **14**, 841 (1974).

15. P. R. Forman, A. Haberstich, H. J. Karr, J. A. Phillips, and A. E. Schofield, Phys. Fluids **14**, 684 (1971).

16. H. Herold and F. C. Jahoda, Rev. Sci. Instrum. **40**, 145 (1969).

17. J. E. Hammel, R. W. Peterson, and A. R. Sherwood, Status Report of the LASL Controlled Thermonuclear Research Program for a 12-Month Period Ending October 1970, Los Alamos Scientific Laboratory report LA-4585-MS.

18. P. R. Forman, F. C. Jahoda, and R. W. Peterson, Appl. Opt. **11**, 477 (1972).

19. A. Haberstich and P. R. Forman, Bull. Amer. Phys. Soc. **13**, 1489 (1968).

20. F. C. Jahoda, R. A. Jeffries, and G. A. Sawyer, Appl. Optics **6**, 1407 (1967).

21. T. D. Butler, I. Henins, F. C. Jahoda, J. Marshall, and R. L. Morse, Phys. Fluids **12**, 1903 (1969).

22. R. F. Gribble, W. E. Quinn, and R. E. Siemon, Phys. Fluids **14**, 2042 (1971).

23. C. R. Harder, F. L. Ribe, R. E. Siemon, and K. S. Thomas, Phys. Rev. Lett. **27**, 386 (1971).

24. K. S. Thomas, C. R. Harder, W. E. Quinn, and R. E. Siemon, Phys. Fluids **15**, 1658 (1972).

25. K. S. Thomas, H. W. Harris, F. C. Jahoda, G. A. Sawyer, and R. E. Siemon, Phys. Fluids **17**, 1314 (1974).

26. K. F. McKenna, R. Kristal, and K. S. Thomas, Phys. Rev. Lett. **32**, 409 (1974).

27. P. R. Forman, S. Humphries, Jr., and R. W. Peterson, Appl. Phys. Lett. **22**, 537 (1973).

28. R. Kristal, Appl. Opt. **14**, 628 (1975).

29. M. Daehler and F. L. Ribe, Phys. Rev. **161**, 117 (1967).

30. M. Daehler, G. A. Sawyer, and K. S. Thomas, Phys. Fluids **12**, 225 (1969).

31. R. E. Siemon, Appl. Opt. **13**, 697 (1974).

32. J. N. DiMarco, L. C. Burkhardt, P. R. Forman, R. B. Howell, and H. J. Karr, Jr., Bull. Amer. Phys. Soc. **18**, 1327 (1973).

33. Glasstone and Lovberg, **Controlled Thermonuclear Reactions**, D. van Nostrand, Princeton (1960), p. 32.

34. L. Spitzer, **Physics of Fully Ionized Gasses**, (Interscience, NY, 1962) p. 133.

35. Glasstone and Lovberg, op. cit., pp. 10-20.

36. F. C. Jahoda and G. A. Sawyer in **Methods of Experimental Physics**, R. Lovberg, Ed. (Academic Press, New York, 1971), Vol. 9B, p. 1.

37. A. W. DeSilva and G. C. Goldenbaum, in **Methods of Experimental Physics**, H. R. Griem and R. H. Lovberg, Eds. (Academic Press, New York, 1970) Vol. 9, Part A, Chap. 3.

38. N. R. Bretz and A. W. DeSilva, Phys. Rev. Lett. **32**, 138 (1974).

39. D. W. Muir, office memorandum to F. C. Jahoda, Mar. 4, 1974.

5.8 CONTROL

5.8.1 Introduction

The purpose of the control system is to provide for the proper operational sequencing of the various systems within the SFTR, as well as to monitor for improper operation of the system and to implement a safe shutdown procedure when necessary. The control system could be a completely analog system employing relay operations, meter readouts, signal lamps, and audible alarms with provisions for operator interactions at each step, similar to early Scyllac operation. Conversely, it could be completely computer-controlled, with data being recorded and stored in memory, and requiring no operator action except to initiate the operation. Finally, the control system could consist of some combination of these two extremes, similar to present Scyllac operation. The advantage of the analog system is its apparent simplicity and reduced cost. However, such a system is inflexible, slow, and requires much effort on the part of the operator, thus easily leading to operator error. In addition, such a system in an experimental machine such as the SFTR will undoubtedly require many changes and modifications to accommodate an evolving experimental physics program and thus what was intended to be a simple inexpensive system quickly becomes a complicated costly system requiring much effort to document and maintain.

The advantage of the computer-based system is the complete automation of all actions with the greatly reduced probability of error and the high degree of flexibility inherent in a computer-based system. The disadvantage is the effort required in precisely defining all control functions, in the programming of the computer, the documentation, and maintenance effort required. It is sometimes argued that the lack of operator interaction in an experimental procedure results in a loss of insight in

the process; however, similar arguments can be made for the increases of insight gained through employing computer control. A combination analog and digital control system could also be designed to have some of the advantages of both types, but such a system would also have some of the disadvantages. The present Scyllac control system follows the latter approach.

A machine as large as the SFTR will require the monitoring and accumulation of data from thousands of sensors. The assimilation of these data by an operator on the time scale required to take appropriate action in an emergency procedure is beyond the capability of one or even a battery of operators. Computer operation will therefore be a necessity for many of the functions, and the advantages of a completely computerized system appear to outweigh the disadvantages. Thus, we opt for a completely computerized system with the capability of strong operator interaction through the computer during normal operation of the experiment.

The control system will be designed as a distributed multicomputer network. A multicomputer design will be the most flexible and can easily accommodate future design changes and modifications. The system will provide for a rapid data reduction with graphic display to enable the operator to study the data between each discharge. Because of the high speed and precise timing requirements, the spark gap trigger system will be an analog system as discussed in Sec. 5.3.5.1, with the initiation signal being provided by the computer. The safety interlock system will also be essentially analog (e.g., interlock switches, electrical lockouts), but will be monitored by the computer so that the machine operator can quickly locate the cause of any operational shutdown.

The control system will be designed to allow the systematic testing of the various subcomponents of the machine to aid in the location of malfunctioning components. This will decrease the time required to locate and repair a malfunction and thus increase the overall availability of the machine.

5.8.2 System Design

The basic design of the control system consists of a main control computer, which is interconnected via a communication bus to several system computers. The system computers provide the detailed control functions with the master computer handling system timing functions, monitoring for and interrupting on fault conditions, and determining the status of the system. The main control computer will be located in the control room, with the subsystem computers typically located in shielded areas near the system being controlled.

The major systems in the machine to be controlled or monitored are:

- Vacuum and Tritium Handling System
- METS Refrigeration System (Phase II)
- METS Energy Transfer System (Phase II)
- Compression Bank Energy Transfer System (Phase I)
- Implosion-Heating System
- Preionization System
- Precision Timing System
- Diagnostics System
- Safety Interlock System
- Display Computer

Various subsystems can be controlled independently, e.g., the compression bank charge subsystem or the pulse charge subsystem of the implosion-heating system; however, these stand-alone subsystems will be categorized with the major systems with which they are associated. The degree of control or monitoring that a system requires will vary significantly throughout the machine and therefore the size and complexity of the associated computers will also vary. For example, the preionization system computer will only be required to charge the PI banks and monitor for malfunctions in 640 capacitor and start gaps, whereas the compression bank computer must control the charging of 19 200 capacitors from 8 power supplies and monitor the operation of 4800 start switches and 1280 crowbar switches. The PI computer will therefore be much smaller than the compression bank computer and may, in fact, be combined with one of the other system computers.

Figure 5.8-1 shows the various interconnections in the control system. An important consideration in this type of design is to define carefully the interface standards between the various subcomponents. This includes the interface standard between the main control computer and various system control computers, as well as the interface between the computers and the machine. The interfacing standard probably will be the CAMAC standard now in existence. Use of the CAMAC standard will allow the use of equipment that has already been developed under this standard and will also allow devices developed for this system to be used in other systems. Also, component and software development can proceed independently of the actual computer system to be used.

The CAMAC interface will be serial for those sections of the machine with many points to monitor and no critical timing requirements. It will be parallel for those areas of control where timing is a problem. In addition, a microprocessor can be embedded in the control system to insure very rapid

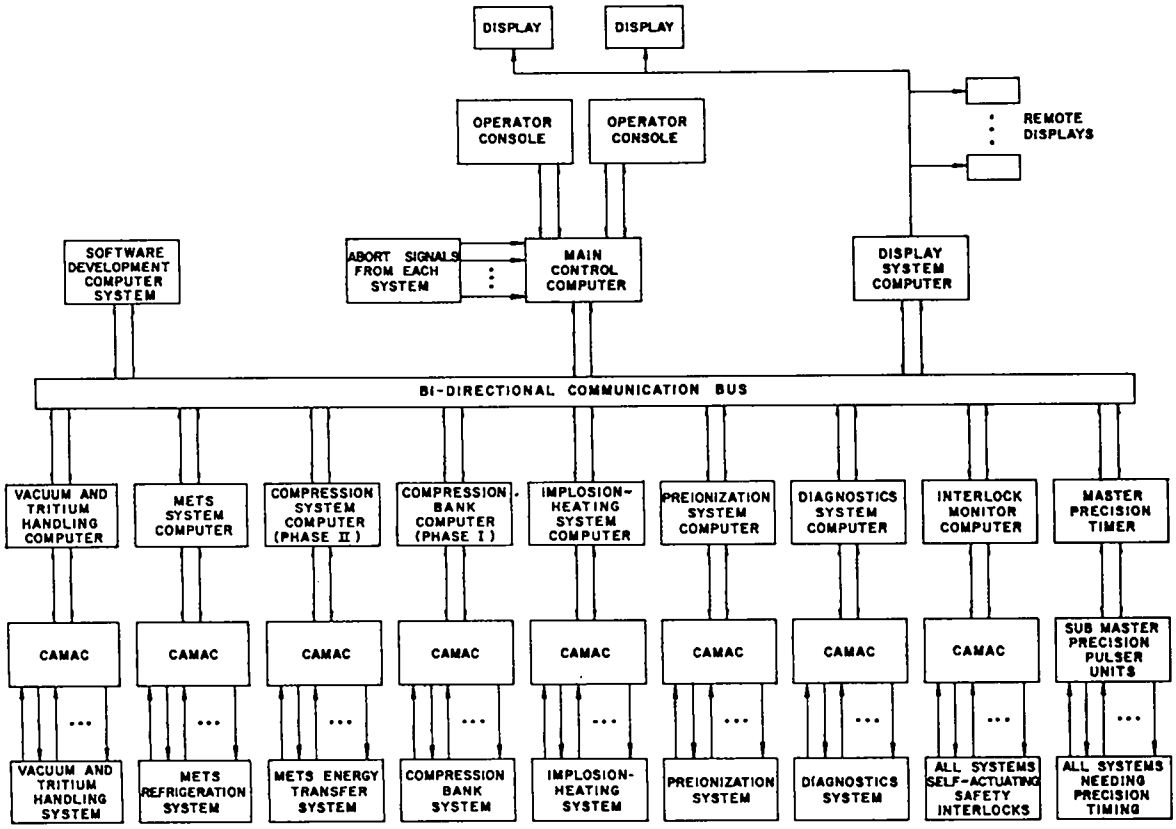

Fig. 5.8-1.
Block diagram of the SFTR control system.

response when needed. For applications such as the trigger systems, where the microprocessor is not fast enough, analog circuitry will be used as indicated by the precision timing system. Analog circuitry will also be used in personnel and machine safety applications. This analog circuitry will then be monitored by computer so that the operator will be informed of the cause of any malfunction and can take appropriate action.

It should also be noted that the CAMAC standard is being used on the Scylla IV-P experiment, which will provide a technology base for its use on the SFTR.

The requirements and control of the systems within the machine will be discussed in the following sections.

5.8.2.1 Tritium Handling and Vacuum System

The tritium handling and vacuum system control is an integral part of the system itself (see Sec. 5.6.4). Thus, the function of the control computer is that of system monitoring, timing, and determination of operating conditions. The normal mode of operation of the system is to evacuate the plasma chamber, introduce the proper mixture and volume of gas, and diagnose the data acquired during the event. These actions will be initiated by the control computer. The progress of the actions will be followed by the control computer and displayed at the control console for the machine operator.

In the event of a failure of a part of the system or an accidental release of tritium, the tritium handling system will immediately revert to a failure mode of operation to clean up the tritium spill and will signal the main control computer via a high priority interrupt to go into a failure mode of operation and bring the machine to a nonoperational status. Such a procedure will include ceasing all charging, dumping all stored energy, shorting all capacitor banks, and opening the METS energy-storage coils. After the failure mode actions have been taken, the status of the machine will be displayed at the control console.

5.8.2.2 METS Refrigeration System

As with the tritium handling and vacuum system, the METS refrigeration system is an integral part of

the system itself. The primary function of the control computer is system monitoring. The overall purpose of the refrigeration system is to provide and store cryogens for the METS superconducting coils (Sec. 5.4.3). The control computer will determine whether or not the system is operating properly and will display the status on the operator console. Fault conditions detected by the control computer will result in failure mode of operation that disarms the machine until the trouble is corrected or the METS system is locked out.

5.8.2.3 METS Energy Transfer System

The METS energy transfer system is completely controlled and monitored by the control computer. The computer will insure that the storage coils are superconducting, control the charging of the storage coils, and initiate the switching of the current from the storage coils into the compression coils. All components in the system will be monitored simultaneously to insure proper operation. The shot will be aborted via a high priority interrupt in the event of a component failure. The normal operating sequence of the system is described in Sec. 5.4.3.1.

5.8.2.4 Compression Bank System

The compression bank system supplies the energy for the compression field during Phase I of system operation, as discussed in Sec. 5.4. The control computer performs all control function as well as system monitoring. The computer will control the charging of the compression bank, and the initiation of the switching operation. Monitoring for proper operation of the components will be carried out and the shot aborted in the event of component failure. The operation consists of charging the compression bank, which is carried out in 30 s, and which triggers the master ignitron 530 μs before the time required for peak compression field. The crowbar switch is closed when the field reaches its peak. The compression bank consists of 20 480 capacitors, 5120 start ignitrons, and 5120 crowbar ignitrons. All of these components will be monitored for proper operation and the machine operator alerted to any malfunctioning component.

5.8.2.5 Implosion-Heating System

The implosion-heating system consists of the implosion-heating capacitor bank as well as the pulse charge system and the trigger systems for the start gaps and crowbar gaps. The control computer controls the slow charging of the pulse charge system, but the actual triggering of the system must be accomplished with more precision than can be accomplished by the computer. The triggering is carried out by the precision pulser system. The computer will monitor the system for proper operation and will alert the machine operator to any malfunctioning components.

5.8.2.6 Preionization System

The preionization system is small and simple. The computer will control the charge cycle and provide component monitoring. Triggering will be accomplished by the precision pulser system.

5.8.2.7 Diagnostics System

The diagnostics system consists of a series of instruments: streak cameras, neutron counters, etc. (see Sec. 5.7.2). The diagnostics system computer will be used to calibrate the diagnostic equipment in addition to its use in acquiring and reducing the data. It will also provide data storage for a few tens of events to aid the experimenter in evaluating the data. The precision timing pulses required by the diagnostic equipment, such as in the Thomson scattering measurement, will be provided by the precision pulser system.

5.8.2.8 Precision Pulser System

This system provides pulses with nanosecond resolution for triggering the implosion-heating system and precise timing of the diagnostics system. The pulser system is controlled directly by the main control computer. The main control computer checks that all machine systems are ready and then triggers the precision pulser, which initiates the plasma burn cycle. Until the precision pulser is triggered, it is possible to abort the shot, but once the pulser is triggered, the shot must be completed.

5.8.2.9 Safety Interlock System

The safety interlock system provides for personnel and machine safety and can be considered to consist of two parts. The machine is protected by both fast analog protection circuitry and computer programming. The computer provides the main protection; however, the machine operator can also terminate a shot via the analog circuitry in the event of a dangerous condition.

The personnel safety interlocks must be handled differently—people can walk into dangerous situations at any time even when the machine is turned off; therefore, a fail-safe personnel safety interlock system will be installed and monitored, but

not controlled, by the computer. A warning system that consists of horn, bells, and flashing lights to alert personnel of dangerous situations will be part of the safety interlock system.

5.8.3 Basic Computer Design

5.8.3.1 Computer Protection

The environment in which the computers must function is very harsh and several specifications have been made to give the computer as much protection as possible. First, "clean power" is specified for the computer and diagnostics, and "dirty power" for the rest of the machine. The clean power is to be split from the dirty power at the 13.8-kV transformers and kept separate thereafter. Also, each rack of computer equipment is to be fed from an isolation transformer. Within each rack the power is to be distributed on one side of the rack and logic signals on the other. A double-electrically-isolated shield room is specified to house the computer and data acquisition equipment. In addition, 120-dB power line filters are specified for each leg of the incoming power. Strict attention will be paid to the grounding system to keep ground-loop problems to a minimum.

The CAMAC equipment will be mounted in racks which will appear as extensions of the outside wall of the shield room, and clean power will be fed through copper pipes from inside the shield room.

In addition, the control signals to the power supplies and other systems will be coupled, using techniques that have proved successful in other LASL fusion experiments.

5.8.3.2 Standard Nomenclature

Standard systems of nomenclature have proved valuable in the design and maintenance of large systems; therefore, a uniform system of notation to be used throughout the entire design has been defined. This uniform nomenclature is valuable because it enables personnel of diverse backgrounds to communicate. It also aids in teaching the operation of machine to new personnel and the technicians who help run and maintain the system.

The basic idea is to have a uniform nomenclature that can communicate the information desired, but that is not so cumbersome as to fall into disuse. Also, it should be versatile enough to be usable. Therefore, the following eight-character standard format was chosen:

1	2	3	4	5	6	7	8
V	V	W	W	X	Y	Y	Z

where VV is a two-character abbreviation for the major system, WW is the device name, X is the device type, YY are digits to distinguish between multiple units, and Z is the signal type. The abbreviations used to date are shown in Table 5.8-1. The standard 8-character nomenclature can be preceded by two more characters, making a 10-character, or larger, name capable of handling multiple identical systems.

A typical power supply cycle will now be described. A preionization primary bank supply will serve as an example. A typical cycle would be:

1. Open the shorting balls.
2. Open the dump Jennings switch.
3. Close the load Jennings switch.
4. Close the ac contactors.
5. Monitor the voltage on the bank.
6. Wait for full charge.
7. Open the ac contactor.
8. Open the load Jennings.
9. Fire the machine.
10. Close the jump Jennings.
11. Drop the shorting balls.

This power supply, named PIBKS01, is shown in Fig. 5.8-2. The typical operating cycle can now be described using the signal names that cause the various actions to occur. The first signal sent by the computer would be PIBKA01B which would actuate the air cylinder and open the shorting balls. The computer now checks PIBKA01S to confirm the desired effect. If the shorting balls fail to open, the computer would now flag the operator and take the proper error exit. If the shorting balls opened, the computer would now send PIBKJ02D, which would open the dump Jennings switch; the proper sense signal PIBKJ02S would now be tested to confirm that the proper action occurred. As each function is performed, the computer tests the proper input signal to confirm proper action. The remainder of the write-up will ignore the test signals.

PIBKJ01L is now transmitted, connecting the power supply to the load. The load must be connected before the ac power energizes the power supply since the supply will overvolt if not connected to a load. Signal PIBK01P is now sent and the supply begins to charge the PI bank. The voltage across the bank is monitored by the computer using signal PIBKM01V, which is an input to an analog-to-digital converter. Again, if this signal fails to show the proper behavior the computer can abort the

TABLE 5.8-1

ABBREVIATIONS USED IN THE SYSTEM OF STANDARD NOMENCLATURE

A. Column 1 and 2 describe system

PR	primary	AR	air
CA	crowbar-A	VC	vacuum
CB	crowbar-B	IL	interlock
PI	preionization	SF	sulfur hexafluoride
IH	implosion heating	CO	compression
GA	gas	DI	diagnostics

B. Column 3 and 4 for device name

BK	bank	TP	turbo pump
BF	buffer	PS	pressure sensor
BO	booster	IG	ion gauge
CT	cable test	TC	thermocouple
BI	bias	MV	manual valve
PC	pulse charge	HR	horn
TR	trigger	BL	bell
CO	compressor	BE	beacon
VL	value	WT	water temperature
FP	forepump	WF	water flow
MR	manual regulator	PO	power on

C. Column 5 for device type

S	supply	L	light
D	divider	J	Jennings switch
G	gauge	C	contactor
P	protection	B	breaker
A	actuator	W	warning
M	monitor		

D. Columns 6 and 7, 2-digit number that distinguishes between multiple units

E. Column 8 signal type

V	volts	T	torr (pressure)
I	current	L	load
S	sense switch	D	dump
P	power on-off	B	shorting balls
O	open/close (valves)		

charging of the power supply. When the supply reaches the proper bank voltage, the computer drops signal PIBKC01P disconnecting the ac power. Next, the computer drops PIBKJ01L disconnecting the load. This is done to protect the power supply from transients when the capacitor bank is dumped into the load coil.

The PI ready signal is now sent to the main control computer, which can then initialize the Fire Pulse if the machine is in an operational condition. If the machine were undergoing testing, the PI bank Fire Pulse could originate from the PI subsystem. If a failure has been detected, the computer can send PIBKJ02D and the energy in the bank will be dissipated in the water resistors. If it is a successful shot, the dump Jennings are closed to drain any remaining charge in the capacitors. In either case, PIBKJ02D is the next signal to be sent by the computer, then PIBKA01B is dropped, closing the shorting balls, and the cycle is now complete.

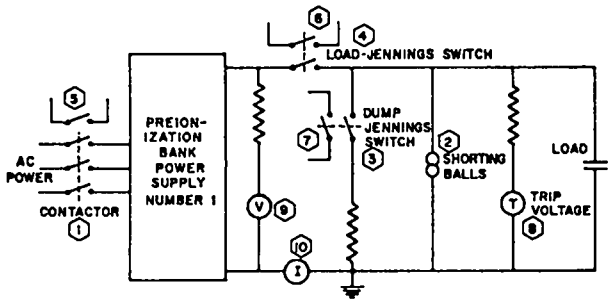

SUPPLY NAME	MAXIMUM RATINGS
PIBKC01P	60 kV, 1A

OUTPUT SIGNALS

SIGNAL NAME	ACTION WHEN TRUE
① PIBKC01P	CLOSES AC CONTACTOR CONNECTING POWER
② PIBKA01B	OPENS SHORTING BALLS
③ PIBKJ01L	CLOSES LOAD SWITCH CONNECTING LOAD
④ PIBKJ02D	OPENS DUMP JENNINGS

INPUT SIGNALS

SIGNAL NAME	INDICATION WHEN TRUE
⑤ PIBKC01S	POWER SUPPLY CONNECTED TO AC
⑥ PIBKJ01S	POWER SUPPLY CONNECTED TO LOAD
⑦ PIBKJ02S	BANK CONNECTED TO DUMP RESISTOR

ANALOG SIGNALS

SIGNAL NAME	SHUNT VALUE	INDICATION
⑧ PIBKM01V	10 VOLTS	MONITORS BANK
⑨ PIBKM02V	10 VOLTS	MONITORS SUPPLY
⑩ PIBKM03I	10 VOLTS	MONITORS SUPPLY CURRENT

Fig. 5.8-2.
Typical power supply schematic.

5.8.3.3 Main Control Computer and Operator Consoles

The operator consoles will interface to the main control computer through the defined standard interface. This will allow the control console to be treated as just another input/output device and will allow the machine to begin operation with a very simple control console, which can then be easily replaced in the future by more elegant ones. It also allows the machine to be easily reconfigured by the operating program through redefinition of the input and output signals.

The main control console will communicate with the subsystem computer on two different paths. It will transmit and receive information on the standard communication path in those situations where there is sufficient time. In addition, a fast interrupt system will be used to transmit abort signals between the control computers and the various subsystem machines. The control computer should have a vectored interrupt structure to enable it to respond quickly to the abort signals from the subsystem control computers.

It should be stressed that the subsystems will protect themselves, and only after each subsystem has given an all-is-well signal will the main control system start the precision pulser firing system. This will insure that the entire system is vulnerable to a subsystem malfunction for only a minimal time.

5.8.3.4 Cathode Ray Tube Display System Computer

Graphic displays are a powerful means of man-machine communication. Graphics devices, however, cause a heavy load on a control computer. Therefore, to insure the control computer's rapid response to varying situations, the graphics devices will be driven by a separate computer system.

Two types of displays will be used. Live displays, which have selective erase, will be used to communicate with the main control console. This will allow the maximum man-machine communication where it is needed.

Storage tube displays will be scattered throughout the machine and will allow users to interrogate the control computer and view results from many stations throughout the machine with a much smaller amount of overhead than that required by the live displays.

5.8.3.5 Precision Pulser (Timing) System

The timing measurements of the various subsystems vary from tens of minutes to nanoseconds. To accommodate such a wide range of timing requirements, the timing is split into coarse and fine or precision timing systems.

The coarse timing is provided by the main control computer. The main control computer can communicate with the various subsystem control computers and vary the timing to accommodate the various systems.

Once all the subsystems are in a "go" condition, the main computer sends a pulse that triggers the precision pulser system.

The precision pulser system contains a master pulser which is capable of driving several submasters. Both the master and submaster pulsers have variable delays that can be used to synchronize the start pulses. The submaster channels can then be delayed in increments of 10 ns. The output of the submaster is boosted to a 8-kV pulse, which is then used to fire the various systems.

The system submaster pulsers will be cabled radially from the master pulser, centrally located in

the master control room, to insure simultaneity of the submaster start pulses. The variable delays built into the submaster units can then be used to control the timing to within 10 ns.

5.8.4 Software Development Machine

Since the cost of the software (programming) usually far exceeds the cost of the hardware for a typical system, a software development machine will soon pay for itself many times over by reducing the program development time for the system. This machine should have all the core storage necessary to support developmental software, such as editors, high-level languages, and debug programs that aid program checkout such as trace and patch routines.

This machine should be capable of running in the time-sharing mode with multiple input/output devices such as Tektronix Model 4010 CRT units. Time-sharing will further reduce program development time by allowing many programmers "simultaneous" access to the machine.

The development machine will, in turn, reduce the amount of core storage needed on the worker computers. It will also reduce the need for sophisticated input/output devices on these machines. Figure 5.8-3 is a schematic of this subsystem.

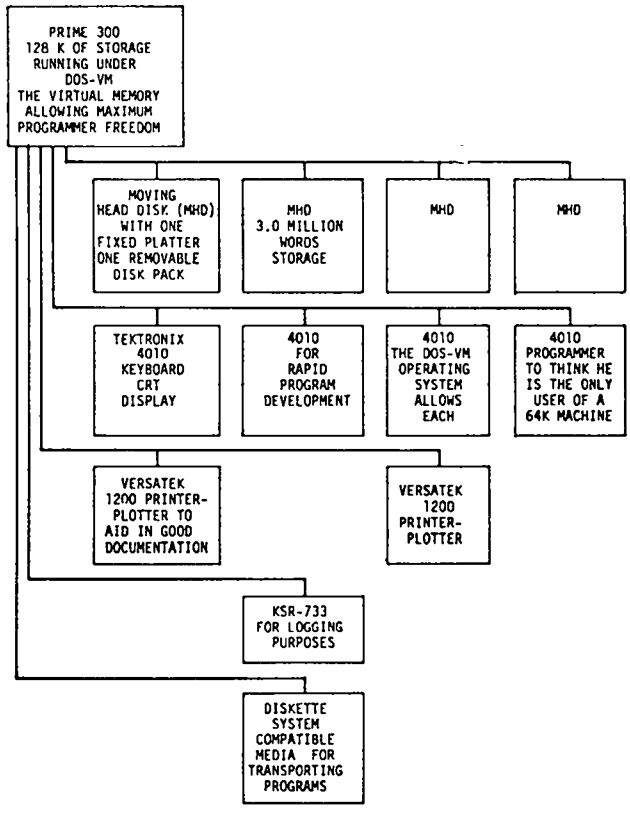

Fig. 5.8-3.
Software development system.

VI. FACILITIES

6.1 GENERAL DESCRIPTION

The facilities for the SFTR include not only a large amount of covered area and associated utilities to house the experimental equipment, such as the plasma chamber, trigger systems, and compression system, but also include the construction required for the handling of tritium and activated materials. The major elements making up the facilities are: Concrete Shielding Structure and Remote Handling Equipment, Tritium Handling Installation, METS Refrigeration Installation, METS Maintenance Area, Compression System Area, Trigger System Area, Diagnostics and Control Room, Shops Area, Warehouse and Receiving, and Administrative Area.

Several approaches to SFTR structure design were considered. The initial approach placed the entire installation inside a large square structure approximately 120 m on a side and four stories high; however, it was found that such a structure was larger than needed, and did not lend itself to economical construction techniques so that the cost of the facilities was unduly high. Removing the corner of the structure came close to satisfying the space requirements, but placing all areas inside the torus presented egress problems for the personnel involved in the operation and, again, was not well suited for economical construction techniques. In the layout that was finally selected, a toroidal-shaped structure is placed over the main experimental equipment, with the support facilities located in inexpensive buildings around the outside of the torus.

The overall facilities layout is illustrated in Fig. 6-1, with plan views of the various levels shown in Figs. 6-2 through 6-4. The basic approach is to place a main toroidal building around the plasma chamber and shielding structure, the compression system area, and diagnostics area. Room is also provided for the trigger system, with floor space available for limited maintenance operations. The diagnostics area is located on the ground floor adjacent to the inside of the shielding structure, and a single-story control room is located at ground level in the center of the building to allow for uniform cable runs between the control room and the torus. A hot cell is located on the basement level inside the torus to handle radioactive components from the plasma chamber. The hot cell is also located adjacent to a main 3-m-wide basement-level passage which runs beneath the shielding structure from the receiving area to two elevators inside the torus so that equipment and material can be moved in and out of the inner area of the torus. Little maintenance will be carried out inside the torus so that only a limited number of personnel will normally be working in this inner area. Egress from the torus is provided by the 3-m-wide main passage plus three additional 1.8-m-wide personnel passages running under the shielding structure to the periphery of the main building. The METS refrigeration equipment, METS maintenance area, tritium facility, shops and maintenance area, receiving and storage areas, and administrative areas are placed in appropriately sized structures around the outside of the main toroidal building. Such an approach allows a more conventional building design to be followed, thus resulting in lower structural costs.

Table 6-1 lists the square footage associated with each of the major areas within the facility. Experience gained from the present Scyllac facility has been used in determining the proper size of the support areas. In general, a support area for SFTR which is three to four times that of the present Scyllac experiment is felt to be sufficient. Shop support can also be provided as required from the CTR Office Building, located close to the SFTR. The office building will also provide the office space requirements for SFTR personnel.

6.2 MAIN STRUCTURE

The main toroidal structure houses not only the plasma chamber and shielding structure, but also the compression system consisting of the 128 METS dewars, the vacuum interrupters and transfer capacitor banks, the trigger system for the implosion-heating system, and the diagnostics area. The building is a 12-sided structure in a toroidal shape. The enclosure is 30 m wide, 12 m high, and the periphery of the building is 50.3 m from the center of the torus. A cross section of the structure is shown in Fig. 6-5. The plasma chamber and shock-heating system are located inside a concrete structure which provides a biological shield from neutron radiation and also a secondary containment vessel in

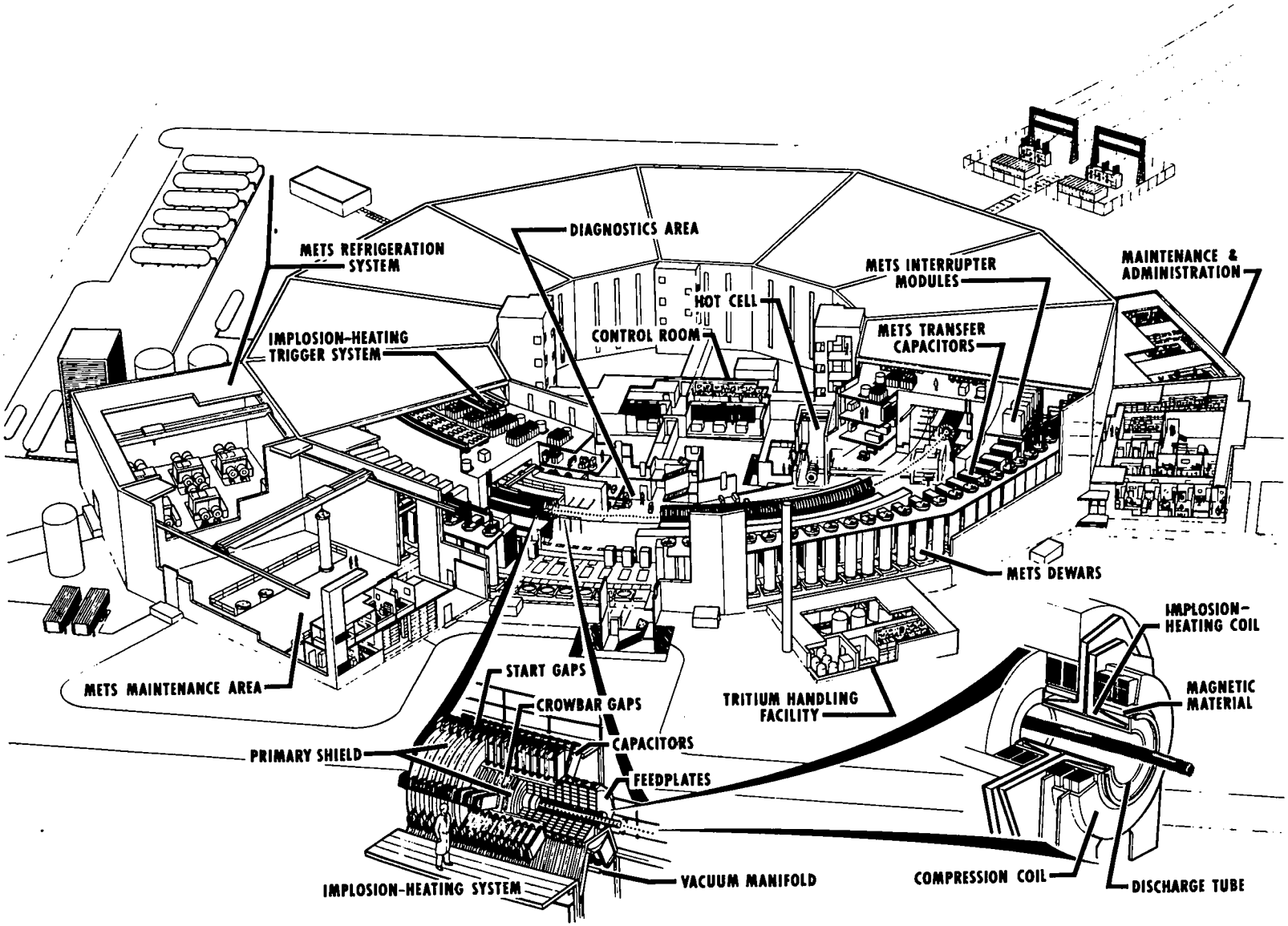

Fig. 6-1.
General view of the Scyllac Fusion Test Reactor.

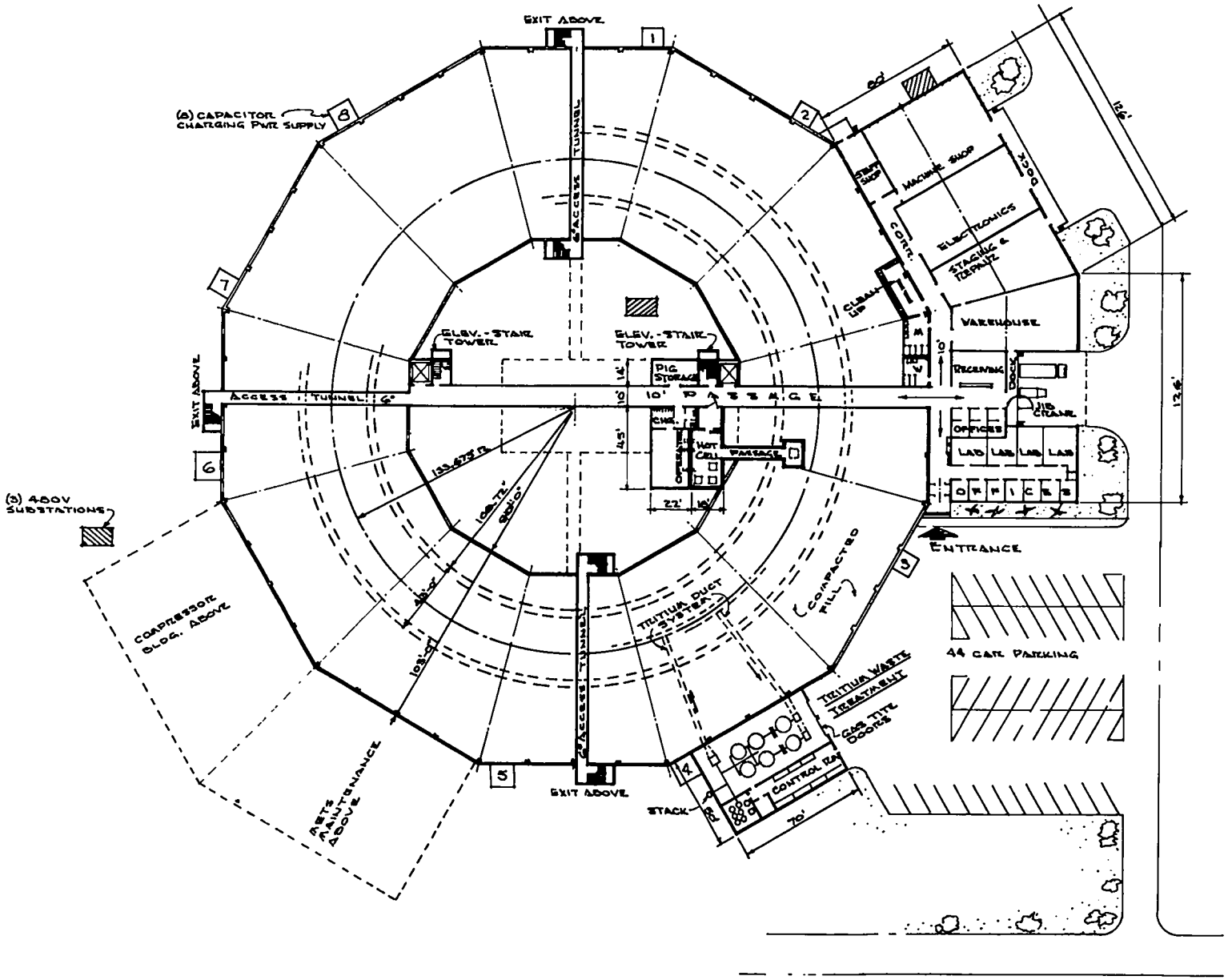

Fig. 6-2.
Basement-level floor plan.

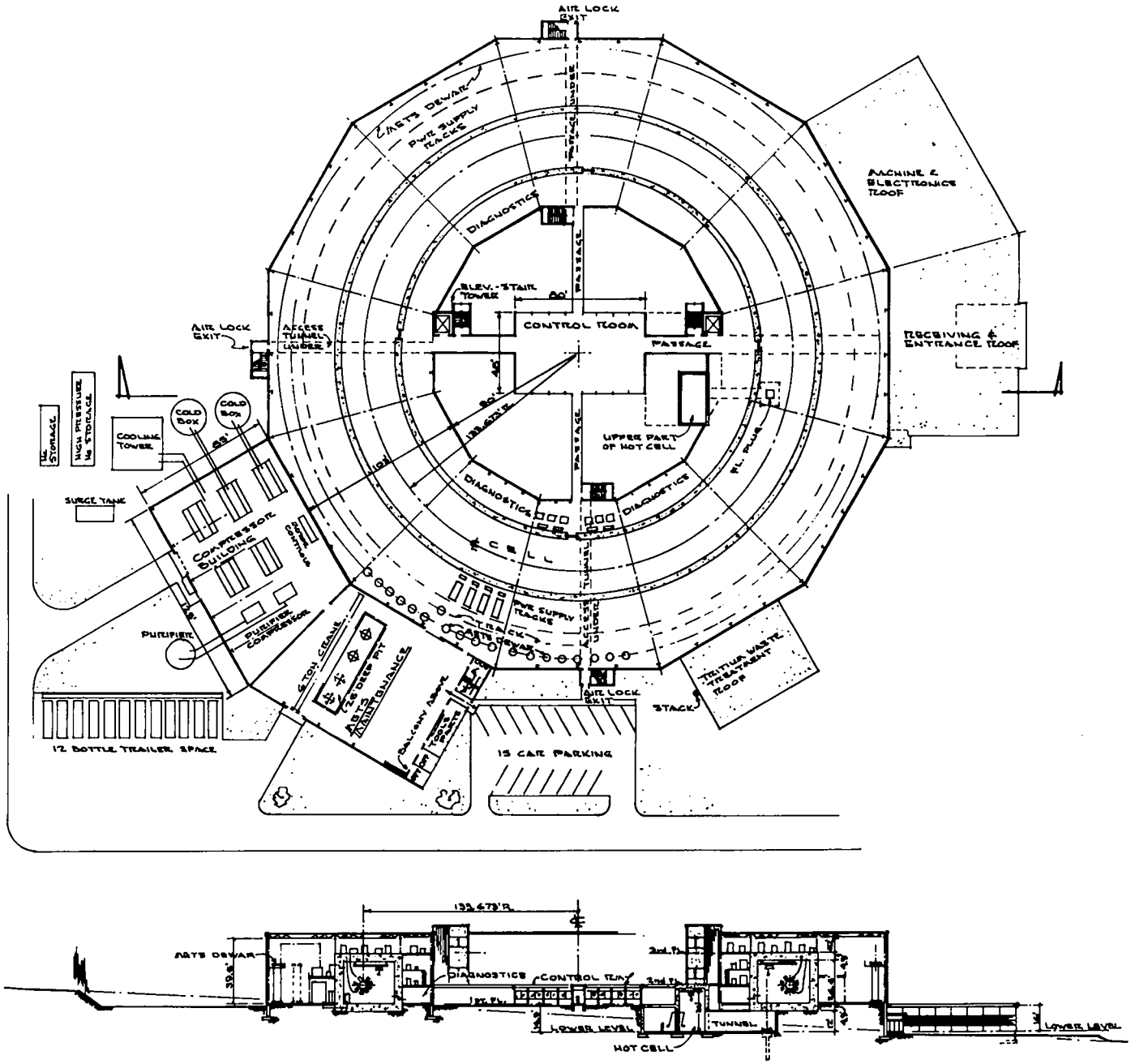

Fig. 6-3.
Ground-level floor plan and overall elevation view.

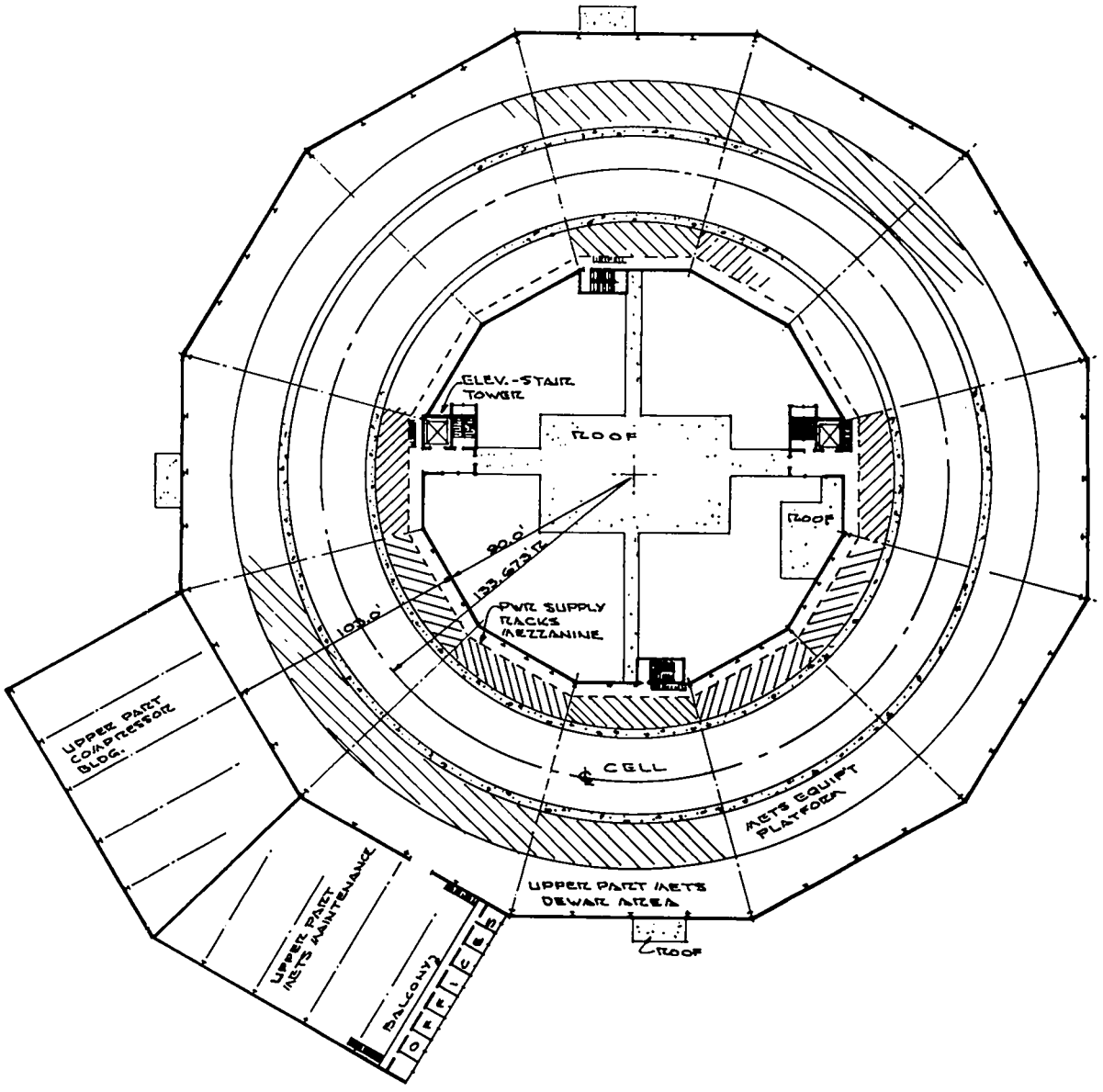

Fig. 6-4.
Upper-level floor plan.

the event of a tritium spill from the plasma chamber. The wall thickness of the concrete shield is approximately 1.5 m, the inside height is 8 m, and inside width is 10 m. The plasma chamber will be placed on a steel support structure to be erected after the structure has been completed. The submaster gaps for the trigger system will also be located inside the structure. Four overhead cranes, which can be controlled remotely, will provide for initial installation, as well as maintenance during operation. After operation with DT, the plasma chamber will be radioactive, and maintenance functions must be handled remotely. As long as the major shield is in place, personnel will have access to the inside of the concrete shield structure so that capacitor and spark-gap maintenance can be done without the need for remote handling equipment. In the event that a portion of the plasma chamber must be replaced, the capacitors and gaps will be removed from the module and the cabling and vacuum system disconnected. A remote handling fixture on the crane will permit removal of the main shielding

TABLE 6-1

SQUARE FOOTAGE OF MAJOR ELEMENTS IN THE SFTR FACILITY

Main toroidal building	91 600 ft^2
Tritium handling	3 500
METS refrigeration system	9 500
METS maintenance area	9 500
Control room	3 800
Machine and staff shop	3 600
Electronics maintenance and repair	4 900
Receiving and warehouse	2 800
Small laboratory space	1 500
Office space	1 600
Total	132 300 ft^2

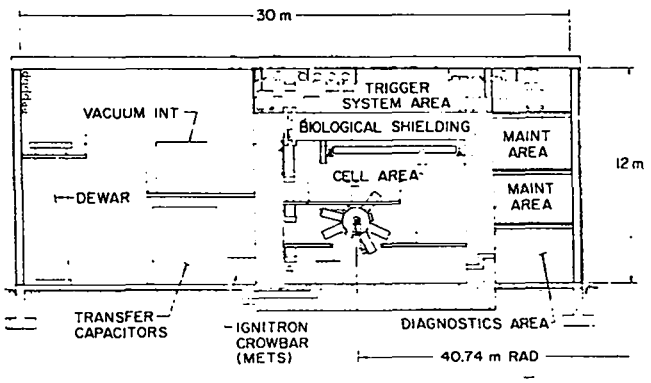

Fig. 6-5.
Cross section of main toroidal structure.

and the module section will be unwelded. As many as four 40-cm modules can be handled as a single unit by the remote handling facilities. Four modules are estimated to weigh 4 tons so that a 5-ton crane will be adequate. When the module section has been unwelded, the crane will move the module to the hot-cell entrance located in the floor of the concrete shielding structure (see Fig. 6-2). The module will then be placed on a dolly in the hot cell for repair. A repaired module section will be introduced into the shielding structure and welded into the plasma chamber in the same manner.

A large number of openings will be required in the concrete shielding structure. Cable feedthroughs, as shown in Fig. 6-5, will be required for the implosion-heating trigger system cables, the pulse-charge system cables, and the compression system cables. Diagnostic ports through the inside wall will be necessary. Personnel and equipment access will be through four doors, one in each quadrant on the inside wall of the structure. The cables penetrating the structure will require a 15-cm^2 conduit every 38 cm around the torus, both in the ceiling and in the bottom. The cable seal system will be sufficiently tight to satisfy the tritium release requirements (see App. II). A 45-cm diagnostic port will be provided every 3.2 m or every wavelength for a total of 80 ports.

Two maintenance levels are shown in Fig. 6-5 above the diagnostics area. Only a very low level of maintenance activity, requiring a minimum of personnel, will be carried out in these areas. The areas will also be used for staging during construction and can provide space for additional experimental equipment.

The trigger system must be located as close as possible to the implosion-heating capacitors and gaps in order to reduce cable lengths; thus, the trigger system is placed on top of the shielding structure with cable feedthroughs, as discussed earlier.

The energy-storage system will be adjacent to the outside wall of the shielding structure, with the crowbar ignitrons placed in clusters next to the wall at the cable penetrations. The capacitor banks will be just outside the ignitron clusters, and the vacuum interrupters will be on a steel rack over the transfer capacitors. The dewars containing the superconducting energy-storage coils will be located adjacent to the outer wall of the building. The piping required for the cryogenic coolants will be on the outside wall over the dewars. The cabling between the various components of the compression system will be run in floor ducts wherever possible. Cranes will not be provided in the compression system area. Instead, hydraulic lifts and dollies will be used for the vacuum interrupters and capacitors, while the ignitrons can be handled directly by personnel. The dewars will be mounted on individual dollies and moved to maintenance facilities on permanent tracks installed in the floor around the torus.

6.3 METS REFRIGERATION AND MAINTENANCE AREA

METS refrigeration system components, such as the compressors and control panels, requiring protection from the elements are to be placed in a structure approximately 900 m^2 and 12 m high. The METS maintenance area will be in an adjoining structure of similar size. The two structures will be located next to the main toroidal structure, as shown in Fig. 6-3. Those refrigeration system components, such as the gas-storage tanks and cooling tower, are

to be placed outside, next to the refrigeration building.

An access way between the METS maintenance area and the main structure allows a dewar to be moved on the track system into the maintenance area. The maintenance building will not be tall enough to allow the storage coils to be lifted out of the dewar directly, so the dewar is to be placed in an 8-m-deep pit to provide sufficient overhead clearance. The pit will accommodate four dewars simultaneously. A 6-ton crane provided in the METS maintenance area will handle the dewars and storage coils. A small office space and tool room located in the METS maintenance building will have storage space on a balcony above the office and tool room.

6.4 HOT-CELL TRITIUM FACILITY AND CONTROL ROOM

The hot cell is to be located inside the torus at the basement level adjacent to the main 3-m access corridor. A corridor also leads from the hot cell to a door in the floor of the concrete shielding structure, as shown in Fig. 6-2, through which modules of the plasma chamber can pass. The hot-cell facilities can handle as many as four 40-cm modules as a single unit.

The main purpose of the hot-cell facilities is to handle the defective radioactive components of the plasma chamber which are activated after several operations with DT. The parts to be handled by the hot cell are the first wall, Marshall coil and feedplates, magnetic material, and compression coil. Maintenance will be required if the first wall cracks or if an electrical failure occurs in the Marshall coil or compression coil. The hot cell will have two maintenance positions and one checkout position. Positions for storing up to 10 spare units of 4 modules each are also provided in the hot cell. The hot cell has a total area of approximately 144 m^2, not including the connecting corridors.

Defective modules will be lowered through the doorway in the concrete shielding structure onto a remote-controlled dolly in the corridor leading to the hot cell. The dolly will then be moved to one of the two maintenance positions, where work will be carried out by manipulators. It is envisioned that the maintenance operation will consist of unwelding the components of the module as required and replacing the defective components with new components which have been brought in through the main access corridor and introduced into the hot cell. The refurbished group of four modules will then be moved to the checkout position where the coils will be given a high voltage test and the vacuum seals tested. After successfully passing the tests, the modules will be placed in the storage racks as spares for later use. The defective components which were removed from the modules will be placed in "pigs" which will then be moved by truck to the radioactive dump for disposal.

The structure required to house the tritium handling facility will be adjacent to the outside of the main toroidal structure on the basement level as shown in Fig. 6-2. The structure will have doors large enough to permit the processing equipment to be moved in and out of the building. The doors will be gastight to allow the structure to serve as a secondary confinement vessel in the event of a tritium spill. The tritium waste treatment facility is to be in an area of approximately 144 m^2. A duct system will lead from the tritium-waste treatment facility to the shielding structure so that any spilled tritium can be circulated from the plasma chamber through the treatment facility. A 25-m stack will vent the output of the facility when the tritium level has reached a satisfactorily low level. A 75-m^2 control room for the tritium facility will be adjacent to the waste treatment facility. A 21-m^2 tritium storage vault for storing the inventory of gaseous tritium will also be in the facility.

The control room is to be a single-story structure with a floor space of approximately 355 m^2 on the ground floor at the center of the torus, as shown in Fig. 6-3. Four covered passageways lead from the control room directly into the diagnostics area of the main building. These passageways will provide personnel access from the control room to the diagnostics area and also provide sheltered runs for cable ducts between the control room and the main buildings. The control room will contain the main computer equipment in a screen room and the main control panel with appropriate display equipment.

6.5 GENERAL MAINTENANCE AND ADMINISTRATIVE AREAS

The maintenance activities will require a substantial machine shop and electronics shop, such as shown in Fig. 6-2. A 265-m^2 machine shop for production machining jobs and a 50-m^2 staff shop where the CTR staff has access to machine tools are expected to support the normal activities of the facilities. Overload machine work can be handled by the shops in the CTR office building located near the SFTR site or can be done in the main laboratory shops. The electronics shop is housed in a 250-m^2

area where electronic items will be developed and built as required. Normal repair of existing electronics components will be handled in a separate 190-m^2 area containing storage shelves for spare components and parts. In addition to the above shop areas, four small laboratories, with a total floor space of approximately 125 m^2, are provided primarily for diagnostic purposes. The total area devoted to maintenance functions, including the laboratory space, is approximately 880 m^2.

The receiving area shown in Fig. 6-2 is located at the end of the main 3-m-wide passage running under the concrete shielding structure to two elevators, one on each side of the torus. Equipment can thus be offloaded from trucks and taken directly to the appropriate level in the main toroidal building. A 42-m^2 receiving area and 190-m^2 warehouse are provided, but these storage areas are for incoming inspections and temporary storage only. Most of the equipment probably will be moved from a laboratory staging area directly to its permanent location in the facility. During operation of the experiment, the warehouse will be used for storage of spare parts.

It is expected that the major administrative support area for the SFTR will be in the CTR office building. Ten offices are included for those few staff members spending 100% of their time at the facility.

6.6 STRUCTURES AND UTILITIES

The main toroidal building and attached auxiliary structures are designed to take all possible advantage of prefabricated building techniques in order to achieve the lowest possible structural cost. The basic construction will be a structural steel frame with appropriate steel siding and insulation. The roof will consist of insulated built-up roofing supported by open-web steel joints. Modular design will be employed to achieve flexibility as well as economy. The architectural and structural requirements, the heating and ventilating systems, the piped distribution systems, and the electrical service systems will be basically the same for each module. The design will be in accordance with the appropriate ERDA standards and codes. Earthquake loadings will be determined in accordance with the uniform building code for seismic risk zone 2; wind loads will be in accordance with the A.N.S.I. code A58.1, with a 1000-yr mean recurrence level, a basic wind speed of 100 mph with exposure C.

The concrete shielding structure will be constructed from reinforced concrete and will be designed to support the trigger system as well as to provide basic structural integrity. Care has been taken to eliminate as much massive foundation construction as possible. The shielding structure will rest directly on the ground and be sufficiently massive to provide its own foundation. The flooring of the main building and auxiliary buildings is simple reinforced-concrete slab.

Two basic ventilation systems are provided. A special system provides the necessary ventilation for the tritium handling facility, such as for tritium hoods and tritium cleanup in the shielding structure. This system will have a minimum of two supply and two return/exhaust fans, and will also be designed to have reserve capacity for emergency conditions. The design will allow the shutdown of any one fan for maintenance and repair without reducing the required ventilation rate of the system.

The normal ventilation system will furnish air in the quantity and at the temperature and humidity necessary to satisfy the requirements for comfort and the processes and operation in the structure. Refrigerated air conditioning is not expected to be required except in the control room where the computer equipment is located.

Little chilled water will be required for the facility except for the METS refrigeration system. An appropriately sized cooling tower will be provided as discussed in Sec. 5.4.3.17.

Utilities for the SFTR will provide for domestic water, fire water, natural gas, electric power, storm drainage, and sanitation. Due to the size and importance of the electrical power requirements, the electrical power utilities are discussed separately in Sec. 6.7. Domestic water and fire water will be connected to a water system to be installed at the proposed Two-Mile Mesa site prior to the construction of this facility. Back-flow prevention devices will be installed as required. The fire-water line will be looped to insure a reliable flow and will include all necessary hydrants and P.I.V. valves.

The natural-gas line will be connected to a gas main that presently exists on Two-Mile Mesa.

Sanitary waste will be connected to a system to be constructed on Two-Mile Mesa prior to the construction of the SFTR. The system will collect all sanitary waste on Two-Mile Mesa and convey it to the existing Sanitary Waste Treatment Facility at TA-3, which presently has the capacity to handle the additional load.

Storm drainage will be accomplished through open ditches and site grading, except at walks and roads, where drains will be provided.

Chemical waste will be collected locally and transported to the Laboratory's industrial waste treatment group for disposal. A holding tank will be

installed for collecting waste tritiated water. Depending on its tritium concentration, the water will either be exhausted through the stack at the facility or transported to the Laboratory's industrial waste treatment group for solidification and burial.

6.7 ELECTRICAL POWER

The operation of SFTR will put a significant and continuously changing demand on the local power supply system. Since the facility is expected to operate only over a period of a few years, power lines, transformers, and other long-lived distribution equipment must be carefully chosen to avoid expensive devices that cannot be used in future projects. The power supply system will be designed to operate at voltages compatible with existing LASL distribution equipment. That is, 115-kV, three-phase power line, 13.2-kV primary distribution system to several points within the facility, 13.2-kV to 480-V step-down and secondary distribution substations, 480-V power to large motors, dc supplies, etc., and 208/120-V supply for lights and other small loads as required. Installed capacity will be 20 MVA to handle the estimated load, including the METS system.

6.7.1 Power Requirements

The planned operating phases will require significantly different amounts of power. Phase I operation requires 2-MW continuous plus 16-MW pulsed loads, whereas Phase II requires 9-MW continuous plus 9-MW pulsed loads. Table 6-2 lists the various loads to be supplied and the expected operating condition. Pulse loads are, in general, linearly rising ramps approximately 30 s long with a drop to zero load at the end. The power shown in Table 6-2 is the peak load at the end of the ramp. Repetition rate will not exceed one pulse every 15 min. A continuous load of 2 MW is expected to supply building services during any phase of operation. An additional continuous load of 6-8 MW will be needed for the METS refrigeration system.

6.7.2 Impact on Electric Power System

The Los Alamos area is currently connected into the Public Service Co. of New Mexico (PSCNM) distribution network by two 115-kV lines; one from Santa Fe rated at 20 MW, and one from Albuquerque rated at 65 MW. Present planning includes two new lines from a PSCNM substation called Norton, approximately 12 miles east of Los Alamos. These new 115-kV lines will increase the total available power from PSCNM to 115 MW by 1981 and to approximately 200 MW by 1985. The Norton substation will be part of the PSCNM 345-kV network connecting Albuquerque, Farmington, and Ojo Caliente. Figure 6-6 shows the arrangement forecast for 1980. The 345/115 kV transformer at Norton has been ordered.

Power available for the SFTR in FY-81 will be 42 MW if the first 115-kV line to Norton is completed and LASL load grows, as forecast, from the current 50 MW to 88 MW. The total power available includes the 20-MW generating capacity at the Zia power plant in Los Alamos on a short time load basis (15 MW continuous). Since the expected SFTR load is 20 MW or less, the currently planned power source will be adequate.

In the event that the Warm METS option is adopted, a separate, dedicated 115-kV line will be required. This is discussed in App. I.

6.7.3 Power Distribution System

Figure 6-7 shows the proposed electrical distribution system at the SFTR site. The incoming 115-kV power line from ETA substation (see Fig. 6-6) will supply all power to the facility through a 115-kV to 13.2-kV, 20-MVA transformer; 13.2-kV switchgear will be used to control power to 11 locations within the area. Locations numbered 1 to 8 on Fig. 6-7 are for 2-MW dc power supplies used to charge the transfer capacitor banks during Phase I operations. The three shaded blocks in Fig. 6-7 represent 13.2-kV to 480-V substations. Each substation will contain one 2000-kVA, 13.2-kV/480-V step-down transformer and 480-V circuit breakers to feed the various loads in one-third of the building. The substation near the control room will supply the instrument and control power. The two substations outside the torus will supply most of the motors, lights, and building services. Power for motor control centers and other large loads will be supplied at the 480-V level. Power for lights, receptacles, and other small loads will be supplied by 480/120/208-V transformers located throughout the building. Clean power panels will be provided for critical instrument loads. These panels will be fed by 480/120/208-V isolating transformers. The substation near the METS refrigeration area will also contain transformers and motor starters for the large motors driving compressors in this area, and will have a total capacity of 10 MVA.

TABLE 6-2

ESTIMATED POWER REQUIREMENTS FOR SFTR

Load	Power Required (MW)	Notes
Shock heating Charge system	0.7	60-s pulse
Compression system Capacitor charging		
Phase I	16	30-s pulse
Phase II	5	30-s pulse
Cold METS storage Coil charging	3	30-s pulse
Cold METS Refrigeration	6-8	Continuous
Tritium handling Vacuum pumps Cleanup pumps	0.1	Continuous during clean-up operation only
Building heating & Air conditioning	0.5	Continuous
Instrument power	1	Continuous
Building lights, Receptacles, and misc.	0.7	On as needed

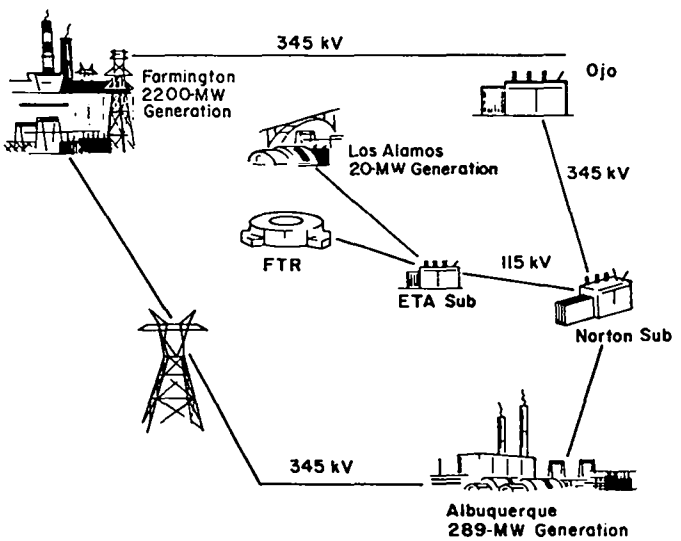

Fig. 6-6.
Northern New Mexico high voltage power distribution network as planned for 1980.

All substations and the eight capacitor charging dc power supplies will be outdoor equipment. Weather protection will be provided by sheet metal factory-built housing similar to the "protected-aisle" switchgear used in high voltage switchyards. Switching equipment, housing for the power supplies, and maintenance personnel weather protection will be built in modules that bolt together and that can be readily disassembled for removal or replacement. Concrete pads or piers will be designed to suit the equipment selected. All 13.2-kV interconnecting cables will be under ground.

Three existing 13.2-kV power lines near the SFTR site on Two Mile Mesa can be tapped and brought into the outdoor substation for back-up power if the 115-kV primary line should fail. Sufficient power for essential building services can thus be provided although these sources are not sufficient for normal operations.

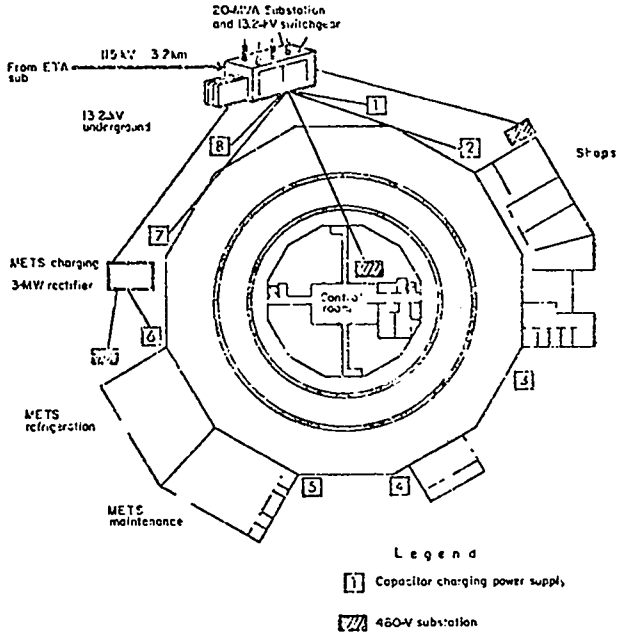

Fig. 6-7.
Power distribution at the SFTR site.

Certain loads, such as those for the tritium handling facility, cannot be turned off for the time required to correct a power failure or to switch over to emergency power manually. These loads will be connected to a 480-V power source with automatic switching to an engine-driven alternator that will start in a few seconds and carry the load until normal power can be restored.

6.8 SITE SELECTION

6.8.1 General

A detailed site selection study for the SFTR was made by the LASL Engineering Department, and the results presented in an internal report. Criteria for the site selection were developed and presented in a separate report. In accordance with these criteria, consideration was given to population distribution, proximity to other facilities and operations, utilities and services, and to the meteorology, hydrology, geology, and seismicity of the candidate locations. Special attention was given to consequences of hypothetical tritium release.

The area of site selection search was limited to the ERDA-controlled land of Los Alamos County (Fig. 6-8). This area represents approximately 104 km^2 (40 $miles^2$) of the county's 285-km^2 (110-$mile^2$) area, and many ERDA research facilities are located there. The city of Los Alamos, with a residential population of approximately 11 000, lies to the north. The residential areas of White Rock, La Vista, and Pajarito Acres, with a combined population of about 4000, lie to the south and east.

6.8.2 Selection of Sites for Initial Study

Eight sites, all within the Technical Area of the ERDA-controlled land in Los Alamos County, were selected for initial study. Detailed maps, aerial photographs, and utility drawings of the Technical Area greatly shortened the time required for this phase of the work. In addition, information was used from the Fluor Corporation report and the Dames and Moore studies for both the New Plutonium Facility and the New Pulsed Ultra-High Flux Facility.

The estimated area required for the new site was between 10 and 15 acres, depending on topography. On early review, it was apparent that a number of favorable locations could be found within the Technical Area. As a result, selection requirements for the sites to be included in the study were made somewhat restrictive. Locations were selected with consideration given to the following.

Population. Favorable distance to population center of Los Alamos, White Rock, and the trailer court on East Jemez Road was required. (It is recognized that safety features to be built into the new facility will make it feasible to use locations adjacent to population centers.)

Hazards. Sufficient distance is needed from areas of potential hazards, such as the Los Alamos airport operation or explosion research being conducted within the Technical Area, so as not to warrant special design considerations in the facility.

Topography. Favorable topography and plot shape were considered so as to minimize the cost of grading and costs associated with general facility layout or operation.

Accessibility. Favorable location is needed with respect to the center of Technical Area operations, including access over all-weather roads.

Ground Rules and Criteria

AECM 6301 (General Design Criteria).
AECM 6203 (Site Development Planning).
AECM 2406 (Physical Protection AEC Property).
AECM 0552 (Industrial Fire Protection).
Relatively "flat" area is desirable.
Proximity to the Intense Neutron Facility is desirable.
Proximity to present operations is desirable.

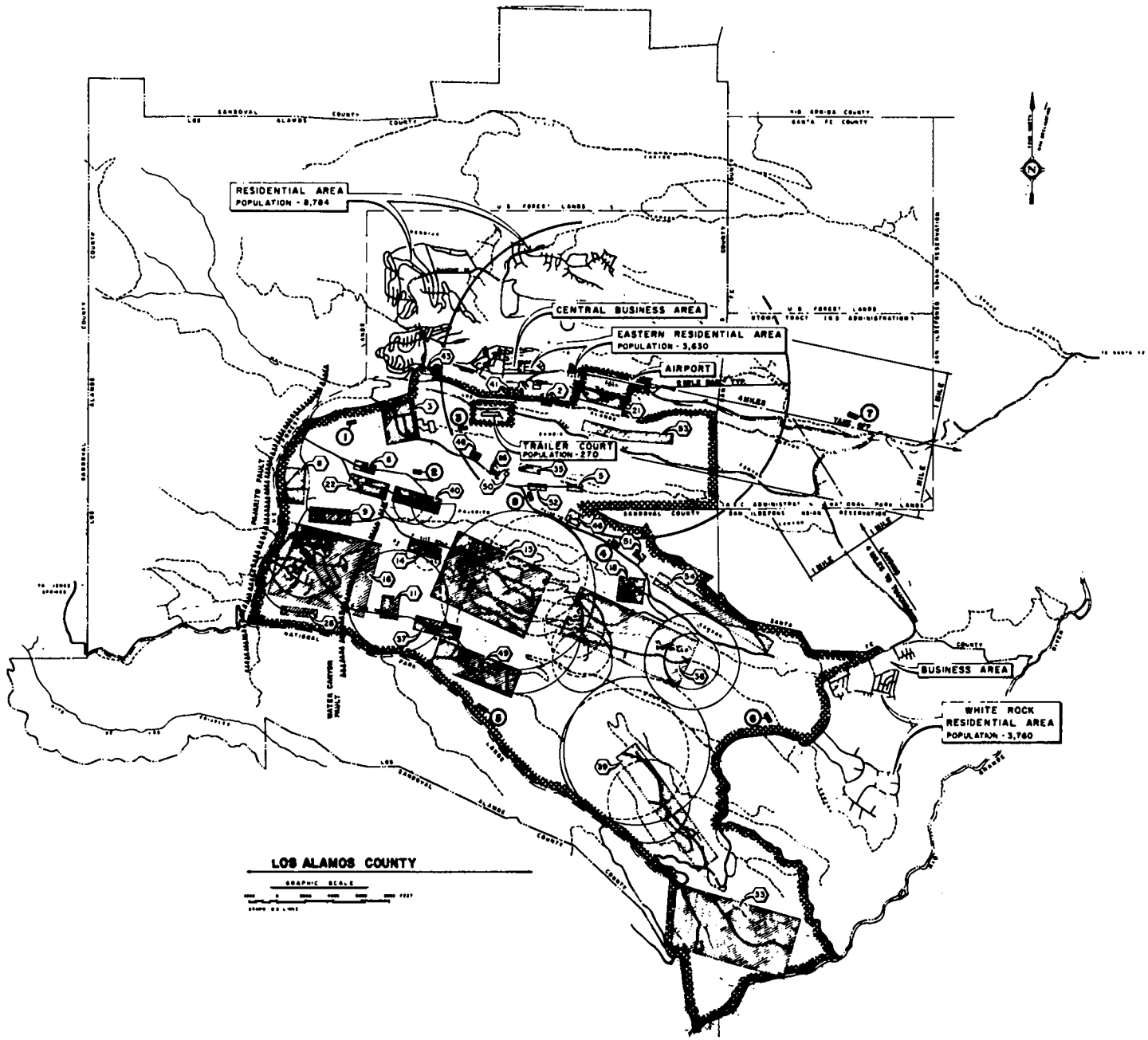

Fig. 6-8.
Map of Los Alamos County showing proposed site location.

Good vehicular access is required.

Must be outside a security area so that Soviet Bloc visitors can have access.

Future expansion (at least double) must be available.

6.8.3 Description of Study Sites

The eight sites selected for study are shown in Fig. 6-8. The following description of each site is based on available maps, utility drawings, and visual inspection.

Site 1 is located on the west edge of the present TA-3 area, adjacent to and on the south side of State Road Loop 4. The area is heavily wooded with ponderosa pine trees and slopes upward to the west at 10% or less. Excavation of the welded tuff rock in the area is assumed to be difficult. The site is located within a chain-link fenced area but is not in a security area. Fire Station No. 1 is no more than a 2-min run distant. The nearest fault is Pajarito fault, about 1.067 km (0.663 mile) to the west. No access to the area exists at the present time, necessitating the construction of a new paved roadway across Two-Mile Canyon. Utilities in the area include a 13.2-kV power line (S-17) of limited capacity approximately 450 m (1500 ft) to the southwest. A telephone service manhole is located across Two-Mile Canyon from this site, and extension to this site would be under ground by way of the fill anticipated for the road across the canyon. A 0.305-m (12-in.), 100-psi natural-gas line crosses the site parallel to the water line.

Site 2 is located within a security area and is on the north side of Two-Mile Mesa Road approximately 1.372 km (0.85 mile) east of the road turnoff to TA-22. The area is relatively flat for 0.091 to 0.122 km (0.06 to 0.08 mile) adjacent to the road and then slopes off approximately 10% to the south. A 13.2-kV pole line crosses the area. No gas or water lines were noted. A shot impact area limits the southern boundary of this site. The Pajarito fault is located approximately 2.743 km (1.7 miles) to the west.

Site 3 is located on the mesa top to the east of TA-3 and the Sigma Building (SM-66), about midway between the trailer court and TA-48. The only access to the area is a dirt trail which skirts the emergency radio installation. The area is generally clear except for a scattering of juniper and pinon trees, and is relatively flat, sloping gently to the east. The area is essentially open to public access. Fire Station No. 1 is within a 5-min run. Excavation in the tuff rock at this site would be routine. The nearest fault is the Los Alamos fault, located 1.93 km (1.2 miles) to the northeast. The only utility in the area is a dedicated 13.2-kV pole line (S-20) which traverses the site in an east-west direction.

Site 4 is located on the north side of Pajarito Road, approximately 0.7 km (0.4 mile) west of Rex Drive. The area is relatively flat with a heavy covering of pinon, pine, and juniper trees. A 115-kV pole line runs along the north edge of the site. Another 115-kV pole line traverses the southwest corner. The Pajarito fault lies approximately 7.010 km (4.36 miles) to the west. A 0.203-m (8-in.) water line and 0.076-m (3-in.) gas line run parallel to and north of Pajarito Road. A 0.400-m (16-in.) water line runs parallel to and south of Pajarito Road. TA-51, a radiation exposure experimental facility, is located to the east. The site contains four Indian ruins. The boundary of ERDA-controlled land is approximately 0.304 km (0.19 mile) to the north. The adjacent land is designated Indian Sacred Area. Excavation in the tuff rock would be routine.

Site 5 is located approximately 1.61 km (1 mile) southeast of the entrance road to TA-49, on the north side of State Road 4. The area is cut by arroyos and is of moderate slope, generally to the east. It is covered with a moderate stand of pinon and juniper trees. Excavation in the tuff rock at this site would be routine. The nearest fault is the Water Canyon fault located about 3.54 km (2.2 miles) to the west. The utilities in the area are limited to a 13.2-kV aerial electrical line (S-17), an aerial telephone line running along State Route 4 at this location. A 0.152-m (6-in.) cast-iron water main and a 0.076-m (3-in.) 100-psi natural-gas line parallel State Road 4 on the north side in the vicinity of the site. Neither of these lines is adequate to serve the proposed facility.

Site 6 is located on the north side of State Road 4 opposite Pajarito Acres in the White Rock area. It has a moderate slope to the east and a moderate cover of pinon and juniper trees. Excavation in the tuff rock and basalt 2 at this site would be difficult. The fire station at White Rock is within a 5-min run. The nearest fault is the Water Canyon fault, located approximately 10 km (6.2 miles) to the west. There are no utilities in this area except those serving the Pajarito Acres residential area.

Site 7 is located in the Otowi tract of the Bandelier National Monument which is under General Services Administration control and presently reserved for LASL development. The area under consideration is near the "Y" where State Road 4 branches to Los Alamos or White Rock, and is on the north side of the Los Alamos branch. The area is subject to the 100-yr flood problem. A moderate cover of pinon and juniper exists at this site which also has moderate to steep slopes. The tuff

rock and conglomerate are assumed to be difficult to excavate. The nearest fault is the Guaje Mountain fault located about 7.24 km (4.5 miles) to the northwest. There is no access to the area and there are no utilities there.

Site 8 is located on the northeast corner of the intersection of Pajarito Road and Puye Drive. It is 2.6 km (1.6 miles) south of the Los Alamos airport runway. The site has sparse vegetation and is relatively flat, with a gentle slope to the east. Two 115-kV power lines, a 13.2-kV pole line, and a 24.8-MPa (3600-psi) hydrogen line traverse the area. A 0.203-m (8-in.) water line and a 0.076-m (3-in.) gas line run parallel to and north of Pajarito Road. A 0.400-m (16-in.) water line runs to a test reactor, presently shut down, and a classified material disposal plant. A Zia branch office is located to the north, across Puye Drive. The Pajarito fault is approximately 4.876 km (3.03 miles) to the west. Excavation in the tuff rock at this site would be routine.

6.8.4 Site Selection

During the early phase of the Site Selection Study, Sites 3, 4, 5, 6, 7, and 8 were eliminated.

Site 3 was eliminated because the buildable area is too small for both the SFTR and a planned CTR office building. Future expansion obviously would be precluded. Access to the site is difficult and a new road would have to be built in an area inconvenient for traffic control. Not only is this site too remote from the present CTR technical operation area and the Intense Neutron Source Facility, but it is too close to the residential trailer court.

Sites 4 and 8 were eliminated because they also are already too small for both the SFTR and the office building and are too far from present technical CTR operations and the proposed site for the Intense Neutron Source Facility.

Sites 5, 6, and 7 were eliminated because they are extremely remote from CTR technical operations and the Intense Neutron Source Facility and their use would involve long travel times. Excavation in much of these three areas is difficult, although in parts it would be routine. Site 6 is subject to noise and pressure pulses from explosive testing at TA-36, and Site 7 is subject to the possibility of a 100-yr flood. Basically, these sites are poor construction sites because of the moderate to steep slopes.

A population distribution study of the sites under consideration was made and appears in Sec. 2 of the Site Selection Study report. The results of this study show that radiation doses at the sites considered, as a consequence of various postulated facility accidents, are far below established exposure guidelines. Thus, the population distribution had no bearing on either of the two remaining sites.

Cost estimates for the development of Sites 1 and 2 included the cost of

1. Electric power,
2. Water supplies from two separate sources,
3. Gas supply from a single source,
4. Site grading and access roads.

The estimate showed that the difference in development costs for the two sites is approximately $1M, a sum not of major significance when compared to the total cost of the facility. Location of the facility is therefore proposed for either Site 1 or 2 on Two-Mile Mesa.

VII. SAFETY AND ENVIRONMENTAL CONSIDERATIONS

7.1 OVERVIEW

Because of the preliminary nature of the SFTR design, a comprehensive environmental impact statement cannot be formulated at this time. However, in this section we consider those safety and environmental implications of the SFTR experiment that can be estimated from existing design detail. Although our conclusions may change somewhat with subsequent analysis, major aspects of the SFTR safety and environmental impact described below are not expected to alter significantly.

The SFTR site will be located within 2 km of the Los Alamos (population 15 000) town site and approximately 40 km from Santa Fe (population 55 000). Approximately 3 g (3×10^4 Ci) of tritium will be stored at the SFTR site. If suddenly released, the tritium could result in a maximum integrated population dose of 200 man-rem. The operational radioactive hazard will arise from (14-MeV) fusion neutrons, x-radiation, and neutron-induced gamma radiation, all of which are reduced to or below background radiation levels by ~2 m of concrete, biological shielding. This radiation spectrum will present no public hazard. Radioactive structural waste will be generated at a rate of 20 Ci/yr and approximately 15 g T_2/yr will be transported to and from the SFTR site. The chemical and sanitary waste will be similar to that generated by the ongoing Scyllac experiment at LASL and, therefore, is considered negligible. The major occupational hazard will be associated with the high voltages needed to operate the SFTR experiment, and will also be similar to those encountered by the present Scyllac experiment. The potential for a thermonuclear "runaway" is zero, although mechanical failure of magnets and high-current leads may occur; protection of personnel from electrical hazards and missiles generated by mechanical failures will be provided according to LASL procedure and practices. The potential for normal and off-normal safety and environmental hazard is quantified in the following sections.

7.2 DESCRIPTION OF SFTR SITE

The SFTR site is on the western edge of the Pajarito Plateau adjacent to flanks of the Sierra de los Valles; a map of the area is shown in Fig. 7-1. The area is at an elevation of about 7600 ft and contains a heavy cover of pines and 0.3 to 1 m of soil. The slope is 10 degrees or less eastward. In places the tuff bedrock is exposed. The surface is cut by a few small channels that drain into Two-Mile Canyon.

7.2.1 Demographic Description

Approximately 400 000 people inhabit a circle of ~100-km radius centered on Los Alamos. Nearly two-thirds of this population is concentrated in Albuquerque, about 100 km to the south. Another one-ninth is located in Santa Fe, about 40 km to the southeast. Except for the 15 000 residents of Los Alamos, the remaining population is distributed among small towns, ranging in size from a few hundred to a few thousand people, and Indian Pueblos of several hundred people each. The nearest community is Espanola, a town of about 2000 people, located about 20 km to the northeast. About 11 000 of the Los Alamos population live in the residential area of Los Alamos proper and the remaining 4000 reside in the developments of the White Rock community.

At any particular time these people are scattered throughout the Los Alamos area. It is impossible to predict their exact locations, but it is meaningful to distinguish between a daytime population distribution and a nighttime distribution. The distributions for angular sections 45° wide and 1 km deep with respect to the LASL meteorological tower are shown in Table 7-1. Movements of people to work and to school and the influx of workers into the area have been considered.

The economy of the Santa Fe-Los Alamos area is based largely on government (federal and state) operations, a large tourist trade, arts and crafts, agriculture, and some light and service industry (mostly associated with the tourist trade). The Los Alamos Scientific Laboratory accounts for much of the federal employment, while the New Mexico state governmental offices in Santa Fe provide the state jobs.

Agriculture is practiced only to a limited extent in the immediate vicinity (within 20-40 km of Los Alamos). In this area many people raise vegetables in home gardens, but rarely depend on this activity for more than half of their subsistence. Outside this area, agriculture is practiced by much of the rural

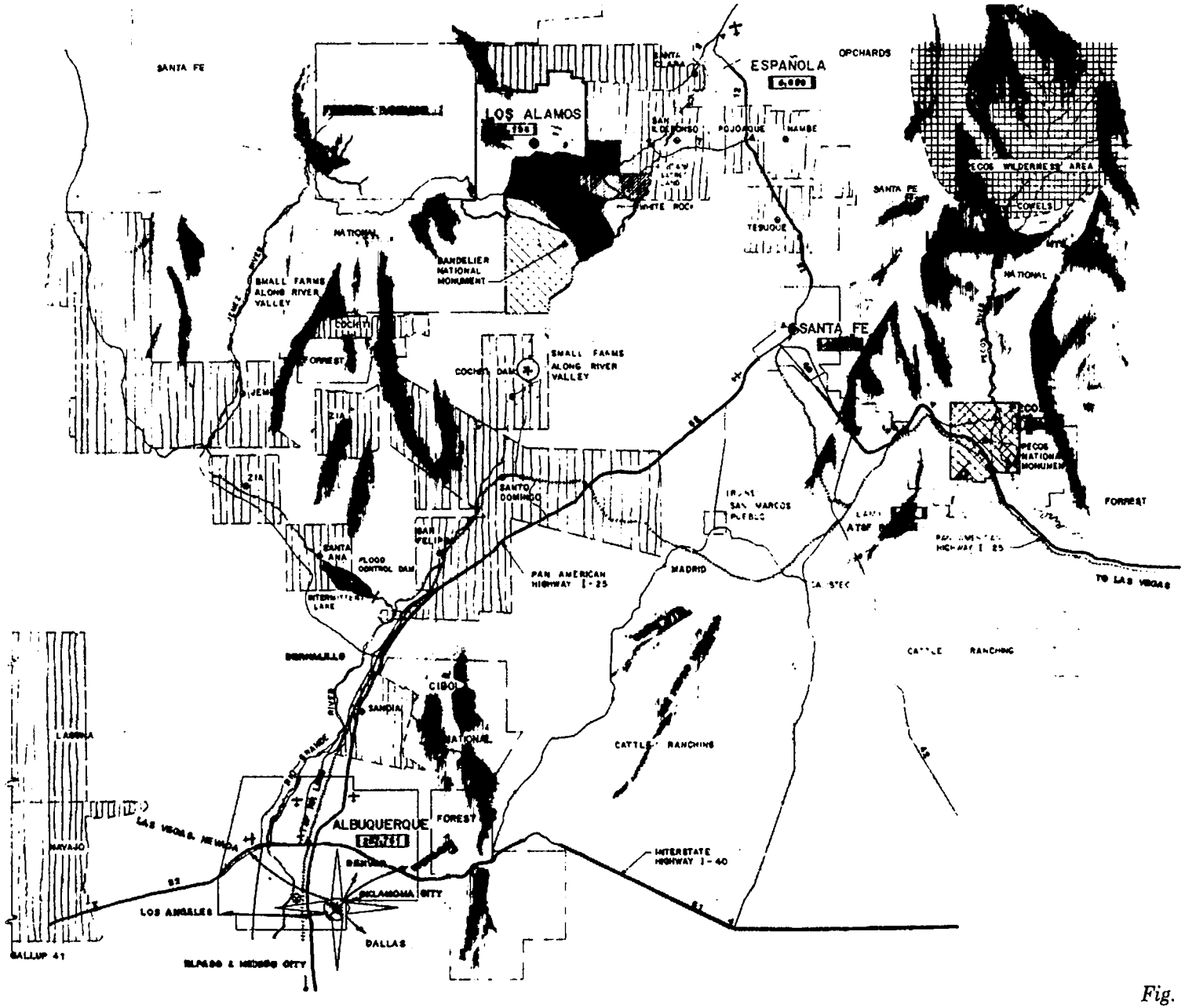

Fig. 7-1.
SFTR site and surrounding area.

TABLE 7-1

POPULATION DISTRIBUTION IN LOS ALAMOS, NM, LOCALE

Distance Interval (miles)	Total Population in Segment, Daytime/Nighttime							
	0°-45°	45°-90°	90°-135°	135°-180°	180°-225°	225°-270°	270°-315°	315°-360°
0-1	694/448	46/0	320/0	26/0	310/0	107/0	554/0	1987/802
1-2	3464/2735	926/1467	244/0	42/0	85/0	62/0	0/0	1235/2019
2-3	1747/1874	1042/1965	175/0	15/0	952/0	129/0	0/0	0/0
3-4	0/0	496/0	393/0	9/0	0/0	0/0	0/0	0/0
4-5	0/0	0/0	2/0	0/0	0/0	0/0	0/0	0/0
5-6	0/0	0/0	0/0	0/0	0/0	0/0	0/0	0/0
6-7	0/0	0/0	0/0	39/0	0/0	0/0	0/0	0/0
7-8	0/0	0/0	2624/3861	46/27	0/0	0/0	0/0	0/0
8-9	0/0	0/0	0/0	0/0	0/0	0/0	0/0	0/0
9-10	0/0	0/0	0/0	0/0	0/0	0/0	0/0	0/0
10-11	0/0	0/0	0/0	0/0	0/0	0/0	0/0	0/0
11-12	0/0	0/0	0/0	0/0	0/0	0/0	0/0	0/0
12-13	0/0	215/215	0/0	0/0	0/0	0/0	0/0	0/0
13-14	0/0	0/0	0/0	0/0	0/0	0/0	0/0	0/0
14-15	0/0	0/0	0/0	0/0	0/0	0/0	0/0	0/0
15-16	0/0	5478/5478	0/0	0/0	0/0	0/0	0/0	0/0
16-17	400/400	1000/1000	0/0	0/0	0/0	0/0	0/0	0/0
17-18	0/0	450/450	0/0	150/150	0/0	0/0	0/0	0/0
18-19	0/0	600/600	0/0	0/0	0/0	0/0	0/0	0/0
19-20	0/0	0/0	0/0	0/0	0/0	0/0	0/0	0/0
20-21	0/0	0/0	0/0	0/0	0/0	0/0	0/0	0/0
21-22	150/150	650/650	0/0	0/0	350/350	0/0	0/0	100/100
22-23	0/0	0/0	545/545	0/0	0/0	0/0	0/0	250/250
23-24	0/0	700/700	0/0	0/0	0/0	481/481	0/0	0/0
24-25	0/0	0/0	55339/55339	0/0	50/50	0/0	0/0	50/50

population, some for subsistence and income augmentation and some on a strictly commercial basis. Limited truck farming has been made possible in the river valleys by irrigation. Tree fruits, chili peppers, beans, corn, and alfalfa are the principal crops. Very little of this produce enters interstate commerce. Most of the unforested land, although sparsely vegetated, is used for low-density grazing of beef cattle. Some milk is produced in the Santa Fe area, but none in the immediate vicinity of Los Alamos. A small dairy in Nambe, about 25 km east of Los Alamos, and another in Santa Fe sell milk produced in the area. The only other agriculturally oriented activity in the area is logging in some of the highland forests.

7.2.2 Meteorological Description

The important meteorological elements in environmental assessment are winds, from the viewpoint of pollutant transport and physical damage, precipitation (as it affects the hydrology), and lightning; temperature, humidity, and pressure are of secondary importance.

Major spatial variation of surface winds in Los Alamos is caused by the unusual terrain. Under moderate and strong atmospheric pressure gradients, flow is channeled by the terrain features of the area, while under weak gradient flow, a distinct diurnal slope wind cycle exists. The interaction of these two domains gives rise to a westerly flow predominance on the western part of the Laboratory site and a southerly component at the east end of the mesas. At most sites near-calm conditions exist 10-15% of the time, 80% of the wind speeds are less than 3 m/s, and less than 1% of the time 10-min-averaged winds are greater than 16 m/s. Figure 7-2 is an example of wind roses for one location at TA-3 for conditions stratified by gross thermal stability. Table 7-2 gives the model inputs for estimates of χ/Q vs distance curves, and the resulting curves are given in Figs. 7-3 and 7-4. The point source strength is Q, and χ is the concentration of a given released substance. The recorded peak gusts are 42 m/s, and gusts exceeding 20 m/s occur on an average of 47 days during the year.

The precipitation averages 0.46 m/yr, with nearly 40% occurring as thundershowers in July and August. Thunder is reported 60 days/yr. The temperature and humidity are typical of the altitude and geographic region. Monthly averaged temperatures range from −2°C to 20°C, and diurnal changes of 13°C are typical. The average relative humidity is 40%. Figures 7-5 and 7-6 present relevant temperature, humidity, and precipitation parameters on a monthly basis.

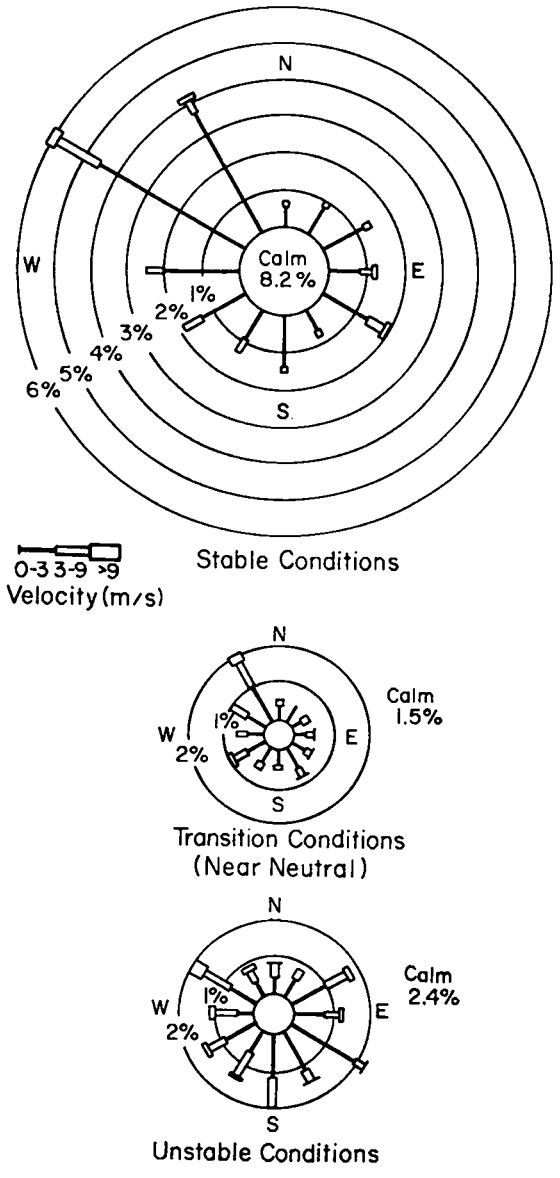

Fig. 7-2.
Wind roses for TA-3 location of SFTR (see Fig. 7-1).

There are three atmospheric transport routes by which a moderately large population could be exposed to radioactive releases from the proposed SFTR site. One route is toward the NNE and the western residential area. Air flow from the SFTR site to the Western Area must cross the head of Pajarito Canyon and Los Alamos Canyon (see Fig. 7-7, 030°

TABLE 7-2

MODEL INPUTS FOR χ/Q ESTIMATES

Transport direction	NNE	E	ESE
Primary receptor	Western Area	TA-3, Trailer Ct.	White Rock
Source height	30 m, 50 m	30 m, 50 m	50 m
Mean wind	1 m/s	1 m/s	0.5 m/s
Dilution rate	Pasquill B	Pasquill E	Pasquill F
Mixing depth	100 m	100 m	50 m
Approximate frequency of occurrence	12%	4.5%	20%

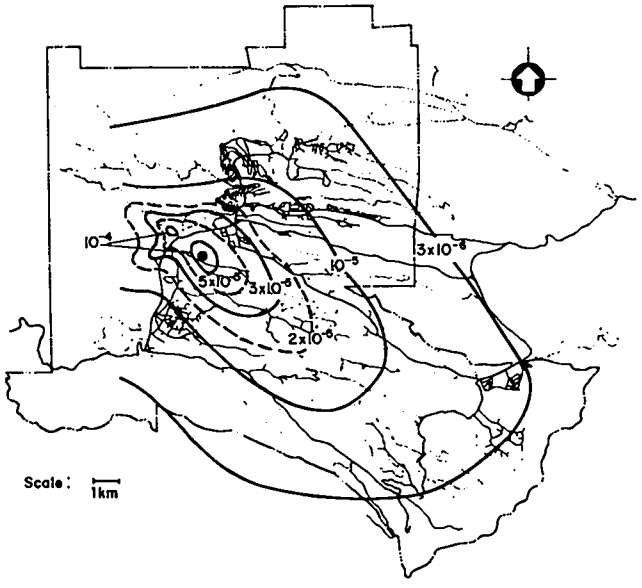

Fig. 7-3.
Annual average χ/Q (s/m³) for SFTR source at 30-m stack height.

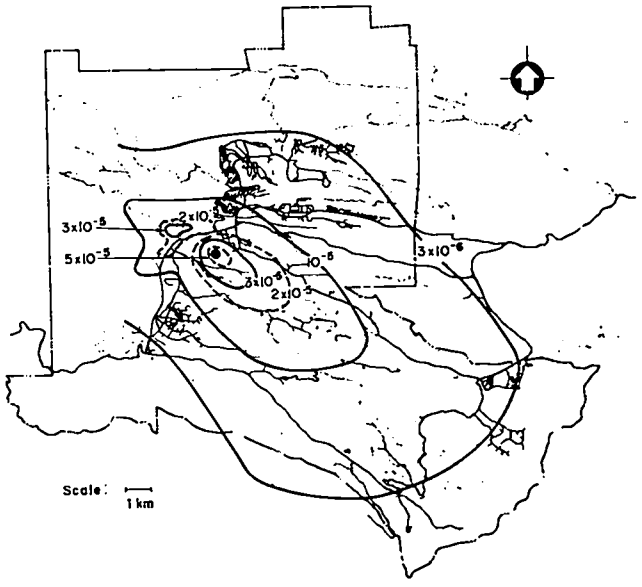

Fig. 7-4.
Annual average χ/Q (s/m³) for SFTR source at 50-m stack height.

azimuth). The circulations induced by flow over such terrain account for significant mixing and dilution of containment clouds. The second path is across TA-3 and the Trailer Court in an easterly direction. The potential release cloud would encounter the heads of Pajarito and Sandia canyons as shown in Fig. 7-7 (085° azimuth) and present smaller perturbations to the flow than would Los Alamos Canyon. In both cases a decoupled flow within the canyons is likely. An injection of contaminant (e.g., T_2O or HTO) into such a flow would reduce the quantity of material transported to the residential sites, but would also carry it down (or up) the canyon under different and probably more restrictive mixing conditions. This situation represents the third condition: a down-canyon drainage wind. The canyon flow occurs frequently and is characterized by light winds and reduced turbulence. In addition, the lateral dispersion is bounded by canyon walls, giving potentially high concentrations downstream. The most likely canyon for atmospheric drainage from the SFTR site is Pajarito Canyon, which opens in the White Rock community about 10 km down-canyon; similar effects will hold for any canyon traversed by the cloud.

To establish confidence in concentration estimates, certain source factors must be determined, such as source size and duration, associated heat

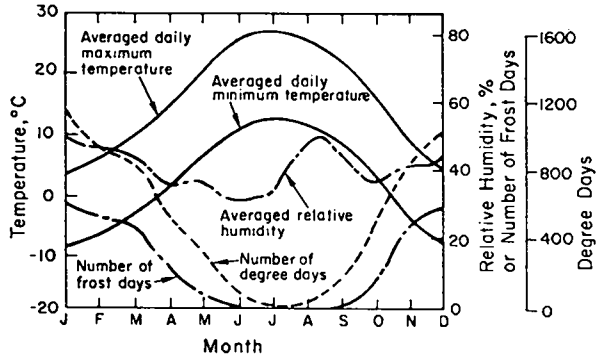

Fig. 7-5.
Average annual variation of thermal and humidity conditions at Los Alamos, NM.

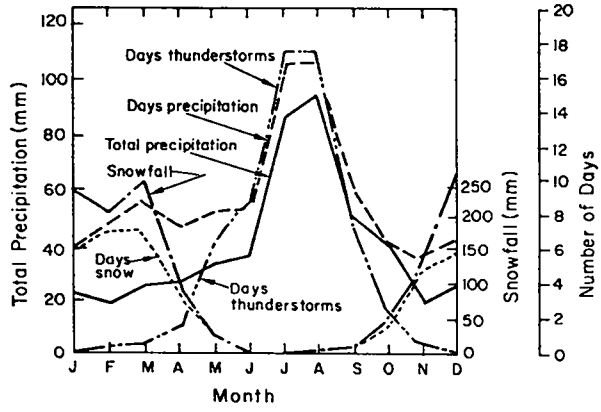

Fig. 7-6.
Average annual variation of precipitation at Los Alamos, NM.

release, particle sizes, and some elements of the chemistry of the released material for scavenging estimates. Also, many of the meteorological data on the influence of terrain, as shown in Fig. 7-7, are speculative and need to be upgraded by field studies and computational models. Despite these potential shortcomings, estimates of downwind concentration can be made. In the sample calculations presented here, a Gaussian plume model is used for a continuous, elevated-point source, as described in Ref. 1. Initial buoyancy, particle settling, deposition, and transformation during travel are ignored. Sections 7.3.1 and 7.4.1 give calculational results for chronic and accidental releases, respectively.

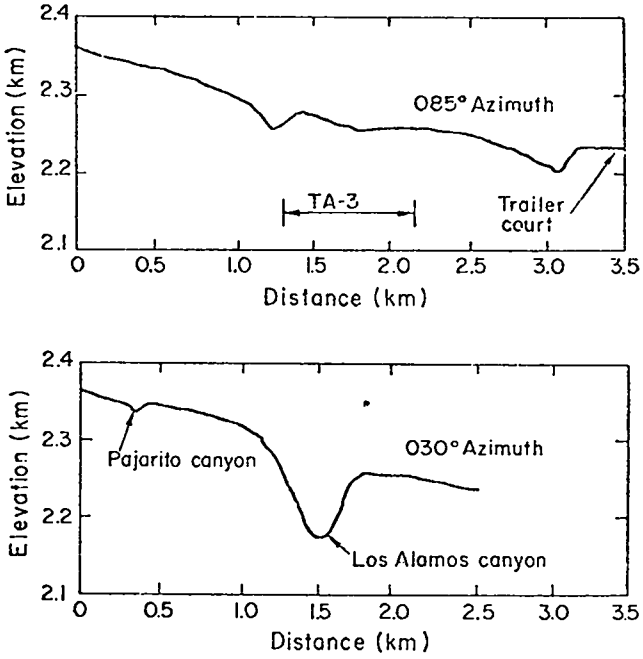

Fig. 7-7.
Terrain variation along the 030° and 085° azimuths from SFTR site..

7.2.3 Geologic and Hydrologic Description

Volcanic-flow rock and sediments underlie the site at the western edge of the plateau. A generalized section showing rock units and their thicknesses is given in Table 7-3 and is based on a test hole located about 1 mile northeast of the SFTR site.

The Bandelier Tuff consists of three members: Tshirege, Otowi, and Guaje (youngest to oldest). The Tshirege member is composed of a series of nonwelded to welded ashflows of rhyolite tuffs. The flow underlying the site is a welded tuff. The Otowi member is a nonwelded pumiceous ashflow of rhyolite tuff, and the Guaje member is made of an ashfall rhyolite pumice.

The Tschicoma Formation is composed of latite and quartz latite flows and pyroclastic rocks. The Puye Formation is composed of gravels and boulders of latite, quartz latite, rhyolite, and pumice in a matrix of silt and sand.

The individual ashflows of the Bandelier Tuff dip gently eastward off the flank of the mountains formed by the Tschicoma Formation. Because the tuffs are volcanic in origin, they have become highly

TABLE 7-3

GENERALIZED SECTION OF SITE UNDERLAY

Unit	Thickness (m)	Depth (m)
Bandelier Tuff		
Tshirege member	189	189
Otowi member	66	255
Guaje member	18	273
Tschicoma Formation	107	390
Puye Formation	119	498
Tschicoma Formation	82	581
Puye Formation	3	583
Tschicoma Formation	156	73

jointed during cooling. The Pajarito Fault is a north-south trending fault about 1070 m west of the site. It is a normal fault and is down-thrown to the east. The estimated displacement is 122 m. The Water Canyon Fault also has a north-south trend and terminates about 1 mile southeast of the site. This fault is also a normal fault with maximum displacement of 24 m. The movement on both faults has been post-Bandelier.

Drainage from the site goes into Two-Mile Canyon, into Pajarito Canyon, and eventually into the Rio Grande. The stream in Pajarito Canyon is intermittent. The alluvium is thin but may contain small amounts of water seasonally. The water is perched on the underlying tuff, but no water is perched in the volcanic rocks and sediments above the main aquifer. The main aquifer of the Los Alamos area is the only aquifer that can supply municipal and industrial water. The top of the aquifer at the site lies at a depth of about 110 m in the lower part of the Tschicoma Formation or upper part of the Puye Formation. The aquifer slopes gently eastward from the recharge area in the Jemez Mountains to the discharge area along the Rio Grande.

Los Alamos falls within seismic zone 2 of the Uniform Building Code.[2] On the basis of geologic evidence, historical data, and seismic records since 1962, an earthquake of 5.5 magnitude will occur every 100 yr, with an epicenter located somewhere in the Rio Grande depression between Questa and Albuquerque (an area extending 80 km north and 80 km south of Los Alamos and which is 32 to 64 km wide).

The Los Alamos area lies in the Rio Grande depression, which was formed by a complex series of faults. The seismicity of this part of the depression is (1) less than the Albuquerque to Socorro segment (of recorded earthquakes in New Mexico, 95% occurred in this latter segment) and (2) substantially less than similar areas in Southern California.

Ground subsidence caused by the withdrawal of water, by landslides, and by renewed volcanism at the SFTR site has been considered. Ground subsidence is unlikely because of the already low ground water level and physical structure of the water-bearing levels. Landslides, excluding rock falls at the canyon lip, do not occur because of the geological structure and dry condition of the mesa rock. Indications are that volcanic activity is decreasing; in the past 20 yr fumaroles have not been active and thermal springs have become cooler.

7.2.4 Access and Security Aspects

The site is located on the west edge of the TA-3 area (Fig. 7-1) and adjacent to the east side of State Road 4. It is 1.22 km from the LASL Administration Building and 1.53 km from the nearest fire station. A paved road to TA-6 provides direct access to the site. In addition, a paved road is to be constructed across Two-Mile Canyon to shorten the access to TA-3. Because the site lies within a security area, a fence will be required to the south to separate it from classified technical areas, and a second fence to the north will be required to restrict public access.

7.3 SAFETY AND ENVIRONMENTAL CONSIDERATIONS DURING NORMAL OPERATION

Operation of the SFTR is not expected to create any significant personnel safety problems not already encountered and successfully dealt with at existing reactor or accelerator facilities. The dose equivalent (DE) from direct radiation will be under 500 mrem/yr, less than the design goal of 1 rem/yr for new facilities.[3] Exposures from other sources of radiation (tritium-induced activity) will be minimized by shielding, remote handling, gloveboxes, personnel control, etc.

Environmentally, the DE's to the public from routine operation of the SFTR will be the sum of the effects of small releases of activated air and tritium and of the direct neutron radiation during D-T power pulses. These DE's are analyzed in detail in the sections that follow and are summarized below.

ANNUAL WHOLE-BODY DOSE EQUIVALENT
(mrem/yr)

	Tritium (max)	Activated Air	Direct Neutrons (estimated)	Total
Site Boundary	0.2	0.06	<4	<4
Edge of Townsite	0.03	0.01	<1	<1

These DE's are very small compared with normal background radiation in Los Alamos County (130-180 mrem/yr) and with the radiation protection standards for the public given in ERDA Manual Appendix 0524 [500 mrem/yr (maximum) or 170 mrem/yr (average)],[3] and do not constitute a significant risk to public health. In addition, it should be emphasized that D-T operation of the SFTR is expected to last only about 1 yr, or long enough to produce the radiation doses given in the above table.

7.3.1 Tritium Inventory and Release

The quantities of tritium on-site in the SFTR will amount to tens of kilocuries. Every effort has been made to keep the tritium inventory to a minimum, to keep most of the tritium in accident-proof configurations, to allow an absolute minimum in the form of gas, and to exercise all necessary care in the release of tritium to the environment. Some of the measures incorporated in the design and operational procedures in the SFTR facility are given below.

The normal plant inventory of tritium (T_2) is expected to be 3 g, with a projected absolute maximum of 7 g or 70 000 Ci. About 90% will be secured in a fire- and blast-proof vault having a combination lock; the vault may be alarmed. Figure 7-8 is a schematic of the distribution of the tritium inventory throughout the facility.

The 15 mg, or 150 Ci, of tritium that will be used in a burn pulse will be transferred to the cell, plasma chamber, and associated piping and pumps for 10 min. Four such D-T shots are planned per day. After each shot the $(D,T)_2$ mixture will be transferred from the SFTR cell for processing and reclamation. The remainder will be in the form of tritiated water on molecular sieve beds or as uranium hydride. About 10% of this remaining tritium will be in a tritide form. Except for tritium in the SFTR discharge tube, all tritium will be in metal containers or metal piping.

Tritium handling, shipping, and release to the environment will be carefully controlled to meet appropriate federal regulations. All contaminated gas exhausted from the SFTR facility will have an average tritium concentration less than 0.2 $\mu Ci/m^3$. Since the stack exhaust rate will be 4.7 m^3/s (10 000 cfm), the daily tritium release will be less than 82 mCi. Stack gas will be continuously monitored, and the discharges will be recorded by the LASL Health Division on a monthly basis.

A second form of tritium waste will be tritiated water from the tritium waste treatment dryers and cell cleanup dryers. The waste treatment dryers should operate for several months to a year without

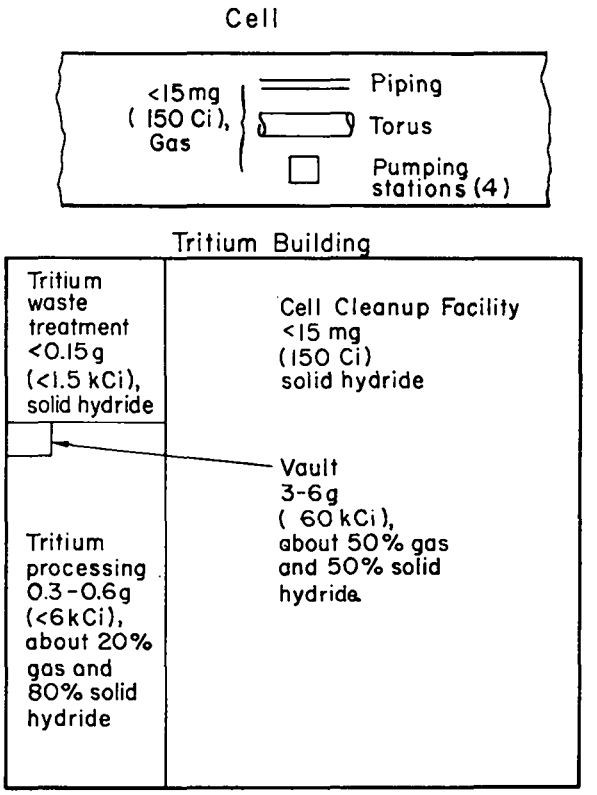

Fig. 7-8.
Schematic diagram of tritium inventory in the SFTR facility.

regeneration. The tritium content in these units will depend almost exclusively on the degree of the $(D,T)_2$ chemical reaction with the plasma chamber wall. If it is assumed that 1% of the $(D,T)_2$ mixture reacts with the wall to form $(D,T)_2O$, 6 Ci/day will be collected, or 1500 Ci/yr. The water collected in the units would consist mostly of D_2O collected from the deuterium pulses, and would amount to 8 ℓ/day of vapor, or 2 kg/yr. Thus, if no other releases of tritium occurred, regeneration of the dryers would give 1500 Ci of tritium in a few pounds of water. This water might be processed elsewhere, but probably would be sealed in double containers for burial.

Maintenance operations in the hoods might release too much tritium to be stacked. An effort will be made to process such gas in the tritium waste treatment (TWT) unit which handles 7 ℓ/s (15 cfm) at a pressure of 600 torr. If such an operation processed air of 30% relative humidity at 25°C for 15 min, about 40 g of water would be collected. The result would be more frequent regeneration of the dryer with a corresponding reduction in the tritium concentration in the collected water.

Accidental tritium releases in the tritium preparation hood or in the vault might release up to 3 g of T_2 which would be handled by the 7-ℓ/s TWT unit. Tritium releases in hoods would be handled similarly, but would result in a smaller inventory in the 7-ℓ/s dryer. In these cases, regeneration of the dryers would depend on the humidity of the air and the processing time; for a release in the vault, regeneration probably would be initiated following collection of the tritium.

Aside from stack gas and tritiated water collected by the dryers, the only tritium waste routinely released from the site would be found on contaminated hardware and equipment which would be buried in sealed containers according to standard LASL procedures. Valve seats might require routine replacement. Cryosorb panels in the cryosorption pumps might also have a limited life; the tritium contamination here would probably be less than a curie.

Central to the successful control of the relatively small quantities of tritium used by the SFTR experiment are (1) the monitoring of small quantities of tritium and (2) the institution of unambiguous and accurate control and inventory procedures. Control and inventory procedures are discussed in more detail in the following subsections. Radiation doses from "routine" tritium releases are also discussed.

7.3.1.1 Tritium Control and Inventory Procedures

Tritium Assignments. Tritium inventories will be assigned to individuals, and transfers between individuals will be handled by signed receipt, using forms similar to those presently in use by LASL Group CMB-3. Monthly summaries of these inventories will be compared with a physical inventory taken at the same time. Permanent tritium inventory records will be kept. No deuterium inventory will be kept; deuterium will be considered expended upon receipt.

Tritium Security. All tritium that is easily portable will be stored in a vault with a combination lock. It will be treated as classified material, and the vault may be subject to routine security checks during nonworking hours. Each person is responsible for the security of tritium assigned to him.

Physical Inventory. A physical inventory of the tritium in the SFTR will be made each month. Several of the quantities will be estimated. The inventory will normally consist of the following:

1. One or two 12-ℓ containers of T_2 stored in the vault. No more than one container will be full.
2. Tritium recovered as uranium deutero-tritide and stored in steel containers in the vault. Normally, any tritium to be sent out for recovery will be picked up at the time of delivery of a shipment (a 12-ℓ container of T_2 would normally be received once every two or three months).
3. Tritium recovered possibly as $(D,T)_2$ stored in one or two 12-ℓ containers either for reuse or for shipment. $U(D,T)_3$ storage would be correspondingly reduced.
4. Tritium located in the preparation hood as solid on one or two uranium beds within metal containers, and tritium (during working hours) in one or two metal storage bulbs.
5. Tritium as solid on one or two uranium beds (traps) within metal containers in the recovery hood. These traps would be transferred to the vault each week.
6. Tritium gas within the discharge tube and in transfer lines and metal containers. A few times a day 100-200 Ci of tritium would be at pumping stations, in lines in the cell, or in the discharge tube for short intervals during working hours.
7. Tritiated water in the TWT unit.
8. Tritiated water, possibly in the Cell Cleanup Facility (CCF).

Tritium Measurements.

1. Tritium receipts: Tritium will be received in standard 12-ℓ containers at 2 atm pressure. The tritium content as assigned by the supplier will constitute the primary measure of the tritium in each container. This content will be checked by a PVT measurement. Mass spectrometer analysis of the gas will be made periodically as the gas is used. Since the gas will be measured as it is used, a cumulative accounting of this tritium will provide an independent determination of the tritium in a given container. When significant (few percent) differences appear between assigned and measured values, appropriate measures will be taken to determine the cause.

2. Tritium stored as $U(D,T)_3$ and $U(H,D,T)_3$: The stainless steel containers of uranium tritiated hydride will be measured calorimetrically. Mass spectrometer analyses will give the composition of the hydrogen isotopic concentrations. For low tritium concentrations, PVT and mass spectrometer analyses might be used without calorimetry. Tritium on $U(D,T)_3$ traps in the preparation and recovery hoods will be calculated from PVT and mass spectrometer analyses and careful accounting of gas transfers onto and off the traps.

3. Gas storage containers in vault: If $(D,T)_2$ is collected as the gas, either for reuse or for shipment off-site for recovery, PVT and mass spectrometer analyses will determine the quantities. The receiver, however, will normally assign a more accurate value to the contents, and this value will be accepted. In case of unreasonable variances, the $U(D,T)_3$ container could be measured calorimetrically before decomposition, collection, and shipment.

4. Storage containers in hoods (standard volume containers): Again, PVT and mass spectrometer analysis and careful accounting will be used to determine tritium stored in these containrs.

5. Tritium Waste Treatment Facility (TWT): Any water collected from regeneration cycles will be sampled and the tritium content determined by scintillation counting or other standard techniques by Group H-1. Tritiated water going into the TWT will be measured by PVT methods and analyzed occasionally. Unaccounted-for tritium will probably be assigned to this unit except in case of known losses or unreasonably large quantities.

The careful accounting of the tritium contained in the large number of mass spectrometer samples—each of low tritium content—scarcely seems warranted. Also the error is large in mass spectrometer analyses of samples containing appreciable quantities of protium such as might be expected in overnight outgassing, etc.

6. Cell Cleanup Facility (CCF): Excellent estimates of the tritium content in this facility can be expected, since transfers to this unit will usually involve the transfer of accidentally released, but measured, quantities of tritium. This unit probably will be little used.

7. Labeling of piping and ducting: All piping and ducting will be painted a characteristic color and carefully labeled for immediate identification.

8. Alarms: The alarm system has not been designed in detail. In general, tritium air concentrations above predetermined values will activate visual and audio alarms in areas where overconcentrations occur and at control points. The following section describes the tritium monitoring system envisioned for the SFTR facility.

9. Group H-1 responsibilities: Group H-1 will have control of tritium safety measures, routine maintenance of counting equipment, monitoring of personnel, and preservation of records.

7.3.1.2 Tritium Monitoring Procedures

Monitoring for tritium will be done by state-of-the-art, flow-through ionization chambers modified as noted below when monitoring for tritium in activated air. Such instruments are available with electrometer sensitivities of 10^{-15} to 10^{-17} A. A 20-ℓ chamber can measure a tritium concentration of 0.2 $\mu Ci/m^3$ (resulting in chamber current of 4×10^{-15}A). Such instruments can be used for stack monitoring with sensitivities down to the maximum permissible concentration (MPC_a) for the public (0.2 $\mu Ci/m^3$).

Tritium monitoring in the cell and cell exhaust air presents a special problem. During a D-T pulse of 4.5×10^{18} n, approximately 20 Ci of ^{16}N, 100 mCi of ^{13}N, and 20 mCi of ^{41}Ar would be produced in the cell air. Most of the ^{16}N produced is partially trapped in the air spaces of the inner confines of the primary shield and capacitors. Because of its short half-life, only the amount formed outside the shield needs to be considered during monitoring for tritium in the cell in the presence of the activated air. Thus, the maximum total concentration of high-energy beta radiation outside the shield is about 6 $\mu Ci/m^3$.

Tritium in such an atmosphere can be monitored easily by a technique recently developed at LASL.[4] The method employs concentric ion chambers with a thin common wall separating the inner flow-through signal chamber from the outer compensating chamber. The currents produced by the high-energy radiation from the two chambers can be completely

subtracted, leaving only the current from the tritium in the inner chamber. In the above atmosphere, a tritium concentration of less than 0.1 $\mu Ci/m^3$ can be measured with a 20-ℓ (inner) chamber using a 30-s time constant.

Monitors with dual chambers will be used for the cell and possibly for the stack. The cell hood monitors, because of their lower tritium sensitivity requirements, will not be equipped with dual chambers. Single-chamber monitors will also be used in the tritium-handling hoods and in rooms where air activation does not occur.

The signal to the valves in the exhaust air ducts that route the tritium to the recovery systems must sometimes be given rapidly when, within a 24-h period, about 20 mCi of tritium have passed a sampling point. Although this action could be accomplished with rate instruments, system response will be faster if the current coming directly from the ion chamber is integrated. Such integrating circuits are common and can be wired to give a signal at the desired instant. These integrating monitors are planned for all five tritium hood exhaust ducts, the 2800-//s duct, and for monitoring the performance of both tritium recovery systems. Where air activation is a problem, dual concentric chambers will be employed. Figure 7-9 summarizes the location, type, and function of each tritium momnitor at the SFTR facility.

When ion chambers are used to measure tritium concentrations of less than 1 $\mu Ci/m^3$, radon in the air can be a serious problem. Therefore, the concrete walls in the cell will be coated with a sealant to reduce the cell concentration from this source to less than 10^{-13} Ci//. Radon in the inlet air will be at the (outdoor) ambient concentration ($\sim 10^{-14}$ Ci//), and will be no problem.

Alternative methods to ionization chambers for monitoring tritium are available. Proportional counters and plastic scintillators have been developed for continuous monitoring of airborne tritium. The counters have the advantage of pulse-height discrimination and, therefore, may be useful in removing much of the radon alpha and high-energy beta radiation background. Unfortunately, these counters also have disadvantages which may include strong memory effect, a requirement for a continuous gas supply, a long waiting time or long time constant, and lack of sensitivity.

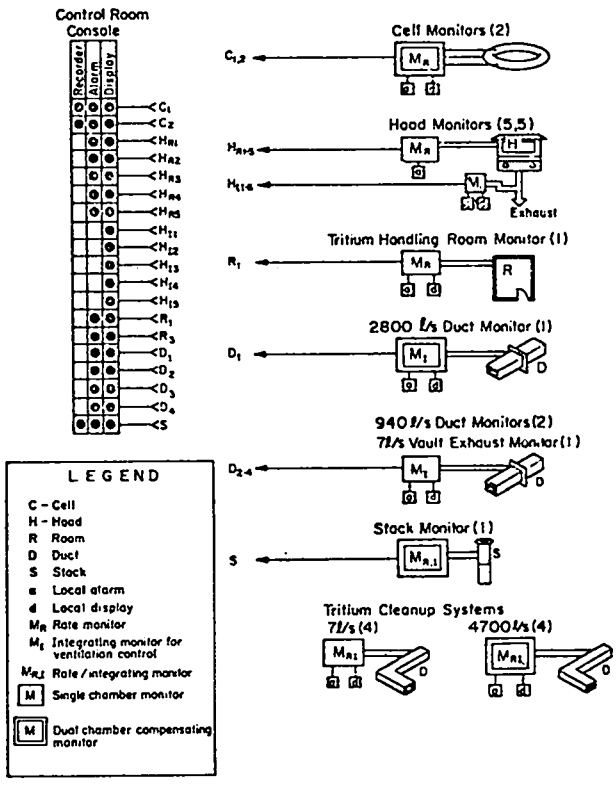

Fig. 7-9.
Schematic of tritium monitoring system and control functions.

7.3.1.3 Radiation Dose Rate Resulting from Routine Tritium Releases

No simple method is available to estimate the amount of tritium that will routinely leak or diffuse from the various containers, pumps, or plumbing. Whatever this leakage rate, the tritium recovery systems will trap all but an insignificant amount before the tritium containment air is exhausted into the atmosphere through the stack. The design of the cleanup/recovery systems is such that the average daily concentration in the stack will not exceed the maximum permissible concentration for the public of 0.2 $\mu Ci/m^3$ for tritium as HTO or T_2O in air. With a stack flow of 4.7 m^3/s the maximum discharge rate will be about 82 mCi/day. It is expected that the long-term average concentration in the stack will be substantially less than the MPC_a. However, the

TWT and CCF will be operated to keep the stack exhaust tritium under the daily limit of 82 mCi. This maximum discharge rate is expected to be maintained in the event of accidental releases. Such releases may involve, for instance, part of the 150 Ci of tritium in the reaction chamber resulting from mechanical failure of the chamber wall during a D-T pulse. Such a failure may occur 2-3 times per month during the 1 yr of D-T operations. Other significant releases are extremely improbable. Small releases involving less than 1 Ci are expected when contaminated plumbing is disassembled.

Annual average isopleths (χ/Q in s/m^3) were calculated for the SFTR site based on wind and other atmospheric data compiled at the LASL Administration Building Weather Station (located about 1.5 km from the proposed site). These data are plotted in Figs. 7-3 and 7-4 for two stack heights (30 and 50 m). No allowance was made for terrain features which would interrupt the normal flow toward the population centers.

From the isopleths for the 30-m stack, the annual doses to persons persistently exposed to tritium being chronically released at the maximum discharge rate from the SFTR stack were calculated and transferred to the same isopleth curves. The tritium was assumed to be completely oxidized, and absorption through the skin was included. Figure 7-10 gives the chronic tritium whole-body dose curves. On the basis of these calculations no member of the public would receive over 1 mrem/yr even if the maximum average release rate were to be increased manyfold.

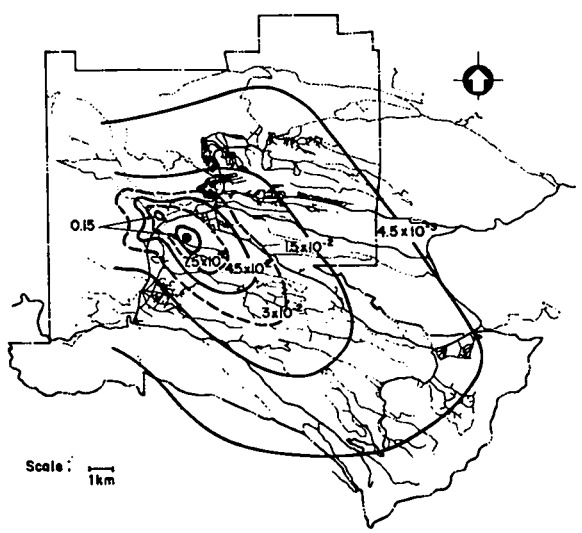

Fig. 7-10.
Chronic tritium whole-body isodose curves (mrem/yr) for SFTR tritium released from a 30-m stack.

7.3.2 Direct Neutron Irradiation Exterior to the SFTR Cell

The neutron source is conservatively estimated to be 4.5×10^{18} n per D-T burn pulse and 10^3 pulses/yr. These neutrons will be generated in a toroidal plasma chamber (minor radius 0.1 m, major radius 40 m) surrounded by magnet coils, electrical insulation, and a primary shield.

The main function of the primary shield (Sec. 5.3.2, laminated aluminum, graphite, and borated-leaded polyethylene) is to limit the activation of capacitors and reduce damage to organic insulators. Secondary but important functions of the shield are the reduction of air and wall activation in the cell and the shielding of personnel from the high gamma exposure rates of the activated toroidal structure. This problem is discussed in some detail in Sec. 7.3.3.

The neutron dose per 4.5×10^{18} D-T burn pulses in the cell (Fig. 7-11) is given in Fig. 7-12. The effectiveness of the primary shield in reducing the neutron dose can be seen. Combined with the primary shield, the 1.5-m-thick cell wall of ordinary concrete provides sufficient shielding to reduce the dose equivalent (DE) immediately outside the tunnel to less than the design value of 0.5 rem/yr. Since the SFTR experiment is expected to be completed with fewer than 4.5×10^{21} D-T neutrons produced, the 0.5 rem can be assumed as the maximum DE for the experiment, since the D-D neutrons are not expected to add much to the background radiation by virtue of their lower numbers and energy. The corresponding dose values in the parking area and at the closest site boundary, without additional shielding, are approximately 100 mrem/yr and 8 mrem/yr, respectively. The conservativeness in the shielding calculations and in the assumptions of no additional intervening walls or equipment strongly suggests a further reduction of these neutron doses by at least a factor of 2 or 3.

7.3.3 Neutron Activation of Equipment, Cell Atmosphere, and Shielding

The neutron activation in the cell and resulting DE rates to personnel following D-T burn pulses were calculated using the same neutron transport code used for Fig. 7-12. The calculations assume a specially designed, 0.5-m-thick laminated primary shield (Sec. 5.3.2) which immediately and almost completely surrounds the toroidal structure. Because of electrical and vacuum lines, complete shielding is unattainable.

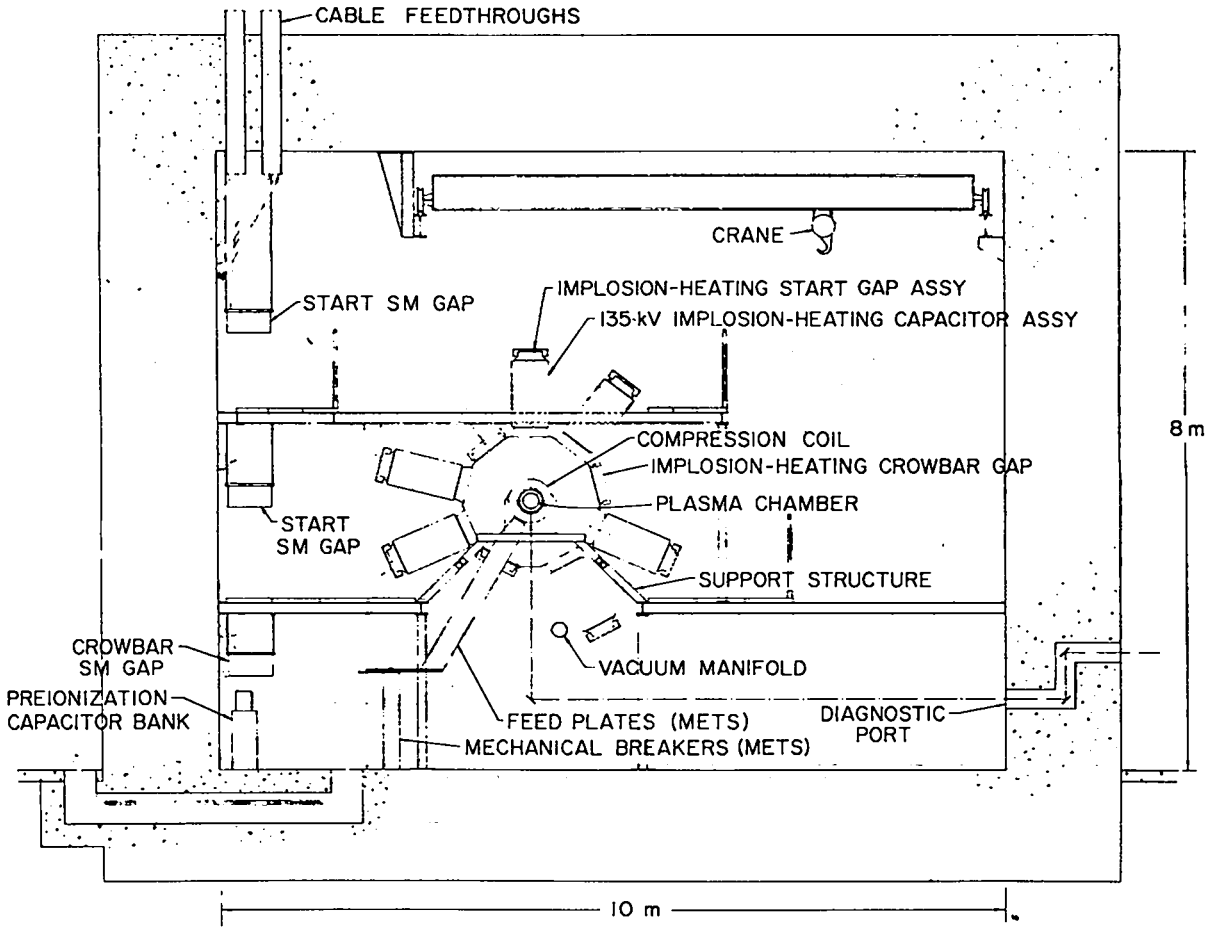

Fig. 7-11.
Cross section of SFTR cell, radiation shielding, and structure that is susceptible to activation by neutrons.

Calculations show that activation products outside of the primary shield present no significant exposure problems to personnel in the cell. Similarly, the quantities of radioactive gases discharged to the environment will be minimal. The only appreciable radiation levels occur when the primary shield is removed for maintenance or replacement of sections of the activated toroidal structure.

7.3.3.1 Activation of Cell Air

Table 7-4 summarizes the results of calculations made to determine the quantities of radioactive gases formed in the cell during a D-T burn pulse yielding 4.5 x 10^{18} 14-MeV neutrons. This is considered a maximum yield. The planned spacing between pulses will not permit concentrations of the radioactive gases to build up within the cell.

Reentry into the cell following a pulse will not be restricted because of the gases, since even for the case of ^{13}N the maximum DE rate is less than 3 mrem/h. Of greater concern to personnel is the structural activation following a pulse (Sec. 7.3.3.2).

Of the nuclides listed in Table 7-4 only ^{13}N and ^{41}Ar are of local environmental concern; ^{16}N (half-life, 7.1 s) will decay to insignificant levels before reaching anyone outside the SFTR cell. Even the activity of ^{13}N (half-life of 10 min) will decrease appreciably as it is slowly removed from the cell and carried downwind from the SFTR site. Nitrogen-13 is a pure positron emitter and, like ^{41}Ar, which is both a beta and gamma emitter, will be responsible for both skin and whole body doses received by an exposed person downwind. The 110-min half-life of ^{41}A will be reduced by one-half by the time it reaches the environment.

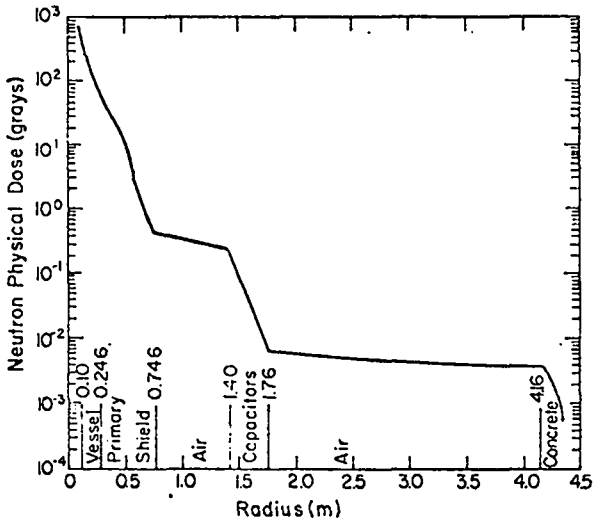

Fig. 7-12.
Neutron physical dose per 4.5 x 10^{18} D-T neutrons deposited in the SFTR cell.

Using an average wind speed of 2 m/s to calculate the decay of the ^{13}N and ^{41}A as they are carried downwind, and the isopleths in Fig. 7-3 for a 30-m stack, the annual beta skin and gamma whole body DE's were calculated for an annual production of 4.5 x 10^{21} D-T neutrons and plotted in Figs. 7-13 and 7-14. From these it is concluded that the activated tunnel atmosphere does not constitute a significant public hazard.

The activity induced in the cell wall (biological shield) is not expected to contribute to the exposure rates resulting from the total neutron-induced radioactivity in the tunnel. As in the case of the capacitors, the neutron fluence per shot outside of the primary shield is reduced to the point where the resultant activities in the tunnel wall are insignificant.

7.3.3.2 Structural Activation

Activation of structural equipment and material within the SFTR cell is considerably reduced by the laminated primary shield that surrounds the plasma chamber. For instance, the activity of each of the capacitors closest to the shield following a maximum yield D-T pulse (4.5 x 10^{18} n/pulse) is only about 0.2 mCi. Thus, the initial exposure rate from all capacitors at floor level is less than 1 mR/h,* and quickly decays.

At floor level and with the shield in place, the exposure rates after 10^3 pulses over 1 yr from the copper compression coils, plasma chamber, and primary shield structure are somewhat higher: about 250 mR/h initially, 40 mR/h in 1 h, 5

**1-mR/h exposure rate is equivalent to a 1-mrem/h DE rate.*

TABLE 7-4

RADIOACTIVE GASES FORMED IN THE CELL FOLLOWING A MAXIMUM-YIELD D-T BURN PULSE

Nuclide	Initial Activity (Ci)	Physical Half-Life (min)	Effective Half-Life[a] (min)	Initial DE Rate (mrem/h)		Total Activity Released at Stack Exhaust/10^3 D-T Pulses[b] (Ci)
				Gamma	Beta	
^{13}N	0.11	10	8.6	9.2	3.3	15
^{16}N	17	0.12	0.12	5 x 10^4	1.7 x 10^3	0.044[c]
^{41}Ar	1.8 x 10^{-2}	110	40	2	0.57	12
^{39}Ar	4.5 x 10^{-9}	1.4 x 10^8	62	~0	~0	4.5 x 10^{-6}
^{14}C	3.0 x 10^{-7}	3.0 x 10^9	62	0	~0	3.0 x 10^{-4}

[a] *Decrease in activity in tunnel (or concentration) due to cell ventilation rate of 2.8 m^3/s in addition to physical decay.*

[b] *Based on 10^3 maximum-yield D-T burn pulses (4.5 x 10^{18} n/pulse).*

[c] *Based on production of only 2 mCi outside of the primary shield (per pulse).*

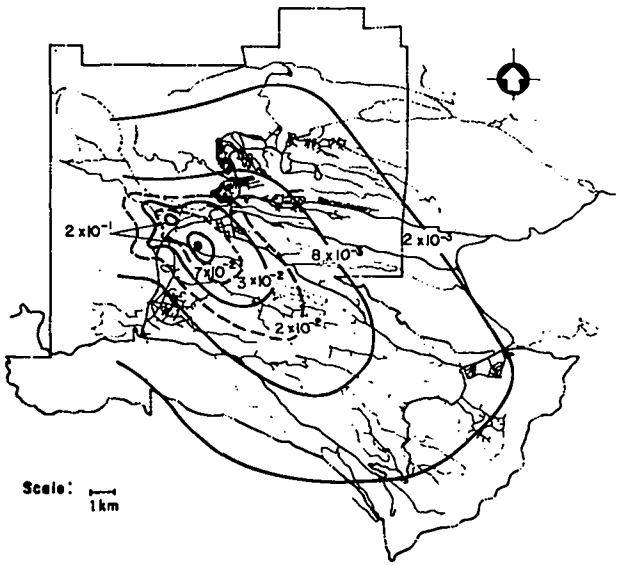

Fig. 7-13.
Beta radiation skin isodose curves (mrem/yr) for SFTR activated air released from a 30-m stack.

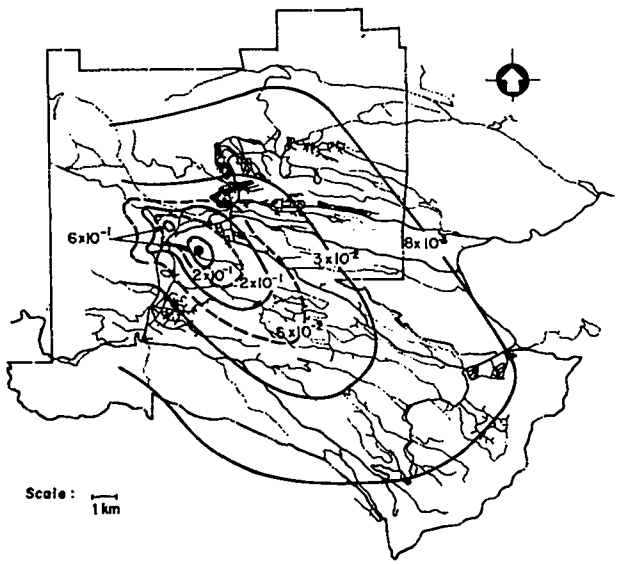

Fig. 7-14.
Whole-body gamma-ray isodose curves (mrem/yr) for SFTR activated air released from a 30-m stack.

mR/h the following day, and about 2 mR/h in a week. The shielding effect of the capacitors is not included but is expected to be significant. They would be helpful in supplementing any local shielding provided for those working in the cell room after shutdown.

Within the primary shield, the activities are, as expected, quite high. When the shield is removed for maintenance or replacement of a section of the plasma chamber, remote handling will be required. The exposure rate from a 0.4-m coil section will be high initially (~15 R/h at 1 m), but will decay to ~100 mR/h 24 h later. On the other hand, a 0.4-m discharge tube would have corresponding rates of 1 and 200 mR/h. Handling of these tube and coil sections with the primary shield removed would be done remotely.

The above estimates are the result of calculations based on 10^3 D-T maximum yield pulses per year and are thus high compared to those expected during the early part of the D-T phase of the experiment. This is particularly true for the activities and corresponding exposure rates a day or more after shutdown when the long half-life isotopes begin to dominate.

7.3.4 Power Requirements and Thermal Effects

Power requirements of SFTR are described in detail in Sec. 5.4 and Appendix I. Warm METS* requires a dedicated 115-kV transmission line from the Norton switch line (near Buckman Mesa) to carry power to the ETA switchyard and ultimately to a switchyard at the SFTR site. The peak power requirement will be 141 MVA, with an average power of 7 MWe. Most of this power will be dissipated at the SFTR site and will have insignificant environmental effects. For instance, the energy dissipated on each charging operation equals 7.4 times the magnetic field energy stored in the Warm METS energy-storage inductor. The field energy, in turn, is dissipated eventually in the inductor itself, the compression coil, and the crowbar. Therefore, a total energy of 4.2 GJ is dissipated during each pulse, accumulating to 8.4 TJ (2.3 MWh) over the 2000 shot life-expectancy for the experiment. This accumulated energy is small when compared, for example, with the lighting load of of an industrial building complex (lighting load of 55 W/m^2 is assumed).[5] This implies that a floor space of 80 m^2 will represent the same integrated load over a 2-yr period, if the year consists of 2112 h of lighting. On the other hand, the duty factor for 2000 shots over a 2-yr period is 0.12; hence, the instantaneous thermal output of the environment is the equivalent of the light load of a 670-m^2 floor space. The power requirements and associated thermal effects, therefore, will not be serious.

**Of the various options for energizing the compression coils, the "Warm METS" scheme requires the most power, so we assess its impact.*

7.3.5 Radioactive Waste

Routine operations of the SFTR will result in the generation of significant quantities of both tritium-contaminated and neutron-activated waste materials, possibly requiring some special handling and disposal techniques.[6,7] At present the Laboratory generates small volumes of both waste types which are routinely disposed of by controlled burial in pits and shafts at the Laboratory's Radioactive Solid Waste Disposal Area. The technique required depends upon both the amount and type of contamination present. The projected contaminated and/or activated waste materials originating from SFTR operations will be handled and disposed of in a like manner. The quantity of radioactivity disposed of in the waste burial area will not be increased significantly as a consequence of the normal SFTR operation.

Once operations with tritium are initiated, it is anticipated that several tens of milliliters of tritiated water, containing up to several curies of tritium, will be generated daily. This material will be absorbed for disposal as a solidified matrix. Disposal will be accomplished by packaging in special asphalted containers and deposited into special asphalt-lined deep shafts drilled in the LASL Radioactive Waste Burial Ground. Asphalt has been shown in LASL tests to provide excellent long-term containment of tritium. Alternative means of solidification and stabilization of the tritium for disposal will continue to be investigated.

Activated hardware requiring replacement and disposal will probably include sections of the reaction chamber, compression coils, capacitors, and cables. Total waste volume for these materials may range between as little as 56 and as much as 280 m^3/yr, depending largely upon the ability to reduce volume in the more bulky pieces, e.g., crushing or cutting of reaction chamber sections requiring disposal. A capability to store these activated hardware pieces at the SFTR site for short times will be provided, as necessary, to effect a reduction in radiation shielding required for handling and transport of these pieces.

Calculations based upon projected neutron yields and the known materials of construction of the chamber and associated components show initial induced activities ranging from about 3 and 60 Ci for chamber sections and compression coils, respectively, down to less than 100 mCi for cables and capacitors. Activities, however, will be short-lived, decaying to levels ranging from about 400 mCi to a few microcuries in 1 wk or less. Consequently, routine disposal by pit burial at the LASL Radioactive Waste Burial Area can be accomplished with a minimum of handling difficulty, shielding requirements, or risk of personnel exposure problems.

Calculations also show that there will be an insignificant buildup of long-lived activities in these pieces over the lifetime of the SFTR operations. Final disposal of the hardware also will not pose major problems other than as a result of the sheer bulk of material involved.

7.3.6 Chemical, Sanitary, and Other Wastes

Chemical Waste. Chemical waste will be collected at the place of use and transported to the Laboratory's industrial waste treatment group for disposal.

Sanitary Waste. Sanitary waste will be handled by a system to be constructed on Two-Mile Mesa before the construction of SFTR. The system will collect all sanitary waste on Two-Mile Mesa and convey it to the existing TA-3 Sanitary Waste Treatment Facility which at present has the capacity to handle the additional load.

Radioactive Contaminated Liquid Waste. A holding tank will be installed to collect waste water from those rooms where tritiated water may be collected. Depending on the tritium concentration, the water will either be stacked at the facility or transported to the Laboratory's industrial waste treatment group for solidification and burial. No radioactive contaminants other than tritium are expected in the waste water.

7.3.7 Transport of Radioactive Materials

The main radioactive materials to be transported will be the tritium received at the SFTR site and the radioactive solid waste materials requiring disposal. No problems are anticipated in the routine handling and transport of these materials. DOT transport requirements will be met in all such operations. Tritium will be received from the suppliers as molecular tritium gas contained in DOT-approved shipping containers. All tritium transported and stored at the LASL site will be packaged in the approved containers.

Both tritium-contaminated and activated waste materials will require transport to the LASL waste disposal site. Wastes of these types are handled routinely at the Laboratory. Calculations indicate that after decay times of 1 wk or less, activated hardware requiring disposal will have exposure rates of <200 mR/h at 1 m. As a result, only a minimum of shielding, if any, will be required for safe transport to the waste disposal area. No transport problems

are anticipated. Tritium waste will be packaged at the SFTR site in approved transport and disposal containers.

7.3.8 Land Usage and Despoilment

About 4 acres will be required for the building and parking lot, and trees and underbrush will have to be removed. The pine trees at the site are not old enough to be used for lumber. Consideration will be given to the maintenance of green belts wherever possible to enhance the esthetics of the area and to promote recovery of vegetation.

There will be excess top soil and tuff after the site is leveled. Usable top soil will be stockpiled for rehabilitation of the area around the buildings. The tuff will be used in construction of the access road across Two-Mile Canyon.

The urbanization resulting from construction of the site will increase the surface runoff into Two-Mile Canyon. Surface drainage will be maintained during and after completion of construction to minimize erosion as well as to transport sediments into the canyon.

7.4 SAFETY AND ENVIRONMENTAL CONSIDERATIONS DURING OFF-NORMAL OR ACCIDENT CONDITIONS

On the basis of past experience and conjecture with the Scyllac experiment, the major accident hazards associated with the SFTR will be: (1) mechanical failure of magnetic coils and vacuum enclosure, (2) high voltages, and (3) fire. With careful design and operational procedure, the probability of an accident from any of these three possibilities has been reduced to near zero for Scyllac. Although the same low probabilities will exist for the SFTR experiment, the following subsections address specific operational hazards recognized for the SFTR, and, when possible, the consequences of related, hypothetical accidents are described.

7.4.1 Consequences of a Sudden and Total Release of Tritium

Once D-T operations are under way, tritium will be found in storage containers in the vault, on uranium beds in the tritium handling hoods, cryogenically trapped within pumping stations, and on molecular sieve beds in the tritium cleanup systems. The entire inventory (~3 g) might be released from these various containers by an act of sabotage or a major accident, such as the crash of a large aircraft into the building. However, the release of the SFTR tritium inventory in toto would not be catastrophic.

Exposure to personnel in the building is almost impossible to predict because of the possible variations and complexities of any accident scenario. Furthermore, property damage and probable fire, with accompanying injury and death, would probably overshadow any danger from exposure to tritium. Gaseous tritium is many orders of magnitude less toxic than tritiated water vapor and should present no significant exposure problem. Any tritium oxidized in a fire would rapidly escape from the building with other combustion products. Such a fire would have to be controlled from an upwind position, or self-contained breathing apparatus would be needed.

In case of sabotage, the tritium cleanup systems would be called into service automatically unless they were out of commission. In that event, the tritium, as gas or oxide, would find its way to the environment either slowly at ground level or up the stack, depending on the condition of the ventilation system.

Calculations were made to estimate the personnel exposure outside the building, assuming that all tritium is in the form of HTO. Three standard meteorological conditions, release heights of 0 and 30 m, and a wind speed of 1 m/s were used. Biological parameters included a biological half-life for HTO of 10 days, a tritium quality-factor of 1, and a breathing rate of 3.47×10^{-5} m^3/s. Absorption through the skin was assumed only for the case of the extended release. The result for the rapid stack release is plotted in Fig. 7-15. In the case of an extended release via stack, the average time-integrated concentration at any point downwind is lower by a factor of 1.5 to 2. Consequently, the intake through the lungs is decreased proportionately. Intake through the skin, however, is increased from zero for a very short release to an amount nearly equal to that taken in through the lungs for an extended release. Hence, Fig. 7-15 may also be used for the case of the extended release to arrive at exposure estimates correct within a factor of 2.

A release at ground level can occur only very slowly and this situation is treated in Fig. 7-16. The dose equivalent (DE) is based on a release lasting up to 8 h, but should the release take longer, the DE is decreased further because of increased lateral dispersion.

The largest DE would occur at the site boundary (approximately 300 m from the SFTR building). The DE to an individual at this location for releases up the stack or at ground level as a function of the fraction of the total inventory (3 g) released is plotted in

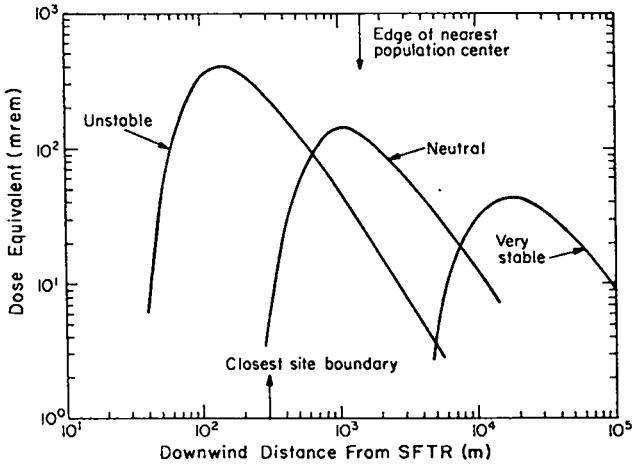

Fig. 7-15.
Dose equivalent downwind from an instantaneous release of 3 g of T as HTO as a function of distance for three meteorological conditions, a 1-m/s wind speed, and a 30-m stack height.

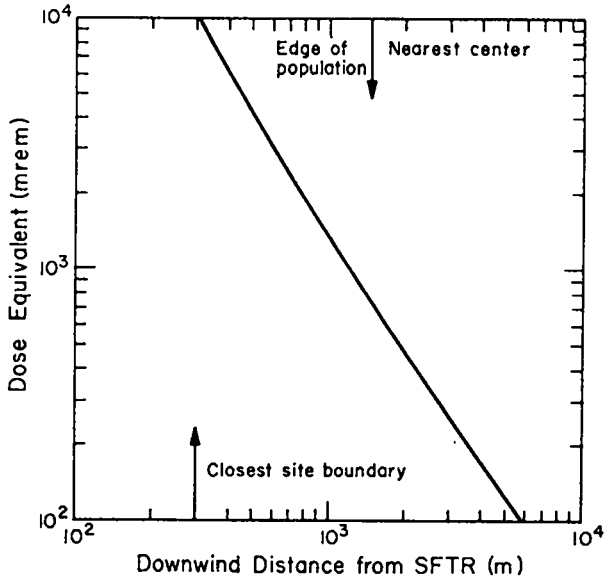

Fig. 7-16.
Dose equivalent downwind from a ground release of 3 g of T as HTO extended over a period of 8 h for a meteorological condition and a 1-m/s wind speed.

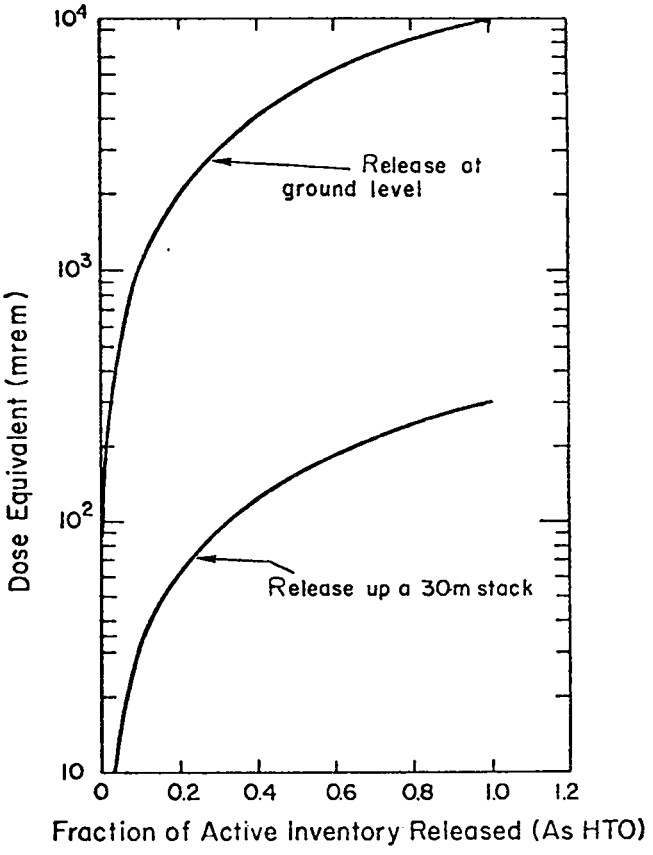

Fig. 7-17.
Infinite-time DE at the closest site boundary (300 m) as a function of the fractional release of the tritium inventory (3 g) released as HTO.

Fig. 7-17. The worst atmospheric condition for this distance was used in estimating the doses: approximately neutral for a release up the stack; stable (Pasquill F) for the ground release. A wind speed of 1 m/s and a stack height of 30 m were used. A gradual release lasting no longer than 8 h was again assumed. If an extended release were to take place, ample time would be available to evacuate people from the downwind area.

In the event of such releases, a large segment of the local population could be exposed, albeit the individual doses would be quite small. The population dose was calculated for two cases: a release in the direction of the Los Alamos townsite and one in the direction of Santa Fe (40 km to the southeast). In the first case, a neutral meteorological condition was assumed; in the second case, a moderately stable condition was used. These two conditions represent the worst situations for the two population centers, assuming that the release occurs instantaneously up a 30-m stack. The maximum DE at Los Alamos is about 110 mrem and the population dose is estimated to be about 200 man-rem. In the Santa Fe case, the corresponding values are 4 mrem (average) and 160 man-rem. No allowance was made for

terrain features that would dilute the concentration or for protection afforded by shelters.

Given that the local radiation background DE is approximately 150 mrem/yr, the tritium exposure resulting from the (highly improbable) release of a substantial fraction of the active tritium inventory does not constitute an unreasonable risk to the public.

7.4.2 Catastrophic Failure of Discharge Tube During a D-T Experiment

Loss of vacuum containment from crowbar failures is expected to occur relatively frequently during the early check-out phase of the SFTR operation. Reliability of the SFTR firing sequence and vacuum wall will be established before D-T experiments proceed. As discussed in Sec. 5.2, local vacuum-wall failures during a D-T discharge would release only a small fraction of the ~15-mg T_2 inventory. The bulk of the tritium would be collected on the cryogenic roughing pumps. In the unlikely event of a massive failure of the discharge tube and subsequent release to the SFTR cell of all tritium used in that shot, the tritium concentration within the cell would exceed 6000 times MPC_a. The cell cleanup facility (CCF) would then be activated and the tritium removed from the cell air in a matter of hours. Details of this procedure are discussed in Sec. 5.2. No serious consequences to operating personnel or the general public are envisioned for a (highly improbable) massive failure of the SFTR vacuum.

7.4.3 Fire Hazards within the Cell

During assembly, calibration, and initial operation of the toroidal structure, the fuel will be combustibles usually associated with construction. Although these combustibles will be kept to a minimum, they will constitute a significant fire hazard. A temporary or portable automatic sprinkler system is a feasible method of protection during this period. In addition, hose lines and extinguishers (water type, CO_2, and ABC type powder units) will be provided. There will be no release of radioactive material as a result of a fire during this time, and ventilation and air exhaust systems will be adequate to cope with any smoke and heat.

Once the facility is in operation, an automatic fire detection and suppression system will be installed in the cell. The likeliest cause of fire is "fire fuel" (rags, thin plastic sheet, or shavings, paper packing materials, etc.) that become oil-soaked and are ignited electrically. A less likely source of fire is spark-gap failure during which a low energy fireball of hydrogen is released. Although such a fire could ignite tissue paper, the cables or capacitor oil probably would not ignite.

The cell will contain approximately 4000 gal of castor oil—a relatively stable hydrocarbon that requires preheating before ignition. Its flash point is about 204°C and its ignition temperature about 445°C. In case of fire, castor oil is no more hazardous to health than ordinary combustibles, normally remains stable, and does not react with water. It has a slight tendency toward auto-ignition when left on saturated cellulose waste in poorly ventilated closures. In a cell fire, we assume that no more than 500 gal of castor oil would be available for burning. Such an oil fire could be extinguished by standard foam, high expansion foam, dry chemical, or vaporizing liquid type agent. First consideration will be given to Halon 1301, and the somewhat cheaper, but more toxic, Halon 1211 also will be considered.

The cell will contain a significant amount of polyvinyl chloride insulated cable which will soften at about 80°C and melt at 104°C but which is difficult to ignite. When it does ignite, it produces acrid, highly corrosive fumes which are mainly hydrogen chloride. The extinguishing agents mentioned above will also control the burning PVC, but they must be applied quickly because of the corrosive gas.

Other combustible and corrosive materials, such as polyethylene cable insulation or neoprene insulation, are likely to be present in the cell, but will not be of consequence.

The cell ventilation system will be designed to exhaust the bulk of the hot gases and smoke under most fire conditions. Some exhaust filtration will be necessary, as will drains and retention tanks to handle any water used in fire-fighting.

7.4.4 Fire Hazards External to the SFTR Cell

7.4.4.1 Fire within Tritium Storage and Treatment Facilities of SFTR

In the presence of tritium, deuterium, and cryogenic fluids, modification of normal fire-control measures will be necessary in the tritium storage and treatment sections of the SFTR. These modifications involve the control of personnel entry and fire hose usage. Otherwise, safety measures will be typical of laboratory and equipment rooms, and should include an automatic sprinkler or CO_2 system. Activation of any suppression system should automatically interrupt the ventilation until the ventilation is restarted by a manual override. High expansion foam, CO_2, and Halon 1301 systems could

be used in areas of specialized hazard and limited size. In areas where capacitors are stored or used, and where there are large numbers of cables that would be vulnerable to water, a Halon 1301 suppression system like that for the present Scyllac experiment will be the choice.

The tritium inventory in the storage vault poses the largest radiological hazard. Part of the tritium will be a gas under 2 atm pressure in a rugged metal container. The remainder (<3g) will be $U(D,T)_3$, a pyrophoric hydride, also in a metal container stored within a closed metal cabinet. The likelihood of fire in the vault is very small. The main fire risk is from combustible materials brought in during shut-down and renovation periods.

In case of fire, personnel entry may be limited to mandatory usage of supplied-air suits because of the high potential but localized danger.

The quantity of tritium in the tritium processing room (a few thousand curies) will be an order of magnitude lower than that in the vault. All but a small fraction will be uranium tritide or deuterotritide in metal containers within a vented enclosure. Supplied air and controlled use of spray-type fire nozzles (particularly on the hooded enclosure) constitute the special fire-control features in this room, although high expansion foam systems will also be considered.

In the TWT and CCF rooms, tritium levels should be sufficiently low (one or two orders of magnitude lower than that in the tritium processing room) and the confinement of the tritium in the dryers should be sufficiently secure to eliminate the need for special fire-control measures.

The deuterium supply will be in a single cylinder (280 ℓ STP), and normally only one tank (several months' supply) will be on hand. Deuterium, like hydrogen and helium, has a negative Joule-Thomson coefficient at room temperature, so that rapid expansion of deuterium or hydrogen in air at room temperature can lead to self-ignition. Such fires might be left to burn (so long as the valve on the cylinder is kept cool) to avoid the creation of an explosive deuterium-air mixture. The tank of deuterium is also a hazard if it explodes or if deuterium is somehow released to aggravate a fire or to give an explosive deuterium-air mixture. Deuterium leaks can be hazardous, but should be rare.

Ten to twenty liters of liquid helium and liquid nitrogen will be contained in dewars and equipment in the tritium processing and TWT rooms. Because these liquids could vaporize rapidly during a fire and burst their containers, emergency procedures must be developed to deal with this hazard. If the containers burst, about 1 Ci of tritium would be released (in the hood), and occasionally a maximum of 150 Ci could be released during operation.

Special dry-chemical and standard carbon dioxide extinguishers can be placed throughout the facility with no restriction on use, except possibly on a deuterium fire. Noncombustible and fire-proofed equipment should be used where practicable, consistent with the degree of tritium hazard (highest in the storage vault). A limited number of emergency showers will be installed.

In summary, the major fire hazard for the SFTR is expected to be the PFN and transfer capacitor banks (high voltage, oil) which are far removed from the major tritium hazard (storage vault). A great deal of experience has been accumulated at LASL in the safe handling of both large capacitor banks and tritium. With only a few extrapolations from present LASL practice, the fire and tritium control expertise required for the SFTR facility is already available.

7.4.4.2 Fires Associated with the Transfer Capacitor System

The transfer capacitor system is composed of low voltage capacitors connected in a series-parallel arrangement to provide a 100-μF capacitance at 60 kV. The capacitor is composed of materials presently used in the standard Scyllac-type energy-storage capacitor. The capacitor plates are aluminum foils which are separated by several layers of Kraft paper impregnated with castor oil. The switches used on the capacitor bank are standard, commercially available ignitrons.

There is little fire hazard associated with the capacitor bank. The major hazard arises if, for some reason, a capacitor should rupture and expel the castor oil onto an area where there might be a possibility of ignition. A capacitor case can be ruptured if the capacitor shorts and energy from parallel connected units is dissipated in the ruptured capacitor. Experience shows that up to 30 kJ of energy can be dissipated in one of these capacitors with little danger of rupture. Each unit contains approximately 11 kJ of energy, which is not sufficient to cause rupture, and the energy from parallel units will be limited by a cable connection which will act as a fuse under fault conditions.

The probability of a unit rupturing is therefore very small; consequently, the fire hazard associated with the transfer capacitor bank is very small.

7.4.4.3 Hydrogen Explosions

The quantities of deuterium and tritium that will be handled in the SFTR are minor by normal standards. Nevertheless, explosions involving these

materials, give concern because of the potential release of tritium in quantities that may be radiologically hazardous. The conditions that might lead to such explosions are discussed below.

Some limits of flammability (fl.) and detonability (de.) for hydrogen and deuterium in air and oxygen are as follows[8] (vol%): fl. H_2 in air, 4.00-74.20; fl. H_2 in O_2, 4.65-93.9; fl. D_2 in O_2, 5.00-95.0; de. H_2 in air, 18.59. For hydrogen in air, other properties are[9]: ignition temperature, 858 K; ignition energy (30 vol% H_2), 0.02 mJ; heat of combustion, 285 kJ/mol; and flame temperature, 2318 K. Because the flammability limits of hydrogen-air mixtures are relatively insensitive to pressure,[9] the limits for a low-temperature solid mixture are not expected to be markedly different.

The largest hydrogen source is the 0.28-m^3 STP deuterium supply cylinder discussed in Sec. 7.4.4.1. Because the attendant tritium hazard is only incidental, no special precautions are required, particularly since the tritium handling room is well ventilated and the tank is normally gaged so that an appreciable loss could be noticed. The small quantity of $U(D,T)_3$ (several liters of T_2 equivalent) in metal containers and under hoods is also of little concern, especially since careful PVT and analytical measurements will be made several times a day in the preparation and use of this material.

Tritium will be received in gaseous form in a metal container with 3 g (11 *l* STP) of tritium at a pressure of 2 atm. Only one filled container will be on hand in the vault at any one time. A leak in this container would be immediately detected by a tritium monitor, and an alarm would be sounded. After more than half the tritium has been used, an air leak into the container could create an explosive mixture containing less than 5 *l* of tritium. Since some of this gas is used and analyzed weekly, an air leak would be detected fairly soon. Ignition of this gas is unlikely, and use of a small-diameter tube during transfer would prevent flame propagation into the storage container.[9] The remaining tritium stored in the vault as $U(D,T)_3$ should present no hazard except in case of fire.

A fraction of a liter of deuterium and tritium will be stored in metal containers in the tritium handling room hood. Analytical and PVT measurements would quickly detect any air contamination in these containers. About 0.1 *l* of this gas is transferred at low pressure to four 10-*l* injection containers. Because of the low pressures involved, no hazard exists either in the injection system or the discharge tube.

Perhaps the highest potential for a hydrogen explosion exists in the cryogenic fuel-ash exhaust system. Here, outgassed oxygen, oxygen from the decomposed wall of the discharge tube, or air from equipment and piping leaks could mix with the D_2 or $(D,T)_2$ exhaust gas to form explosive mixtures. In the D-T runs the gas is cryogenically pumped into cryopumps at 4 K at each of four stations. About 0.1 *l* of $(D,T)_2$ will be condensed as solid in these pumps. Since the pumps have a total volume of 20 to 40 *l*, the volume of $(D,T)_2$ is too small to create physical damage were an explosion to occur. Also, the gas is subsequently expanded and analyzed before it is cryogenically pumped (for more accurate measurements in a standard volume, if desired) or reacted with uranium. Thus, the chance for a damaging tritium explosion in the tritium exhaust and recovery operations is extremely remote.

Because of the rapid sequencing of the deuterium runs (one every 15 m), the deuterium-ash will be collected daily on four cryopumps (5- to 10-*l* volume) located in the hooded pumping stations. The volume of deuterium gas collected daily would be 3 *l*, based on a duty cycle of 15-m, 8-h operation and a deuterium volume per shot averaging about 0.1 *l*. Thus, the pump to deuterium gas volume ratio would be less than 13. At one stage a cap will be placed over the pump to give a volume ratio of only 6. This compares with a D_2O (at 273 K) to D_2 (at 273 K) ratio of 8.5, a volume ratio marginal in its ability to avoid explosion pressures significantly above 1 atm. Instantaneous pressures might be expected to be markedly higher.[10] Further, since the deuterium will be collected as a solid, an intimate mixture of oxygen and other gases with deuterium could be condensed as a solid, in which case the solid could be shock-sensitive. Since less than 1 *l* of deuterium would be in a pump, the energy of the explosion would be less than about 10 kJ. Because the pump will be enclosed in heavy piping, an explosion resulting in the release of liquid nitrogen and helium into the pump enclosure could cause a rapid discharge of the gas (and liquid) through filling ports in the pump and into the hooded enclosure. Although less than a curie of tritium would be involved in such an accident, it might be safer to transfer deuterium to the TWT more frequently than planned. This problem will be investigated thoroughly before D-T experiments are begun.

The deuterium will be transferred under low pressure to the large TWT cryosorb pump, an operation that presents no obvious explosion problems. Every day the cryosorb pump will be warmed, the deuterium and other gases will expand, and helium will be flushed into the 2000-*l* TWT ballast tank. Although potentially explosive mixtures are possible in this operation, the energy generated will be relatively small, the equipment strong, and the likelihood of initiation of the reaction in the closed

system remote. Sufficient air will be present or added during this operation to keep the final average deuterium concentration well below the lower explosion limit of ~5 vol%. A similar condition may arise if hydrogen is injected to aid in the D_2-O_2 reaction as discussed in Sec. 5.6.3.5. Here, again, the injected quantities would be kept small.

In summary, some possibility exists for a deuterium explosion, but the energy would be small in most cases (40 kJ). Furthermore, the explosion would be confined in most cases by strong equipment and hooded enclosures. The probability of a hazard from direct tritium release is very low. Redundancy of equipment, supply lines, and pumping stations should eliminate interruption of operational schedules. Added safety measures, such as more frequent deuterium transfer from the stations, oxidation of the deuterium by hot copper oxide before mixing with air, or provision of barriers, would not be difficult but seem unwarranted. Grounding of equipment and selection of fire-resistant equipment are worth consideration.

7.4.5 Magnet Malfunctions

Most of the mechanical energy that could be released as kinetic energy is stored within the compression field magnets. Table 5.4-5 gives the energy storage, size, and number of magnets in the compression system. A 14.8-cm coil stores 345 kJ, and this hoop strain energy amounts to 2.33 MJ/m or 25.6 MJ/m^3 (3.8 J/g) of compression coil. This compares to 570 J/g for H_2. Hence, the potential exists for slight and localized damage to surrounding equipment if a structural failure should occur within the coil and this stored energy were released as kinetic energy. The resulting destruction would be limited to a highly localized area of the SFTR cell at a time when personnel would not be present. The primary radiation shielding surrounding a module probably would be sufficient to contain the energy release, and local damage to the implosion-heating coil and/or vacuum wall might occur. Similar kinetic energy releases associated with leads and cables are possible, but simple design of support and restraining structures should eliminate this problem. Past experience in this area with Scyllac and Scylla experiments at LASL can be applied directly to the SFTR.

The SFTR magnets may fail from overheating and localized electrical breakdown, as happens in current CTR experiments at LASL, but such failures are considered experimental nuisances rather than hazards so long as proper precautions are instituted.

7.4.6 Failure of Cryogenic Energy-Storage and Transfer System

The temperature of liquid nitrogen and liquid helium is low enough to damage human tissue. If surfaces cooled by these fluids or their evolved gases are touched, the tissue temperature may be lowered below 273 K, where damage occurs. Such cooling does not occur immediately because the blood supply acts as a heat source to the tissue and the contact of a cryogen with warm tissue creates a gas film which is not a good heat conductor (if cold metal is touched, the tissue is damaged much more rapidly). This delay occasionally permits successful counteractive measures to be taken when an exposed part of the body is splashed by cryogenic fluid. Two measures contribute significantly to an individual's safety: (1) shutting off the flow of cryogen or escaping the area, or both, (2) immediate flooding of the tissue or clothing with water. Water's enormous heat capacity, its inertness and availability make it vital in safe cryogenic operations.

Safety glasses will be worn when personnel are working with laboratory and industrial cryogenic and pressurized, or potentially pressurized, systems. Where splashing is a definite possibility, face shields will be worn. Individuals will be trained not to look directly into open cryogenic lines without adequate eye protection, since even small mechanical or thermal disturbances can cause ejection of cryogenic fluid. Personnel may also be required to wear special clothing, gloves, or footwear. Gloves should be clean and dry. Loose-fitting gloves are preferred because they can be removed quickly.

Spills and leaks are by far the most common failures in cryogenic systems. Ruptures, although fairly rare, create the greatest safety hazards. A serious condition would exist if the coil dewar were not properly vented and if the 10 coils in one of the 128 METS dewars should go normal, thereby causing the liquid helium in the dewar to vaporize. Releasing this much helium gas into the area of the main building would reduce the oxygen concentration to 14% if mixing were uniform. But complete mixing would be difficult to achieve, and consequently local oxygen concentrations would be much lower than 14%. For this reason the 0.33-m (13-in.) dewar vent lines will be piped to the outside of the building to eliminate the danger of asphyxiation. In addition, although the storage coil dewar area will be safe for normal activities, it is to be an exclusion area when coils are charged or otherwise tested. All outdoor cryogenic storage areas will conform to standard industrial safety practice for cryogenic storage and will be fenced exclusion areas.

Liquefied helium and nitrogen are capable of condensing (and solidifying in the case of helium) air that may come in contact with them. The liquid, and especially the solid, air can block vent paths and jeopardize vessels because of pressure buildup. In the METS system the liquefied helium will be transferred in closed piping loops pressurized to greater than atmospheric pressure to prevent the backflow of air. Relief devices will be designed to prevent any back leakage of air.

Air coming in contact with a surface cooled below 82 K will partially condense, with the condensate containing approximately 52% oxygen, and will continue to condense as long as air with 21% oxygen is available to the surface. Such an oxygen-enriched mixture will significantly enhance burning rates of combustibles and even permit some materials to become combustible that might not qualify as such in normal air. The system will be designed to preclude condensate formation and to ensure that the runoff, if any, does not create a hazard. This can be accomplished by making sure that the runoff does not come in contact with combustibles or components which become embrittled or cease to function at low temperatures.

It may not be desirable to have vacuum jackets around all components which carry cryogenic fluids, but at least the lines must be covered with blankets or possibly foams. Since most foams are cellular structures, oxygen-enriched air may accumulate in the cells, particularly if the foam is of the open cell type. This effect can be minimized by providing a barrier against the infusion of air. Foams for this application will be selected on the basis of their fire resistance. If glass or mineral wool blankets are used, care will be taken to assure that they contain no oil to react with the oxygen-rich condensate.

Cryogenic systems and components probably will not cause or contribute to any fires which might occur in the experimental area. On the other hand, these units can be damaged by adjacent fires. In fact, the plastic dewars could fail and discharge their contents if subjected to high temperatures for extended periods. In most cases, the protective overpressure blowout discs would release the pressure buildup within the dewar before the dewar itself ruptured. The released gas would be either nitrogen or helium and there would be no increase in the fire intensity. Such a release of cold inert gas might actually help to control a fire.

7.4.7 Fuel Injection Accidents

If the amount of $(D,T)_2$ fuel supplied to the SFTR is too small or too large, the discharge would result in an off-optimum thermonuclear burn. For a given set of operating parameters (shock heating, compression field, etc.), the $(D,T)_2$ filling pressure is selected to maximize the fusion yield, and any deviation from this optimum filling pressure will result in a poor yield. In essence, the plasma represents an important element in a highly tuned electrical circuit, and either under- or over-fueling will de-tune that circuit and result in an off-optimum thermonuclear yield. Hence, the possibility of nuclear or thermal "runaway" for the SFTR is zero.

7.4.8 Consequences of Utility Failures

The SFTR power supply is protected against overvoltages and short circuits between phases or to ground in conventional fashion. If bulk power ceases to be supplied during charging of the energy-storage inductor, then charging simply discontinues and the current maintains the existing magnetic field in the inductor by circulating through the free-wheeling diodes. This current decreases exponentially with the time constant L/R = 7.4 s, and the magnetic field energy is dissipated in the inductor winding and busses. This dissipation amounts to an additional loss of no more than 14% over that occurring normally on charging when the magnetic field energy is eventually dissipated elsewhere in the system. Appendix I describes in detail the consequences of a utility failure at the SFTR site. Generally, no significant environmental effect or safety hazard can be identified as a result of a massive and sudden utility (electrical power, water, etc.) interruption.

7.4.9 Unusual Occurrences

Although detailed accident analyses have not been made, the above-mentioned descriptions, calculations, and conjectures are indicative of the worst consequences possible in the event of a cataclysm (earthquake, tornado, airplane crash, volcanic eruption, act of war, dedicated vandalism). The damage, injury, and death caused by such unusual occurrences will undoubtedly be caused directly by the occurrence itself rather than by the SFTR facility. The radioactive inventory (active structure, tritium) will be secured in limited access areas (SFTR cell, tritium storage vault, etc.) which will be surrounded by thick concrete walls and substantial structure. The small quantity of tritium is probably the only item of interest to international bandits, and the few grams of tritium stored on the site will be safely secured and inventoried (Sec. 5.2).

7.5 SUMMARY AND CONCLUSIONS

From the viewpoint of safety and environment, operational and accident aspects of the SFTR do not differ significantly from the current Scyllac experiment. Although the use of tritium and the production of moderate amounts of structural activation present one major difference, these hazards can be controlled with existing and well-tried techniques. Even with the unlikely simultaneous failure of control and release of the total tritium inventory, the consequences to the public and the environment would be minimal: Radioactive hazards outside the SFTR cell during a D-T shot are nonexistent, and the more serious dangers of fire hazard and high voltage can be controlled by existing procedures. Any perturbation created by the SFTR on the demographic, meteorological, hydrologic, and geologic character of the site will be insignificant. Terrain, vegetation, and wildlife will not be adversely affected if appropriate conservation and construction methods are used in SFTR construction.

REFERENCES (Chap. VII)

1. D. H. Slade, Ed., "Meteorology and Atomic Energy," USAEC report TID-24190 (July 1968).

2. "Uniform Building Code," Intern. Conf. Building Officials (1973).

3. "Standards for Radiation Protection," USERDA Manual Chapter 0524 (April 1975).

4. R. A. Jalbert, "Monitoring Tritium in Air Containing High-Energy Beta Emitters Using Ion Chambers," Proc. Am. Nucl. Soc. (to be published).

5. D. G. Fink and J. M. Carroll, **Standard Handbook for Electrical Engineers**, 10th ed. (McGraw Hill, New York, 1968).

6. "Radioactive Solid Waste Management Policy," Los Alamos Scientific Laboratory internal document (Sept. 27, 1973).

7. L. J. Johnson, "Information on Solid Radioactive Waste Management at LASL," Los Alamos Scientific Laboratory internal document (May 13, 1974).

8. C. D. Hodgman, R. C. Weast, S. M. Selby, Eds., **Handbook Chemistry and Physics**, 39th ed. (Chemical Rubber Pub. Co., Cleveland, OH, 1956).

9. D. B. Chelton, "Safety in the Use of Liquid Hydrogen," in **Technology and Uses of Liquid Hydrogen** (MacMillan, New York, 1965).

10. F. J. Webb, "The Use of Liquid Hydrogen for the Production of Cold Neutrons Inside a Nuclear Reactor," **ibid**.

VIII. COST ESTIMATE

8.1 INTRODUCTION

The design of SFTR is sufficiently detailed for a cost estimate to be made. Systems, such as the vacuum system, that use commercially available components or systems, such as the METS refrigeration system, that have components similar to existing equipment can, of course, be costed with more confidence than those requiring further development, such as the implosion-heating system or the first wall and Marshall coil. Cost estimates for commercially available systems were made from catalog prices when possible and from estimates based on experience with projects such as Scyllac. For components or systems requiring developmental work, cost estimates were made by extrapolating from costs for existing equipment where possible. Estimated costs of the facilities, manpower, and raw material required for the components are more susceptible to error than are commercially available items; consequently, conservatively high estimates have been made.

8.2 SUBSYSTEM COSTS

Cost estimates are divided into the following areas: First Wall and Marshall Coil Assembly; Implosion-Heating System; Preionization System; Primary Shield; Compression Banks (Phase I); METS (Phase II); Tritium Handling and Vacuum System; Diagnostics System; Control System; Facilities. The cost estimate for each system will be discussed in the following sections.

8.2.1 First Wall and Marshall Coil Assembly

The most difficult and uncertain cost estimate in the project is that of the first wall and Marshall coil assembly. Ceramics will probably be used to enable the first wall and Marshall coil to withstand the high neutron flux and still maintain adequate electrical insulation strength; however, the processing, manufacture, and assembly of these ceramic components have not yet been done for theta pinches, and such development may require several man-years of effort. Initial efforts are under way and simple ceramic first walls will be used in 1976 in LASL Z-pinch and staging experiments.

The cost estimate is based on present concepts of materials and construction. Development of the coils will require an effort of roughly 50 man-years, and since it must be done before the machine can be funded, development costs are not included. The cost of the ceramic will be negligible compared to the cost of the fabrication facilities and time required for fabrication. The major expense will be that for furnaces and grinding machines and the labor cost for operating the equipment. The cost estimate is shown in Table 8-1.

The estimate includes the cost of labor, capital equipment, and material. It is assumed that the assemblies will be constructed over a period of 2 yr and that only half of the total assemblies will be usable. A 40% contingency factor is included to cover the high uncertainty in the overall process and design.

8.2.2 Implosion-Heating System

The implosion-heating system consists of the current feedplates between the implosion-heating capacitors and the Marshall coil, capacitors and start gaps, crowbar gaps, pulse-charge system, trigger system, and structural material in the plasma chamber and for the trigger and pulse-charge system. The ferrous material between the implosion-

TABLE 8-1

COST ESTIMATE OF FIRST WALL AND MARSHALL COIL

Material	$ 0.60M
Copper plating equpment	0.13
Casting equipment	0.10
Ceramic furnaces	0.78
Metalizing furnaces	0.78
Bronzing furnaces	0.78
Grinding equipment	0.39
Miscellaneous equipment	0.25
Facilities	0.50
Labor (2 yr)	3.06
Equipment assembly and testing 20%	1.47
Contingency 40%	3.54
Total	$12.38M

heating system and the compression coils is also included in this cost estimate.

Many components, such as the trigger system, are commercially available and require little or no development, while others, such as the 135-kV capacitors and gaps, require moderate development efforts which are not included in the estimate. The low engineering estimate is due to the repetitive nature of the system. The estimate is given in Table 8-2.

8.2.3 Preionization System

The preionization system is small, and components are already developed, and only a moderate amount of engineering will be required. Costs are given in Table 8-3.

8.2.4 Primary Shield

Although the primary shield cannot be purchased from a commercial vendor, the required material is available commercially and the fabrication could possibly be carried out on contract. The estimate in Table 8-4 was made by costing the required volume of materials and estimating the fabrication and installation costs. Little development work will be required, but a large contingency is used because of lack of experience with the manufacture of such systems.

TABLE 8-2

COST ESTIMATE FOR IMPLOSION-HEATING SYSTEM

Current feed plates	$ 1.20M
Capacitor connectors	0.86
135-kV capacitors	1.15
Start gaps	7.7
Crowbar gaps	3.8
Start-gap trigger system	3.65
Crowbar trigger system	1.50
Pulse-charge system	0.93
Ferrous material	0.17
Structural material	1.1
	22.06
Equipment assembly and testing 20%	4.41
Engineering 10%	2.21
	28.68
Contingency 15%	4.30
Total	$32.98M

TABLE 8-3

COST ESTIMATE FOR PREIONIZATION SYSTEM

1.85-μF 60-kV capacitor	$0.32M
Scyllac-type start gaps	0.35
Trigger system	0.22
Charge system	0.04
Miscellaneous hardware	0.30
	1.23
Equipment assembly and testing 20%	0.25
Engineering 5%	0.06
	1.54
Contingency 10%	0.15
Total	$1.69M

TABLE 8-4

COST ESTIMATE FOR PRIMARY SHIELD

Borated graphite	$ 3.89M
Aluminum structure	0.64
Borated polyethylene	1.37
Lead-borated polyethylene	7.04
Engineering	1.00
Fabrication	2.56
	16.51
Assembly 5%	0.83
	17.34
Contingency 30%	5.20
Total	$22.54M

8.2.5 Compression Bank (Phase I)

The compression bank is made up entirely of commercially available components for which reliable cost information is available. Efforts are under way at Los Alamos to develop a lower priced capacitor; however, in Table 8-5 the present price of capacitors is assumed. The only innovation required in this system is the optical fiber isolated trigger system which will require a small amount of development work, and the first metal-to-metal crowbar switch which will require a larger development effort. As in the implosion-heating system, a small engineering effort is assumed because of the highly repetitive nature of the system.

TABLE 8-5

COST ESTIMATE FOR COMPRESSION BANK (PHASE I)

Energy-storage capacitors	$ 7.17M
Start ignitions	0.48
Crowbar ignitrons	2.69
Metal-to-metal crowbar switch	3.2
Compression coils	1.43
Trigger systems	1.26
Cabling	0.80
Charge system	2.15
Charge racks	0.64
Miscellaneous hardware	1.92
	21.74
Equipment assembly and testing 20%	4.35
Engineering 10%	2.17
	28.26
Contingency 10%	2.83
Total	$31.09M

TABLE 8-6

COST ESTIMATE FOR METS (PHASE II)

Storage coils	$22.50M
Cryogenic disconnects	4.80
HVDC interrupters	6.48
Charging power supply	0.18
Electrical leads	1.02
Isolation connectors	0.32
Cabling	1.86
Storage coil dewars	3.20
Liquid and gas distribution	0.92
Refrigeration and cryogenic storage	7.48
	48.76
Equipment assembly and testing 20%	9.75
Engineering 10%	4.88
	63.39
Contingency 15%	9.51
Total	$72.80M

8.2.6 METS (Phase II)

The METS system consists of components requiring little work, such as the refrigeration system, as well as components requiring a substantial amount of development, such as the HVDC interrupter and the superconducting coils. The development effort has not been included in the cost estimate for each component. The estimated cost of system installation also includes the small amount of labor required to modify the cabling on the compression capacitor banks. The low engineering cost reflects the fact that the equipment is purchased commercially and the engineering is that required for the installation and system interconnections. Table 8-6 lists the METS costs.

8.2.7 Tritium Handling and Vacuum System

The major equipment cost in the tritium and vacuum system is that of the cell cleanup facility. Unfortunately, the cost estimate for this equipment has the highest error because the unit is significantly larger than any that is presently available. Little development effort is required, and estimates can be made by extrapolating from smaller existing systems.

Most of the remaining equipment is available commercially and can be costed with greater confidence. The main uncertainty is in the exact number of control functions, such as readout, alarming, and sampling frequency, which will achieve optimal efficiency and safety in system operation. The estimate includes the cost of the storage and transfer system, tritium purification equipment, gas metering and mixing, and the analytical equipment. Sufficient uranium beds are included to allow for some T_2 in storage as well as in off-site tritium recovery facilities.

A high maintenance item is the fast operating downcomer valve which must endure approximately 800 closures a month. As a result, a second valve is included on the downcomer to allow replacement of the Viton gasket in the fast operating valves.

Table 8-7 is a summary of the estimates for the system. Cleanup system costs constitute by far the major portion of the cost, and a partial breakdown of that system is listed, although more detailed costs were generated.

8.2.8 Diagnostics System

The diagnostics system will be made up of presently available instruments integrated into a large sophisticated system which will require a development effort of approximately 12 man-years. The estimate is given in Table 8-8.

8.2.9 Control System

The control system consists of a main computer and a number of satellite computers with the

TABLE 8-7

COST ESTIMATE FOR TRITIUM HANDLING AND VACUUM SYSTEM

Uranium beds	$0.04M
Cryogenic pumping systems	0.13
Dewars	0.02
Piping and valves	0.16
Diagnostic equipment	0.02
Gas control equipment	0.04
Hood enclosures	0.06
System control equipment	0.03
Tritium waste treatment system	0.13
Cell cleanup facility	
2 Preheaters	0.52
2 Catalytic reactors	0.44
2 Heat exchangers	0.18
2 Blowers	0.17
4 Dryer towers	0.44
	2.38
Engineering 20%	0.47
Equipment assembly testing 25%	0.59
	3.44
Contingency 15%	0.52
Total	$3.96M

TABLE 8-8

COST ESTIMATE FOR DIAGNOSTIC EQUIPMENT

Digital streak cameras (4)	$0.28M
Plasma luminosity TV monitors (80)	1.20
Neutron scintillators (80)	0.08
Neutron counters (20)	0.01
Coupled-cavity interferometers (4)	0.08
Thomson scattering (4)	0.40
Excluded flux (80)	0.16
	2.21
Equipment assembly and testing 20%	0.44
	3.25
Contingency 15%	0.49
Total	$3.74M

associated interface equipment and cabling. All control system components are available commercially from computer manufacturers and the costs are based on catalog prices. System development and engineering are included in most of the subsystem costs. The engineering required for system interfacing is assumed to be 15%. Table 8-9 lists the costs.

TABLE 8-9

COST ESTIMATE FOR CONTROL SYSTEM

Main control computer system	$0.127M
Software development system	0.216
CRT control	0.171
PI control	0.100
Implosion-heating control	0.378
Tritium and vacuum control	0.100
METS control	0.111
Compression bank control	1.654
Diagnostics control	0.505
Precision pulser system	0.861
Cabling	0.048
	4.22
Equipment assembly and testing 20%	0.84
	5.06
Contigency 10%	0.51
Total	$5.57M

8.2.10 Facilities

The facilities cost estimate includes not only items relating to the structure itself, such as the cell, remote handling facilities, control room, experimental enclosure, and maintenance bays, but also site preparation, utility connections, and access roads. The construction of the facilities is straightforward, with the exception of the concrete cell which has 1-1/2-m-thick walls. Care has been taken to keep the size of the building to a minimum and to take a cost-effective approach in the design and type of construction.

Table 8-10 gives a summary of the facilities estimate. The building estimates are based on cost per square foot for similar types of structures, whereas the concrete estimates are based on volume costs. The utilities estimate has been determined by using a structural percentage figure of the structural costs plus cost for length of runs to the nearest existing utility that can handle the facility adequately. Because of the large electrical power requirement, a separate estimate has been made for the electrical utilities, including an appropriately sized substation and distribution system.

8.3 SFTR SYSTEM COST

The cost estimate for the entire SFTR experiment is given in Table 8-11. The cost for Phase I operation is $133.16M, and an additional $72.80M is required

TABLE 8-10

FACILITIES COST ESTIMATE

Cell	$ 3.3M
Remote handling facilities	1.2
Torus structure	3.2
METS system buildings	1.3
Receiving, assembly, and maintenance areas	1.4
Tritium waste building	0.7
Control room	0.6
Electrical power	0.8
Utilities	1.2
Site development	1.6
	$15.3
Engineering 20%	3.1
Contigency 10%	1.5
Total	$19.9M

TABLE 8-11

COST ESTIMATE FOR SFTR SYSTEM

First wall and Marshall coil	$ 12.38M
Implosion-heating system	32.98
Preionization system	1.69
Primary shield	22.54
Compression bank (Phase I)	31.09
Tritium handling and vacuum system	3.96
Diagnostics system	3.05
Control system	5.57
Facilities	19.90
	133.16M
METS system (Phase II)	72.80
Total	$205.96M

for Phase II. The cost of the experiment is therefore $205.96M. Some of the cost associated with the Phase I compression bank ($31.09M) could be saved by going directly to a METS system.

8.4 CONSTRUCTION SCHEDULE

Figure 8-1 shows a simplified logic schedule for the SFTR project. The timing is based on the assumption that funding for early facility design and site preparation will be available by October 1977, and major procurement and construction funds approved by October 1978. The logic diagram shows the milestones for the various subsystems in the project, as well as the more critical design review points and information restrictions.

Certain equipment items will require the longest possible developmental time, and will determine the schedule's critical paths:

- Plasma tube first wall (ceramic)
- Marshall coil assembly
- Compression field coil
- Compression field metal-to-metal crowbar switch
- 150-kV shock heating field capacitors
- Superconductive energy-storage coil
- Cryogenic disconnect switch.

The schedule assumes that much of the materials research and fabrication development for these items will proceed well in advance of any specific construction funding for SFTR. Actually, much work is already in progress.

Facility construction (Title III) is estimated to require 3 yr. So that equipment installation and checkout can begin as early as possible, it is assumed that beneficial occupancy is obtained 9 months before facility completion. This will allow sufficient time for Phase I operations (capacitor-driven compression bank) to begin by April 1984. Certain systems closely associated with the facility, e.g., cell cleanup system, remote handling equipment, and the cryogenic system refrigeration machinery, may be installed even before the beneficial occupancy date.

After an estimated 1 yr of Phase I experimental operations, the facility will be converted for Phase II (superconductive-coil-driven compression bank) operation. This will involve retrofitting the compression capacitor bank for operation as a transfer bank, and a period of integrated systems checkout with the METS system. Phase II operations should begin by January 1986.

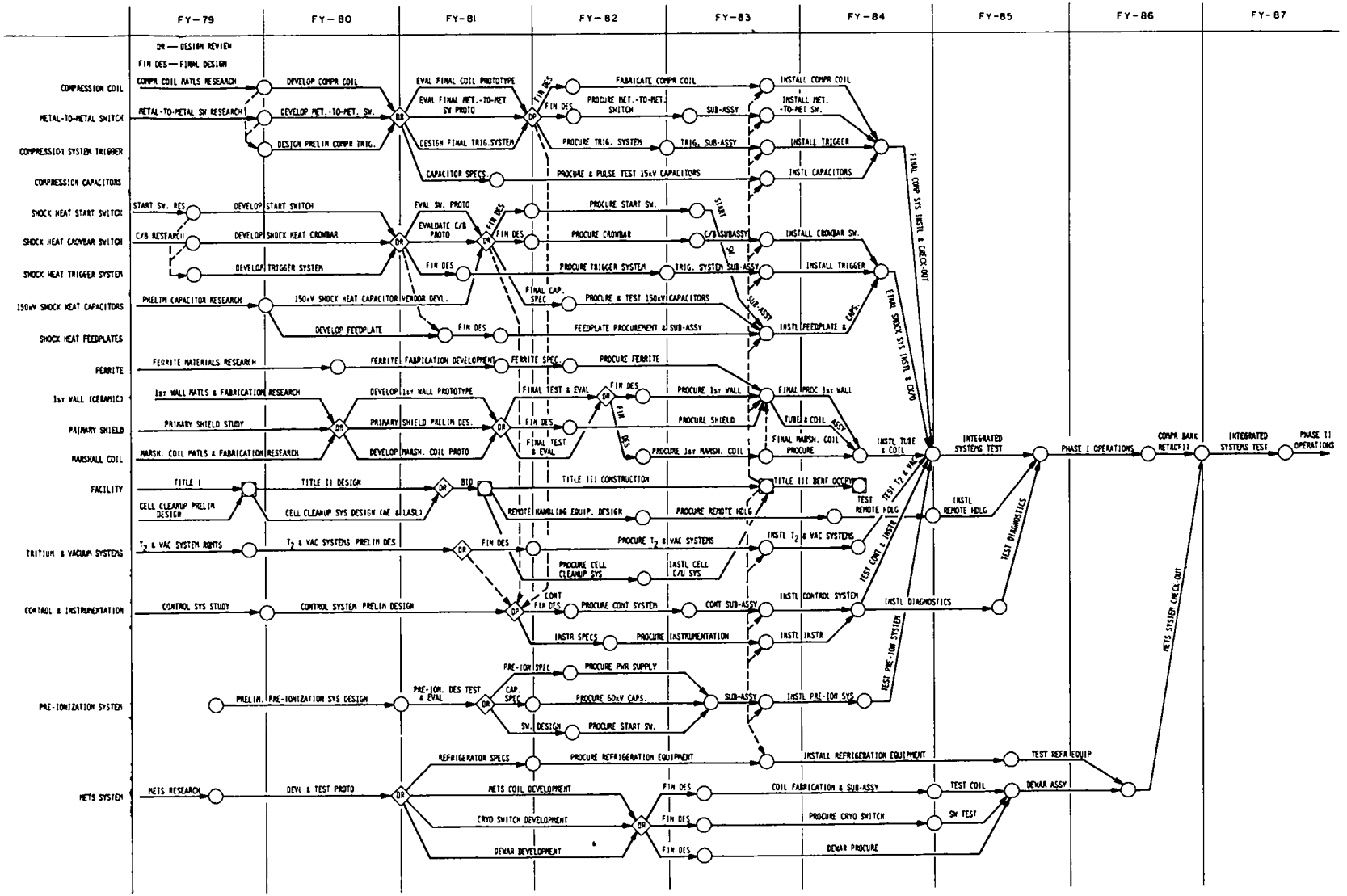

Fig. 8-1.
SFTR construction schedule.

APPENDIX I

ROOM TEMPERATURE MAGNETIC ENERGY STORAGE

A.1 SUMMARY

The Warm METS system proposed here is a viable magnetic energy transfer and storage alternative for SFTR. It will provide the compression energy by conventional technology, using a room temperature 500-MJ energy-storage inductor. The inductor is to be charged on-line from the Public Service Co. of New Mexico's 115-kV transmission system. This system is feasible and when built with stationary equipment it is the most economical system for magnetic energy storage. Rotating machinery is therefore not discussed. The compression coil, energy transfer capacitors, and transfer initiating current interrupters are the same as for the superconducting METS.

A.2 CIRCUIT DESCRIPTION

The circuit is shown in Fig. A-1. The energy-storage inductor is described in Sec. A.3, its dc resistance and inductance are 0.18 Ω and 1.344 H. During energy transfer, the resistance rises to 140 Ω because of eddy currents.

The inductor is charged by the rectifier transformer circuit shown in Fig. A-1. The transformer is energized from the 115-kV bulk power system. The load seen by the 115-kV system is plotted in Fig. A-2, where the time constant T = 7.4 s and the time interval over which charging takes place is 34 s. The maximum load occurs at the end of charging just before the load is dropped. Turn-on and load dropping are both effected by the 115-kV circuit breaker Cb1. The switching sequence is given in Table A-1. The load dropped at the end of charging is 141 MVA, 136 MW as seen in Fig. A-2.

The 12-phase rectifier transformer uses freewheeling diodes and is rated at two-thirds the peak load or 90 MVA with 8% impedance. The output rectifier uses solid state diodes.

A load study[1] shows that light flicker and the possible cumulative effect of the 2000 mechanical pulses on the turbine generators at Los Alamos when SFTR fires must be considered in the design. Both effects can be tolerated if:

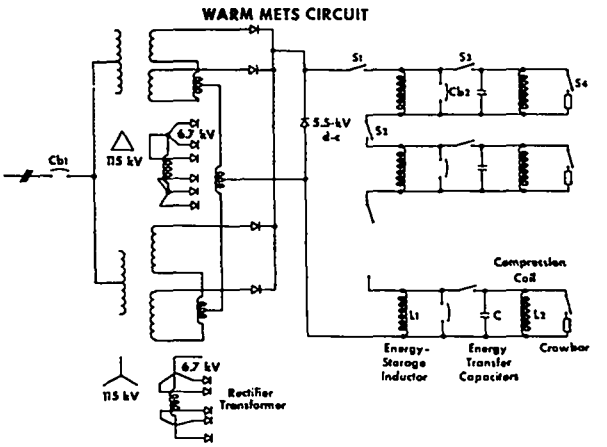

Fig. A-1.
Circuit for direct line charging of an inductive energy-storage ring.

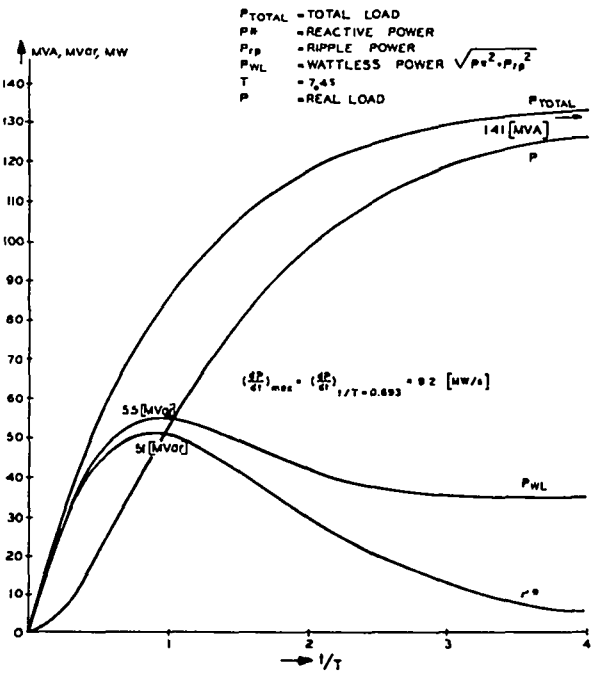

Fig. A-2.
Power load to the 115-kV line.

TABLE A-1

SWITCHING SEQUENCE

Operation		Breakers[a]		Switches			
No.	Description	CB1	CB2	S1	S2	S3	S4
1	Prepare circuit circuit for charging	0	0	1	1	0	0
2	Start charging	1	0	1	1	0	0
3	End charging	0	0	1	1	0	0
4	Reduce I^2R loss at idling	0	1	1	1	0	0
5	Prepare for energy transfer	0	1	0	0	1	0
6	Initiate transfer	0	0	0	0	1	0
7	Crowbar	0	0	0	0	1	1

[a]0 = open; 1 = closed.

1. The 345-kV transmission line from the Four Corners plant to Albuquerque with a 345/115-kV transformer is in operation in 1980; and
2. One 115-kV transmission line from Norton to Los Alamos is dedicated at least during the hours that the experiment is run or an additional 115-kV transmission line is installed from Norton at a cost of approximately $0.9M.

The New Mexico Public Service Company's bulk power system as planned for 1980 is shown in Fig. A-3. This system includes the 345/115-kV substation extension at Norton. The load study indicates the voltage levels listed in Table A-2. The table shows that the voltage drop on the 115-kV side of the experiment will be 9.6% and the flicker when the load is dropped will be 2.3% at Santa Fe (Zia). This flicker is close to the limit of acceptability.

The circuit breaker Cb1 is a 115-kV breaker with vacuum cells and with a maximum interrupting rating of 4 kA and momentary rating of 40 kA. The circuit breakers Cb2 are 300- to 400-kJ units as developed for the METS program.

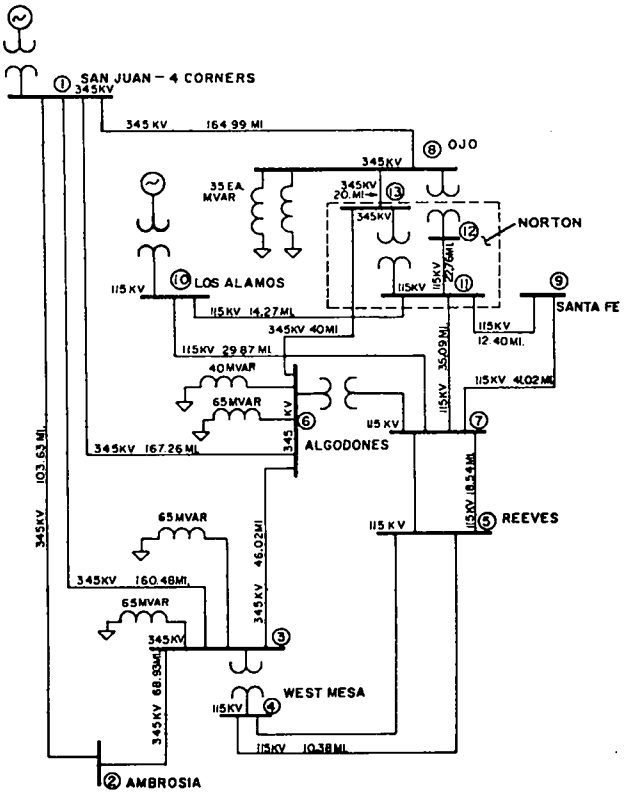

Fig. A-3.
The New Mexico Public Service Company's power system for 1980.

A.3 ENERGY-STORAGE INDUCTOR

A.3.1 General Description

Only the most important design equations and features of the energy-storage inductor are given here. All derivations and many design details are

TABLE A-2

UNIT VOLTAGE AT SEVERAL POINTS IN THE BULK POWER SYSTEM WITH DEDICATED 115-kV LINE NORTON TO LOS ALAMOS

Load		Voltages at Locations[a]			
MW	MVar (reactive)	ETA[b]	Zia	Norton	Experiment
0	0	1.025	1.019	1.031	1.032
55	55	.996	.991	.997	.936
136	10	1.002	.999	1.005	.985

[a]These unit voltages have been scaled linearly with load from a similar table given in Ref. 2 for different load numbers: for 40 MW, 40 MVar and for 100 MW, 7 MVar.

[b]Eastern Tech Area.

reported in Ref. 2. The inductor consists of 1280 round coils with two turns each, all coils assembled in toroidal fashion. An alternative design, in which each coil is surrounded by a two-turn secondary winding designed for energy transfer at improved transfer efficiency, was rejected because of extra energy requirements for the counterpulse circuit. Economy requires the use of copper conductors for room temperature operation, although a cryogenic aluminum design is feasible.

A.3.2 Charging Circuit

The inductor is charged from a virtually constant voltage source. The current is thus given by

$$i = \frac{V}{R}\left(1 - e^{-\delta\tau}\right) \tag{1}$$

where

$$\delta \equiv \frac{1}{T} = R/L \tag{2}$$

and

$$\frac{V}{R} \equiv I_o \tag{3}$$

and where τ denotes time. The loss over a charging cycle is given by

$$R\int_o^t i^2\, d\tau = I_o^2 L\left(x + 2e^{-x} - \frac{1}{2}e^{-2x} - \frac{3}{2}\right) \tag{4}$$

where $x \equiv \delta t$.

We have for each of the 1280 coils, $I_o = 27.1$ kA, t = 34 s, T = 7.4 s, L = 1.05 mH, and R = 0.14 mΩ.

The total energy fed into the R-L system (W_{tot}) when expressed in units of the total stored magnetic energy (W_m) has the following limit when $x \ll 1$;

$$\lim_{x<<1}\left(\frac{W_{tot}}{W_m}\right) \approx 1 + \frac{2}{3}x \tag{5}$$

For large values of x,

$$\lim_{x>>1}\left(\frac{W_{tot}}{W_m}\right) \approx 2(x - 1) \tag{6}$$

The corresponding expressions for the maximum power demand occurring at the end of the charging cycle are[2]

$$\lim_{x<<1}\left(\frac{P_{max}}{W_m}\right) \approx \frac{2}{t} + \frac{1}{T} \tag{7}$$

$$\lim_{x>>1} \left(\frac{P_{max}}{W_m} \right) \approx \frac{2}{T} \quad . \tag{8}$$

Equations (5) and (6) show that charging is done with minimum power loss, if $x \ll 1$, for which energy input equals energy stored. Though Eq. (7) is a good approximation for the charging cycle of a superconducting coil, Eq. (8) is used for Warm METS where T = 7.4 s, x = 4.62, and hence $W_{tot}/W_m = 7.42$; $P_{max}/W_m = 0.275\ s^{-1}$.

The inductance of a thick-walled toroid is[2]

$$L = \lambda \mu N^2 \frac{A}{\ell} \tag{9}$$

where

μ = $0.4\pi\ 10^{-8}$ H/cm
λ = toroidal form factor
N = number of turns
A = effective flux linkage area
ℓ = coil length (if the solenoid consists of M identical coils, we have $\ell = 2\pi R_{maj}/M$).

The toroidal form factor for the minor aperture radius R_i and the major toroidal radius R_{maj} is given by

$$\lambda \approx 1 + \frac{\kappa}{4} \left(\frac{R_i}{R_{maj}} \right)^2 \tag{10}$$

where

$$\kappa = 1 + \frac{2}{3} \frac{b}{R_i} + \frac{1}{6} \left(\frac{b}{R_i} \right)^2 \tag{11}$$

and where the coil height

$$b = \frac{Nq}{p\ell} \tag{12}$$

with q denoting the conductor cross-sectional area, and p the coil packing factor.

The flux linkage area is then

$$A = R_i^2\ \pi\kappa \quad . \tag{13}$$

We choose b = 41.2 cm, R_i = 166.0 cm, R_{maj} = 1001 cm, p = 0.336, λ = 1.007, κ = 1.1755, N = 2, and use a total of 1280 coils.

The maximum flux density is B_{max} = 1.68 T, with a corresponding minimum in the aperture B_{min} = 1.20 T. The center value within the minor circle is B_o = 1.40 T.

The dc resistance of each of the 1280 coils is given by

$$R_{dc} = \rho N \frac{2\pi \left(R_i + \frac{b}{2} \right)}{q} \tag{14}$$

where

$$\rho = \rho_o\ (1 + \alpha\theta) \tag{15}$$

and

ρ_o = $10^{-4}/61\ \Omega$cm
α = $1/234.5\ °C^{-1}$
θ = average copper temperature

The pulse resistance can be approximated by an ac resistance consistent with the frequency spectrum described in Sec. A.3.3. The ac resistance is given by

$$R_{ac} = R_{dc} \left[\phi(\zeta) + \psi\ (\zeta) \frac{\eta}{m} \sum_{\nu=1}^{m} \nu(\nu-1) \right] \tag{16}$$

where

$$\zeta = \frac{h}{\delta} \tag{17}$$

with

h = strand thickness
δ = skin depth
= $\sqrt{(2/(\omega\mu)(\frac{\ell}{a}))} \approx$ {28 cm for charging; 0.25 cm for discharging}
a = Σ copper widths over ℓ
m = (number of conductors)(number of strands stacked radially)
η = transposition weight (= 1 for the perfectly transposed winding; = m for the nontransposed winding)

and

$$\phi(\zeta) = \zeta \frac{\sinh 2\zeta + \sin 2\zeta}{\cosh 2\zeta - \cos 2\zeta} \tag{18}$$

$$\psi(\zeta) = 2\zeta \frac{\sinh \zeta - \sin \zeta}{\cosh \zeta + \cos \zeta} \quad . \tag{19}$$

Of course, $\phi(0) = 1$; $\psi(0) = 0$. Equations (18) and (19) show that with our time constant T = 7.38 s there is basically no need for stranding, because we get $R_{ac}/R_{dc} = 1.001$. However, because of the requirement that the flux be extracted within 0.7 ms, the winding must be stranded, as shown in the following sections.

A.3.3 Flux Extraction

The energy is transferred from the storage inductor to the compression coil by way of the transfer capacitors C shown in Fig. A-1. The current in the compression coil for this oscillatory transfer is easily derived, and may be written

$$\frac{i_2}{I_{10}} = \left(\frac{\omega_2}{\Omega_0}\right)^2 \cdot \left[1 - \left(\frac{\Delta}{\Omega} \sin \Omega t + \cos \Omega t\right) e^{-\Delta t}\right] \tag{20}$$

where I_{10} is the initial current in the energy-storage coil, and

$$\omega_1^2 = 1/(L_1 C) \qquad \Omega_0^2 = \omega_1^2 + \omega_2^2$$

$$\omega_2^2 = 1/(L_2 C) \qquad \Delta = \delta_1 + \delta_2$$

$$\delta_1 = R_1/L_1 \qquad \Omega^2 = \Omega_0^2 - \Delta^2 \quad .$$

$$\delta_2 = R_2/L_2$$

The following numbers apply for the present design:

$L_1 = 1.05$ mH; $L_2 = 0.98$ mH; $C = 0.101$ mF

for which the required stored energy $1/2\ L_1 I_{10}^2$ may be approximated by the empirical formula with $R_2 =$ 50 mΩ being the fixed parameter:

$$W_1/W_0 \approx (1 + 0.033\ R_1/R_2)\Big|_{R_2 = 0.05\ \Omega} \quad , \tag{21}$$

which is easily verified with Eq. (20) for a limited range in W_1. Here, $W_o = 459.8$ MJ. Equation (21) shows the importance of low ac resistance. With $R_1/R_2 = 2$, for example, 6.6° of the stored energy is dissipated during the transfer.

It is important to consider the eddy current problem because the 7.4-s time constant requires substantial radial thickness of the winding (i.e., 41.2 cm), and because the 0.7-ms transfer time implies a frequency of 0.7 kHz. Figure A-4 shows the frequency spectrum for the compression coil current pulse, and the 0.7-ms rising pulse. The current decays with a 250-ms time constant following the crowbar of the coil. The low frequency components are generated by the duration of the pulse, and the high frequency components by the fast rise. The 0.7-kHz frequency used for ac resistance calculations corresponds to the one indicated by an arrow in the frequency spectrum. It can be seen that the area under the frequency spectrum is divided approximately in half by the frequency chosen for the resistance calculations.

We propose 100 conductor strands and obtain from Eqs. (16)-(19) $\zeta = 0.928$, $\phi = 1.064$, $\psi = 0.240$ for $\omega = 4490\ s^{-1}$, which yields a ratio of ac resistance to dc resistance of $R_{ac}/R_{dc} = 801$, and thus $R_{ac} =$ 0.111 Ω. For this set of numbers we obtain from Eq.

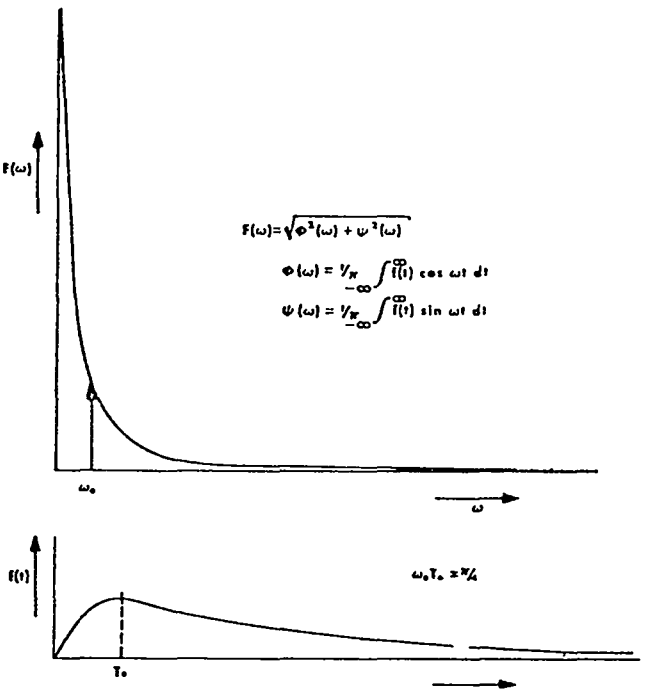

Fig. A-4.
Frequency spectrum (above) of the compression coil current waveform (below).

(21) the energy loss in the storage coil ($W_1/W_0 - 1$) = 7.4%, and the total transfer loss in both energy-storage coil and compression coil ($W_1/W_2 - 1$) = 11.6%. With the compression coil design current I_2 = 26.6 kA, corresponding to a compression field energy W_2 = 443 MJ, and a central field of 5.1 T, the stored energy is W_1 = 494 MJ.

The coil winding is shown in Figs. A-5, 6, and 7, with Fig. A-5 indicating the dimensions of the toroidal winding, and Figs. A-6 and 7 showing the dimensions of an individual coil (all dimensions in millimeters).

A.3.4 Temperature Rise and Cooling

The resistivity of the coils is given by Eq. (14) so one can determine the instantaneous temperature rise $\Delta\Theta$ resulting when all

$$\int_0^\tau I^2 R \, dt$$

energy is stored in the thermal mass of the conductor,

$$\Delta\Theta = \frac{1}{\alpha}\left(e^{\alpha F(\tau)} - 1\right) \qquad (22)$$

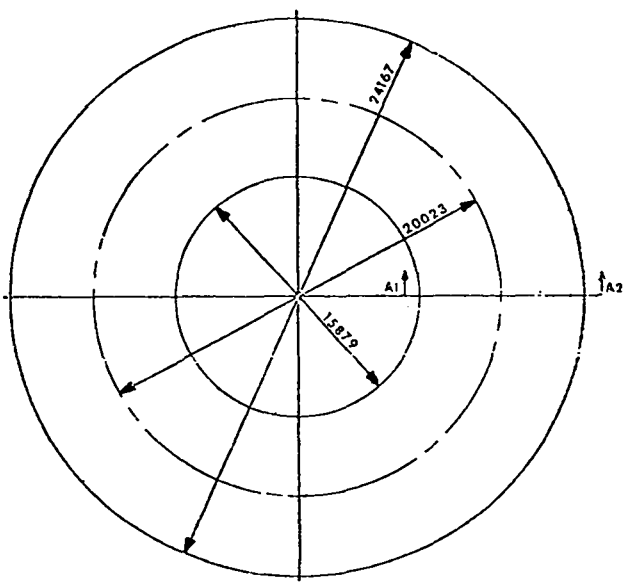

Fig. A-5.
A 24-m-diam toroidal inductive storage ring consisting of 1280 coils. One of the coils making up this torus is shown in Fig. A-6.

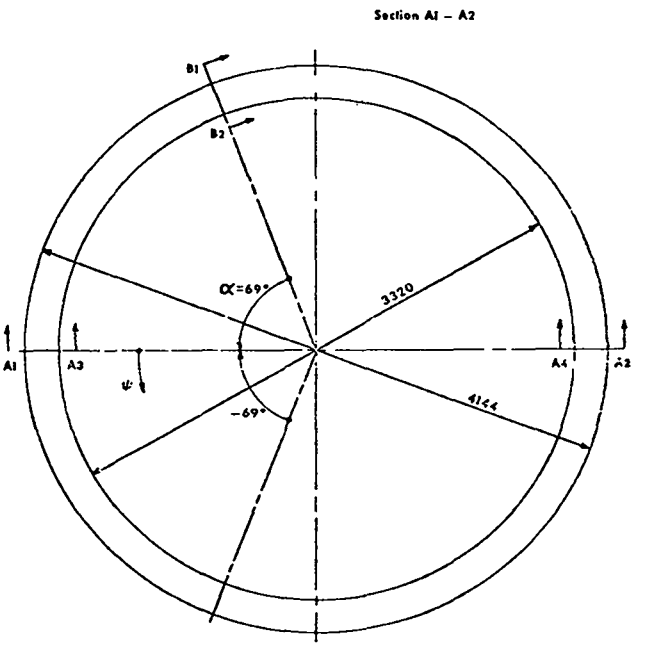

Fig. A-6.
Dimensions of each of the 1280 individual coils of the storage ring.

where

$$F(\tau) = \frac{\rho_o T}{\gamma C_m}\left(\frac{I_o}{q}\right)^2 \left(x + 2\,e^{-x} - \tfrac{1}{2}\,e^{-2x} - \tfrac{3}{2}\right) \qquad (23)$$

with

C_m = 0.389 J/g°C } for copper
γ = 8.9 g/cm^3 }
T = L/R
x = τ/T
q = conductor cross-sectional area cm^2
ρ_o = resistivity at start of pulse.

The temperature rise per pulse is $\Delta\Theta$ = 7.6°C, and the temperature rise for any number of pulses is less than 20°C if the winding is water-cooled at a flow rate of 20 ℓ/s. The cooling water requirement is given by this flow rate at an average load of 6 MW. The consequences of coolant flow interruption are discussed later.

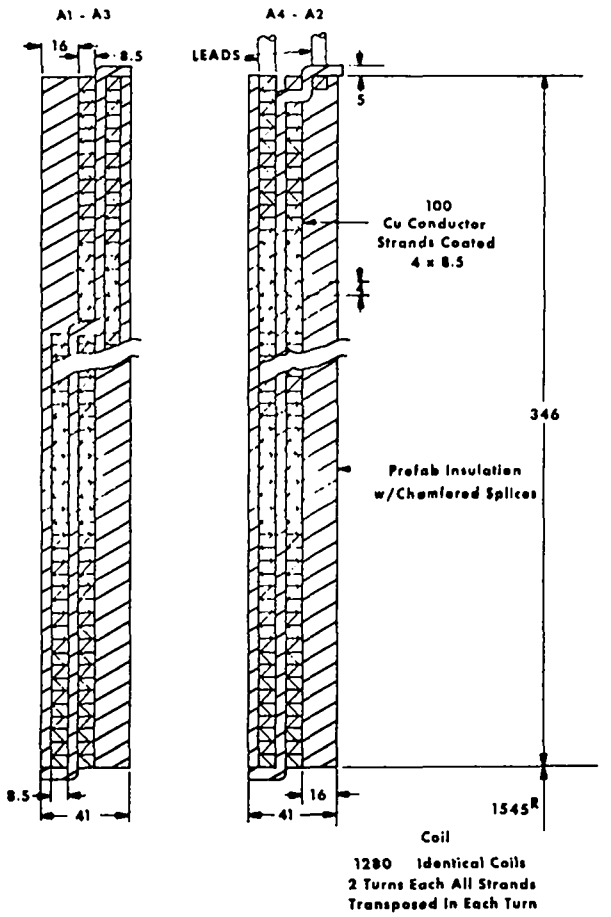

Fig. A-7.
Cross sections of the individual coils.

A.3.5 Structural Considerations

The basic structural design requirements have been developed in conceptual form from the preliminary design data of this proposal. These considerations include:

1. Support of the torus against magnetic pulse forces tending to move each coil inward towards the major axis.
2. Support of each coil against hoop stresses developed by magnetic pulse forces.
3. Support of the torus weight as a whole.

The analysis in this report covers concepts related to the above three structural considerations, including the selection of materials and sizing studies.

A.3.5.1 Torus Inner Support Structure

A concrete ring structure is envisioned for supporting the torus against the net magnetic force in the midplane. This magnetic force tends to move each turn towards the major axis. Figure A-8 illustrates the concept. The magnetic force per turn is

$$F = 2\pi B_o I R_{maj} \left(\frac{1}{\sqrt{1 - y^2}} - 1 \right) \qquad (24)$$

with B_o = 1.4 T, I = 27.1 kA, and where y = 0.195 is the ratio of minor to major diameter. We find F = 46.6 kN/turn (10.5 kips/turn). Since there are two turns per coil, F_c = 2F = 93.2 kN/coil (21 kips/coil).

There are 1280 pie-shaped coils around the major axis of the torus. The average width of each slice is given by

$$\bar{w}_c = \frac{2\pi R_{maj}}{1280} . \qquad (25)$$

Using (25) gives $\bar{w}_c$ = 0.0491 m. The innermost radius of the torus is b = 7.94 m, and the width of each coil at that point is w_{ci} = 0.0390 m.

Assuming that we select a concrete cylinder of outer radius b, (conservatively) to support a 90° arc of the inner wall of the torus as shown in Fig. A-8, and that a uniform pressure p is imparted to the contact surface of the concrete cylinder, we have

$$F_c = \int_{\frac{\pi}{4}}^{\frac{3\pi}{4}} p \sin\theta \cdot r \, d\theta \cdot w_{ci} \qquad (26)$$

which gives for each coil

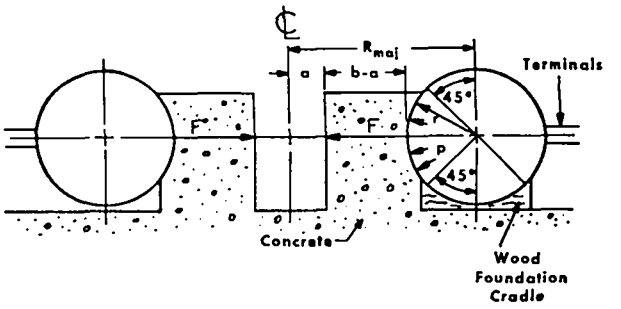

Fig. A-8.
Concrete retaining structure to support the radial magnetic forces F.

$$F_c = \sqrt{2}\, p r w_{ci}$$

$$r = 2.001 \text{ m} \quad . \tag{27}$$

Solving (27) for the pressure p, we have

$$p = \frac{F_c}{\sqrt{2}\, r w_{ci}} \quad . \tag{28}$$

Substituting the data into Eq. (28) gives p = 128 psi.

The maximum compressive hoop stress (in the concrete) for a thick-walled cylinder under uniform external pressure is[3]

$$S_{2max} = - p \frac{2b^2}{b^2 - a^2} \quad . \tag{29}$$

The maximum radial stress is

$$S_{3max} = \tfrac{1}{2} S_{2max} \quad . \tag{30}$$

Selecting 3000-psi concrete material, and a concrete inner radius a = 7.00 m, we obtain

$$S_{2max} = -1100 \text{ psi}$$

$$S_{3max} = -550 \text{ psi}.$$

The minimum factor of safety (F.S.) is

$$\text{F.S.} = 3000/1100 = 2.7.$$

This factor of safety appears to be adequately conservative.

A.3.5.2 Hoop Stress in Coil

Because of the concrete support structure shown in Fig. A-8, and internal pressure in each coil tending to cause uniform dilation of the coils, there will be discontinuity stresses at $\Theta = 45°$ and $\Theta = 135°$. It is desirable to know the magnitude of the stress discontinuities, and whether the windings will be subject to collapse from net compressive stress. To avoid buckling at these points, the magnetic pressure on the coil must exceed the pressure p [Eq. (28)]. Then the coil is always in tension.

Since the peak field at the inside of the torus is 1.68 T, the magnetic pressure is

$$p_m = \frac{B^2}{2\mu_o} = 1.12 \times 10^6 \text{ N/m}^2 = 163 \text{ psi} \quad . \tag{31}$$

This exceeds the pressure p = 128 psi, hence no buckling occurs. Note that the hoop stress is ~5.6 (radius thickness) times p_m where the coil is unsupported, and 5.6 times $p_m - p$ at the concrete support. The discontinuity is therefore 714 psi, which is low. The yield strength of annealed copper is 3200 psi.

A.3.5.3 Cradle Support Design for Foundation of Toroid

The wood foundation cradle in Fig. A-8 must support the coil weight, which is W_t = 280 kg (1721 lb). The bearing area of material supporting each coil is A_b = 0.1355 m^2 (210 $in.^2$). Thus, the bearing unit stress will be $S_b = W_t/A_b$ = 7.1 psi. A toroidal cradle foundation of yellow pine (yield strength is 440 psi for compression across grain) about 6 in. thick at the thinnest point should be sufficient to support the coils. The grain orientation is immaterial because of the low unit stress. Care should be taken to avoid contact with soil, and the wood should be prepared against decay. The foundation could be built in pie-shaped sections for each individual coil. Two circumferential bands of mild steel can be used to ensure against slippage of the pie-shaped sections. There should be negligible meridional stress, so these bands should be pretensioned only enough to provide a compact foundation.

A.3.6 Optimization

The cost vs minor diameter is given in Fig. A-9 for the approximate design parameters, where the maximum flux density in the aperture is the variable; L, R, and field energy being constant. The cost, number of turns, major diameter, and conductor cross section are dependent variables. The cost varies over a range 5 ÷ 1 as one varies the diameter over a feasible range of values. The coil with the least number of turns is the least expensive, and to all intents and purposes the minimum number of turns per section is 2. A torus with only single turn sections would have a minor radius approximately equal to the major toroidal radius and no room would be left for the winding.

For an aluminum conductor, the minimum number of turns per section is 4 (3 not being considered because of poor coil space utilization at 3, 5, 7 turns in double pancake coils) costing approximately $2.8M on the scales of Fig. A-9. Though this number amounts to a savings of approximately 40% of the 4-turn copper coil, the 4-turn aluminum coil costs still more than the 2-turn copper coil.

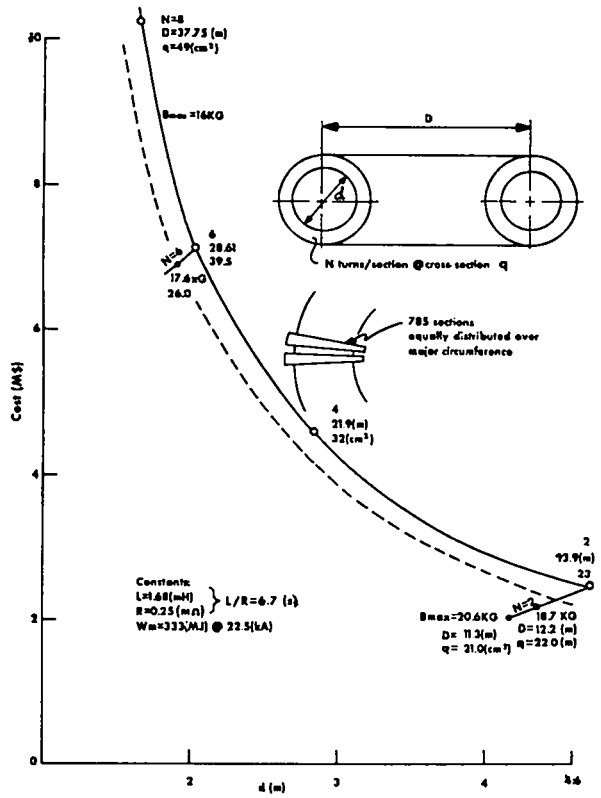

Fig. A-9.
Cost vs minor diameter for different magnetic fields and turn ratios of energy-storage coils.

The cost curves have been determined by calculating the copper weight, and rating it at 4.8 \$/kg. If we base our estimate on 6 \$/kg of coil mass, then the cost of the energy-storage inductor with the design parameters discussed is \$6.1M. For comparison, the outer coils for the 1014 main ring magnets at the Fermilab cost 4.80 \$/kg for material plus manufacturing in 1970; however the 1975 replacement cost is thought to be 8.80 \$/kg.

A.4 SUMMARY OF COST

The cost of the Warm METS option is given in Table A-3. The total cost is equivalent to 7.1 ¢/J of energy transferred into the compression field. The purpose of the switchyard extension at Norton and of the 115-kV transmission line from Norton is explained in the next section.

A.5 OPERATIONAL CONSIDERATIONS

Section A.2 mentions the voltage drops and voltage flicker levels leading to the proposal of the dedicated 115-kV transmission line mentioned there. This line is dedicated to SFTR during its operating hours. The line could in principle be one of the two lines to Los Alamos shown in Fig. A-3, i.e., the one from Norton or the one from Algodones.

TABLE A-3

WARM METS COST SUMMARY

Switchyard extension at Norton	\$ 0.2M
Overhead 115-kV transmission line Norton to SFTR site \$50k/mile	0.9
Switchyard, outdoor, 115 kV, incl. Cb1	0.2
Rectifier transformer	0.6
Rectifier	0.9
Auxiliary equipment and controls	0.6
Engineering	0.2
Disconnect switches	1.3
Energy-storage inductor	6.1
Circuit breaker connecting busses	0.7
1280 current interrupters at \$6.5k each	8.3
Cooling	0.2
Energy transfer capacitor bank, 235 MJ	9.4
Total	\$29.6M

However, during hours of SFTR operation only one transmission line remains for Los Alamos, and that would be insufficient in the event of an outage. For this reason, an additional 115-kV transmission line and the necessary switchyard additions at Norton are listed as line items in the cost summary. The switchyard additions at Norton are to include a 115-kV line circuit breaker. This transmission line would probably use the same right of way as the existing line to the Eastern Tech Area (ETA) and proceed from there to the SFTR site.

Auxiliary power necessary for cooling the water pump, as well as power for the operational controls, would come from the distribution site, but the line circuit breaker Cb1 would receive power from the dedicated 115-kV system. The circuit protection is designed to trip Cb1 when the site distribution system fails. This is necessary to prevent continuation of pulsed operation when auxiliary power is down.

The station battery system for the SFTR switchyard is to be operated from the site distribution system and not from the dedicated line system. Switch Cb1 is operated from the station battery system as is customary.

REFERENCES (Appendix I)

1. W. N. Hannah, "Service to Proposed Pulsed Load at Los Alamos," private communication dated March 20, 1975.

2. Herbert F. Vogel, Robert J. Bartholomew, and M. Kristiansen, "500 Megajoule Inductive Energy Storage and Transfer at Room vs Liquid Nitrogen Temperature," Los Alamos Scientific Laboratory report in preparation.

3. Raymond J. Roark, **Formulas for Stress and Strain** (McGraw-Hill, 1965).

APPENDIX II

CABLE PENETRATIONS

Of major concern for tritium leakage is the penetration of the biological shield by large numbers of electrical cables. Each 40-cm module of the reaction vessel will require approximately 36 cables for its operation. These include high voltage pulse, dc charging, control, and diagnostics types of varying sizes. The largest cables will be pulse types with a diameter of 2.86 cm. For purposes of space allocation it will be assumed that all cables are of this larger size.

The reaction vessel torus will consist of 640 modules requiring between 23 000 and 24 000 cables, most of which must penetrate the biological shield while maintaining the integrity of the core structure with respect to neutron radiation, fire, and possible tritium spills.

Conduits for the cables will be located in the roof of the shield and in the floor (Fig. A-10). The roof conduits will handle the cables required for the charging and firing of the shock heating system, while those in the floor will connect to the METS banks to drive the compression system.

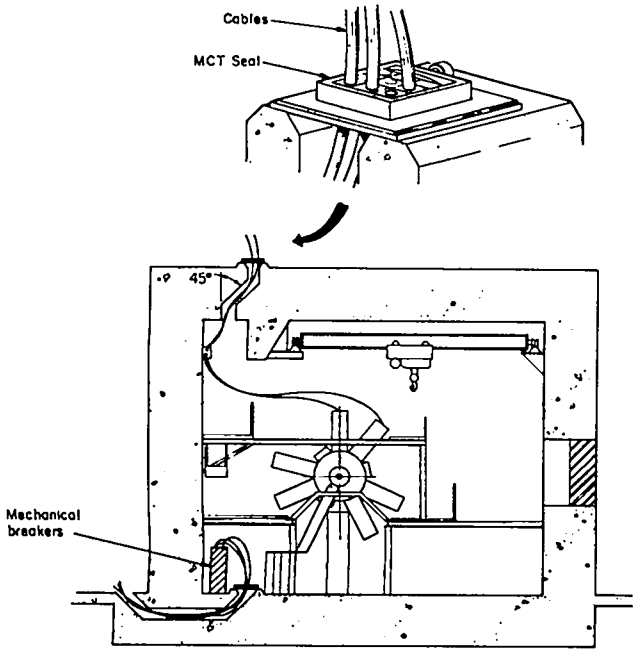

Fig. A-10.
Cell cross section showing cable penetrations.

The necessary number of cables will require a 15 x 15 cm^2 conduit every 38 cm around the torus, both in the roof and floor. This will allow cable packing of 40% or less, even assuming the larger cable sizes. Conduits will be steel or glass-epoxy. Because this number of conduits will remove about 40% of the concrete along one portion of the roof structure, additional steel reinforcing will be required between the conduits.

The conduits will be directed at an angle of 45° from the vertical to prevent direct neutron streaming from the reaction tube. In addition, a concrete beam will be cast as part of the roof structure to neutron-shadow the conduit orifices and to make up the mass loss in the shield caused by the conduit penetrations. The cables themselves will aid in neutron shielding as their bulk is largely PVC and polyethylene.

The cables will be sealed by Multi Cable Transit (MCT) assemblies, manufactured by Nelson Electric. The assembly consists of a heavy steel frame with modular rubber blocks that are compressed around each cable as shown in Fig. A-10. The seals accommodate cable sizes from 5/32 to 3-3/4 in. in diameter, and cables can be added or removed with relative ease. The MCT units provide an air seal up to 25 psi, and are resistant against 1700°F fire for 1 h or longer.

While the MCT assemblies are designed to be airtight, the integrity of the cable penetrations against a tritium spill is not entirely dependent on the mechanical perfection of these air seals. Of equal importance is the maintenance of a negative air pressure of approximately 1 in. of water within the shield structure. This effectively prevents diffusion of tritium upstream through a leak in a cable.

Assume a leak equivalent to a 1/8-in.-diam round hole:

$d = 0.01$ ft (1/8-in. diameter)
$\ell = 0.2$ ft (Length of seal)
$p = 5.2\ \mathrm{lb/ft^2}$ (1 in. H_2O)
$\rho = 0.075\ \mathrm{lb/ft^3}$ (Density of air).

Then the equivalent head of air is

$$h = \frac{p}{\rho} = \frac{5.2\ \mathrm{lb/ft^2}}{0.075\ \mathrm{lb/ft^3}} = 69.3\ \mathrm{ft}\ .$$

Using the Darcy equation for flow through a duct

$$h = f \frac{\ell}{d} \frac{V^2}{2g}$$

$$69.3 = f \frac{0.2}{0.01} \frac{V^2}{2(32.2)}$$

$$fV^2 = 223.55 ,$$

where

V = Flow velocity
g = 32.2 ft/s^2
f = Darcy friction factor

and the Reynolds number is

$$Re = \frac{Vd}{\nu}$$

where

ν = Kinematic viscosity of air = 1.7 x 10^{-4} ft^2/s

$$Re = \frac{V(0.01)}{1.7 \times 10^{-4}} = 58.82 \ V .$$

If we assume laminar flow through the 1/8-in.-diam hole:

$$f = \frac{64}{Re} \quad \text{and} \quad h = \frac{64}{Re} \frac{\ell V^2}{d \ 2g} .$$

Substituting for Re

$$h = \frac{32 \ \nu \ell V}{g d^2} .$$

The velocity is

$$V = \frac{h g d^2}{32 \ \nu \ell} = 205 \ ft/s .$$

With this velocity the Reynolds number is

$$Re = \frac{Vd}{\nu} = \frac{205(0.01)}{1.7 \times 10^{-4}} = 12 \ 059$$

which indicates turbulent flow contrary to the laminar assumption. We must therefore use the Darcy curves to find values of the friction factor f that will satisfy the two equations:

$$V = \left[\frac{223.55}{f}\right]^{1/2} \quad \text{and} \quad Re = 58.82 \ V .$$

Relative roughness is assumed to be in the order of 0.04.

A velocity of 55 ft/s gives

Re = 3235 and f = 0.072

$$V = \left[\frac{223.55}{0.072}\right]^{1/2} = 55.7 \ ft/s .$$

Thus, the flow in a leak of this size is in the region between laminar and turbulent flow. Actual leaks caused by a misfit in the rubber clamping blocks would be in the form of thin gaps in which the flow would lie in the laminar range.

Assuming a laminar flow through the leak and a given tritium concentration inside the shield structure, the diffusion equation

$$\frac{\partial c}{\partial t} + V \frac{\partial c}{\partial x} = D \frac{\partial^2 c}{\partial x^2}$$

can be used to obtain the concentration of tritium to appear at the outside of the leak.

For steady-state conditions

$$\frac{\partial c}{\partial t} = 0$$

$$V \frac{dc}{dx} = D \frac{d^2 c}{dx^2} .$$

The solution of this equation[1] is

$$\frac{C}{C_o} = \exp\left(-\frac{Vx}{D}\right)$$

where

C_o = T_3 concentration within the containment
C = T_3 concentration just outside the containment

V = Gas flow velocity through the leak
x = Distance along leak
D = Diffusion constant for tritium.

The diffusion constant for hydrogen in air[2] is 0.611 cm^2/s. Converting units and adjusting for the higher atomic weight of tritium, we obtain

$$D_{T_3 \text{ in } H_2} = 5.37 \times 10^{-4} \text{ ft}^2/\text{s} .$$

Using this value of D and the flow velocity found above, we can get the relative tritium concentration ratio outside and inside the containment:

$$\frac{C}{C_o} = \exp - \left[\frac{55 \times 0.2}{5.37 \times 10^{-4}} \right] = e^{-20484} .$$

The value of C/C_o is so small as to indicate that the concentration-driven diffusion of tritium against the pressure-driven flow through the duct is essentially zero.

If we now postulate a narrow slot-like leak 0.010 in. wide and 1.0 in. long and perform the same exercise we get

Hydraulic radius of slot

$$= d_r = \frac{\text{Area of slot}}{\text{Perimeter of slot}}$$

$$d_r = \frac{(1.0)\ (0.010)}{2.02}$$

$$\cong 0.005 \text{ in.} = 0.0004 \text{ ft.}$$

Using four times d_r for narrow orifices, the velocity is

$$V = \frac{hg(4d_r)^2}{32\nu\ell} = 5.25 \text{ ft/s}$$

and

$$Re = \frac{V(4d_r)}{\nu} = \frac{5.25(0.0016)}{1.7 \times 10^{-4}}$$

$$= 49.4 \text{ (Laminar flow)} .$$

Then

$$C/C_o = \exp \left(- \frac{Vx}{D} \right)$$

$$= \exp \left(- \frac{(5.25)(0.2)}{5.37 \times 10^{-4}} \right) = e^{-1955} .$$

This concentration ratio is still negligible even with the much lower velocity of flow. Finally, if we assume an extremely narrow leak 0.001 in. wide by 1 in. long we obtain

$$d_r = \frac{1.0(0.001)}{2.002} \cong 0.0005 \text{ in.} = 4 \times 10^{-5} \text{ ft}$$

$$V = \frac{(69.3)(32.2)(16 \times 10^{-5})^2}{32(1.7 \times 10^{-4})(0.2)} = 0.053 \text{ ft/s}$$

and the concentration ratio is

$$C/C_o = \exp \left(- \frac{(0.053)(0.2)}{5.37 \times 10^{-4}} \right) = e^{-19.7}$$

$$C/C_o = 2.7 \times 10^{-9} .$$

Even with extremely fine leaks the concentration ratio is lower by more than 8 orders of magnitude. The conclusion to be drawn is that the cable seal system will be effective as long as there is negative air pressure within the containment.

Installed cable seals will cost between $5 and $6 per cable, giving a total cost of $115 000 to $144 000 for the complete torus.

REFERENCES (Appendix II)

1. J. W. Dailey and D. R. F. Harleman, **Fluid Dynamics** (Addison Wesley, 1966).

2. D. E. Gray, Ed., **American Institute of Physics Handbook** (McGraw-Hill, 1972).

☆ US GOVERNMENT PRINTING OFFICE: 1976—677-343/90